

DTIC FILE COPY



AGARD-CP-459

AGARD-CP-459

AD-A218 658

# AGARD

ADVISORY GROUP FOR AEROSPACE RESEARCH & DEVELOPMENT

7 RUE ANCELLE 92200 NEUILLY SUR SEINE FRANCE

AGARD CONFERENCE PROCEEDINGS No.459

## High Resolution Air- and Spaceborne Radar

RESTRICTION STATEMENT A  
Approved for public release;  
Distribution Unlimited

DTIC  
ELECTE  
JAN 24 1990  
S E D

NORTH ATLANTIC TREATY ORGANIZATION



DISTRIBUTION AND AVAILABILITY  
ON BACK COVER

90 01 23 2 48



AGARD-CP-459

NORTH ATLANTIC TREATY ORGANIZATION  
ADVISORY GROUP FOR AEROSPACE RESEARCH AND DEVELOPMENT  
(ORGANISATION DU TRAITE DE L'ATLANTIQUE NORD)

AGARD Conference Proceedings No. 459  
HIGH RESOLUTION AIR- AND SPACEBORNE RADAR

Accession For	
NTIS GRA&I	<input checked="" type="checkbox"/>
DTIC TAB	<input checked="" type="checkbox"/>
Unannounced	<input type="checkbox"/>
Justification	
By	
Distribution/	
Availability Codes	
Dist	Avail and/or Special
A-1	

Papers presented at the Avionics Panel Symposium held in The Hague, Netherlands  
8-12 May 1989.

## THE MISSION OF AGARD

According to its Charter, the mission of AGARD is to bring together the leading personalities of the NATO nations in the fields of science and technology relating to aerospace for the following purposes:

- Recommending effective ways for the member nations to use their research and development capabilities for the common benefit of the NATO community;
- Providing scientific and technical advice and assistance to the Military Committee in the field of aerospace research and development (with particular regard to its military application);
- Continuously stimulating advances in the aerospace sciences relevant to strengthening the common defence posture;
- Improving the co-operation among member nations in aerospace research and development;
- Exchange of scientific and technical information;
- Providing assistance to member nations for the purpose of increasing their scientific and technical potential;
- Rendering scientific and technical assistance, as requested, to other NATO bodies and to member nations in connection with research and development problems in the aerospace field.

The highest authority within AGARD is the National Delegates Board consisting of officially appointed senior representatives from each member nation. The mission of AGARD is carried out through the Panels which are composed of experts appointed by the National Delegates, the Consultant and Exchange Programme and the Aerospace Applications Studies Programme. The results of AGARD work are reported to the member nations and the NATO Authorities through the AGARD series of publications of which this is one.

Participation in AGARD activities is by invitation only and is normally limited to citizens of the NATO nations.

The content of this publication has been reproduced directly from material supplied by AGARD or the authors.

Published October 1989

Copyright © AGARD 1989  
All Rights Reserved

ISBN 9783305301



Printed by Specialised Printing Services Limited  
40 Cingwell Lane, Loughborough, Leicestershire LE11 3JZ

## THEME

Imaging techniques are important sources of information in military operations. They may serve for purposes such as target detection and location, reconnaissance, classification and identification of fixed or moving objects as well as for orientation over unknown terrain. Despite considerable advances in electro-optical imaging systems the radar sensor has become an attractive alternative for several reasons: large range performance, penetration of weather, smoke, dust and foliage, day and night operation. On the other hand high resolution radar techniques such as synthetic aperture radar (SAR) and inverse synthetic aperture radar (ISAR) promise geometrical resolution of about 1m and less.

The proposed symposium is focussed mainly on SAR and ISAR techniques. Conventional imaging radar such as side-looking radar (SLAR) and MM-wave radar will be considered as well. Furthermore, the use of superresolution signal processing techniques for radar imaging will be addressed. It was the goal of this symposium to:

- present the state-of-the-art of high resolution radar, including descriptions of existing or planned systems and concepts
- identify limitations of existing systems concerning resolution, processing speed, size and weight, ECM resistance etc
- present advances and trends in electronics and microwave technology that promise solutions to the identified issues
- present novel algorithms and architectures for real-time signal and data processing
- discuss new radar imaging principles and applications of military relevance
- consider calibration necessities and possibilities

\* \* \*

Les techniques d'imagerie sont des sources précieuses de renseignements dans les opérations militaires. Elles peuvent servir à différentes fins telles que la détection et la localisation de la cible, la reconnaissance, la classification et l'identification d'objets fixes ou mobiles et l'orientation lors de survol de terrain inconnu.

Malgré les progrès considérables réalisés dans le domaine des systèmes d'imagerie électro-optiques, les senseurs radar représentent aujourd'hui une option intéressante et ceci pour plusieurs raisons:

- grande portée
- pénétration de l'atmosphère, de la fumée, de la poussière et du feuillage
- fonctionnement 24h sur 24h.

D'autre part, les techniques des radars de haute résolution tels que les radars à ouverture synthétique (SAR) et les radars à ouverture synthétique inverse (ISAR) laissent prévoir une résolution géométrique d'environ 1m ou moins.

Le symposium proposé concerne principalement les radars SAR et ISAR, mais les radars à imagerie classique tels que les radars aéroportés à balayage latéral (SLAR) et les radars à ondes millimétriques seront également pris en considération, ainsi que la mise en œuvre de techniques de traitement du signal à très haute résolution, dans l'imagerie radar. Les objectifs du symposium étaient les suivants:

- présenter l'état de l'art dans le domaine des radars de haute résolution à partir de descriptions de systèmes et de concepts actuels ou prévus
- préciser les limites des systèmes existants en ce qui concerne la résolution, la vitesse de calcul, le poids et l'encombrement, le degré d'immunité aux contre-mesures électroniques (ECM) etc...
- présenter les progrès réalisés et les tendances dans le domaine de l'électronique et de la technologie III susceptibles d'apporter des solutions aux questions soulevées
- présenter les nouveaux algorithmes et les nouvelles architectures pour le traitement du signal et le traitement des données en temps réel
- discuter des nouveaux principes de l'imagerie radar et des applications d'intérêt militaire
- examiner les besoins en matière d'étalonnage et leurs possibilités

## AVIONICS PANEL

Panel Chairman: Dr R.W.McPherson  
A DS POI  
Department of National Defence  
M/G: N George R. Peatkes Bldg  
Ottawa, Ontario, K1A 0K2  
Canada

Deputy Chairman: Dr R.Klemm  
Forschungsinstitut für Funk und  
Mathematik EFM  
Neuenhafer Strasser 20  
D 5307 Wachtberg 7  
Federal Republic of Germany

## TECHNICAL PROGRAMME COMMITTEE

Chairman: Dr R.Klemm

## PROGRAMME COMMITTEE MEMBERS

Dr W. Keydel  
Director Institut für Hochfrequenztechnik  
DFVLR e.V.  
D 8033 Oberpfaffenhofen  
Federal Republic of Germany

Ing. I. Crovella  
Aeritalia-Saipu  
Gruppo Sistemi Avionici e Equipaggiamenti  
10072 Caselle Torinese Torino  
Italy

Mr J. Dorcy  
Directeur des Etudes de Syntheses  
ONERA  
29, Avenue de la Division Leclerc  
92320 Châtillon s. Bagneux  
France

Mr Richard L. Wirt  
Chief, Common Avionics Division  
ASD E-NAC  
Wright-Patterson AFB  
OH 45433  
USA

Mr E.W. Jackson  
Business Development Manager  
Marconi Space Systems Ltd  
Anchorage Road, Portsmouth  
Hants PO3 5PU  
United Kingdom

Mr J.P. Hardange  
Ingénieur Groupe GRA-1  
Thomson-CSI  
173 Avenue Pierre Brosolette  
92120-Montrouge  
France

Mr M. Jacobsen  
Manager, Airborne EW Systems  
Dept., Al-G Aktiengesellschaft  
Sedanstraße 10  
D 7900 Ulm  
Federal Republic of Germany

Dr R. Giles  
Chief Scientist  
Thorn EMI Electronics Ltd  
120 Blyth Rd.  
Hayes, Middx UB3 1DJ  
United Kingdom

## AVIONICS PANEL EXECUTIVE

1 Lt Colonel James E. Clay  
Tel: (1) 47 38 57 65 Telex 6101761  
Telex: (33)(1) 47 38 5799

Mailing Address:  
**From Europe and Canada:**  
AGARD OLAN  
ATTN: Avionics Panel  
7, rue Anredde  
92200 Neuilly sur Seine  
France

**From US:**  
AGARD NATO  
ATTN: Avionics Panel  
APO New York 09777

CONTENTS

	Page
TIEME	ii
AVIONICS PANEL OFFICERS AND TECHNICAL PROGRAMME COMMITTEE	iv
TECHNICAL EVALUATION REPORT	*
	Reference
KEYNOTE ADDRESS by J.Hartog	v
<b>SESSION I – GENERAL ASPECTS OF HIGH RESOLUTION RADAR</b>	
ASARS-2 PERFORMANCE PREDICTION AND TEST RESULTS by R.Thoené, D. Flerl and D Black	1*
LE RADAR MULTIMODE HAUTE RESOLUTION par N.Lannelongue, J.Rozes et E.Renaud	2*
CONCEPTS FOR HIGH RESOLUTION SPACE BASED SAR/ISAR SYSTEMS -- PRELIMINARY DESIGN CONFIGURATIONS by C.Bösswetter, A.BWolfram, T.K.Pike and J.M.Herner	3 ✓
TRADE-OFFS IN A SPACE BASED SURVEILLANCE RADAR by I.McMillan	4 ✓
IMAGERIE RADAR EN BANDE W par O.Du Plessis et D.L.e Coz	5*
A FREQUENCY AGILE 94 GHz PULSE-DOPPLER RADAR WITH DUAL POLARISATION CAPABILITY by H.Barth, W.Menzel, A.Plattner and J.Schroth	6 ✓
APPLICATION OF SUPERRESOLUTION METHODS FOR AIRBORNE RADAR by U.Nickel	7 ✓
THE EFFECTIVENESS OF ECM NOISE MODULATIONS IN SCREENING SURFACE TARGETS FROM SYNTHETIC APERTURE RADAR by D.C.Wicks	8*
<b>SESSION II – HIGH RESOLUTION RADAR SYSTEMS AND THEIR OPERATIONAL ENVIRONMENT</b>	
Paper 9 withdrawn	
THE PIARUS PROJECT: DESIGN OF A POLARIMETRIC C-BAND SAR IN THE NETHERLANDS by P.Hoogeboom and P.J.Koomen	10 ✓
THE ASTOR TECHNOLOGY DEMONSTRATOR PROGRAMME by P.L.Andrews	11*
Paper 12 withdrawn	
ASARS-2 A REVIEW AND STATUS REPORT by J.R.Kotlarski	13*
ROSAR (HELICOPTER-ROTOR BASED SYNTHETIC APERTURE RADAR) by H.Klausing, H.Kaltschmidt and W. Keydel	14 ✓

\* Printed in classified publication CP 459 (Supplement)  
 † Not available at time of printing

	Reference
CAPABILITIES OF BISTATIC SYNTHETIC APERTURE RADAR FOR COVERT BATTLEFIELD SURVEILLANCE by C.D.Hall	15 ✓
BISTATIC SYNTHETIC APERTURE RADAR EXPERIMENT USING A SPACE ASSET by D.M.Martinsek and E.R.Martinsek Jr	16*
LOCOSAR: UN SIMULATEUR DE RADAR A ANTENNE SYNTHETIQUE (SAR) par P.Plau et M.Busson	17*
MMW SAR ON RPV FOR BATTLEFIELD SURVEILLANCE by A.Farina, U.Carletti, E.D'Addio, C.Morabito and R.Pangrazi	18 ✓
<b>SESSION III - SPECIAL COMPONENTS FOR USE IN HIGH RESOLUTION RADAR</b>	
Paper 19 withdrawn	
GENERATION PROGRAMMABLE DES IMPULSIONS MODULEES LINEAIREMENT EN FREQUENCE par J.Richard et J.M.Falot	20 †
Paper 21 withdrawn	
REAL-TIME ADAPTIVE RADIOMETRIC CORRECTION FOR IMAGING RADARS SYSTEMS by J.R.Moreira and W.Poetzsch	22 ✓
Paper 23 withdrawn	
CONCEPT FOR A SPACEBORNE SYNTHETIC APERTURE RADAR (SAR) SENSOR BASED ON ACTIVE PHASED ARRAY TECHNOLOGY by A.Brunner, E.Langer, H.Oll and K.H.Zeller	23A ✓
<b>SESSION IV - MOTION COMPENSATION FOR SAR</b>	
A MOTION COMPENSATION STUDY FOR THE PHARUS PROECI by M.P.G.Otten	24 ✓
PERFORMANCE EVALUATION OF A SAR MOTION COMPENSATION SYSTEM by D.J.Difilippo and M.R.Vant	25*
A SOLUTION FOR REAL TIME MOTION COMPENSATION FOR SAR WITHOUT USING INERTIAL NAVIGATION SYSTEMS by J.Moreira	26 ✓
MILLIMETRIC SAR MOTION COMPENSATION by M.G.Cross	27*
<b>SESSION V - DETECTION AND IMAGING OF MOVING</b>	
L'IMAGERIE DES CIBLES MARINES A LA FRONTIERE ENTRE LE SAR ET L'ISAR par M.Fenou	28
PROBLEMS IN ISAR PROCESSING WITH RANGE RESOLUTION BY STEPPED FREQUENCY BURSTS by G.Krämer	29 ✓
A NOVEL PROCESSING TECHNIQUE FOR THE PRODUCTION OF VERY HIGH RANGE RESOLUTION ISAR IMAGERY by P.B.Thomas and C.J.Baker	30*

\* Printed in classified publication CP 459 (Supplement)  
† Not available at time of printing

	References
A FAST ISAR-IMAGING PROCESS AND ITS INHERENT DEGRADING EFFECTS ON IMAGE QUALITY by K.H.Bethke and H.Rode	31 ✓
RADAR OBSERVATIONS OF A FORMATION OF TWO FIGHTERS -- A CASE STUDY FOR ISAR IMAGING E.J.Willems	32 ✓
1D-ISAR IMAGING OF MANOEUVERING AIRCRAFT by J.Ender	33 ✓
THE AN/APS-137(V) ISAR IMAGING SYSTEM by J.M.Smith	33A*
SHIP CLASSIFICATION WITH THE AN/APS-506 MARITIME SEARCH RADAR by G.E.Huslam and M.R.Vaut	34*
RADAR TARGET IMAGE BY ISAR CASE STUDY S.Marinli, S.Pardini and E.Prodi	35 ✓
AIRBORNE DOPPLER RADAR FLIGHT EXPERIMENTS FOR THE DETECTION OF MICROBURSTS by H.-J.Blume, C.D.Lytle, W.R.Jones, E.M.Braccalente and C.L.Britt	35A ✓
SESSION VI -- SIGNAL AND DATA PROCESSING	
CONCEPT AND RESULTS OF THE DLR REALTIME SAR PROCESSOR by A.Moreira	36 ✓
SAR IMAGE CONSTRUCTION TECHNIQUES -- ARCHITECTURES AND IMPLEMENTATION by R.Schotter	37]
SIMULATION D'IMAGES DE CIBLES GEOMETRIQUES POUR RADAR A OUVERTURE SYNTHETIQUE par J.M.Nisar	38
CODAGE D'IMAGES SAR par P.Tourtier	39

\* Printed in classified publication CP 472 (Supplement)  
† Not available at time of printing

## KEYNOTE ADDRESS

by

Major General J.Hartog  
 Armaments Director and Procurement Executive  
 Royal Netherlands Air Force  
 P.O.Box 2500  
 2500-ES The Hague  
 Netherlands

It is for me an honour and a pleasure to respond today to the invitation to present the Keynote Address to this AGARD Avionics Panel Symposium. It is in particular a pleasure to welcome you to the Netherlands as it is selected to host your meeting. The Symposium indeed is entitled "High Resolution Air and Spaceborne Radar", however -- as is required from a keynote address -- I would like to put this subject in the broader perspective of the future requirements and development of aerospace avionics.

A few years ago an annoyed Senator remarked at a court hearing in the United States about a certain aircraft production programme (the F-14) that "this is the last time this nation buys a twenty million dollar combat aircraft. The Senator in question was proved right, albeit in a different way from what he meant. What happened with this aircraft is also happening even more often in practically all the western countries, in view of the financial and economic situation connected with the use of increasingly sophisticated technologies. Therefore we may well ask with justification whether new technologies will enable the improvement of the defence in an affordable manner.

Some essential aspects concerning new technologies to improve conventional defence are provided within the context of the currently applicable strategy as reflected in the Conceptual Military Framework which was accepted by NATO in December 1985. The Conceptual Military Framework provides a coherent assessment of the long-term (until the year 2000) strategic and tactical objectives, tasks and necessary military means of the NATO Alliance. Its aim is to provide a basis on which guidelines and priorities for long-term planning can be founded. Thus, and also taking account of the various national pre-conditions, national plans can be developed for the allocation of defence equipment, personnel and infrastructure.

Before World War II military strength was considered mainly in terms of quantity; what counted was how many weapons a country had. The first advanced military technologies did not arrive until World War II of which radar, the jet engine and missile technology are striking examples. Since then the quality of weapon systems, in terms of speed, accuracy and destructive power, has become more important than the quantity. There is therefore no point any longer in thinking in quantitative terms, that is to say in counting who has the most weapons. The ability to maintain a balance of power depends increasingly on available technology and its exclusiveness. Keeping a qualitative lead in terms of technology may counteract a shortfall of quantity. This is why military research and development will play such a crucial part in maintaining the balance of power. New results in (military) research and development may easily undermine the balance. Thus, arms control is to a large extent decided by the degree of technological change together with the financial resources and the willingness of the initiator to decide the extent to which increasingly advanced technologies will be created and used. With these irrefutable facts, that is to say the controllability of the economic and technological inventory, a typical illustration is given of the peace and security problem. Economic and technical creativity is decisive and can in fact not be limited by an agreement. It is a factor to be decided by a power itself. It controls its own progress towards the realization of its objectives.

The Conceptual Military Framework accepted by the NATO countries reflects the situation in 1985 and starts from the premise that the Warsaw Pact will maintain its numerical superiority and will energetically try to make up any qualitative backwardness. The document therefore urges a combination of quantitative and qualitative improvements. The emphasis is on quality which is to be improved mostly by introducing advanced technologies. In NATO these ideas have crystallized in the Conventional Defense Improvement Program (CDI).

What are these so-called 'emerging technologies', of which many people, rightly or wrongly, expect miracles? A multitude of publications and comments show that as regards basic techniques and ideas not much new can be expected in the next two decades other than what is already predictable. Possible research areas are practically fixed. Nevertheless, vast sums of money are involved in this, with the added complication of selection and establishment of priorities for the most promising research areas.

Those who deal with the politics concerning technology, strategy and arms control may recognize six technological tendencies at least until the end of this century.

- a) **Increasing accuracy and homing capacity** of all sorts of weapons at sea, on land and in the air by using accurate navigation, radiation detection, manoeuvrability and processing techniques, also against mobile targets, such as satellites and ballistic missiles, resulting in an increased vulnerability of each static and mobile object.

- b. **Reduced visibility**, including aerodynamic design and using material that considerably reduces the chance of flying objects being detected. A reduction in electromagnetic, acoustic, and heat radiation will contribute to this. It means that detection of objects occurs so late that it considerably reduces the warning time needed for reaction.
- c. **Increase in mobility** of both launching pads and command, control and communications facilities (C<sup>3</sup>I).
- d. **Extra hardening techniques**, by using new methods and materials, reducing the vulnerability and therefore the accessibility of targets.
- e. **A more effective strategic defence**, in particular a ballistic defence by integral use of radiation weapons.
- f. **Data processing techniques**, by analysing and collating data being fed in by many kinds of sensors. It offers the opportunity to obtain a quicker and better understanding necessary for decision making and, moreover, provides a means to verify the implementation of arms control agreements.

These six tendencies show the cause and inevitability of a vicious circle that is in the arms race spiral of striving to maintain a balance of power. Each move in the game to obtain a comfortable position is answered by a more powerful counter-move. The moment of the counter-move is mainly a technology transfer problem. In other words, each technique has its anti-technique. Countermeasures continue to be necessary and investments in armaments are continued. From the listing of technological tendencies the conclusion can be drawn that in a possible conflict, he who most controls the frequency spectrum stands the best chance of winning, because all leading techniques are based on the production, interception or interference of some form of radiation and this in particular represents the domain of interest of this Symposium. A second conclusion that can be drawn from the listing of technological tendencies is that currently developments in electronics – and therefore avionics – dominate progress in nearly all areas of interest. This explains why really significant improvements in aircraft design are not to be expected until after the year 2000, with the exception of electronics. Electronics now has prime place in the weaponry game; you only have to step inside the operations room of a modern warship to appreciate to what extent. The windows on the world outside are not portholes but screens; air and surface radars, sonars, thermal imagers, laser rangefinders. In some areas, the electronics sector gains from a cost-cutting environment, because it is able to make available arms more effective. Moreover, technological advances are constantly creating their own needs: detection and avoiding, detection, guiding and deflecting weapons; jamming and counter-jamming signals, and this is what I meant earlier by technique and anti-technique.

Mechanical controls in aircraft are replaced by computer-controlled actuators, and software algorithms actually fly the plane; miniaturized, more sophisticated and more tightly coupled sensors, displays and avionics, are now tied directly into the computerized flight control system, known as "control configured vehicles". The confluence of these new technologies will bring higher performance and "survivability" to the next generation of military aircraft. This in a nut shell represents the situation of today, but application of essential and significant developments still requires many years. To bridge this timeframe, as a timely and economical alternative, military aircraft are now increasingly being upgraded in order to satisfy the need to stay abreast of the operational environmental complications.

It has become a fact of life to experience the increasing disharmony between the 20-25 year life cycle of systems, the 10 year evolution of the operations environment and the 5 year technology time constant. This disharmony indeed is increasing as a result of the continuously faster developing technology. The expected environment in which military aircraft have to operate is evolving rather spectacularly, mainly as a result of the proliferation of precision-guided anti-aircraft weapons and electronic countermeasures. The mentioned disharmony between available technology and the operational, economical and structural lifetime of an aircraft, initiates the need for a continuous flow of modifications. The two facets – anti-aircraft weapons and electronic countermeasures – represent the argument to the statement that: "The winner in the future will be the one who sees the other first". We are talking here, of course, about the "beyond visual range" capability and indeed that is mainly a matter of avionics and visionics. The military aircraft development market therefore has arrived at an upgrade market to allow those mainly electronic developments to be incorporated in addition to some improvements to the structure in order to stretch the lifetime. The examples are upgrades to F-4, F-8, F-14, F-15, F-16 and A-7 aircraft. The military aircraft of the nineties will be characterized by upgraded aircraft of the eighties and even seventies. Such a conclusion is also significant for this audience.

Having provided a description of your working environment, let me approach more specifically the subjects of your Symposium, and give my view on the support we require from aircraft avionics. For civilian aircraft crews the development of very accurate navigation and approach systems in combination with advanced autopilots and with autoland systems can be seen as the most important developments until now as far as avionics are concerned. Another important development was installation of ground proximity warning systems and weather radars which improved the safety tremendously.

Until about 1970 military pilots were happy with improving navigation systems and improving fire control radars. In the seventies, the introduction of fly-by-wire and of digital avionics changed the world for military pilots. With the old analog systems, changing the avionics was a costly and difficult affair. Today in airplanes like the F-16 or F-18, an important increase in performance of the airplane as a weapons system can be realised by a software change to one or more of the on-board computers.

Looking into the future, adding new electronic systems to civilian aircraft will make the aircraft easier and safer to operate. In some cases the crew can be reduced from three to two. The development drivers in the civilian world are efficiency and safety.

In the military world the main driver is the efficiency of the aircraft as a weapon system, meaning, better accuracy in weapon deliveries and an improved survivability in an hostile environment. The developments in electronics in the 50's and 60's have led to the addition of a large number of sensors and subsystems to the avionics systems of military aircraft. The architecture of a standard avionics system consists of one or more databus systems with a large number of Line Replaceable Units. Each Line Replaceable Unit with its own specific electronics, and of course its cooling and power requirement. Most of the time the information from all the subsystems can be presented to the pilot in many options or combinations of options. Especially in modern single seat aircraft we see that the pilot gets much more information than he can absorb and use at a certain moment. To reduce the workload and filter the data for the pilot in an efficient way will be a challenge for the engineers.

The speed with which new technologies and with them new countermeasures become available in the western world as well as in the Soviet Union, makes a more frequent adjustment of weapon systems necessary. The required changes in ECM systems are hard to follow. Avoidance of threats guided by radar systems by reducing radar cross section is one way, but it is also a very expensive way. Avoidance of the threat by terrain masking against groundbased systems in combination with ECM for the airborne systems will continue to be a valuable option in the coming decades.

The development of passive terrain avoidance systems and more accurate navigation and weapon delivery systems based on an onboard digital terrain database seems very promising. In this respect we still lose a lot of aircraft and crew due to uncontrolled flight into terrain. The use of a digital terrain database for a better ground proximity warning system will be very effective in peacetime as well. The development of megalite memory chips will make it possible to store the necessary data for large geographical areas in small fighter type aircraft. Of course it will be necessary to develop the required databases with a sufficient level of accuracy. It should be realized that in the context of electronic warfare, passive systems might represent the most promising prospects.

A new area that also seems very promising is the area of helmet mounted displays. The majority of our conventional offensive aircraft cannot operate at night. Addition of a digital terrain data system in combination with Forward Looking Infra Red and Low Light Television, if the information can be presented to the pilot in an acceptable way, will increase the capabilities of current aircraft considerably. At the same time however the development of laser technology is ongoing. New sensors in the visible part of the spectrum will become increasingly vulnerable to weapon systems that make use of laser energy. Even the eyes of the pilot have to be protected against those types of weapons. There may be a time that the pilot can not look at the outside world any more when he is over enemy territory. This outside world may have to be artificially presented to him in the visor of the helmet. That also protects him from blinding by lasers.

Another important area is the area of target identification and classification. With the improved air to air weapons like the Advanced Medium Range Air to Air Missile becoming available and larger number of aircraft being capable of using these weapons, the identification problem becomes more important. The NATO identification system is a model. The implementation of a Multifunctional Information Distribution System will enable a more efficient use of all sensors available. Of course the implications of electronic combat will make the usefulness of systems like the Multifunctional Information Distribution System questionable. From my experience in my previous NATO assignment and as the Netherlands representative in the NATO Air Defence Committee, I can assure you that one of the most complex problems in the Central Region during a military conflict will be Airspace Management. With all current plans for the holding of different types of Unmanned Air Vehicles by the Armies and Air Forces, in combination with all organic Surface to Air Missile Systems that are deployed already, Airspace management becomes challenging indeed. However, a system like the Multifunctional Information Distribution System seem unavoidable in this scenario.

The requirement to present more data to the pilot in such a way that he is able to interpret the data correctly and in the right priority makes the use of colour displays more urgent. The requirement for the industry to develop displays that do not take too much room, have enough contrast in sunlight conditions and can stand the military specifications is a great challenge indeed.

An interesting change that has taken place already is the fact that the development of microelectronics in the civilian world in many areas is ahead of the state of the art military avionics. This should be used as much as possible to lower the cost of military systems. Building military hardware using standard components that are available on the civilian market should lower the development and production costs.

The speed and memory capacity of current and future microprocessors will be such that several of the current bulky Line Replaceable Units can be combined in a single black box with Line Replaceable Modules. The volume and weight of each subsystem will decrease and the reliability will improve tremendously. If the predictions are right, at the introduction of Very High Speed Integrated circuit technology. What I witness as the Netherlands prime representative in the E-16 Steering Committee is that within a few years (1998) introduction of functional avionics clusters will be a reality. As I said before, the next ten years seem destined to become a decade of retrofitting existing aircraft with new avionics. It is not very

likely that the defence budgets in the western world will grow in the same way as they have done in the past. The only way to find money for new systems will be to decrease the cost of maintenance, meaning less people required to do the maintenance of the same number of aircraft.

The biggest challenge in the near future will be the development of all the necessary software, which can be illustrated by the 600,000 required instructions in a combat aircraft. The more systems are integrated the more challenging the software development tasks will be. Another area of concern will be the flight test requirements of all the advanced systems. When do we know for sure that all the bugs are out of the software, and that the system does have a sufficient level of confidence?

It might be useful to summarize the most significant remarks of this presentation by stating:

- the aircraft of the nineties will be characterized by upgraded aircraft of the eighties and even seventies.
- electronics and avionics dominate aircraft improvements during the coming decade.
- he who most controls the frequency spectrum stands the best chance of winning a potential conflict.
- the best beyond visual range capability marks the winner of an airbattle.

To finalize this address, gentlemen, calculation power, computer models and improved communications free the hands of investigators in order to concentrate on more refined objectives. On the other hand, emerging technologies provide a much more detailed impression of human skills like seeing, hearing, the use of language and likely artificial intelligence, identifying the latter as "learning by experience". Exciting experiences lay in front of us and, to quote a Chinese phrase: "If people do not anticipate the future, they very soon have to take care to today".

It has been an honour for me to have addressed this audience that will make all those miracles come true. I wish you all a fruitful Symposium.

CONCEPTS FOR HIGH RESOLUTION SPACE BASED SAR/ISAR SYSTEMS

- Preliminary Design Considerations -

C. Borrwetter, A.P. Wolframm, T.K. Pike  
MBB Space Systems Group  
8012 Ottobrunn, FRG

and  
J.M. Hermer, Thomson-CSF, Montrouge, France

AD-PCCS 835

SUMMARY

The paper reflects some results of preliminary feasibility considerations for a next generation space based multi-mode SAR/ISAR system. Key element of next generation SAR systems, as currently designed for future remote sensing applications, is the active phased array antenna. Based on this antenna technology, some new operational modes are discussed, which currently are not and also in the ERS-1 era will not be available in earth observation from space. They include:

- \* Wide swath/medium resolution SAR mode
- \* Narrow swath/high resolution SAR mode
- \* Squinted SAR mode
- \* Very high resolution Spotlight/multi beam mode
- \* Moving target MTI/ISAR mode

The paper addresses different beam pointing techniques (mono-beam, multi-beam in azimuth/elevation) for strip mapping SAR modes as well as for MTI/ISAR modes. Basic requirements for selection of orbits are also discussed. The MTI/ISAR mode intended to detect and possibly classify from space clusters of fast moving small targets against the clutter background of the earth surface probably constitutes the highest risk in terms of requirements for onboard real time processing capabilities, pointing accuracies and coverage. For all modes some basic system parameters are given.

1. INTRODUCTION

A new generation of space based remote sensing systems is under consideration in different European countries as well as in the US. Besides the "classical" microwave instruments (radiometers, scatterometers, SAR) passive multi-channel scanning devices in the visible and IR region and imaging spectrometers as well as active optical instruments like laser systems and backscattering lidars for monitoring the environment are currently designed and developed. In parallel advanced multi sensor image processing, data fusion and change detection concepts for application on ground and possibly in space, are also under development. In addition, future remote sensing instrumentation is investigated by ESA for deep space missions e.g. for autonomous probes to image comets, asteroids or other extra-terrestrial bodies.

The development in Europe is driven by different programs: EOPP and TRP (ESA), ESPRIT II (CEC), EUREKA and several national programs. It is obvious that these technologies may and will support future space based earth observation and reconnaissance systems as well. Due to their all weather and day/night capabilities microwave imaging techniques play an important role in earth observation.

The major milestone in this area is ESA's ERS-1 satellite scheduled for launch in 1990. However, due to its severe constraints and therefore very limited capabilities ERS-1 is not considered as a technological candidate for a future European space based observation system. The next generation, currently designed for the post ERS-1 era and the Polar Platform, differs radically from previous designs due to the availability of space based active phased array antennas. This technology allows for antenna beam pointing and beam width control by judicious selection of phase and amplitude weighting for the transmit/receive (T/R) modules. This in turn allows the definition and reconfiguration of new operational modes in addition to the usual broadside strip mapping mode with fixed swath width and resolution [1] [2]. A number of benefits may be derived, directly related to the use of active phased arrays:

- Electronic beam steering in elevation/azimuth for different coverage modes
- Programmable antenna patterns for sidelobe and nadir return suppression for each pointing direction
- Adaptive cancellation of sidelobe jammers
- Increased redundancy, reliability and life time due to the avoidance of high power concentration as in classical "single point of failure" designs

It is obvious that multi-sensor imaging systems with high resolution under all weather day/night operational conditions result in increased data rate requirements. Therefore, in classical system designs, a trade-off between swath width, resolution, available power and other platform resources leads to a compromise to solve the dilemma. In next generation systems the potential of redundancy reduction techniques, to be performed on board, will be used to reduce the effective data rate of the system thereby decreasing the requirements of the data link, additional data relay satellites or on board data recording devices. However, work in this area [5] indicates, that the possible savings by optimal encoding schemes may not be too large, since the SAR source entropy in most cases will not be too much less than the maximum possible. The advanced concepts of on board on ground real time processors (parallel processors, binary optics [12]) currently under consideration will provide more degrees of freedom for the design of future systems and ground segments.

Due to the enormous cost for the development of these technologies and their inherent

multi-mode operational capabilities the next generation systems could be designed as "joint services" systems serving the needs of both the civil remote sensing as well as the military/political user communities. In the following the feasibility of a next generation space based multi-mode SAR/ISAR system is discussed and preliminary design considerations are reflected.

## 2. GENERAL SYSTEM CONCEPT

Although the definition of a system concept requires careful analysis of the user requirements we can identify some basic operational modes sufficient to cover most applications. They include:

- \* Wide swath/medium resolution SAR mode
- \* Narrow swath/high resolution SAR mode
- \* Squinted SAR mode
- \* Spotlight SAR mode
- \* MTI or ISAR mode

The first two are regular strip mapping modes with fixed broadside antenna pointing. While the first mode assures global coverage the intention of the second mode is to image special areas of interest whose position is known.

The third mode is of the fixed pointing type also, however the antenna pointing direction in azimuth is no longer perpendicular to the orbit but squinted by a positive or negative angle. This could be of interest in a multi jammer environment to look through the individual jammers. Another advantage of this mode could be a "mapping ahead" capability. This would enable the system to switch to the high resolution mode during the same pass.

In the Spotlight SAR mode the synthetic aperture length (= coherent integration time) is drastically increased by pointing the high gain antenna to the small area of interest during the fly-by. If proper azimuth processing is applied to the data the resulting azimuth resolution is improved according to the increased aperture length. Range resolution is determined by the time-bandwidth-product in range as in any other conventional SAR system. Since the ultra-high resolution Spotlight mode covers a small area of special interest only (for example a 20 km x 20 km illuminated patch) it is commanded by one of the survey modes to "lock on" to the specific area to be imaged.

The MTI/ISAR mode is dedicated to the detection and possibly imaging of moving targets, which could in principle be ground targets or other moving objects with a velocity component relative to earth. The fixed targets (= ground) are suppressed to a certain extent. This imaging mode should be based on target motion rather than platform motion. It therefore needs as much a priori knowledge on the specific targets as possible from other modes in order to image them with high resolution.

The definition of an orbit is a complex process since it affects not only the design of the instrumentation but also the coverage and repetition cycle for the observation system. It is also dictated by the availability and position of ground stations as well as a data relay satellite, if available. Obviously, orbit selection is mainly driven by user requirements, which in turn are not yet established. The paper therefore focuses on instrument feasibility based on simplified orbit assumptions:

- \* low altitude orbit: inclination = 60°, altitude = 1000 km
- \* high altitude orbit: inclination = 30°, altitude = 5000 km
- \* equatorial orbit: inclination = 0°, altitude = 6371 km

One of the basic questions is to define an orbit satisfying the requirements of the different modes. A thorough feasibility analysis has also to consider the time schedule, the available launcher, the satellite platform for accommodation and the resources available for the instrumentation. The current understanding is based on the results of the Advanced SAR Feasibility Study performed by the MBB/Thomson-CSF/Canadian Astronautics/RS Consult team for ESA in 1988 [1][2]. With respect to the given time frame for implementation the ARIANE IV was chosen as launcher and the extended POT Bus /ASTRO Bus as platform. They are considered as baseline for the current paper.

## 3. HIGH RESOLUTION RADAR IMAGING MODES

High resolution imaging modes have to be discussed in two dimensions: along track and cross track (range). A fine resolution in the along track direction is achieved by means of the synthetic aperture principle (SAR) and in range direction through a short pulse. As it is not possible to transmit the required power during the pulse duration equivalent to the desired resolution a long coded pulse is transmitted and compressed at reception. Design considerations will be given in the along track direction first and then methods to achieve high range resolution will be discussed afterwards.

### 3.1 High Resolution SAR Modes

In the simplest case high along track (azimuth) resolution is achieved by using an antenna as short as possible in the along track direction, collecting a large number of return echoes and processing these according to the regular SAR principle (Fig. 1a). Due to the very short antenna (for example 1 m) very high Doppler frequencies are generated which have to be sampled adequately. For a spacecraft in an altitude of 1000 km pulse repetition frequencies of more than 20 kHz would have to be used, resulting in a too short range observation time or swath width in range. Extreme problems with pointing accuracy in elevation and timing accuracy in range would have to be solved. In unfavourable cases the radar may even not be able to image the target because of transmit/receive interference. Also, as the antenna dimensions are reverse to the normal case, this kind of antenna construction is incompatible with other modes (Table 1). Since phased array radars have been used, another method of achieving a high along track resolution has been introduced, called Spotlight SAR. In this case the required synthetic

aperture is generated by squinting the antenna beam towards the target while the radar is passing by on its normal track (Fig.1 b).

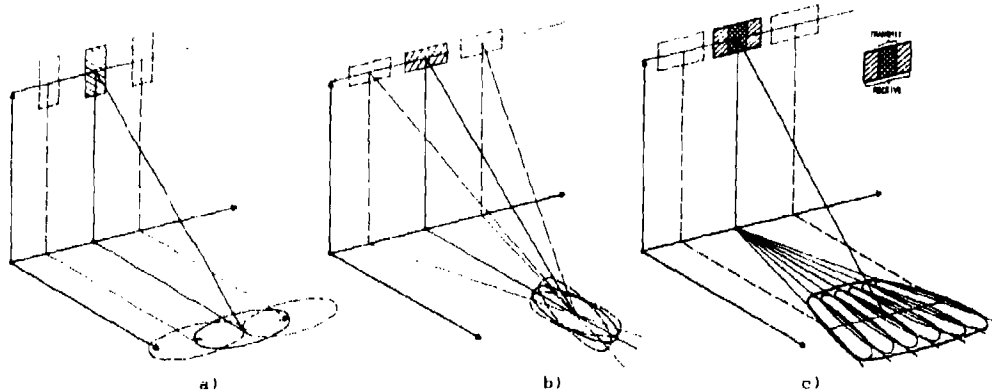


Fig. 1 High Resolution Concepts in Azimuth  
a) Regular SAR b) Spotlight SAR c) Multibeam SAR

critical parameters are underlined>	High Res SAR	Spotlight	Multi Beam
PRF	high	low	low
Data Rate	high	low	high 2)
Strip Map	continuous	discontinuous	continuous
SNR	good	good	marginal
Peak Power	moderate	moderate	high
Beam Pointing Requ. az	low	high	low
rg	high	low	low
Data Window Pos Tolerance	critical	high	high
Processing Requirements	high	moderate	high 2)
Mode Sequencing	difficult 1)	possible	possible
Special problems	1) antenna dimensions not compatible with other modes		2) complex multi channel receiver

Table 1 : Comparison of high resolution SAR modes

As the antenna beamwidth in the along track direction is in the same order of magnitude as the achievable pointing accuracy, problems only have been shifted. With this kind of SAR it is namely only guaranteed that one hits a target but not necessarily the wanted target. Another disadvantage is that the mapping process is discontinuous.

Ground based multi beam radars exist since many years and airborne multi beam phased array radars are in use for some time. For spaceborne remote sensing satellites phased array radars are under consideration and will be launched in 1991/92. However, these systems will achieve a resolution of 5 m along track and 30 m in range on ground only. For better resolutions either systems as described above have to be used with all their disadvantages or a new technique has to be introduced in space. One solution, as described in [2], is to implement the well known multi beam phased array radar as shown in Fig. 1 c and Fig. 2. The basic principle is for example described in [14].

In multi beam radars, as in conventional phased array radars, the backscattered signals from the individual radiating elements are first amplified. But then instead of being coherently added, the individual signals are split into M equal parts. Each of these signals is then phase shifted according to geometrical laws in order to form their own special beam after coherent addition. If the system has been properly designed the signal-to-noise ratio (SNR) of all beams is the same as in a normal phased array radar and all beams are contiguous. With respect to a SAR application the advantage of this complicated radar lies in the fact that a wide swath continuous strip map

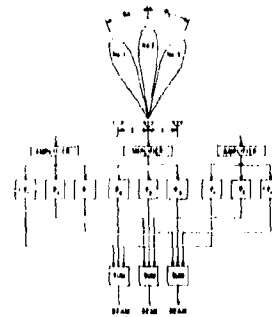


Fig. 2 Simultaneous postamplifier multi-beam formation using array antenna [14]

with an  $M$  times finer along track resolution ( $\approx 0.5m$ ) can be achieved without the extreme pointing problems and discontinuities of the above described SAR principle. Any not too large misalignment is compensated for by a reasonable swath width in elevation, and in the along track direction this only means a slight (uncritical) shift in time. The problems are the complexity and data rate of the radar system. Instead of having just one beam forming network,  $M$  networks have to be implemented and operated. If we take the regular SAR high resolution concept of Fig. 1a as a basis and want to relax the elevation pointing problems by widening the swath by a factor of  $N$ , the SNR has worsened by a factor  $N^4$ . Therefore in order to keep up a comparable SNR we have to implement  $M = N^2$  beams. The data rate only increases by a factor of  $N$ . If  $M$  becomes unrealistic a proportionally higher amount of power has to be transmitted instead.

In elevation, beam forming and range resolution are independent from each other. In most cases a single beam is used (Figure 3 a) with variable depression angle (elevation scan). Only when a very large swath width is required (survey mode),  $N$  beams might be required (Figure 3 b). If the beams are generated in a time shared manner (SCANSAR) then the maximum observation time on the target and therefore the along track resolution are degraded by a factor of  $N$ . Simultaneous multiple beams in elevation should only be used if there is no other way to achieve the required SNR, as the antenna gain increases with the number of elevation beams  $N$  for the same swath width.

The resolution in range is in the first place proportional to the signal bandwidth. This means that it is desirable to transmit an as high bandwidth as possible. There are several waveforms which are suitable for high range resolution radars, like: linear FM, non-linear FM, phase coded, complementary coded and burst waveforms. On the other hand the SNR is proportional to the receiver bandwidth. The best compromise are either a high bandwidth linear FM (chirp) on transmit with deramp-on-receive (stretch) or stepped frequency transmission with pulse integration on receive. Advantages and disadvantages with respect to a standard high bandwidth linear FM transmission and pulse compression are compared in Table 2.

As the swath width of a stepped frequency system is only a few hundred meters this waveform is thought to be applicable only for a few special applications. In the following Table 3 the performance of a pulse compression / synthetic aperture radar is shown for point targets for the same system at two different ranges of 1000km and 5000 km.

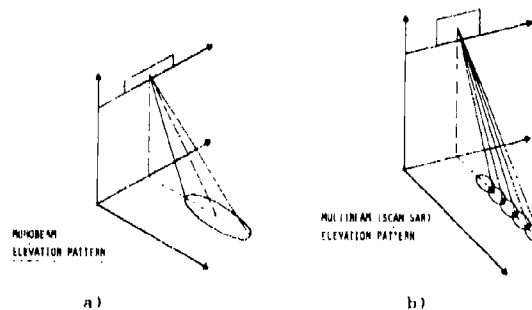


Fig. 3 Coverage in elevation  
a) monobeam b) SCANSAR

critical parameters are underlined>	chirp / pulse compression	chirp / deramp-on-receive	stepped frequency pulse integration
Instant bandwidth	high	moderate	low
SNR	low	moderate	high
ADC rate	high	moderate	low
Swath width	small	small	very small
Beam point. req.	Az n/a	n/a	n/a
	Rq high	moderate	moderate
Data Window Pos. Tolerance	critical	moderate	critical

Table 2: Comparison of high range resolution techniques

	/ km	1000	5000
Range			
Ground velocity	/ m/s	6600	3400
Average power	/ W		1000
Antenna dimension	/ m*m	10.0	1.66
Radar cross section	/ m <sup>2</sup>		1
Wavelength	/ m		0.03
Losses	/ dB		10
SNR	/ GB	24.2	6.1

Table 3: Performance of a pulse compression/synthetic aperture radar

The above system has a single look azimuth resolution of 5m. A better resolution will be achieved through multi beam / chirp / deramp-on-receive. A loss in antenna gain at transmit because of an  $M$ -times widened beam will be compensated through a (deramp-on-receive) stretch factor of  $M$ . A reasonable figure for  $M$  is 10. This means that this system is capable of producing single look images with resolutions of about  $0.5 m \times 0.5 m$ . If

slant ranges of more than 5000 km are desired the average transmit power has to be increased, but little improvement is possible due to technological limits.

#### 4. MTI/ISAR MODE

##### 4.1 OVERVIEW

An imaging mode to detect and possibly classify moving objects is of great concern for airborne and space based observation systems, since single moving targets or moving clusters are used as activity indicators. Due to the large amount of data to be processed and evaluated MTI modes are used as screening aids in airborne reconnaissance systems. Classical airborne SAR MTI concepts make use of the positive or negative Doppler shifts generated by the radial velocity component of moving targets as observed by the SAR antenna. Clutter suppression is obtained if the velocity component of moving targets is large enough to be detected outside the antenna mainlobe spectrum. However, these concepts suffer from the following drawbacks:

- \* slow movers are hard to detect since the small Doppler shift keeps them within the antenna mainlobe spectrum
- \* due to the unknown velocity component the reference function cannot be exactly determined and therefore does not match the individual targets. This causes a defocusing effect in azimuth ( $\rightarrow$  loss of resolution relative to fixed targets)
- \* in the image domain the individual Doppler shifts for each moving target translate into a corresponding azimuth position shift. This has to be compensated for if the moving target instantaneous position is to be determined
- \* Fixed target feed through  
If antenna azimuth sidelobes are not sufficiently suppressed any strong target is moving through the antenna azimuth pattern during the pass. This means that strong fixed targets appear in the MTI image as false moving targets thereby confusing the MTI evaluation process (either man or algorithm).

Some of the drawbacks are subject to improvement due to implementation of a so called post detection logic after the Doppler filter bank to improve the detection capabilities and to separate between the true and false moving targets.

Due to these well known limitations of the Doppler filter approach advanced concepts for airborne application are under consideration. They include:

- \* Monopulse MTI
- \* Displaced Phase Center Antenna (DPCA)
- \* Two Antenna Concepts (Interferometer Approach)

If these concepts have been already implemented for space applications, for example for an US reconnaissance satellite launched recently, is not known.

Another promising technique to image moving objects with higher resolution is called Inverse Synthetic Aperture Radar (ISAR). Commonly, this term is used to refer to a configuration where the radar is fixed and the target moves relative to the radar. A special case in this sense is the imaging of rotating targets without transversal velocity components. In this configuration the theoretical cross range resolution limit is given by

$$\text{Rho} = \text{Lambda} / 2 \cdot \sin \theta$$

It depends on the wavelength  $\text{Lambda}$  and the observation angle  $\theta$  only. The limit is reduced due to movement of the target through many range resolution cells during rotation, if their size is comparable to the target size. Polar Format Processing or Extended Coherent Processing is therefore to be used in order to correct this effect [1] [4] [5]. The application of this imaging principle for rotating targets at far range was first demonstrated by LRIR (Long Range Imaging Radar) to map the surface of the moon and Venus [3] [5].

The generalization of this imaging concept to moving targets with both rotational and transversal velocity components is considered in a number of papers [6] [7] [8] [9] [10]. An excellent overview is given by Ausherman [3]. In the literature main emphasis is given to airborne and ground based systems. The application of ISAR imaging to space based platforms is discussed in [11].

##### 4.2 MTI/ISAR CONSIDERATIONS

In the framework of the so called European Defense Initiative consideration is given to ground and space based ISAR systems to detect and classify small targets travelling at high speed in East-West direction through the atmosphere in Central Europe. While the ground based ISAR configuration looks more feasible due to the available resources and fixed geometry relative to earth, space based systems suffer from two serious drawbacks:

- \* very limited resources relative to ground based systems
- \* necessary compromise between coverage (availability, number of satellite platforms required) and suitable illumination geometry (small radial velocity components)

Fig. 4 shows a basic sidelooking configuration for an ISAR system to search and track moving targets from space. This configuration, however, is not believed to be feasible, since this shallow looking geometry suffers from poor sub-clutter target detection capability and motion through many range resolution cells. If targets would travel through many thousand range resolution cells during the observation time ("out-of-plane motion") high resolution ISAR processing would be very difficult if not impossible to implement. Although a geostationary orbit would be attractive from the ISAR point of view, two other orbit alternatives were chosen based on power budget and ambiguity considerations:

- \* equatorial orbit with tangential look direction (Fig. 5)
- \* inclined orbit with perpendicular look direction (Fig. 6)

These two orbit models satisfy the most stringent ISAR requirement for broadside target

beam crossing at low radial velocity components and sufficient coverage/repetition cycle. The equatorial orbit provides for continuous coverage of the northern hemisphere using 3...4 platforms only. However, due to the tangential look direction targets and ground clutter may not be separable in the time domain. For the inclined orbit with perpendicular or at least steep look direction this separation could in principle be done.

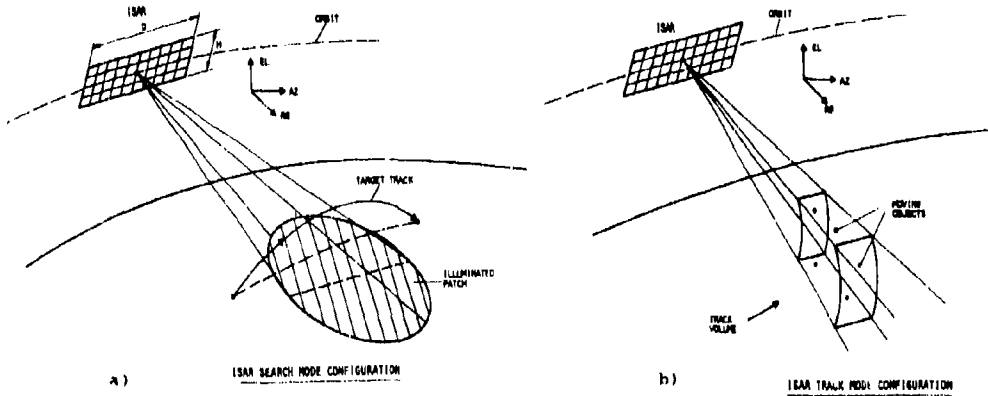


Fig. 4 Basic Sidelooking ISAR Configuration

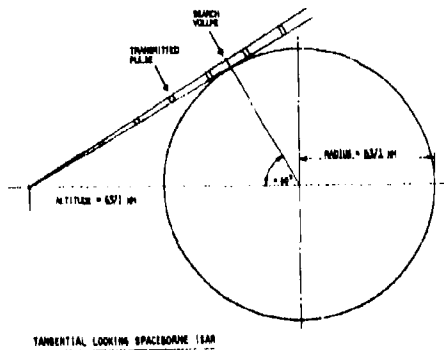


Fig. 5 Tangentially Looking Spaceborne ISAR

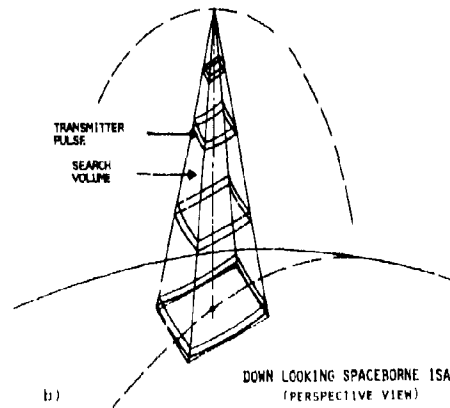
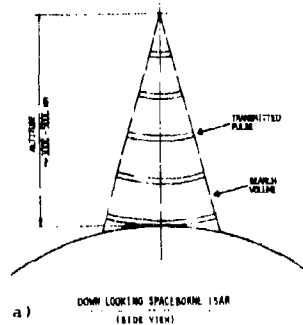


Fig. 6 Down Looking Spaceborne ISAR  
a) Side View b) Perspective View

Two operational phases are considered as necessary for an observation task of this kind:

- \* Search mode: Resolution 15 ft (Fig. 4a)
- \* Track mode: Resolution (goal) 1 ft (Fig. 4b)

During the Search mode the system should be able to detect clusters of fast moving objects passing the fixed beam perpendicular to the radar LOS. Slower civil air traffic could be separated in the Doppler domain via filtering in the down looking configuration.

#### b) Track Mode

However, this orbit gives less coverage. This means a longer repetition cycle or a larger number of platforms. Obviously, these considerations are an important part of a trade-off analysis to identify the optimum system configuration satisfying the user requirements under a given set of constraints.

Choosing the second orbit model the basic assumptions are:

- \* Orbital velocity 6 km/s
- \* Ground track velocity 3 km/s
- \* Target RCS -10...+10 dB/m<sup>2</sup>
- \* Maximum radar range 5000 km
- \* Target velocity Mach 3.5...7
- \* Radar frequency X-Band

The cross range resolution of 15 ft is assumed to be sufficient for this task. After detection of a target cluster the system is switching to the Track mode to resolve the cluster into individual targets and perform classification of some selected targets (based on a threat analysis) by imaging with a resolution in the order of 1 ft. This requires tracking the targets within a certain track volume over a sufficiently large aspect angle.

#### Range Parameters/Both Modes

The required range bandwidths are:

Mode	Search	Track
Slant range resolution	15 ft	1 ft
Compressed pulse width	30 ns	2 ns
Receiver bandwidth	33 MHz	500 MHz
Sample spacing	15 ft	1 ft

Since pulse compression usually is done on IF level the IF/Video bandwidth may be reduced after compression. After quadrature demodulation the sampling rate in each channel equals the receiver bandwidth (burst mode, oversampling = 1). If the maximum target size is assumed as 30 ft it is represented by 2 range samples in search mode and by 30 samples in track mode. If the track volume in range direction is set to 30000 ft = 10 km the number of range bins to be processed in real time during tracking would be 30000.

In order to achieve a satisfactory power budget pulse compression by a factor in the order of 5000 is required. Since the track volume is rather small (relative to swath width in strip mapping mode) the Deramp-on-Receive technique (STRETCH-SAR) is considered. Using a relatively long linear chirp waveform on transmit the returns are deramped on receive using a delayed replica of the transmit pulse. Thereby the large transmit bandwidth is reduced to a smaller instantaneous bandwidth by time stretching. Since time is converted to frequency, range resolution is obtained by frequency analysis of the deramped video signal (by FFT, for example). This range compression concept is useful for applications requiring high range resolution for small swath widths. Its basic principle is well known and discussed in [13], for example. The basic relationship between the bandwidth before and after deramping and the pulse length is:

$$B_{\text{tr}} = \text{echo from track volume} \quad t_2$$

$$B_{\text{tr}} = \text{transmitted pulse length} \quad t_1$$

For a track volume range dimension of 10 km = 30000 ft the echo duration is 66.6  $\mu$ s. Assuming a STRETCH factor of 5, the transmitted pulse length is 5 times this value e.g. 333  $\mu$ s. The transmitted pulse bandwidth of 500 MHz (for the 1 ft mode) with a FM rate of 1.5 MHz/ $\mu$ s translates to an IF bandwidth after deramping of 100 MHz. The time-bandwidth-products are 333 \* 500 = 166,500 on transmit and 333 \* 100 = 33,300 on receive. The number of data points per return is:

$$\text{before deskewing} \quad 2 * B_{\text{tr}} * (t_2 + t_1) = 80000$$

$$\text{after deskewing} \quad 2 * B_{\text{tr}} * t_1 = 66600$$

This is a data reduction of 17%. For unambiguous range the maximum PRF is:

$$\text{PRF}_{\text{max}} = 1/(t_2 + t_1) = 1/400 \mu\text{s} = 2500 \text{ Hz}$$

The sampling rate in each channel is 100 MHz. The buffered data rate is in this case 166.5 MBPS (for 1 Bit/sample) or 666 MBPS (for 4 Bit/sample).

These enormous data rates are caused by

- range resolution requirements
- track volume dimension in range
- word length in IQ channel

The reduced range resolution requirements for search mode do not necessarily call for the STRETCH concept. However, it may also be applied since waveform generation is assumed to be digitally programmable (memory readout technique, for example).

#### Azimuth Parameters/Search Mode

In this mode the system uses a fixed antenna beam looking down at steep angles. The targets, believed to travel in East-West direction, pass the beam with only small radial velocity components, dependent on the specific phase (starting phase, midcourse, terminal phase). If the satellite orbit is chosen to be traveled in opposite direction, the ground track velocity of the platform and target velocity add, resulting in short aperture times.

For a given cross range resolution of 15 ft the maximum antenna length is 30 ft = 10 m. The required synthetic aperture length (single look, X-Band, orbit altitude 5000 km) is 16.6 km corresponding to an aspect angle of 3.3 mrad = 0.2°. The effective velocity is  $v = 3 * 1 = 4 \text{ km/s}$  for a Mach 3.5 target. This means an effective synthetic aperture time of 16.6/4 = 4 s. The Doppler bandwidth required for 15 ft resolution is = 704 Hz (single look processing). If the power budget consideration allow to shorten the antenna length, multi-look processing may be introduced. Using look-to-look comparison techniques, information on the target tracks could be derived. This in turn could be used to fit trajectory prediction models.

#### Elevation Parameters/Search Mode

The task requires the observation of an area extending over = 3000 km in North-South direction. This swath cannot be covered simultaneously since it would require unrealistic power resources. Therefore, elevation scanning with an instantaneous swath width of = 100 km for each scan position is assumed. This requires 30 elevation scans (a quite large

value) to cover the total area of interest. The elevation beam width will be  $1.14^\circ$  in this case, corresponding to an antenna height of 5 ft. For each scan position the aperture time is 4 s resulting in  $4 \times 30 = 120$  s for the total scan cycle to complete. During the scan cycle the platform and targets (Mach 3.5) move  $4 \text{ km/s} \times 120 \text{ s} = 480 \text{ km}$  relative to each other in East-West direction ( $\approx 30$  synthetic apertures). In order not to lose the targets azimuth scanning could be necessary. The general question here is how a sufficient coverage could be achieved at all.

#### Azimuth and Range Parameters/Track Mode

After detection of the targets (or target clusters) or by external command the system changes to track mode to image the targets with 1 ft resolution in azimuth and elevation plane. This requires the individual target to be tracked over a certain aspect angle. For an X-Band system and a resolution of 1 ft this aspect angle is  $50 \text{ mrad} = 2.8^\circ$ . This corresponds to a synthetic aperture length of 249 km for an orbit altitude of 5000 km. Based on an effective relative platform-target velocity of 4 km/s the aperture time ( $\approx$  track time) is 62 s.

If the track volume dimension is defined as  $5 \text{ km} \times 5 \text{ km} \times 5 \text{ km}$  a high gain antenna with a pencil type beam width of  $1 \text{ mrad} = 0.05^\circ$  is required. This would be an aperture size of  $100 \text{ ft} \times 100 \text{ ft}$ . The tracking angle in the plane perpendicular to the radar LOS would be 50 beam widths in this case. This value probably is too large due to grating lobes.

Probably, the two antennas for search and track mode may be combined into one. The following power budget consideration shows that the antenna dimension could be reduced. An other possibility would be to use the search mode antenna for track mode also, however turned by  $90^\circ$ .

The number of range bins within the track volume is  $5000 \text{ m} / 1 \text{ ft} = 16660$ . The number of radar pulses to be processed during one track cycle of 62 s duration is 155000.

Since the system looks down at steep angles the targets within the track volume are separated from the ground return in the time domain, if the PRF is chosen properly. Since the target-earth geometry is changing over the track cycle, the PRF has to be adapted accordingly, so that the radar transmits a pulse at the same time instant when the large ground return is received. The main question here is how to achieve the enormous pointing accuracy required to track the rather small track volume.

#### Power Budget

The power budget is considered not at the receiver output (raw data) but in the processed image, taking into account the considerable correlation gain for point targets. In the following table the characteristic parameters for each mode together with the resulting power budget are shown.

C/N = ground clutter/noise ratio, S/N = target signal/noise ratio. The contrast ratio  $S/(C+N)$  would apply for stationary targets on clutter background and is given for reference only.

The results are shown in the table below.

MODE	SEARCH	TRACK	TRACK	
			Small Antenna	Turned $90^\circ$
Peak Power / kW	10	1	1	10
Transm. Pulse Width / $\mu\text{s}$	333	333	333	333
PRF / Hz	2500	2000	1000	2000
Antenna Length / m	10 (30 ft)	30 (100 ft)	10 (30 ft)	1.66 (5 ft)
Antenna Width / cm	166 (5 ft)	3000 (100 ft)	1000 (30 ft)	1000 (30 ft)
Relative Velocity / m/s	4000	4000	4000	4000
Range / km	5000	5000	5000	5000
Refl. Coeff. $\sigma^\circ$ / dB	- 20	- 20	- 20	- 20
Target RCS / $\text{m}^2$	1 (0 dB)	0.1 (-10 dB)	0.1 (-10 dB)	0.1 (-10 dB)
Wavelength / cm	3	3	3	3
Noise Figure/Losses / dB	10	20	20	20
Az. Resolution / m	5 (15 ft)	0.3 (1 ft)	0.3 (1 ft)	0.3 (1 ft)
RCVR Bandwidth / MHz	100	100	100	100
Average Power / W	8325	666	333	6660
Peak Antenna Gain / dB	52	69.2	64.5	51.9
C/N Ratio / dB	- 0.4	13.3	0.7	- 11.4
S/N Ratio / dB	11.4	27.3	14.7	2.6
S/(C+N) Ratio / dB	8.6	13.8	11.3	2.3

Table 1. Power Budget Results

The results indicate that from the power budget point of view the Search and Track modes could be combined using the same active phased 30 ft x 30 ft array antenna with azimuth and elevation scanning capabilities. Due to the assumed deramp-on-receive technique the duty cycle is quite large. It should be noted, that the three track mode examples are based on a 10 times lower peak power, 10 times lower target RCS and 10 times larger noise figure/losses. The latter figure could be attributed to defocusing processor losses due to insufficient knowledge of target trajectories. From the power budget point of view the track mode looks feasible in general. The search mode, however, would require 83 kW DC power, assuming an overall efficiency of 10 %. This is indeed a futuristic value.

## 5. CONCLUSION

From the preliminary system design considerations it may be concluded that a space based multi-mode observation system based on active phased array antennas appears feasible to be implemented within the next 15 years. However, for the MTI/ISAR mode there are serious technological and operational risks. The main technological risk areas are believed to be the antenna technology itself as well as the real time (on board) processing technology necessary to handle the large amount of data generated by multi-mode high resolution systems.

As far as the MTI/ISAR mode for an observation task as discussed within the framework of the European Defense Initiative is concerned, the extreme requirements for pointing and trajectory estimation accuracy is believed to be one of the largest risks. The main operational risk for this mode is the coverage. At present it appears very unlikely, that the necessary number of observation platforms would be available, to guarantee complete coverage of the area of interest. However, any further system design considerations require careful analysis of the user requirements, if they exist.

## 6. REFERENCES

- [1] MBB, Thomson-CSF, Canadian Astronautics Ltd., RS-Consult: Advanced SAR Feasibility Study Final Report, ESA contract No. 7363/87/NL/JS, October 1989
- [2] J.P.Hardange, T.K.Pike: Multi-Mode Spaceborne SAR: A New Concept IEEE Radar Conference, Paris, 24.-28.4. 1989
- [3] D.Aurheimer et al: Developments In Radar Imaging IEEE Trans. on Aerospace and Electronic Systems Vol.AES-20, No. 4, July 1984, p. 363-400
- [4] G.Wade, S.Halevy, G.R.Heidbreder, D.L.Menwai: Large Synthetic Aperture Imaging Of Rotating Objects Using Tomographic Reconstruction Algorithms, Military Microwave Conference, London, 1984
- [5] D.L.Menwai: High Resolution Radar Imaging Artech House, Inc., Dedham, Mass., 1981, Chapter 3
- [6] M.J.Prickett, C.C.Chen: Principles Of Inverse Synthetic Aperture Radar (ISAR) Imaging IEEE 1980 EASCON Record, p. 340
- [7] A.W.Rihaczek, W.B.Kendall, H.A.Vorn, E.C.Nunn: Target-Motion Resolution (TMR) Processing 24 th Tri-Service Radar Symposium, Monterey, Ca., 1978
- [8] A.W.Rihaczek, J.L.Demminger, W.E.Schaff: Recent Advances In Radar Signal Processing Via Target Motion Methods 25 th Tri-Service Radar Symposium, Colorado Springs, Co., 1979
- [9] Kirk J.C.: Advanced Concepts and Techniques in Imaging Radar Short Course, State of the Art Limited, München 18.-19.2.88, Chapter 1V
- [10] Wehner, D.F.: High Resolution Radar Artech House, Norwood, Ma., 1987, Chapter 7
- [11] Wehner, D.F.: ISAR Imaging from Satellite Platforms NOSC-TD-563, AD-C031 844L, 30.March 83
- [12] Digital Optical Circuit Technology AGARD Conference Proceedings NP. 362, Schliersee, 11.-12.9.84
- [13] Bömmwetter, C.: Special SAR Techniques: STRETCH Short Course S 2.06 "SAR Principles and Application" Carl-Cranz-Gesellschaft (CCG), Oberpfaffenhofen, 12.-16.10.1987
- [14] Skolnik, M.: Radar Handbook, McGraw Hill, 1970, Chapter 11
- [15] MacDonald, Dettwiler and Associates, Ltd.: SAR Signal Data Encoding/Reduction Study, Final Report, ESA Contract No. 4377/80/NL/PP (SC), March 1983

## 7. ACKNOWLEDGEMENT

The continuing support by the management of MBB (K.Polzer) and Thomson-CSF (J.P.Hardange) is gratefully acknowledged.

AD-1005236



**TRADE-OFFS IN A SPACE BASED SURVEILLANCE RADAR**

Ian McMillan  
Marconi Space Systems Ltd.  
Anchorage Road, Portsmouth,  
United Kingdom.

**ABSTRACT**

The design of a dual polarisation high resolution synthetic aperture space based radar is discussed which incorporates features which allow an adaptable operation mode to be utilised for ocean or land observation. The requirements for wide coverage for ocean observation of shipping at lower spatial resolution and the requirements for smaller area coverage at higher resolution of specific target areas in one instrument presents the designer with a significant challenge.

The described instrument incorporate dual polarisation receive features with selectable polarisation transmit. Wide coverage transmit beams are utilised with a narrow steerable receive beam which follows the time dependent return signals in angle.

The transmission of raw measurements to ground based facilities is impractical for high resolution and the instrument must perform on board much of the necessary data analysis. Such an operation is now practical, if costly in power, and allows for ocean surveillance the transmission of the position of possible targets with a future extension to more 'intelligent' analysis.

The technology trade-off's applicable to such an instrument design for deployment and use in space are examined and the choices made in recent work are presented. With power, mass and cost at a premium and autonomous operation essential, a concept design incorporating a phased array with distributed transmit/receive modules with local intelligence and an all radio frequency and control optical distribution system and control system is examined.

Recent practical results on a reduced scale ground demonstrator of the design of a pulse compression system are compared with the flight requirements.

**INTRODUCTION**

Space based radars used for surveillance of activities on or near the Earth's surface have requirements significantly different from those used in airborne or ground radars. In general, the range to the target, although very large, is known and does not have a large variation. What is required is to image the target area and be able to discriminate in the spatial and radiometric sense reflectivity parameters of the area. Due to the large field of view instantly available a large mapping area is naturally desired. Such radars will be on a moving platform. This restricts the time available to view an area, but can otherwise be exploited as an advantage.

All spacecraft have a limited mass and electrical power and this fact alone all restricts the designer's freedom of choice. Communication between the spacecraft and the users on the Earth is restricted so it is important to pass to the ground as finished a product as possible.

To provide all requirement in one mode of operation is unrealistic but the radar instrument may be designed to fulfil many requirements in different time multiplexed modes.

Modes to image large areas of the sea surface, which has a known background, provide a different requirement to that of imaging the land's surface in high spatial resolution.

A high precision narrow field of view may be considered which may be steered to areas of interest, whilst still incorporating a lower precision wide field of view mode.

#### PERFORMANCE REQUIREMENTS

Imaging radars of this type would typically operate in a polar orbit of around 850 Km altitude which implies an orbit period of near 90 minutes. The ability to discriminate to 10 meters on the Earth's surface in a narrow coverage strip of say 50 Km anywhere from 250 to 750 Km from the spacecraft ground track is practical. Alternatively at a resolution of (say) 50 meters a width of 460 Km may be examined.

To achieve this performance with a real aperture radar would require a very large antenna aperture, however the vehicle motion can be exploited to synthesise such an aperture. This synthetic aperture radar together with a pulse doppler real aperture radar operation can be combined to provide high resolution both in range and azimuth directions.

The examination of the return signals in orthogonal polarisations can reveal additional information about the target. The reception equipment should thus be able to operate in two simultaneous polarisations.

Providing the narrow coverage area which is rapidly steerable implies a phased array antenna system. A series of defined wider beams can also be provided. Since the time of arrival of radar returns from the Earth's surface can be readily predicted such a radar may position a reception beam appropriately in time sequence to intercept the return. This allows a narrow high gain beam to be used, enhancing the link budget and significantly improving the rejection of spurious returns. To perform this function a fast control system and fast beam switching is required.

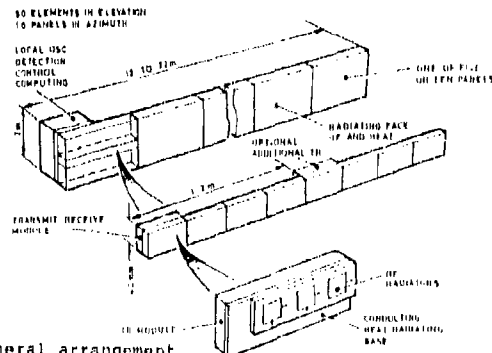


Figure 1 General arrangement

### SOLUTIONS

To provide solutions to these design requirements a number of areas must be examined and an attempt made to match current spacecraft practice and near future developments in the most optimum manner to the overall requirements.

#### Geometrical constraints.

In spacecraft radars there are a number of constraints which are derived from the geometry of the spacecraft to ground distances and angles. These, when analysed, require a system design which either arranges the direct return of the transmitted pulse from the ground directly beneath the spacecraft to arrive back at the spacecraft when it is transmitting or provides a deep null ( $3\sigma$ ) in the reception antenna at that angle. Furthermore since the system is a sampled data system enough samples must be obtained to provide the requisite ability to synthesise a large antenna. This restricts the pulse repetition frequency. In figure 1 a typical design chart is shown relating the prf to the available ground coverage.

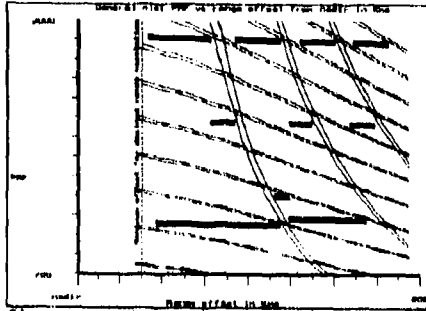


Figure 2 Geometric constraints

Possible coverage areas are shown. This example is at a 825Km altitude for an antenna aperture of 20 by 2 meters using a planar phased array consisting of 500 sub-arrays each of which has an individual transmit receive module operating at 5.3GHz with a transmit peak power of 10w and a pulse length of 50 microseconds.

#### Antenna design

The elevation beamwidth and scan requirements are modest by most standards. A scan width of 22 degs and a narrow beamwidth of 1.5 degs define the elevation aperture. Beam control by quasi-uniform amplitude and phase excitation is desired to maximise the beam power. Since narrow beam patterns and more controlled wide beam of up to 8 degs suffice. The associated azimuth beams are narrow and selectable from 0.1 to 0.5 degs necessitating an antenna length of 20 meters. Dual polarisation is required.

In the past, slotted waveguide arrays have been optimum for concentrated source transmitters, not only for their inherent electrical properties but because the necessary waveguides are box girder structures which provide inherent structural members for the array. Dual polarisation and distributed transmitter receivers balance the choice toward patch microstrip radiators for their simplicity of manufacture and their relatively broadband performance and the ability to have dual feed systems for two polarisations.

Such a structurally thin rf radiator provides a practical heat path for the transmitter-receiver to be mounted behind the antenna and still thermally radiate excess heat through the antenna which rarely points at the sun. The rear of the antenna panel is subjected to direct sunlight for part of the orbit and views cold deep space at 4K for the rest of each orbit. It has therefore to be constrained not to absorb or radiate heat.

Normal operation for broad area operation is to transmit with a wide beam (around 8 degrees) and to receive on a narrow beam of around 1.5 degs. This is first positioned at the extreme edge of the expected return area and then stepped in time across the transmit beam coverage area during the reception time. The receive beam may be broadened in angle when it is away from the edges without degrading the total ambiguity rejection properties of the system. Subarrays for such beams have been manufactured with gains which are measured at 18.2dB compared with the theoretical performance of 19.5 dB on single planar substrates providing dual polarisation. The substrates, being extremely light, give the promise of excellent full array structures with gains close to 20 dB.

## Resultant module plan

**REQUIRED POWER.**

The radiometric resolution of the final image is dependant on the total link budget and the number of independent images that may be averaged. With a modular arrangement one must select the peak power available from each module. Semiconductor amplifiers at C band or X-Band frequencies utilise GaAs PHEMT devices to generate the final output power. Such transistors have a power output dependant on the width of the junction in the device. Simple long gates suffer from the degrading effects of the resistive and reactive effects of the gate as a transmission line. Designers therefore produce multiple parallel gate transmission lines to reduce this effect. These are in effect parallel transistors. Within a die this effect and the low input impedance resulting causes a practical limit to the peak output for a high frequency device that can be usefully used of around seven to eight watts. The prudent system designer therefore designs his system for either that power per element or develops other strategies. With only (say) six watts per element the total power is severely limited or a large number of modules is required.

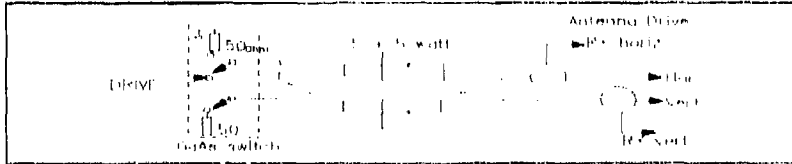


Figure 3 Power Amplifier arrangement

Current beam shape considerations require a minimum number of modules to provide the system whereas cost and complexity considerations provide an upper bound. A balanced output amplifier configuration has been chosen using five watt peak power amplifiers giving a ten watt peak output at up to 100 microsecond pulse length. An additional advantage of this system is that by driving one or other sides of the input hybrid outputs from the amplifiers to one or other outputs may be produced which are directed to the selected antenna polarisation port without additional switching. If in the future it is required to increase the power we change the output device not the system configuration. Such amplifiers use a drain supply which is pulsed to conserve energy. The quasi-linear operation allows tailoring of the transmit rf pulse in amplitude if required to linearise the overall system. This property is used to allow a simpler and lower cost system.

**RECEIVER SENSITIVITY.**

The total link performance requires that the receiver have a low noise factor. The ability to withstand the leakage during transmit periods and the desire for a low consumption limiter made us consider the use of HEMT transistors to give a very low amplifier noise factor, allowing the use of a simple active limiter of only moderate performance, and a negligible associated power consumption. A GaAs switch is used at the input directing the leakage transmit power to a load followed by a 0.8dB noise factor HEMT amplifier. To simplify the matching for low noise and double the amplifier's ability to absorb leakage a balanced amplifier configuration is used with a broad band Lange coupler. Such an arrangement provides a total noise factor referred to the input terminals of around 2dB and a gain of 12dB for 100mW of total dc power. The protection switch can operate in less than 10ns which is more than adequate.

**DOWNCONVERSION OR NOT?**

Many phased arrays provide only amplification at the carrier frequency before combination through phase shifters of the received signals. Provided the distances are short and the mass of the system not critical this is appropriate. The path distance is however twenty meters and with a foldable structure where mass and power are critical. Downconversion with GaAs MMIC elements provides a solution providing three advantages. Firstly conversion to frequencies in the 20 to 300 MHz region allows simple conversion of the signals for optical transmission, secondly the local oscillator drive may be phase shifted by the same phase shifter that is used for transmit beam forming and thirdly by the use of single sideband conversion the need for an input filter can be removed. Such input filters are large and expensive and are difficult to make compatible with millimetre dimension planar MMIC designs.

The downconverter chip is followed by IF amplification at 300MHz using 25dB gain stages which have gain set in 0.4dB quantisation by a controller. The current receiver total current is 305mA at 5v, most of which is used by a non-optimised downconverter device. This can be improved by the specific design of this item.

**COMMON CIRCUITS.**

Central to a phased array system is the ability to vary the phase of the signal being applied or received from the radiators. For reasons of cost and complexity it is desirable to time share this requirement between reception and transmission. Due to the small frequency difference (5.3 and 5.0GHz) between the transmit signal and the local oscillator signal the phase shifter may be shared.

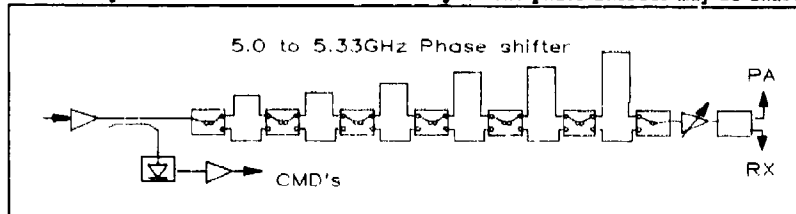


Figure 4 Common circuits and phase shifter

The incoming transmit signal or the local oscillator drive signal is passed through a six bit differential transmission line phase shifter comprising strip lines on a 250 micrometer substrate switched by GaAs switches. Not only is this straightforward and simple but it provides an extremely fast switching transition which is desirable for receive beam dynamic following.

The resultant signal is amplified and switched either to the power amplifier low level stage or to the local oscillator drive for the downconverter. In either case its level is adjusted by the final amplifier controlled digitally to give a defined signal level which is able to be selected for the particular function. In this way the power amplifier output level which is measured by a simple detector may be adjusted to take into account large range temperature effects, change of output with life and individual unit tolerances. If required the total module power may be lowered to provide a measure of amplitude beam control.

The control system requires an additional function. The control system receives its serial digital command bitstream as a amplitude modulated 5.0GHz signal which is demodulated by the common circuits and passed to the control circuit as a baseband signal.

**CONTROL REQUIREMENTS.**

Each TR module must be autonomous but be synchronised from a central source. It must be capable of setting the power connections, gain and phase of the module to pre-stored values for each of the states of the module. Transmission and up to thirty two different receive states may be required for each of (say) sixteen different prf types. Switching between these states is required autonomously during a prf interval with timing quantised in 200nSec periods.

Since each module would be far too complicated with an absolute time standard the internal clock in a module is resynchronised at the beginning of each transmit pulse.

The performance is achieved by a state machine architecture with a crystal clock controlled by a phase locked loop operative at the commencement of each transmit period. The serial digital command pulse with a 10 MHz clock rate synchronises the timing and carries the command information to merely start the transmission.

A previously transmitted command message has pre-stored the image, sub-aperture and range pulse information within each TR module controller for a period of an orbit in advance. This information is specific to a TR module and contains the correction of the required phase information taking into account the deterministic errors in the signal path from the central unit to that modules radiator and back.

Such a control system in a flight model would be an ASIC cmos device. In our demonstrator system a single high performance DSP device is employed to simulate the state machine and the required small semiconductor memory.

Such highly integrated control systems provide significant advantages in simplifying the design requirements on the analogue portions of the TR module since they do not have to be to a consistent absolute calibration and the design can concentrate on the stability requirements.

### Signal distribution

Each TR module requires during the transmit period a low level coherent drive signal containing the desired LF modulation. During the receive period a coherent local oscillator drive signal is required. Command synchronisation signals are required between prf periods which may be binary bit streams amplitude modulated on the local oscillator drive signal. During reception two intermediate frequency signals are required to be transferred to the unit control where they may be summed with the other TR modules' output. This is required to be simply performed for 500 TR modules in such a way that it is low mass and so that the antenna may be folded and deployed.

#### Coaxial.

Thin coaxial cables may be thought practical but even two cables to each module would have a crippling mass penalty in a spacecraft with a 20 meter antenna.

#### Optical.

A viable alternative is to transmit the drive signals to the TR modules by directly modulating a 1.5mW semiconductor laser at the TR module transmit frequency. This is practical at frequencies of 5GHz. The resulting optical signal is split into 32 ways by an optical waveguide splitter ( a passive device of low mass ) and then passed to the TR module in a 1mm external diameter optical fibre with a mass of 0.8gm.m<sup>-1</sup>. Sixteen such systems provide the full array capability. At each TR module a photodetector recovers the RF signal and provides it to the amplitude detector and phase shifter. The fibres are randomly distributed to ensure that a failure does not disable a specific part of the antenna array.

In the return path for the intermediate frequency signals, power is more critical; lasers are impractical due to their support circuitry but for the lower rf frequency Light Emitting Diodes (LED's) can be used. Each if directly modulates a LED producing around 20 microwatts of optical power. One channel produces a wavelength of 830nm and the other 1300nm. These are combined by an optical multiplexer and passed down a 20 meter fibre to the central unit where they are combined in successive optical combiners of 16:1, 16:1 and 2:1 ratios. The dual wavelength signals are then separated by an optical filter and the resultant signals detected in Avalanche PIN photodiodes before being amplified in the usual manner.

It should be emphasised that most of the system is completely passive, very low mass and using a star connection method very failure tolerant. Such optical

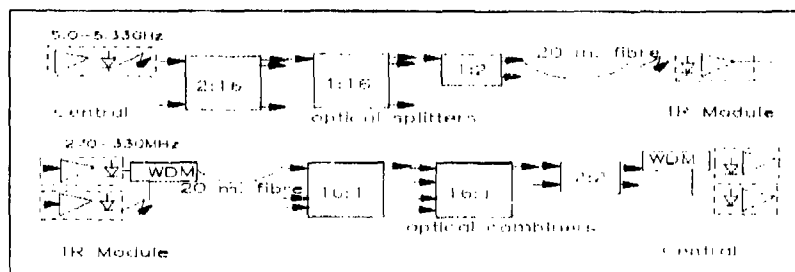


Figure 5 Optical distribution of rf and control signals.

transmission is very phase stable, able to be folded, uses connectorless fused junctions and is predictable in performance.

Such a system has been designed and built for use in a demonstrator to verify the link budgets of a SAR spaceborne imager.

#### PRIMARY POWER.

The primary power in a spacecraft is derived from batteries during operation when the sun is in eclipse. For a full availability system sufficient energy must be stored from photovoltaic cell systems during sunlight to ensure availability during spacecraft darkness.

Significant power is required for space radars and a choice has to be made between deriving the secondary supplies for the distributed element centrally or at the point of use. The low voltages and the current required predicate local power conversion. To avoid high mass and significant resistive loss a high voltage dc bus is used between the primary source and the local power conversion. Semiconductor switches able to handle the higher voltages of a 200v dc bus are now available for the spacecraft user and can be incorporated. This permits a low mass solution. The alternative of a high voltage bus at (say) 20KHz ac transformer coupled to the loads cannot be dismissed but presents problems due to the non uniform power requirements of the local converters.

The current designs of point of use power units operating with megahertz frequency dc to dc converters for the automobile industry show that zero voltage switching converters with synchronous rectification provide excellent efficiency coupled with very small mass and volume of an order not obtainable a few years ago.

Such design methods allow a TR module power unit for a modest seven watts to be readily designed with the appropriate characteristics and in a technology which is compatible with high, (by spacecraft standards), production volume. Coupled with appropriate fail protection input circuits such modules may be attached to a 200v dc supply in a quasi-star connected system which provides adequate reliability.

#### Radar signal generation

Pulse doppler systems of this type require bandwidths between 10 and 52MHz to provide the required range resolution due to the varying incidence angle of the beam with the Earth's surface. Individual beams should be optimised for their bandwidth.

Correlation between transmit and received signal by surface acoustic wave transversal filters is a practical and apparently low power method but usually require temperature control of the filters which mitigates against any low power properties. Recent designs, with direct digital generation of I and Q baseband transmit signals which are modulated on to the carrier, allow arbitrary waveforms to be produced and are much more satisfactory, permitting instantly stable waveforms to be generated. A significant additional benefit is the ability to pre-distort the transmit waveform to counteract any phase or amplitude distortion present in the combined transmit receive path. Such systems require high speed low power d-a and a-d conversion and 20nSec cycle time low power semiconductor memories. Such systems have now been demonstrated with 50 MHz sampling and 40 MHz bandwidth and allow fast versatile pulse doppler systems to be used.

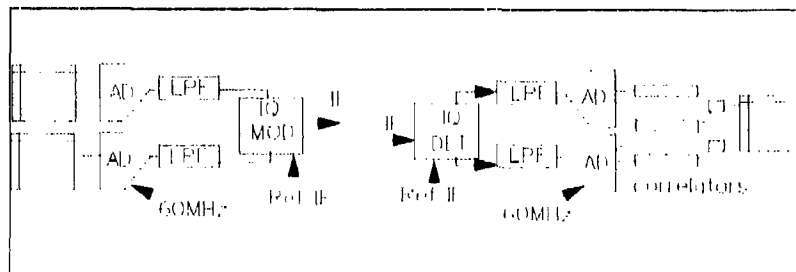


figure 6 Digital LFM generation and correlation

Direct digital correlation to compress the pulse can be credibly designed at lower speeds using specific VLSI devices in 80S cmos designs. Current demonstrators use 3 micron devices but with evolution to 1.2 micron array devices in the future the higher bandwidth may be correlated. Currently only 12 MHz systems have been built at spacecraft power consumption levels.

#### Instrument control

Such radars require central control with time quantisation of the order of 100nSecs. In the past control has been performed by multiple microprocessors which have operated with microsecond or greater instruction times and therefore the purely radar control has had to be performed by conventional logic. This has been a hindrance to simple control. Modern fast Digital Signal Processor devices have instruction times of the order of 100nsecs and allow most of the 'glue' logic to be dispensed with and allow complex fast operations to be held in program memory.

## ANALYSIS ON BOARD

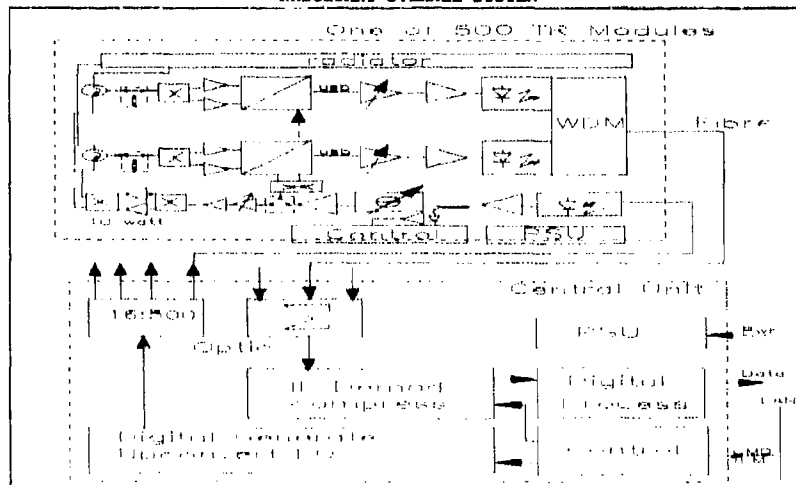
The raw signal return after digitisation may be digitally processed to give the range compressed result, at the required bandwidth, by digital correlation using specific CMOS devices of low power. This can provide the required range resolution.

The generation of the synthetic aperture, usually for more than one independent image to allow subsequent simple averaging, is a similar operation but although the input data rate is slower, it is much more complex due to the size of the data set.

Until recently it would not have been considered for on board implementation since it would not reduce the data rate to the ground unless multiple images could be performed. Advances in devices allow us to consider on board implementation which can reduce the resultant data rate to the ground but more significantly allow examination of the image on the spacecraft and simple analysis to be performed with the analysis result or the result and a small image of the relevant area to be transmitted thereby vastly simplifying the ground task and opening the way to near tactical use of the data particularly for ocean observation.

The technical area most critical for this operation is the power consumption of relatively fast semiconductor memories which predominate in the power consumption of such real time azimuth processors.

## RESULTANT OVERALL SYSTEM



**RESULTANT OVERALL PERFORMANCE**

Operating Frequency            5.3GHz  
 Transmit bandwidth            52MHz  
 Pulse length                    100 microseconds max.  
 Pulse repetition frequency    900 to 2000 Hz  
  
 Peak transmit power           5KW  
 Receive noise factor          2dB  
  
 Antenna beam  
   max gain                      50dB  
   elevation beamwidth        1.4 deg minimum  
                                      8.8 deg maximum  
   azimuth beamwidth         0.14 deg  
                                      or                    0.28 deg  
  
   beam steerable in elevation over 22 degs  
                                      and in azimuth over 1.5 degrees  
   overall dimension deployed 20 by 2 meters  
  
 Compressed receive  
   pulse width                  24 nSecs  
  
 point impulse function on ground  
                                      with -4dB widths of 10 by 10 meters minimum  
  
 primary power            at 200v dc            2.9 to 3.9Kw

**CONCLUSIONS**

Future surveillance spacecraft, for civilian or military use, will have to be designed with a high degree of adaptability. The requirements for adaptability and low cost are equally required in the civilian and the military field. Systems of limited scope and performance will not be acceptable. We have tried in this paper to give one example of a radar design which allows adaptability both during the design and build stage and also in its operational use.

**Acknowledgement.**

Part of the work described has been funded by The European Space Agency and the Ministry of Defence Procurement Executive of the U.K. Acknowledgement is given to my colleagues in ESA, MOD, SPAR Aerospace of Canada and Marconi for many stimulating discussions.

**DISCUSSION**

**J.Dorey**

May we have more comments on the stability of the signal reference, using optical fibres?

**Author's Reply**

The stability requirements fall into three categories -

- a) over the pulse travel time for pulse compression around 5-6 msec
- b) over the maximum subaperture time to allow the synthetic aperture to be formed say 400 msec and
- c) over the life to allow the correct antenna beam shape to be formed.

Category a) and b) are readily met. Category c) requires the rms variation of the 500 or so signal paths to be stable over time to around 5 degrees of angle which is the quantisation level of the phase shifter. Fibres are more stable than equivalent complexity plastic dielectric coaxial cables.

**J.P.Hardange**

What is the power consumption of the optical distribution? Is it important?

**Author's Reply**

The power consumption of the optical distribution system is not negligible, neither is the equivalent consumption of a coaxial system since the coaxial loss over 20m is around 12-14 dB whereas the direct optical loss is < 0.1 dB. A trade between mass, power and mechanical complexity in a deployable array favours optical.

A frequency agile 94 GHz pulse-doppler radar with  
dual polarisation capability

by

Helmut Barth, Wolfgang Menzel, Alfred Plattner, Joerg Schroth  
AEG Ulm  
Postbox 1730  
7900 Ulm  
W.-Germany

ABSTRACT

The design of a coherent, frequency agile 94 GHz radar frontend is reported. This radar includes features like pulse to pulse frequency agility in steps of 10 MHz within a bandwidth of 400 MHz and fixed or staggered PRF in a wide range between 1 and 50 kHz. The output power of 16 Watt and the antenna gain of 45 dB result in an effective radiated power of 89 dBm. The polarisation of the transmitted wave is switchable from pulse to pulse either from RHG to LHG or from horizontal to vertical. This depends on the kind of primary feed horn used for the 300 mm cassegrain antenna. Co- and cross polarized echo signals are received and processed by two separate but identical receiver channels. Line scanning with a rate of 20 scans per second is done by a flat rotating mirror.

INTRODUCTION

Besides of the frequency range around 35 GHz the band at 94 GHz offers another atmospheric window with low attenuation. This high frequency allows the application of very small antennas maintaining a narrow beamwidth. Therefore, systems at these frequencies are ideally suited for a variety of applications where at the same time small size, low weight and high directivity or high lateral resolution are required, e.g. in missile seeker applications.

In this case the radar often works under severe clutter conditions; on the other hand, a high lateral and range resolution is necessary to determine important target features.

To measure signatures of different targets and clutters, a versatile measurement radar system was developed. In the following table, the most important features of this radar are listed:

Frequency	: 94 GHz
Agility	: 400 MHz in steps of 10 MHz
Effective radiated power	: 89 dBm
Transmit polarisation	: switchable from pulse to pulse, RHG/LHG or horizontal/vertical by choice of the antenna feed horn
Range resolution	: 475 mm
Pulse width	: 70 ns
Pulse repetition frequency	: 1 to 50 kHz (fixed or staggered)
Receiver	: 2 channels for co- and cross polarisation
Peak to valley ratio	: 70 dB/Hz
Antenna system	: 100 mm Cassegrain system, 0.7 degree beam width, flat rotating mirror for line scanning
Radar control	: operators keyboard or computer interface

PRINCIPLE OF OPERATION

A simplified block diagram of the radar is shown in Fig. 1. As a frequency reference, a 160 MHz crystal oscillator is used. From its signal all required frequencies, even the PRF, are derived by multiplication, division and up- or downconversion.

In the mm-wave range, the first part of frequency processing is done at half the operating frequency allowing the application of more standard and reliable components and semiconductor devices.

A 46.24 GHz VCO is phase locked to the reference source employing a harmonic mixer. In order to achieve very high spectral purity, the Gunn-diode VCO is additionally cavity stabilized [1]. Its output power is fed into the varactor upconverters for both the transmitter synchronisation and the local oscillator branch. The low frequency input signals of the upconverters provide the frequency agility and a constant frequency offset between transmitter and local oscillator frequencies which, at this stage, amounts to half the receiver IF frequency. The output signals of both branches are locking two second harmonic mode oscillators at their fundamental frequencies [2]. In this way, active frequency doubling with more than 3 dB gain is achieved.

AD-PCOS 837

One of these fundamental/second harmonic mode oscillators acts directly as local oscillator for the two receiver channels while the other serves as injection locking source of the IMPATT power amplifier.

#### IMPATT POWER AMPLIFIER

For this radar application, a high degree of coherency and phase stability is required. Therefore, a transmitter with low phase error is necessary. Since the frequency chirp of pulsed oscillators in the free running state is converted to phase chirp in the injection locked state, two main conditions are derived from the requirements mentioned before:

A low locking gain (e.g. 10 dB) and a high locking range (e.g. 1 GHz) and low chirp of all oscillators in the free running state are essential.

Therefore, the IMPATT power amplifier is composed of a three stage injection locked IMPATT-oscillator chain /3/ shown in Fig. 2 followed by a 4 oscillator hybrid power combiner /4/ shown in Fig. 3. The low power stage of the IMPATT oscillator chain (Fig. 2) employs a 150 mW single drift IMPATT-diode initially optimized as CW-device. This diode is preheated by a DC current of 200 mA. An additional current pulse of 400 mA is required to produce output power. This mode of operation reduces the frequency chirp caused by temperature rise of the device significantly.

For the medium power stage a special designed 1.5 W single drift pulse IMPATT-diode is used. This diode has a significant current-frequency dependence that enables chirp compensation by current pulse shaping (see bias pulse modulator).

A double drift diode delivering 12 W peak is used in the higher power stage. It needs a pulse current of roughly 11 A. Bias pulse shaping is absolutely required for proper operation of this design, but unfortunately it has less influence to its inherent frequency chirp. However, the thereby caused phase chirp is compensated by pre-distortion the phase chirp of the medium power stage.

In this way, a maximum phase ripple of only +3 degree is achieved. The output power of the IMPATT oscillator chain, reduced to 6.4 W by circuit losses, serves as injection power for a four oscillator hybrid power combiner, shown as blockdiagram in Fig 3.

Four IMPATT-oscillators are powercombined by four 3 dB/90° hybrid couplers as shown in the center of Fig. 3. Additionally, the symmetry of this arrangement is used to provide switching of the output ports without any loss of output power. This is done by using a PIN-diode switch in the input path of the power combiner. If the injection signal is fed to port 1', the combined (or sum) power appears at port 2" while the difference power comes out at port 2' and vice versa.

Both output ports are connected to the two transmit/receive duplexers in the antenna frontend, where each port is associated to one polarisation. The combiner is matched by means of broadband isolators at the input ports (inserted between PIN-diode switch and combiner) as well as the output port.

Because the IMPATT-diodes of the oscillators  $O_1$  to  $O_4$  shown in Fig. 3 are operated in a mode similar to a saturated reflexion amplifier, their contribution to the overall phase chirp is as good as neglectable.

Output power per diode is about 7,5 Watt peak, the combiner output power at the ports 2' or 2" amounts to 28 Watt peak.

Circuit losses as well as the insertion loss of the PIN-diode switch reduce the synchronisation power available for the combiner to about 4 Watt peak. The output power at the antenna feed was measured as 16 Watt peak. This is caused by the losses of the isolators, turnstile coupler, T/R-duplexers etc.

#### RECEIVER FRONTEND

A more detailed block diagram of this part of the radar is given in Fig. 4. Directly connected to the circular waveguide antenna feed horn, a turnstile junction serves as polarization coupler separating an arbitrarily polarized incident wave into two rectangular waveguide outputs representing the LHC and RHC polarized components. A circulator serving as T/R diplexer, a PIN-diode STC and a balanced mixer are connected to each of these ports. Depending on the required transmit polarization, the output power of the IMPATT amplifier is fed to one of these circulators.

In order to reduce losses in the receiver paths, the complete arrangement is built into a compact block using E-plane techniques for circulators, STCs and mixers /5/. The turnstile coupler was scaled down from lower frequency versions /6/. The E-plane circulators /7/ show a reduced bandwidth compared to H-plane circulators; their set-up, however, is very simple and easy to fabricate.

Mixer and STC are realized in finline technique /5/ integrated on a single substrate for each channel. The STC provides a maximum attenuation of about 30 dB. The conversion loss of each channel (including circulator, STC, mixer) amounts to 9,5 dB, the SSR system noise figure (including IF contribution) is 13 dB. The mechanical dimensions are 75 x 60 x 20 mm.

#### IF SIGNAL PROCESSING

Both co- and cross-polarized signals are processed in two identical IF amplifiers. Behind a low noise IF preamplifier (NF = 1,5 dB) an IF-STC switch using a dual gate FET is implemented. The additional dynamic range of 40 dB gives an overall STC dynamic range of 70 dB. The slope of both the RF and IF STC is digitally controlled by means of a PROM. Thus the STC slope is accurate and temperature stable.

A range gate with a dynamic-range of 70 dB as well as a precision step attenuator is implemented in the 640 MHz IF path. After filtering, the IF-signal is downconverted to 160 MHz. At this frequency, a logarithmic amplifier with a dynamic-range of 60 dB and a phase-constant limited are implemented. This limiting amplifier has a phase error of less than 8 degrees over 60 dB of input dynamic range. Coherent detection is accomplished using I-Q phase detectors for both channels as well as an I-Q detector for the differential phase of the two channels.

#### MECHANICAL CONSTRUCTION AND SCANNER

The millimeter wave parts of the radar are assembled on a separate thermally insulated chassis which is temperature controlled by means of heating and fan-cooling. This chassis, together with the first IF circuitry, the pulse power supply of the transmitter and the antenna are mounted in the radar head as shown in Fig. 5. To this head, a mechanical scanner with a rotating flat mirror is connected. The flat mirror is metallized on both sides. Thus, with a rotation rate of 600 turns per minute, a scan rate of 20 scans per second is achieved over a operative scan angle of  $\pm 30^\circ$ . The antenna and the scanner are covered with a housing including a low loss radom (0.3 dB).

The radar head is connected via cable to a 19 inch rack containing the second IF level circuitry, the necessary signal processing components, the basic frequency processing and the basic power supply. The Radar can be operated either by a keyboard type operation board or under computer control. The complete radar equipment is shown in Fig. 6.

#### REFERENCES

- /1/ Bischoff, M; Schroth, J.: A mm wave receiver for 60 GHz satellite communication. Communications Engineering International, August 1980, 12-16.
- /2/ Barth, H.: Fundamental Wave Injection Locked 2nd Harmonic Gunn Oscillators at 94 GHz. 1984 IEEE MTT-S Digest, 391-393.
- /3/ Barth, H.: A Three Stage Injection Locked 94 GHz IMPATT Oscillator Chain. 1986 Military Microwaves, Symp. Digest.
- /4/ Barth, H.: A 4-Oscillator Power Combiner Used as a Lossless High Power Polarisation Switch at 94 GHz. 1989 IEEE MTT-S Digest, to be published.
- /5/ Menzel, W.: Compact 94 GHz Dual-Polarisation Radar Receiver Realized Using Different Integration Techniques. MSN, February 1984, pp. 78-85.
- /6/ Crandall, P.A.: A Turnstile Polarizer for Rain Cancellation. IRE Trans. on MTT-3 (1955), pp. 10-15.
- /7/ Solbach, K.: E-Plane Circulators 30 through 150 GHz for Integrated mm-Wave Circuits. 13th Europ. Microw. Conf., 1983, Nürnberg, pp. 163-167.

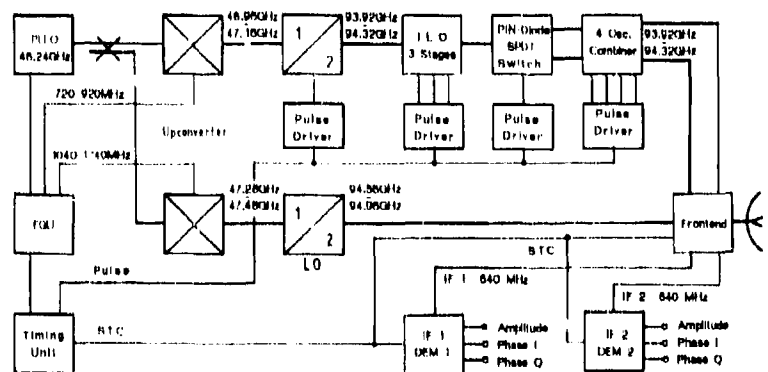


Fig. 1 Simplified Block Diagram of the Radar

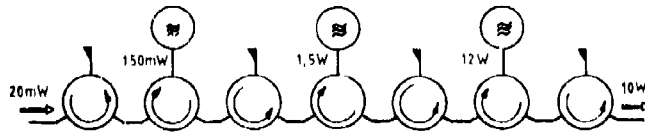


Fig. 2 Three Stage Injection Locked Oscillator Chain

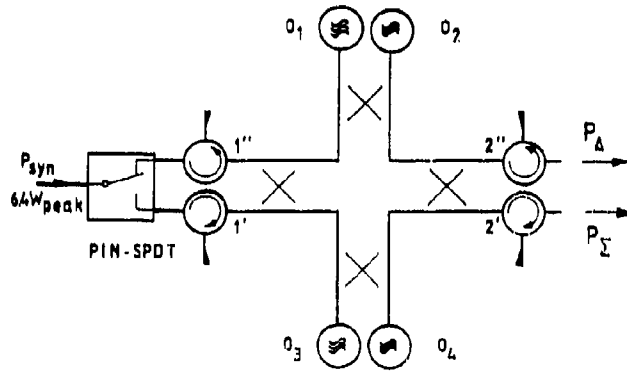


Fig. 3 4 Oscillator Combiner used as High Power Polarisation Switch

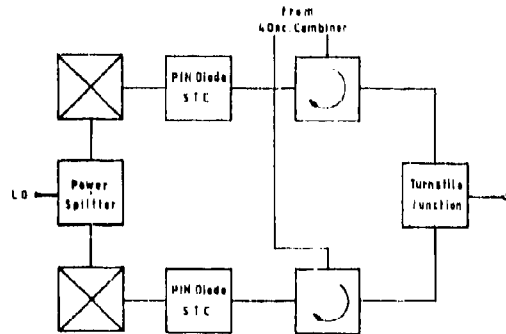


Fig. 4 Receiver Frontend

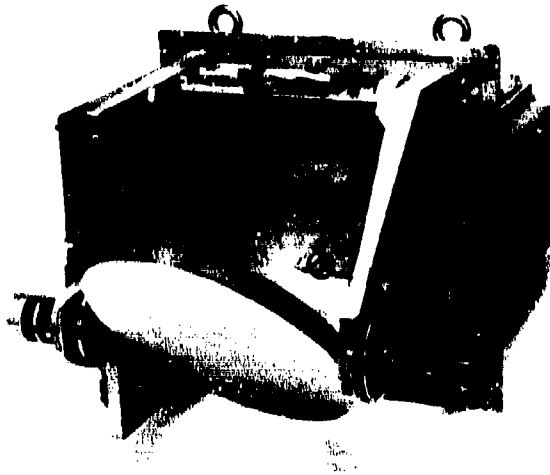


Fig. 5 Radar Head

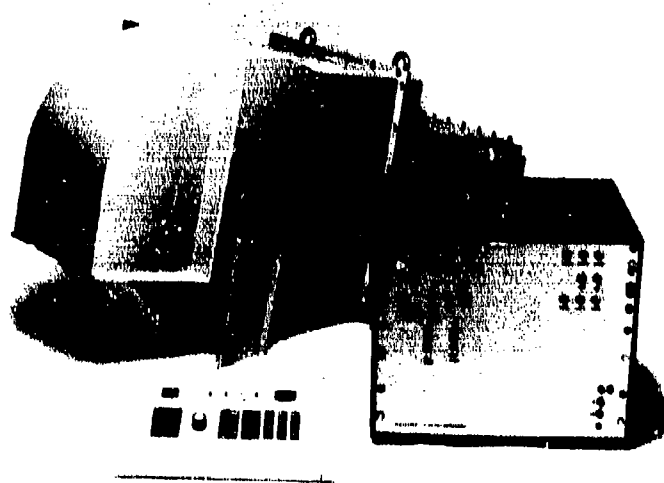


Fig. 6 The Complete Radar Equipment

**DISCUSSION**

**G.A. van der Spek**

Can the system derive the scattering matrix of each resolution cell of a target?

**Author's Reply**

Yes, it is able to determine the complex scattering matrix in a cell of 15m with an absolute resolution of 38cm. The accuracy to determine the distance of the object is typical for pulse radars. Processing is done by the group of Mr. Baars, FGAN-FHP, Wachtberg Werthhoven — see buss. card.



## Application of superresolution methods for airborne radar

D. Nickel  
 FGAN-FPM, Electronics Department  
 Neuenahrer Str. 20  
 D-5307 Wachtberg 7, F.R. Germany

## SUMMARY.

This paper examines the usefulness of superresolution methods for airborne radar. Angular resolution of closely flying targets is an interesting application. For SAR images superresolution methods do not seem to be very helpful. We give a survey of the possible methods and point out problems and constraints.

## 1. INTRODUCTION.

Superresolution methods for spectral and angular resolution enhancement are currently widely discussed. These methods are applied in seismology, speech recognition, and for experimental purposes in sonar, but not yet for radar. The time requirements for radar are the most demanding of the mentioned applications. Modern radar systems have to work completely automatic concerning target detection, estimation, and tracking. On the other hand, the radar signal to be resolved and/or the noise background is normally simpler than in other applications. These different constraints require to reflect upon the radar application. General viewpoints for applying superresolution to ground based radar have been presented in [1,2]. For airborne radar we have different modes of operation and constraints than for ground based radar. For the airborne tracking and surveillance radar we have a severe clutter problem which is a crucial point for superresolution. A special airborne radar mode is the Synthetic Aperture Radar (SAR), which creates pictures for reconnaissance or detects moving targets. This paper examines the use of superresolution methods under these constraints.

## 2. PRINCIPLES OF SUPERRESOLUTION.

By *conventional processing* we denote the forming of a sum beam using a plane wavefront weighting for angular resolution or applying the discrete Fourier transform for spectral resolution. Both types of processing are mathematically equivalent. The use of some amplitude taper to reduce the principal sidelobes is also considered as conventional processing. This type of processing makes no assumptions about the expected signal because it is derived from the Fourier transform, and it is robust against system errors.

*Superresolution methods* obtain their increased resolving power from a more refined model of the expected signal. The signal model is matched to the measured data according to some criterion of fit. The measured data can be the output of the conventional processor (beam output). For statistical reasons this beam-space approach does not give a very high degree of superresolution. Powerful superresolution methods are based on the spatial/temporal samples of the received waveform. This means that angular superresolution can only be achieved with an antenna array. For large arrays we can use subarray outputs.

**Robustness.** Matching a detailed signal model to the data means to interpret the fine structure of the received waveform. Therefore all superresolution methods are sensitive to errors. 'Robustness' with superresolution methods can only be obtained by choosing a realistic signal model and a well defined noise background. Superresolution should always be a second stage of processing, after conventional detection and direction finding.

**Resolution limit.** The classical definition of the resolution limit is given by the ability to separate two spectral lines/point targets. For conventional processing this resolution limit is approximately given by the 3dB beamwidth. The superresolution capability is measured by the fraction of the beamwidth at which two different signals can be resolved. Superresolution does therefore not necessarily mean high resolution, if we have an antenna with a broad beam. The difference in the two definitions of resolution is best illustrated by the following example: If we want to resolve two vehicles, the classical resolution is given by the pixel size, but superresolution tries to match the superposition of the silhouettes of these two vehicles.

## 3. APPLICATIONS FOR AIRBORNE RADAR.

The most interesting application for superresolution methods is angular resolution enhancement, because of the limitations for the antenna aperture. The best application is the resolution of formations of aircraft for the air-to-air looking radar (point targets against a 'white'-noise background). For the resolution of low flying aircraft for the air-to-ground looking radar the effectiveness of the clutter filter is prevailing the potential superresolution. For forward looking radar the conventional MFI may be sufficient, but for a sidelooking array a modern AMTI (for the whole array output vector (space-time processing)) is required.

For SAR image enhancement there seem to be not very useful applications for superresolution methods. In principle the angular SAR pattern is a conventional spectral estimate which could be enhanced by superresolution methods. However, the resolution of SAR, i.e. the time aperture, is chosen as large as possible for the given errors of the samples. Having extended the aperture to the maximum tolerable limit for the robust conventional processing, more sensitive methods can not give better results.

In summary, we have that the main application of superresolution methods for airborne radar is angular resolution of formations of targets.

AD-P005 838

#### 4. DESCRIPTION OF THE MAIN SUPERRESOLUTION METHODS.

**Superresolution arrays.** For a typical array with thousands of elements, it is presently too expensive to digitize all element outputs. In general, one uses *subarrays to reduce the number of channels*. The positions of the centres of the subarrays constitute a superarray. The whole array can be considered as the superarray having the subarrays as elements. One can show that for a regular fully filled array one should avoid regular subarrays because of the grating lobe problem. Grating lobes arise because the superarray positions have distances greater than half wavelength. This results not only in a periodic repetition of the high resolution angular spectrum, but also in a folding-in of targets outside the angular region of interest. If we choose subarrays of different shape such that the superarray is randomly distributed, we can avoid grating lobes. However, the signal model inherent in one superresolution method requires array elements with equal patterns. For sufficiently large number of subarrays we need not to correct for the different subarray patterns because the errors average. Superresolution methods which are restricted to linear equally spaced arrays can not be applied to irregular super/ subarrays.

**Target decorrelation by spatial averaging.** Many superresolution methods can not resolve completely correlated targets (e.g. caused by multipath). We can overcome the problem by modifying the covariance matrix estimate such that the signal covariance matrix has a rank equal to the target number (decorrelation techniques). A popular method to do this is "spatial averaging", which means to average the array outputs over a sliding subarray of  $L$  elements [9]. This is equivalent to averaging the estimated covariance matrix over a sliding  $L \times L$  submatrix along the main diagonal. Equally spaced element positions are necessary for this technique (no irregular superarray). The resulting covariance matrix has a dimension equal to the averaging subarray, i.e. we sacrifice aperture size for target decorrelation. Correlated targets are not considered a serious problem for airborne radar.

**Notation.** For the following description of the superresolution methods we use as a standard notation  $\underline{a}(\theta)$  for the vector for conventional beamforming without any taper (phased array beamforming) in a direction  $\theta$  i.e.  $\underline{a}_1(\theta) = \exp(j2\pi/\lambda)x_1|u|$  for a linear array with elements at positions  $x_1$  ( $1=1..N$ ).  $u = \sin(\theta)$  denotes the projection of the unit direction vector with azimuth angle  $\theta$  on the  $x$ -axis. For a planar array the direction is given by the projection of the unit direction vector on the  $(x,y)$ -plane and we have  $\underline{a}_2 = \exp(j2\pi/\lambda)(x_1u+y_1v)$ . For most methods  $\underline{a}$  can be multiplied with a moderate amplitude taper without changing the performance of the method significantly.

##### 4.1 Linear prediction methods.

These methods are well known and are frequently used for time series analysis. The common property of these methods is that they can be interpreted as methods to extrapolate the received waveform beyond the antenna aperture by a suitable prediction filter. A lot of variants of this type have appeared. The basic procedures are the maximum-entropy (ME-) method or autoregressive model fitting (AR-) method (Burg-Lovinson [4], Marple [6] etc). These methods estimate a continuous angular power spectrum of the form

$$S_{AR}(\theta) = 1 / |\underline{a}(\theta)^H \underline{L}|^2,$$

where  $\underline{L}$  is an appropriate prediction filter vector, calculated from the estimated covariance matrix (spatially smoothed, or with imposed Toeplitz structure, etc).

These methods are good for estimating arbitrary spectra with large sample numbers in time series analysis. For the given case of radar angular resolution (pure spectral lines) the methods are not very well suited. We have blocks of time and space data, the subarray centres may not be equally spaced and most of the fast algorithms are not applicable in this case. In case of a planar array, the methods can not easily be extended to two dimensions. Furthermore, the detection performance with these methods is a serious problem because the distribution of the sidelobes of the estimated spectra is unfavourable (Duggerer p.160 in [4]). To determine the optimum filter length some criteria have been suggested. Simulations showed that an optimum filter length may not exist. One may have either a spectral estimate with small variance and bad resolution or a spectrum with high sidelobes and good resolution, [2].

##### 4.2 Capon-type Methods.

These methods use spectral estimates of the form

$$S_{C,r}(\theta) = (\underline{a}(\theta)^H \underline{Q}^{-1} \underline{r}(\theta))^{-1} r,$$

where  $\underline{Q}$  is the estimated covariance matrix (possibly spatially smoothed) and  $r$  positive and real. The case  $r=1$  is due to Capon, [4] p.119, the extension to arbitrary  $r$  was presented by Pisarenko [6], for  $r=2$  this is also called "thermal noise algorithm" [7]. Methods which use the ratio of  $S_{C,r}$  for different  $r$  have also been suggested, [8].

These methods are applicable to random planar arrays. They have good detection performance, that is to say, the distribution of the estimated spectrum is not very heavy tailed for a sufficiently large number of samples. The typical feature of these methods is the prohibitive amount of computations (matrix inversion, possibly matrix multiplication).

##### 4.3 Signal subspace methods.

For this class of methods it is assumed that the signals to be resolved lie in a lower dimensional subspace of the whole complex space of array output vectors.

**Projection methods** are a subclass in this category. They use angular power density estimates

$$S_p(\theta) = 1: \underline{a}(\theta)^H \underline{P} \underline{a}(\theta) \quad \text{with} \quad \underline{P} = \underline{I} - \underline{X} \underline{X}^H.$$

$\underline{P}$  is a projection matrix and projects on the space orthogonal to the signal space (complement of the signal space, "noise space"). The columns of  $\underline{X}$  are a set of orthonormalized vectors which span the estimated signal space. There are different approaches to get an estimate of the signal space  $\underline{X}$ :

■ *The MUSIC algorithm* [9,10].  $\underline{\Delta}$  is composed of the dominant eigenvectors of the estimated covariance matrix. This method is known for its excellent resolution properties. It is applicable to arbitrary arrays and not for completely correlated targets, except with spatial averaging.

■ *The Hung-Turner (HT-) projection*. Less computational expense is required if  $\underline{\Delta}$  is estimated by simply orthogonalising the measured data vectors [11,12]. If the signal-to-noise ratio is high, the data vectors approximately span the signal subspace. This method performs not bad for strong sources [2], but the problem is that there is only very limited data averaging possible (in contrast to averaging given by the estimated covariance matrix). The method is applicable to arbitrary arrays, but not for completely correlated targets. The HT-projection can be extended to arbitrary number of samples if the columns of the estimated covariance matrix are used as a basis for the signal subspace, [2].

■ *The Kumaresan-Tufts (KT-) method*. If the "noise space" is represented by one single vector  $\underline{\Delta}_N$ , equivalent to the signal space being of dimension  $N-1$ , the projection can be written

$$\underline{E} = \underline{\Delta}_N \underline{\Delta}_N^H$$

The angular spectrum  $S_p$  then takes the form of  $S_{AR}$  and is closely related to it. The methods of Reddi and Kumaresan/Tufts, see (3) for both, have this form. Calculation of the vector  $\underline{\Delta}_N$  is based on eigenvector or singular value decomposition. In contrast to all other projection methods, the Reddi- and KT-method is limited to linear arrays.

A second subclass in this section are *algebraic methods*. Once the signal subspace has been estimated, these methods calculate the desired directions by solving algebraic equations instead of maximizing/minimizing a scan pattern.

■ *Root finding methods*. All projection methods (as well as linear prediction methods and Capon methods) can be turned into algebraic methods in case of a linear equally spaced array with  $x_k = k\lambda$ . In this case one identifies  $a_k(\theta) = z^k$ , with  $z = \exp(j\pi u)$ ,  $u = \sin(\theta)$ . The denominator of the scan pattern  $S_p$  (and also  $S_{AR}$ ,  $S_{CT}$ ) then can be considered as a real-valued polynomial with complex argument  $z$  of degree  $2N$ . The roots  $z_{lk}$  of this polynomial, projected on the unit circle, give estimates for  $a_1(\theta_{lk})$ , i.e. of  $a_k(\theta_{lk})$  and hence of the direction.

■ *ESPRIT algorithm* [14]. This method is applicable to fairly arbitrary arrays; the array has to compose of two (overlapping) subarrays which differ only by a constant shift. The directions are found by analysing the eigenstructure of the auto- and cross-covariance matrix of these two subarrays. Two eigen-decompositions are required: first to determine the signal-alone covariance estimates for each subarray, and then to solve the generalized eigenproblem with the two signal covariance estimates. Superior performance of ESPRIT over MUSIC has been reported, [15].

Although the signal subspace methods have good resolution properties, they require in general too extensive calculations. Only the simple HT-method could be fast enough for airborne applications, but PTMF-methods mentioned below are better suited for automatic processing.

**Hypothesis testing problem.** For all signal subspace methods we need to know the dimension of the signal subspace  $M_s$ . This is a difficult detection problem because the tests must be completely automatic and well defined. For the eigenvector projection (MUSIC) some suggestions have been made [16,17], also for the HT method [12]. In addition to finding the dimension on the signal subspace  $M_s$ , we have to detect the target number which is in general different from  $M_s$ . This is usually done by comparing the peaks of the scan pattern with a threshold. The distribution of the sidelobes of the scan pattern is then important. The behaviour of these tests and the ties arising from cascading two test procedures are an open field for research.

#### 4.4 Parametric target model fitting (PTMF).

These methods have been described in [18,19]. A complete parameterization of the assumed signal vector  $\underline{s}$  is used. Many target models with complicated parameterization are possible. For radar, the point target assumption with unknown amplitude is most appropriate:

$$\underline{s} = \sum_{l=1}^M A_l(\theta_l) \underline{b}_l = \underline{\Delta} \underline{a} \quad (1)$$

The unknown parameters are  $\theta_l$  and the complex amplitudes  $a_l$  ( $l=1, \dots, M$ ), which can be comprised in a complex vector  $\underline{a}$  and a complex  $N \times M$ -matrix  $\underline{\Delta}$ ,  $A_{k,l} = a_k(\theta_l)$ , ( $k=1, \dots, N$ ). The model is chosen such that the mean squared error between measured data  $\underline{z}$  and model  $\underline{s}$  is minimum:

$$\min_{\underline{a}, \underline{\theta}} \sum_{k=1}^N |z_k - \sum_{l=1}^M A_{k,l}(\theta_l) a_l|^2 \quad (2)$$

The minimum over  $\underline{a}$  is a least squares problem and the solution can be written down for each  $\underline{\theta}$ , [18]. Then (2) reduces to:

$$\min_{\underline{\theta}} \sum_{k=1}^N |z_k - \underline{\Delta}(\underline{\theta}) \underline{\Delta}^H z_k|^2 \quad (3)$$

Because of the deterministic amplitude model the method is able to resolve even completely correlated targets. This makes PTMF-methods of special interest to radar to counter multipath.

**Parameter estimation.** The main problem with PTMF methods seems to be the computational expense to minimize the mean squared error function (2). Many ideas for fast minimisation of (2) or (3) have been presented.

■ *Analytical determination* of the optimum parameters for small numbers of elements in special arrangements, not applicable for general planar arrays.

■ *Prony method*. For one data vector ( $K=1$ ) and the number of data components equal to the number of unknowns, the minimisation of (2) reduces to an equation. Solving this equation is called the Prony-method and is closely related to AR-model fitting. This method is restricted to linear antennas.

■ *Alternating projection methods*. The minimisation of the multi-dimensional function (3) can be reduced to a sequence of 1-dimensional minimisations if only one direction is varied while the others are kept fixed. Of course, convergence does not become faster with alternating projections compared with multi-dimensional minimisation.

■ *Newton-type methods*. These are the classical methods for minimising non-linear functions. Although the number of iterations is much less than with a simple steepest descent gradient algorithm, the direction updates are more complicated to compute. This is not very attractive for real-time applications.

■ *Stochastic approximation methods*. The function (3) is minimised for  $K=1$  by a gradient search, but for each iteration step a new data vector  $z_k$  is used. No storage of the data or covariance matrix is required. In addition, one can show that this algorithm can be reduced to a procedure which uses only the outputs of parallel beams. This is very effective for phased array radar. Because the stochastic approximation is also able to follow a non-stationary target situation (if not changing too fast), this algorithm is also suited for tracking targets.

Hypothesis testing. The target number can not be found by minimising (2), because this function is monotonically decreasing with  $M$ . A sequence of white noise tests, [18], is simple to calculate and has been tested in simulations and experiments. This test is sequential with respect to the target number and it requires the minimum number of the expensive parameter estimations.

Experimental results. Simulations and several experiments with real data have proven the superior performance of the PMF algorithm with stochastic approximation for different radar applications. Some experiments are conducted at FPM with the experimental system DESAS which uses a fully adaptive superresolution algorithm. It consists of a planar 8-element array at S-band shown in figure 1. The digitised element outputs of the antenna are fed to a microprocessor. The targets are simulated by the 3 antennas in front of the array. Fig. 2 shows the results of the superresolution. The 3 dots within the circles show the directions of three sources estimated by the stochastic approximation as described in [18]. The size of the dots is proportional to the estimated amplitude. The directions correspond to the true directions better than 0.1 beamwidth. The inner circle indicates the size of the 3dB beamwidth of the antenna and this gives an impression of the separation between the sources. Target separation is approximately 0.5BW and 0.3BW. The 3 most left vertical bars show the averaged estimated amplitude and the crossline indicates a threshold. This is used to reduce the assumed number of targets if the amplitude falls below the threshold. The most right of the four vertical bars shows the test statistic for increasing the number of targets, according to the white-noise test described in [18]. Figure 3 shows the block diagram of direction estimation and target number increasing/ decreasing tests. One can switch the sources on and off or move the sources and the system displays the source situation in real time. The tests for increasing and decreasing the target number together with the stochastic approximation algorithm for direction estimation constitute an adaptive closed loop superresolution. This degree of automation has not been achieved with the other superresolution algorithms yet.

The achieved degree of superresolution with DESAS was always better than 0.5 beamwidth for two sources of equal power. With a well calibrated array resolution goes down to 0.2 beamwidth, but detection then becomes a problem. Targets with unequal power require a longer convergence time for the direction of the weak target. more than 3 targets also require longer convergence time. The limiting factor for superresolution is mainly array inaccuracy, not the signal-to-noise ratio, which simply produces slower convergence.



FIG. 1: FPM-DESAS experimental set-up: 8 element receiving array.

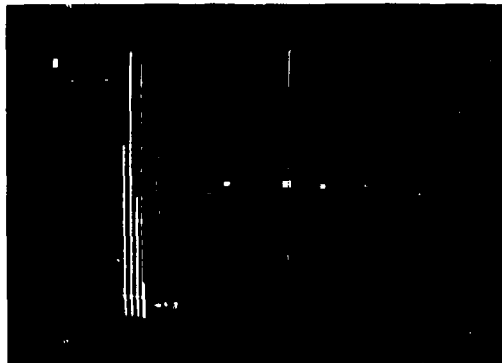


Fig. 2: FFM-DESAS display of results with closed-loop superresolution by stochastic approximation and multi-hypotheses test.

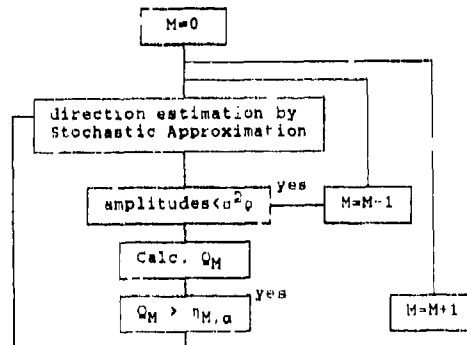


Fig. 3: FFM-DESAS: Structure of closed-loop superresolution with parameter estimation and tests.

## 6. PROBLEMS.

Superresolution methods encounter three problems: high accuracy of the receiving array, large computation time, reliability of the results.

**Accuracy of the receiving array.** Good performance of superresolution methods at a reasonable price can only be achieved by compensating errors by software (*self-calibrating arrays*). We have to provide different points in the receiving chain of each channel for inserting a test signal. Channel offset, amplification and orthogonality errors in the I- and Q-channel, inter-channel amplitude- and phase-errors for different frequency bands can then be corrected digitally. The only important hardware requirement is then channel stability and a sufficient dynamic range (number of bits) for each channel. Channel accuracy requirements decrease with the number of channels. For robustness reasons we will therefore choose to have as many subarrays as we can afford.

**Computation time.** For airborne radar applications the fast PTMF-method by stochastic approximation seems to be best suited. For few targets this method does not require excessive computation time. The main computational load arises from parallel digital beamforming, for which fast special hardware has to be designed.

**Reliability of results.** The probability of detecting the correct target number with superresolution methods is much lower than with conventional processing. Spurious targets due to array errors will appear. Robust superresolution methods will tend to detect a few of a given number of targets in an interference-free environment. For a high probability of correct superresolution good clutter (and possibly jammer) suppression and well defined detection procedures are necessary. The performance of the test procedures needs to be investigated with real data.

## 6. CONCLUSIONS.

For airborne radar, resolution of closely flying targets is the main application of superresolution methods. For SAR there seem to be no possibilities for a reasonable use of superresolution. The adaptive Parametric Target Model Fitting method seems to be the most promising method for the reasons of simplicity, robustness, and reliability.

A planar array with irregular subarrays and hardware for self-calibration would typically be part of a realization. The attainable enhancement in resolution will be not more than 1/3 of the antenna beamwidth. The limiting factor of superresolution will be the array accuracy rather than the signal-to-noise ratio.

## 7. REFERENCES.

- [1] U. Nickel: Angular superresolution with phased array radar : a review of algorithms and operational constraints. IEE Proc. Vol.134, Pt.F, No.1 (1987), pp.53-69.
- [2] U. Nickel: Angular superresolution by antenna array processing. Proc. Int. Conf. on Radar, 24-28 April 1989, Paris, France.
- [3] V.U. Roodi, A. Paulraj, T. Kallath: Performance analysis of the optimum beamformer in the presence of correlated sources and its behavior under spatial smoothing. IEEE ASSP-35, No.7 (1987), pp.927-936.
- [4] D.G.Chilcote (ed): Modern spectrum analysis. IEEE Press New York 1978.
- [5] S.L. Marple: A new autoregressive spectrum analysis algorithm. IEEE ASSP-28, No.4 (1980) pp.441-464.
- [6] V.F. Pisarenko: On the estimation of spectra by means of non-linear functions of the covariance matrix. Geophys.J.R.Astr.Soc.28 (1972) pp. 611-631.
- [7] R.L. Johnson, G.E. Miner: Comparison of superresolution algorithms for radio direction finding. IEEE AES-22, No.4 (1986) pp.432-442.
- [8] M.A. Lugunas-Hernandez, A. Gusuli-Llampallas: An improved maximum likelihood method for power spectral density estimation. IEEE ASSP-32, No.1 (1984) pp.170-173.
- [9] R. Schmidt: Multiple emitter location and signal parameter estimation. IEEE AP-34, No.3 (1986) pp.276-280 (reprint RADC Spectrum Estimation Workshop 1979).
- [10] G. Hienvenu, L. Kopp: Optimality of high resolution array processing using the eigensystem approach. IEEE ASSP-31, No.5 (1983) pp.1235-1248.
- [11] E. Hung, R. Turner: A fast beamforming algorithm for large arrays. IEEE AES-19, No.4 (1983) pp.698-607.
- [12] U. Nickel: Some properties of fast projection methods of the Hung-Turner type, in I.T.Yeung, J.Blomand, R.Duln, J.J.Gerbrands (eds.), Signal Processing III: Theories and Application (North Holland 1986), pp.1165-1168. (Conf.Rec. EUSIPCO-86)
- [13] R. Kumaresan, D. Tufts: Estimating the angles of arrival of multiple plane waves. IEEE AES-19, No.1 (1983) pp.134-139.
- [14] A. Paulraj, R. Roy, T. Kallath: Estimation of signal parameters via rotational invariance techniques - ESPRIT. Conf.Rec. 19th Asilomar Conf. 1985 (IEEE Comp. Soc. Press Washington 1986).
- [15] R. Roy, A. Paulraj, T. Kallath: Comparative performance of ESPRIT and MUSIC for direction-of-arrival estimation. Conf. Rec. IEEE ICASSP 1987, pp.2944-2947.
- [16] M. Wax, T. Kallath: Detection of signals by information theoretic criteria. IEEE ASSP-33, No.2 (1985) pp.387-392.
- [17] H. Wang, M. Kavoh: On the performance characterization of signal-subspace processing. 19th Asilomar Conf. (IEEE Comp. Soc. Press Washington 1986) pp.73-77.
- [18] U. Nickel: Superresolution by spectral line fitting, in: H.W.Schlesler (ed.), Signal Processing II: Theories and Applications (North Holland 1983), pp.646-648. (Conf.Rec. EUSIPCO-83)
- [19] J.F. Böhme: Estimation of spectral parameters of correlated signals in wavefields. Signal Processing 11 (1986), pp.329-337.

## DISCUSSION

### N.Lamcelongue

Are you able to reach absolute calibration of the backscattering coefficient when the STC is active. If yes, can you give us added information (strategie to recover absolute value)?

### Author's Reply

Yes - We save the data of the calculated IF Gain function for each radar scene. By calibrating the STC module we know the gain the STC introduces\* at each of the 256 hex control values. This enables the user to recover the value of sigma.

\*on the IF signal

### J.Richard

Where is the range compression implemented, before or after the AGC - STC System?

### Author's Reply

The range compression module is placed between the AGC and STC modules. The performance of the compression is thereby not affected.



THE PHARUS PROJECT:  
DESIGN OF A POLARIMETRIC C-BAND SAR IN THE NETHERLANDS

by  
P. Hoogeboom and P.J. Koozen  
FEL-TNO  
P.O. box 96864  
2509 JG The Hague  
The Netherlands

AD-8005 834  
SUMMARY

In The Netherlands a digital SAR system (X-band) is used since many years in radar remote sensing research. An example of results and the system's key features are given in this paper. Calibration and high geometric and radiometric accuracy were the keywords to success in remote sensing for this system.

Based on this experience a polarimetric C-band aircraft SAR is designed, that will be finalised in the 1990's. The system is designed using modern technology. In its final version it will make use of a phased array antenna with solid state amplifiers.

Before this system can be developed, a number of problems have to be solved. This is done in several theoretical and practical studies. In one of these preparatory studies a SAR testbed will be constructed, to test parts of the technology that will be used in the final system and to gain experience with airborne SAR in general. This testbed will be described in the paper.

The dataprocessing for the PHARUS system requires the development of software tools, that take geometric and radiometric corrections into account, as well as the calibration. This in turn requires accurate measurements of the aircraft position and attitude.

PREFACE

The PHARUS project (PHARUS stands for Phased array universal SAR) is carried out by the Physics and Electronics Laboratory of TNO (FEL-TNO) in The Hague in cooperation with the National Aerospace Laboratory (NLR) in Amsterdam and the Microwave and Telecommunication Group from the Delft University of Technology. The project is sponsored by the Ministry of Defense and by the National Remote Sensing Board (BCRS, Delft). The program management on behalf of these partners is carried out by the Netherlands Agency for Aerospace Programs (NIVR) in Delft.

1 INTRODUCTION

In the mid seventies radar experiments using a short range scatterometer were started in The Netherlands, mainly for the determination of radarsignatures of agricultural crops. This work was performed at X-band ( $\lambda=3$  cm) and later on also at 36 GHz ( $\lambda=8$  mm) [1]. The measurements were taken during a number of growing seasons to gain more insight in the variations from year to year. This led to work in the area of modeling and crop classification. It was soon recognized that calibration of the data taken at different times and under varying incidence angles is very important but also quite difficult to achieve.

The work described above was carried out by a number of institutes, each one covering a specific discipline. This multidisciplinary cooperation was organized through the ROVE team (Radar Observation on VEgetation). Nowadays the Netherlands Remote Sensing Board takes care of sponsoring this ROVE work. The experience gained with this program led to the use of a digital and calibrated X-band SAR system. Among others the multitemporal crop classification could be demonstrated with this system [2]. It is discussed in more detail in chapter 2.

In the 1980's it was realised that the work had to be extended to more and also lower frequencies and to other areas of interest. These ideas led to the design and the use of a multiband airborne scatterometer. The DUTSCAT multiband airborne scatterometer, designed and built by the Delft University of Technology [6] is capable of acquiring data at 6 frequencies ranging from 1 - 18 GHz.

The datasets from this system form the basis for the knowledge that is necessary to evaluate new applications in the field of remote sensing. Apart from studying the behaviour of targets as a function of frequency or incidence angle, the polarisation dependence can be studied, which becomes of growing importance as the interest in polarimetry increases. In the near future the DUTSCAT will be fitted with a possibility to measure two like polarisations and their phase difference simultaneously, which enables a thorough preparation for the polarimetric SAR system.

The next step is the development of an airborne polarimetric SAR system in the C-band, called Pharus (Phased array universal SAR). The choice of the parameters for this system are based on the experience we gained with the previous programs. This means

that special attention will be paid to the data accuracy. In the end the system will have to deliver radarbackscattermaps: calibrated images with a high level of geometric and radiometric accuracy.

The frequency used for the PHARUS is the same as for the ERS-1 satellite. The "universal" aspect of the PHARUS SAR is found in its twofold application: both military and civil programs in The Netherlands will benefit from it. The PHARUS project consists of two phases: a definition phase and a realisation phase. In the definition phase studies are carried out on antennatechnology and aircraft motion measurement and compensation. Furthermore a SAR testbed is constructed. This relatively simple SAR system will be ready in early 1990 and will be used to study in detail the problems and limitations of aircraft SAR systems. The results of these preparatory studies will guide the design of the final PHARUS SAR, which we hope to realize in 1991 - 1993. More details about the Pharus project in general are given in chapter 3. Chapter 4 deals with the design of the SAR testbed PHARS.

## 2 THE NETHERLANDS DIGITAL X-BAND SLAR

For many years a digital X-band SLAR system has been used for radar remote sensing research in The Netherlands. It demonstrated the possibilities of radar for remote sensing applications. Some properties of this system are given in table 1.

frequency	: 9.4 GHz (X-band)
transmitted power	: 25 kW
pulselength	: 50 / 250 ns (7.5 / 37.5 m)
polarisation	: HH
antenna beamwidth	: 10 mrad ( .6 ° ) twoway
P.R.F.	: 200 Hz
recording	: 4096 * 8 bit sampling @ 50 MHz (3 m)
internal delay line calibration	

Table 1: Specification of SLAR system parameters

By using an internal delay line calibration the system is capable of delivering calibrated images. The geometric and radiometric distortions in the captured data are corrected off line with a computer. This process makes use of the simultaneously recorded aircraft attitude and position parameters, that are delivered by an inertial navigation system. After correction and resampling images of high quality become available [3]. A high image quality is often desirable, for instance in the case of multitemporal crop classification [2,4].

Discrimination between various agricultural crop types in one radar image is sometimes difficult. By combining several images, taken under different incidence angles or at different times in the growing season, unambiguous classification of crops becomes possible. To enable a prosperous identification it is necessary that the images can be overlayed on to each other and that the reflection coefficients (gray values) may be compared between images.

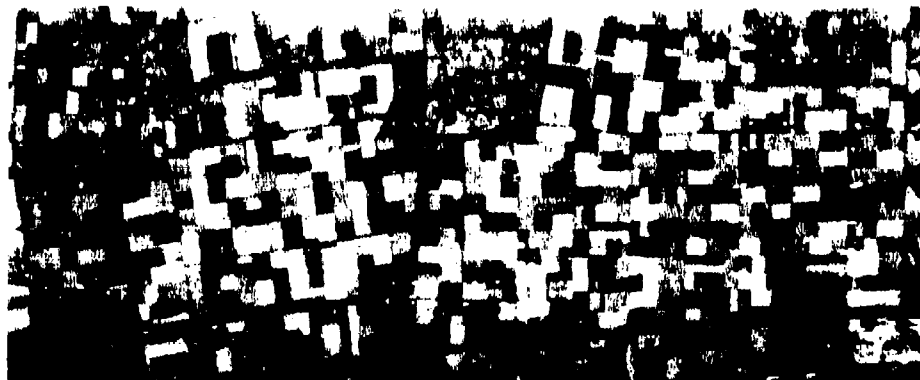


Figure 1: X-band SLAR flight over a testarea in the Flevopolder. Altitude 4000 m.  
Image dimensions: 6 x 15 km.

In figure 1 a SLAR image is shown, taken over the Flevopolder in The Netherlands. This area has been used frequently in remote sensing experiments. The aircraft flew at 4000 meter altitude. The grazing angle ranges from 60° to 30°. The image shows the fine radiometric and geometric quality that is reached through the previously described correction technique. The radiometric accuracy is in the order of 1 dB. In figure 1 the antenna was looking to the left and the aircraft moved from the upper right corner to the left.

A disadvantage of the SIAR technique is the degradation of the azimuth resolution as the range increases. This effect is also noticeable in figure 1. For example the three line features in the dark field just above the small town in the lower right corner of figure 1 are responses of corner reflectors. These point targets are imaged as lines due to the reduced azimuth resolution of approximately 75 meter (3 dB resolution measure). The resolution reduction is one of the reasons to move over to SAR technique in a new radar imaging system.

### 3 THE PHARUS PROJECT

A few years ago three institutes in The Netherlands developed a plan to design and build a polarimetric C-band aircraft SAR system of a novel design, meant as a replacement for our current SIAR system. These institutes are the Physics and Electronics Laboratory TNO in The Hague, the National Aerospace Laboratory NLR in Amsterdam and the Microwave Laboratory of the Delft University of Technology. It took a long time in 1986 and 1987 to raise the necessary funding. This can be seen in figure 2. As a result the system will be completed much later than originally expected.

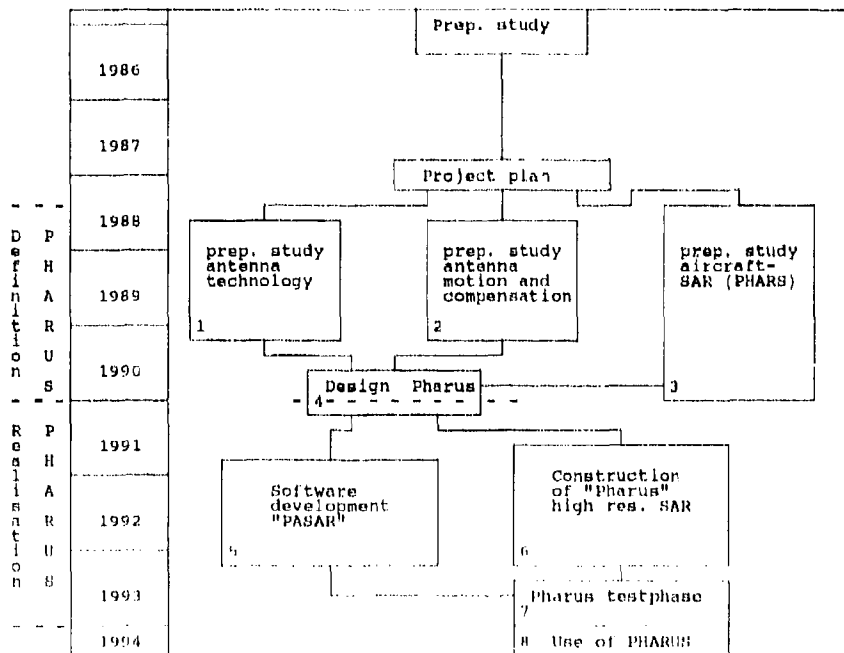


Figure 2: Block diagram of the PHARUS project.

The plans for the PHARUS SAR are based on the experience that was built up with the previously described programs. The choice for C-band was based on the development of the ESA ERS satellite program [5]. However, our initial hope to have it flying simultaneously with the ERS-1 seems to be unrealistic, due to the earlier mentioned delay suffered from fund raising. The SAR tested PHARS will be flying simultaneously with the ERS-1 now, but PHARS is not meant to be an operational system. Of course simultaneous imaging is still possible, but there will be severe limitations on the PHARS data.

Figure 2 shows a block diagram of the PHARUS project. The project consists of two phases, a definition study and a realisation phase. The definition study is intended to increase our knowledge on SAR and to develop the technology that will be used in the final system. In figure 2 it can be seen that three preparatory studies will be carried out before the actual PHARUS system is designed. These studies are considered to be essential for a proper design of the PHARUS.

The system will have an active array antenna, reason why a preparatory study on antenna technology is included. Especially the problems of decoupling between the various polarisations and the integrated antenna design (including power and low noise

amplifiers) will be studied. A satisfactory data quality from a polarimetric SAR may only be expected if the antenna fulfils high requirements.

A second preparatory study, the antenna motion and compensation study is necessary to build up experience with corrections of aircraft or rather antenna movements. The paper by Otten [7] at this symposium treats the subject in detail. Since the aircraft motions give rise to serious problems in SAR imaging, a thorough study is necessary to be able to meet the severe conditions that are put upon a modern imaging system.

In the third preparatory study a SAR testbed will be realised in the aircraft that will probably also carry the PHARUS. The testbed is necessary to study general problems of aircraft SAR and to study the coherent integration processes which in the end determine the sensitivity of the system. Finally the testbed can be used to determine the antenna motions from the radarsignal (via autofocus techniques). The results will be compared with motion measurements taken from other sensors, like an inertial navigation system, gyro's and accelerometers. This forms an important input for the final choice on a motion compensation system. Since the calibration of a radar equipped with an active array antenna is difficult to perform, several calibration schemes will be tested in the PHARS. The next chapter treats the design and realisation of the SAR testbed PHARS in more detail.

Upon completion of the preparatory studies enough experience will have been built up to design the polarimetric PHARUS system. This system can then be realised in the period 1991 - 1993. Simultaneously a flexible software package for SAR processing, called PASAR (Preprocessing of Airborne SAR data) will be developed. Apart from the usual SAR processing, this software package shall perform geometric and radiometric corrections. We hope to make use of the experience that was built up with the processing software for the present SLAR system.

It is still too early to give detailed specifications for the PHARUS system. They will be fixed during the design phase. The plans are heading for a polarimetric SAR with user selectable values for resolution (1.5 - 10 meter), swath (near range, far range or wide swath with reduced resolution) and recorded polarisations (one, two or four polarisations). The frequency will most probably be the same as used for the PHARS: C-band (5.3 GHz). It is expected that the system will be operational by the end of 1993.

#### 4 DESIGN OF THE SAR TESTBED PHARS

In table 2 some key parameters of the PHARS are given. On one hand this testbed can be considered as a simple SAR system with a limited range, on the other hand it is a state of the art technology testbed, designed to test modern technology for the PHARUS SAR. A single patch antenna is used for transmission and reception. This antenna is rigidly fixed to the aircraft (no mechanical motion compensation). The beam can be steered in coarse steps of  $3.5^\circ$  to compensate for the average driftangle. The horizontal beamwidth of the antenna is wide enough to eliminate the influence of aircraft yaw, once the beam is corrected according to the average drift angle of the aircraft, which may vary between  $-12^\circ$  and  $+12^\circ$ .

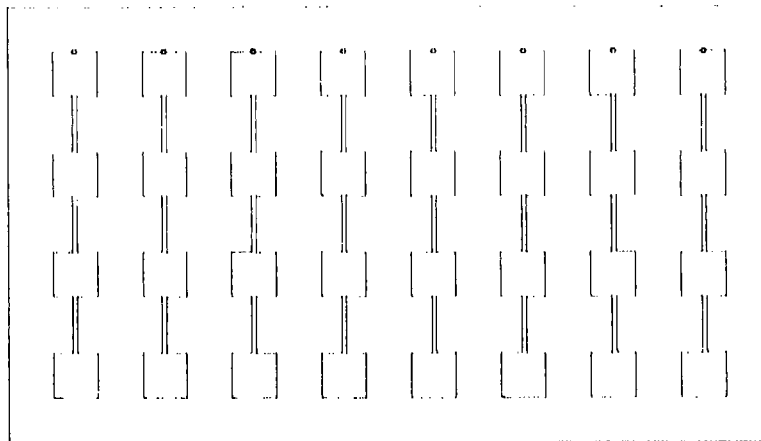


Figure 3: The 8 x 4 element patch antenna for the PHARS, dimensions are 35 x 15 cm.

-frequency	: 5.3 GHz (C-band)
-antenna	: one 8 x 4 element patch antenna for transmit and receive beamwidth 9 * 24 degr, VV pol. coarse step beamsteering (3.5°)
-transmitted power	: 160 Watt peak by 8 transistors
-PRF	: 3500 Hz (fixed)
-pulsewidth	: 32 ns (4.8 m) after compression 12.8 $\mu$ s before compression
-digitisation	: 4096 samples, 8 bits @ 87.5 MHz (range offset IF)
-range	: 6 - 17.7 km
-resolution	: 4.8 Meter in range 6 meter @ 4-6 looks or 1 meter single look in azimuth
-azimuth presumming	: 16 x
-aircraft	: Swearingen Metro; used at an altitude of 6 km, and a speed of 100 m/s

Table 2: Properties of the SAR testbed to be realized in the preparatory study on aircraft SAR PHARS.

The antenna exists of 8 rows of 4 elements each, as can be seen in figure 3. The 4 elements are connected by transmission lines and radiate equally to narrow the vertical antenna beamwidth to approximately 24° as desired. Each row of the array antenna is connected with its own microwave module. The connection, indicated by a small circle at the top of each row is fed through the substrate to the microwave module at the backside of the antenna. The 32 square radiators are equally spaced at approximately 0.75  $\lambda$ . The total dimensions of the antenna are approximately 15 x 35 cm.

The use of distributed power generation with transistors instead of central TWT (traveling wave tube) power generation yields a much smaller than usual peak power in both the PHARS testbed and the final PHARUS system. Each transistor power amplifier in the PHARS delivers 20 Watts, resulting in a total transmitted power of 160 Watts. System sensitivity is realized by the use of a high PRF (3500 Hz) and a large pulse compression ratio of 400. In the PHARUS system the peak power will be increased to approximately 2 kW and possibly the pulse compression ratio will also be further increased.

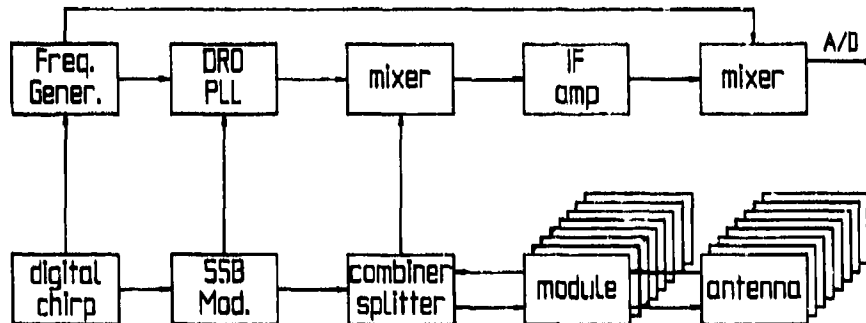
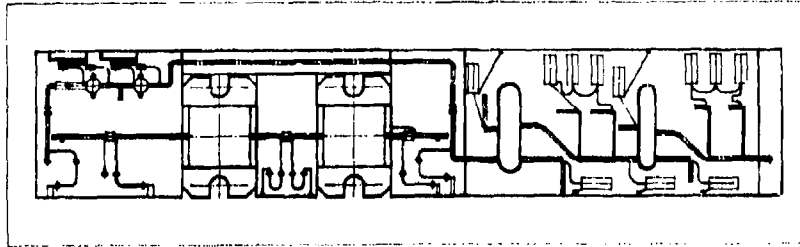


Figure 4: Block diagram of the PHARS system.

In figure 4 a block diagram of the testbed is shown. Most of the microwave electronics is concentrated in the T/R modules, which are described in the next paragraph. The 8 radiating sections of the antenna are each connected to a module. The modules are connected to a power splitter/combiner. On the left side in the block diagram the frequency generation and chirp modulation can be found. The upper right part is the actual receiver.

At the backside of the antenna 8 microwave transmit/receive modules are mounted. Figure 5 shows a drawing of one of these modules. The module measures 4 x 13 cm and is produced in stripline technology on Aluminumoxide substrate. These modules contain a two stage FET power amplifier, a low noise amplifier, a limiter, a 4 bit phase shifter and 2 SPDT switches, to actuate either the receive or the transmit channel. The power transistors are switched on just before transmission of the pulse, and switched off immediately afterwards to reduce the consumed electrical power. The noise figure of the receiver chain is 1.3 dB.

A power splitter/combiner network connects the 8 modules with the actual transmitter/receiver. The transmitter uses a dielectric resonance oscillator (DRO) to generate the microwave carrier. The DRO is phase locked to a crystal oscillator. The 5.3 GHz signal is modulated by a single side band modulator with a digitally generated FM chirp of 31 MHz bandwidth.



antenna connect. low noise amp. SPDT switch two stage power amplifier SPDT switch 4 stage phase shifter splitter/comb. connection

Figure 5: The T/R microwave module. 8 of these are used in the PHARS.

The receiver chain is rather straight forward: the microwave signal is converted down to 350 MHz, the IF frequency. This rather high frequency is chosen, because the PHARUS system will use an increased bandwidth of approximately 100 MHz, necessitating a high IF frequency. The output of the IF section is mixed to an offset frequency of 21 MHz and then A-D converted in 8 bits, with a 87.5 MHz sampling rate.

The range lines are produced at a rate of 3500 Hz, being the radar PRF. The associated datastream is much too large to store on magnetic tape. Our interest goes to the dopplerband between -50 and +50 Hz, which corresponds to the indicated 4 look azimuth resolution of 6 meter. This bandwidth can be sampled by the recording system at a maximum value of 218 Hz. To reduce the range line frequency of 3500 Hz to a 218 Hz sampling rate and to filter out the doppler components outside our band of interest, a Finite Impulse Response filter (FIR) is used as a weighted presummer. This presummer attenuates frequencies outside the interval -164, +164 Hz at least 30 dB, as shown in figure 6. In addition the antenna characteristic further reduces the amplitudes of such high doppler frequencies, because they come from targets that are at the edges of the antenna beamwidth. The doppler frequency transfer functions of the antenna and the FIR presummer are given in figure 6. This plot shows theoretical values; measurements are not yet available. The reduction in dopplerbandwidth by the FIR filter annex presummer is clearly shown.

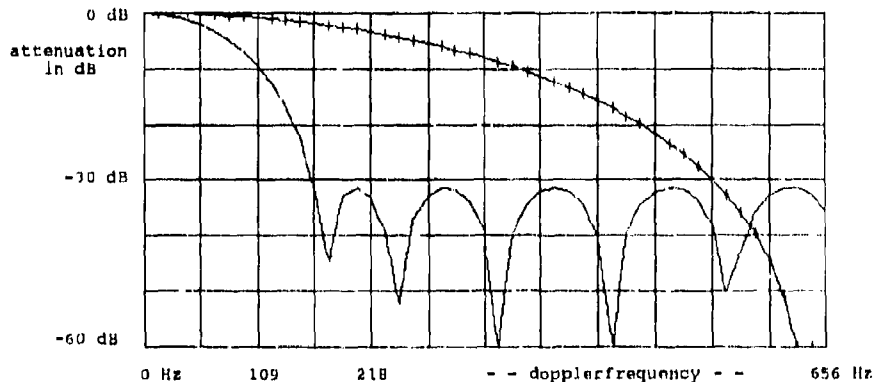


Figure 6: Antenna (line with plusses) and azimuth filter (straight line) characteristic as a function of doppler frequency.

The digital data remaining after azimuth presumming with a factor of 16 will be recorded on a HBR (High Bit Rate) recording system. This system is also used for the SLAR and the DUTSCAT. Apart from the azimuth presumming there is no on board processing for the testbed. By getting down as much data as possible, very flexible experiments are enabled with the system at the cost of long processing times. This is not a major disadvantage since the amount of data that will be gathered with the testbed is small anyway. After all the testbed PHARS is not an operational system.

The aircraft that is used in the project is a Swearingen Metro II, a twin engine business plane, owned by NLR and in use as a laboratory aircraft. It will fly the PHARS and the PHARUS at an altitude of 6000 meter with a speed of approximately 100 m/s. The aircraft is equipped with various sensors to acquire aircraft attitude and position. Among others an inertial navigation system, equipped with laser gyro's is available. The

data of these sensors are also recorded on the BBR recording system that is used for the radar data.

The PHARUS is mounted in the middle section of a standard N-container (bomb), a cylinder of 45 cm diameter and length over 1 meter. This container is attached under the fuselage, close to the center of gravity of the aircraft. At this position the influence of unwanted aircraft motions is minimal and the sensors of the inertial navigation system are nearby.

## 5 CONCLUSIONS

Bearing in mind the experience in remote sensing, build up over more than ten years, a polarimetric SAR system is designed in The Netherlands.

The project is carried out in two steps. In this paper the first step, consisting of a SAR testbed and preparatory studies, is described in detail. This SAR system will have limited capabilities, but is good enough for a number of essential experiments and serves the purpose of acquiring experience with aircraft SAR and its technology.

The system is built up with state of the art technology. Remarkable features are the fixed antenna (no motion compensation) and the low peak power, generated by solid state devices. This low peak power gives the system a very low probability to intercept, an important feature in operational military applications.

The solid state technology reduces the dimensions of the radar considerably and avoids the use of potentially dangerous high voltage power supplies for TWT's. The use of MMIC's in the PHARUS is investigated in the preparatory study on antenna technology. Application of MMIC's would further reduce the dimensions of the radar system.

## REFERENCES:

- [1] Loor, G.P. de, Hoogeboom, P. and Attama, E.P.W., 1982. The Dutch ROVE program, *IEEE Trans Geosci Electron* Vol GE-19, 3-7.
- [2] Hoogeboom, P., 1983. Classification of agricultural crops in radar images, *IEEE Trans GRS* Vol GE-21, 129-136.
- [3] Hoogeboom, P., Binnenkade, P. and Vauquen, L.M.M., 1984. An algorithm for radiometric and geometric correction of digital SAR data, *IEEE Trans GRS* Vol GE-22, no. 6, 570-576.
- [4] Hoogeboom, P., 1986. Identifying agricultural crops in radar images, *Proc ISPRS Symp*, Enschede, 25-29 Aug, 131-135.
- [5] Brooks, S.R., Joyce, H. et.al., 1985. The ERS-1 synthetic aperture radar and scatterometer, *GEC Journal of Research*, vol. 3, No.2.
- [6] Snoeijs, Paul and Swart, P.F.J., 1987. The DDF airborne scatterometer, *Int J Remote Sensing*, Vol. 8, no. 13, 1709-1716.
- [7] Otten, M.P.G., 1989. A motion compensation study for the PHARUS project, *these proceedings*, 74-1 - 24-12.
- [8] Vaillant, D., 1985. VARAN-S: An airborne Synthetic Aperture Radar for research in microwave remote sensing, *Proc EARSeL Symposium*, Strasbourg.
- [9] Ulaby, Fawwaz P., Richard K. Moore and Adrian K. Fung, 1981. *Microwave Remote Sensing active and passive*, Vol. 1 & 2. Addison-Wesley Publishing Company, Reading Massachusetts.

## DISCUSSION

Jacobsen

Are there any ECCM considerations in your programme?

Author's Reply

The PHARUS program is supported by the Ministry of Defense and the National Remote Sensing Board. We try to incorporate important research subjects from both communities. The design of the SAR testbed and of the PHARUS polarimetric SAR is characterised by low peak power, high PRF and high duty cycle, combined with a frequency chirp. From the military point of view this "spread spectrum technique" indeed contributes to a decreased vulnerability of the system and its carrier due to emitted radiation. At the same time the high coherent integration gain expected with this system makes jamming more difficult.



## R O S A R (Helicopter-Rotor based Synthetic Aperture Radar)

by

Helmut Klausung, Messerschmitt-Bölkow-Blöhm, FE 322, D-8012 Ottobrunn  
 Horst Kaltschmidt, Messerschmitt-Bölkow-Blöhm, AM3, D-8012 Ottobrunn  
 Wolfgang Keydel, MNR, Institut für Hochfrequenztechnik, D-9031 Weisling

## Abstract

ROBAR (Rotor-SAR) is a synthetic aperture radar concept based on rotating antennas of a helicopter for pilot sight target detection and target localization with high resolution. The ROBAR concept has potential benefits for civil and military helicopterborne imaging application, if the antennas are mounted at the tips of the rotor blades, for example (Fig. 1). The concept has two main potential benefits, that are, the imaging field of view is 360° and there is no need for a forward velocity of the carrier platform. As opposed to SAR systems based on linear movement of the antenna ROBAR imaging is based on synthetic apertures of a circular shape. Thus, the image formation process requires a polar format processing architecture. The ROBAR principle is also applicable for other radar mapping systems with rotating antennas, not only for helicopters.

## 1. Introduction

ROBAR has been investigated theoretically, by simulations and by experiments, all based on an idealized circular movement of the transmitting and receiving antenna with constant angular velocity. The concept consists of a pulsed radar. A point target in the illuminated swath generates a received signal, which may be correlated with the corresponding reference function to a point spread function. If this processing is done coherently, a synthetic aperture of circular segment shape would be formed. The heart of the ROBAR is the special processing, where the received raw signals are correlated by internally generated or stored reference signals with the result of angular compression, thus getting a high angular resolution.

By simulation techniques we have investigated the real angular resolution depending from the above mentioned parameters and additional other parameters which become important in the future application. We have also investigated in which ranges special reference signals or a common reference signal can be used dependent from the tolerable angular error.

In accordance to the theoretical results and to the results of the simulations we have made an experiment with a real rotating antenna but of course with a scaled down angular velocity of the rotor. The illuminated swath consists of meadows, buildings, bushes, trees and of 4 corner reflectors in a known position. Thus we can proof the results of the theoretical investigations and simulations.

## 2. The ROBAR Concept

Fig. 2 illustrates the basic ROBAR configuration with the illuminating/receiving antennas. The antennas are mounted at the tips of the rotorblades, whereby a circular ring shaped swath is illuminated. The actual illumination geometry depends on the altitude  $H_0$  above ground, the elevation antenna pattern  $\epsilon$  and the depression angle  $\theta$ .

At each position along the track of the antenna at the circumference of the circular path the radar pulses are coherent transmitted, coherent received and stored. The angular distance  $\Delta\alpha = \omega_0/f_p$  with the angular velocity  $\omega_0$  and the pulse repetition frequency  $f_p$  is equivalent to the interpulse period  $t_p = 1/f_p$  by linear movement of the antenna. Since the illuminated swath is a circular ring, the signal processing is a function of rotation angle  $\alpha = \omega_0 t$ .

## 3. Basic Doppler Discussion

The antenna geometry for a single rotation is illustrated in Fig. 3 with the assumption that the ground range to target  $R_{T0}$  at  $\alpha = 0^\circ$  is much greater than the length of the rotorblade  $l$  and the altitude above ground  $H_0$ , i.e.  $R_{T0} \gg l$  and  $R_{T0} \gg H_0$ . For Doppler calculation the following modifications are assumed:

- no forward velocity of the carrier platform
- the antenna phase center is assumed to be at the tip of the rotorblade
- only one point target is illuminated
- inelastic rotorblades.

A point target in the illuminated scene generates a time periodic Doppler shift  $f_D$  in the carrier frequency  $f_c$  of the transmitted signal  $S_T$  [1]. For Doppler processing the range target  $R$  must be calculated first (Fig. 3). The range to target  $R$  is with the angular velocity  $\omega_0$  and the rotation angle  $\alpha = \omega_0 t$

$$R(t) = R_{T0} - l \cdot \cos \omega_0 t \quad (1)$$

For a transmitted signal

$$S_T(t) = A_T(t) \cdot \cos 2\pi f_c t \quad (2)$$

the received signal  $S_R$  with the time periodic Doppler shift results to

$$S_R(t) = A_R(t - \frac{2 \cdot R(t)}{c}) \cdot \cos(2\pi f_c(t - \frac{2 \cdot R(t)}{c})) \quad (3)$$

The frequency  $f_R$  of the received signal is

$$f_R(t) = f_C - \frac{2 \cdot f_C}{c} \cdot \frac{dR(t)}{dt} = f_C - \frac{2}{\lambda} \cdot \dot{R}(t) \quad (4)$$

The Doppler frequency shift  $f_D$  is the difference between the received frequency  $f_R$  and the transmitted  $f_T$ :

$$f_D(t) = f_R(t) - f_T(t) = -\frac{2}{\lambda} \cdot \dot{R}(t) \quad (5)$$

The time periodic Doppler shift  $f_D$  is twice the targets range rate  $\dot{R}$  divided by the wavelength  $\lambda$  of the transmitted RF signal.

With

$$\dot{R}(t) = \frac{dR(t)}{dt} = \omega_0 \cdot L \cdot \sin \omega_0 t \quad (6)$$

the Doppler shift  $f_D$  in frequency is

$$f_D(t) = -\frac{2}{\lambda} \cdot \dot{R}(t) = -\frac{2}{\lambda} \cdot \omega_0 \cdot L \cdot \sin \omega_0 t = -\frac{2}{\lambda} \cdot v \cdot \sin \omega_0 t \quad (7)$$

with the tip velocity of the rotor blade  $v = \omega_0 \cdot L$ .

For  $R_{GO} \gg L$  and  $R_{GO} \gg H_0$  the Doppler function is a sine wave. The complete Doppler cycle (sine wave) corresponds to an omni-directional antenna azimuth pattern. The maximum Doppler frequency shift is

$$|f_{Dmax}| = \frac{2}{\lambda} \cdot \omega_0 \cdot L = \frac{2 \cdot v}{\lambda} \quad (8)$$

for  $\omega_0 t = \pm 90^\circ$  and the minimum Doppler frequency shift is

$$|f_{Dmin}| = 0 \text{ Hz} \quad (9)$$

for  $\omega_0 t = 0^\circ$  and  $\omega_0 t = 180^\circ$ .

If the plane of rotation is not perfectly horizontal, an additional Doppler term occurs, since the effective altitude  $H_0$  is no longer constant but time dependent. For the following calculations this effect will be neglected.

In SAR systems the azimuth resolution is proportional to the bandwidth  $B_D = 2 \cdot |f_{Dmax}|$ , therefore the maximum antenna beamwidth  $\gamma = 180^\circ$  the maximum rotation angle is  $\omega_{max} = 90^\circ$ . The phase history  $\varphi_R$  of the coherent demodulated received signal  $S_R$  is after mixing down to zero carrier frequency:

$$\begin{aligned} \varphi_R(t) &= 2\pi \cdot \int_0^t f_D(t) dt = \frac{4\pi}{\lambda} \cdot \omega_0 \cdot L \cdot \int_0^t \sin \omega_0 t dt \\ &= \frac{4\pi}{\lambda} \cdot L \cdot (1 - \cos \omega_0 t). \end{aligned} \quad (10)$$

The received signal  $S_R$  is with  $A_R = 1$  in exponential format for  $R_{GO} \gg L$  and  $R_{GO} \gg H_0$ :

$$S_R(t) = e^{j \cdot \varphi_R(t)} = e^{j \cdot \frac{4\pi}{\lambda} \cdot L \cdot (1 - \cos \omega_0 t)} \quad (11)$$

with the in-phase part  $I_R$  of the signal  $S_R$ :

$$I_R(t) = \cos \left[ \frac{4\pi}{\lambda} \cdot L \cdot (1 - \cos \omega_0 t) \right] \quad (12)$$

and the quadrature part  $Q_R$ :

$$Q_R(t) = \sin \left[ \frac{4\pi}{\lambda} \cdot L \cdot (1 - \cos \omega_0 t) \right]. \quad (13)$$

Fig. 4 shows the received signal  $S_R$  for the illumination of one point target with  $\lambda = 0,23 \text{ m}$  (1,3 GHz),  $\omega_0 = 0,2 \text{ rad}^{-1}$  and  $L = 6 \text{ m}$  as a function of rotation angle  $\alpha = \omega_0 t$  with  $-90^\circ \leq \alpha \leq 90^\circ$ . For  $R_{GO} \gg L$  and  $R_{GO} \gg H_0$  the signal does not depend on range to target. Fig. 4a shows the in-phase component  $I_R$  and Fig. 4b the quadrature part  $Q_R$  of the received signal  $S_R$ . The dotted line shows the Doppler frequency shift  $f_D$ .

#### 1. Synthetic Aperture

At ROFAR the synthetic aperture  $S$  is defined by the way of the antenna  $A$  with the beamwidth  $\gamma$  during the illumination of a target  $O$  (Fig. 5). This is:

$$S = \gamma \cdot L \cdot \left[ 1 - \frac{L}{R_{GO}} \right]. \quad (14)$$

For far range targets with  $R_{30} \gg L$  equation (14) simplifies to

$$S = \gamma \cdot L. \quad (15)$$

A point target O is illuminated during the rotation angle

$$-\frac{S}{2 \cdot L} \leq \alpha \leq \frac{S}{2 \cdot L} \quad (16)$$

with  $\alpha = \omega_0 t$ . For  $R_{30} \gg L$  equation (16) simplifies again to

$$-\frac{v}{2} \leq \alpha \leq \frac{v}{2}. \quad (17)$$

The integration time  $T_M$  is

$$T_M = \frac{L}{v}. \quad (18)$$

For  $R_{30} \gg L$  with  $S = \gamma \cdot L$  and  $v = \omega_0 \cdot L$  follows

$$T_M = \frac{1}{\omega_0}. \quad (19)$$

### 5. Azimuth Resolution

In SAR systems the azimuth resolution is defined by the point spread function, which is the response of the system to a point target. The point spread function  $S_0$  results from correlation of the received signal with the reference function. This process is a simple way to consider matched filtering. When the received signal and the reference function are matched, the output of the correlator has his maximum. In linear SAR systems the correlator output is a sinc-function and the time resolution is inversely proportional to the Doppler bandwidth  $B_D$ . In most common definitions [2] the azimuth resolution is given by the -3 dB width, which is the angle or distance between the points 3 dB below the peak value of the point spread functions mainlobe. The -3 dB points correspond to the half power level, respectively to the 0,707 ( $\sqrt{0,5}$ ) level of the amplitude.

At ROSAR the point spread function  $S_0$  is not a sinc-function but for  $\gamma = 180^\circ$  in case of  $R_{30} \gg L$  and  $R_{30} \gg H_0$  a Bessel function  $J_0$  first kind of order 0, i.e.

$$S_0(\alpha_x) = J_0 \left( \frac{4\pi}{\lambda} \cdot L \cdot \alpha_x \right) \quad (20)$$

as a function of the angle difference  $\alpha_x$ . Fig. 6 shows the absolute  $S_{0R}$  of the point spread function  $S_0$ , normalized of the maximum value  $J_0(0)$ :

$$S_{0R}(\alpha_x) = \left| \frac{J_0 \left( \frac{4\pi}{\lambda} \cdot L \cdot \alpha_x \right)}{J_0(0)} \right| \quad (21)$$

as a function of the angle difference  $\alpha_x$ , whereby  $\alpha_x$  is normalized to the quotient  $\lambda/L$  in Fig. 6. Fig. 6 shows, that the best attainable angular resolution  $\alpha_{ARmax}$  is

$$\alpha_{ARmax} = \frac{\lambda}{8 \cdot L}. \quad (22)$$

This equation (22) for  $\alpha_{ARmax}$  is only valid for  $\gamma = 180^\circ$  and  $R_{30} \gg L$  respectively  $R_{30} \gg H_0$ . The highest sidelobe of  $S_{0R}(\alpha_x)$  is 7,9 dB below the mainlobe in contrast to the sinc-function of the linear SAR, where the highest sidelobe is 13,2 dB below the mainlobe.

For other beamwidths  $\gamma$  the azimuth resolution can be estimated with the aid of the theory for signals with large time bandwidth product, i.e.  $T_M \cdot B_D \gg 1$ , because time resolution of the compressed pulse is then inverse to the Dopplerbandwidth  $B_D$  [3]. The time resolution for linear SAR  $\Delta t = 1/B_D$  is at ROSAR equivalent to the angular resolution  $\Delta \alpha = \omega_0 \cdot \Delta t = \omega_0/B_D$ . If the assumption of large time bandwidth product is valid and with  $R_{30} \gg L$  respectively  $R_{30} \gg H_0$  the angular resolution  $\alpha_{AR}$  for ROSAR with

$$B_D = 2 \cdot \left| L_{Dmax} \right| = \frac{2 \cdot \omega_0 \cdot L}{\lambda} \cdot \sin \left( \frac{\gamma}{2} \right) \quad (23)$$

will become

$$\alpha_{AR} = 0,88 \cdot \frac{\omega_0}{B_D} = 0,88 \cdot \frac{\lambda}{4 \cdot L \cdot \sin \left( \frac{\gamma}{2} \right)} = \frac{\lambda}{5 \cdot L \cdot \sin \left( \frac{\gamma}{2} \right)}. \quad (24)$$

The azimuth resolution  $\alpha_{AR}$  is independent of the angular velocity  $\omega_r$ . With

$$\alpha_{AR} = \frac{\lambda}{5 \cdot L \cdot \sin(\frac{\gamma}{2})} \quad (25)$$

the azimuth resolution for ROSAR can be calculated. For  $\gamma = 180^\circ$  equation (25) is equal to equation (22), which was derived by the Bessel function  $J_0$ . Fig. 7 shows the angular resolution  $\alpha_{AR}$  as a function of the beamwidth  $\gamma$ , whereby the time bandwidth product is great enough for calculating equation (25). In a distance  $R_{G0}$  the azimuth resolution in metres is

$$\Delta x = \alpha_{AR} \cdot R_{G0}. \quad (26)$$

The range resolution  $\Delta r$  is the resolution of the pulsed radar. With the transmitted pulse length  $\tau$  and the speed of light  $c$ , the range resolution  $\Delta r$  is for  $R_{G0} \gg L$  and  $R_{G0} \gg H_0$ , i.e.  $\theta = 0$

$$\Delta r = \frac{c \cdot \tau}{2}. \quad (27)$$

#### 6. The Range Curvature Problem

While travelling along the circular synthetic aperture, the range to target does not remain constant (Fig. 8). The curvature  $\Delta R_{max}$  of the synthetic aperture is for  $R_{G0} \gg L$  respectively  $R_{G0} \gg H_0$  primarily caused by the radius of rotation  $L$  and the antenna beamwidth  $\gamma$  and is practically independent of range to target:

$$\Delta R_{max} = L \cdot \left(1 - \cos(\frac{\gamma}{2})\right). \quad (28)$$

Now we must determine, how many range cells  $\Delta r$  are associated with  $\Delta R_{max}$ . If  $\Delta R_{max}$  is for instance less than the half of the range cell, the range curvature problem can be ignored. In the other case a correction must be done.

The maximum possible range curvature  $\Delta R_{max}$  with  $\gamma = 180^\circ$  is the length of the rotorblade  $L$  (eq. 28). Fig. 9 shows the shape of  $\Delta R_{max}$  as a function of the beamwidth  $\gamma$ . Because  $\Delta R_{max}$  is for a given beamwidth  $\gamma$  limited, a correction is easily possible.

#### 7. Experiments with a Rotating Platform

At the DLR in Oberpfaffenhofen a first ROSAR experiment with a real rotating antenna but of course with a scaled down angular velocity of the rotorblade has been done to establish the results of the theory and simulations. The radar is a monostatic pulsed radar, i.e. a common antenna is used for both transmitting and receiving. In a known position four corner reflectors were positioned and used for demonstration of the azimuth resolution. The received echosignals have been measured in the I and Q components and the received signal has been correlated with the reference function to a point spread function. Fig. 10 shows the geometry of the measurement configuration for the rotating platform and the illuminated swath with the reflectors in a radial distance of 265 m and in an angular position between  $\alpha_1 = 225^\circ$  and  $\alpha_2 = 240^\circ$ . The parameter of the measurement geometry are given in Table 1. In consequence of the low altitude  $H_0 = 2,5$  m the depression angle  $\theta$  is given to  $0^\circ$ . The measured data were stored and processed by the Experimental Radar Measurement System SARSCAT of the DLR. SARSCAT is a coherent L-band Radar. Table 2 summarizes the parameter of the measurement equipment.

With the transmitted pulse length  $\tau$  of 200 ns the range resolution  $\Delta r$  is 10 m and the total number of range bins is  $N = SW/\Delta r = 8$ .

Table 3 summarizes some ROSAR design parameters for the fourth range bin with the corner reflectors in a radial distance  $R_{G4} = 265$  m and an angular position between  $225^\circ$  and  $240^\circ$ . For this configuration the calculation of the design parameters could be done with the assumptions  $R_{G0} \gg L$  and  $R_{G0} \gg H_0$ . A correction of Range Curvature is not necessary. Fig. 11 shows the in-phase  $I_{R4}$  (Fig. 11a) and the quadrature part  $Q_{R4}$  (Fig. 11b) of the received signal  $S_{R4}$  as a function of rotation angle  $\alpha = \omega_r t$ . The received signal of the fourth range bin  $S_{R4}$  has been correlated with the reference function  $S_{R4}$  to a point spread function  $S_{O4}$ . Fig. 12 shows the reference signal  $S_{R4}$  with the in-phase  $I_{R4}$  (Fig. 12a) and the quadrature part  $Q_{R4}$  (Fig. 12b), i.e.

$$S_{R4}(t) = I_{R4}(t) + j \cdot Q_{R4}(t) \\ = \cos \left[ \frac{4\pi}{\lambda} \cdot L \cdot (1 - \cos \alpha_r t) \right] + j \cdot \sin \left[ \frac{4\pi}{\lambda} \cdot L \cdot (1 - \cos \alpha_r t) \right] \quad (29)$$

as a function of rotation angle  $\alpha = \omega_r t$  with

$$-\frac{\gamma}{2} \leq \alpha \leq \frac{\gamma}{2}.$$

The point spread function  $S_{O4}$  for one rotation with  $\alpha_m = 360^\circ$  results to

$$S_{O4}(\alpha_1) = \frac{1}{\alpha_m} \cdot \int_0^{\alpha_m} S_{R4}(\alpha) \cdot S_{R4}^*(\alpha - \alpha_1) d\alpha. \quad (30)$$

azimuth beamwidth	$\gamma$	48°
elevation beamwidth	$\epsilon$	15°
depression angle	$\theta$	0°
altitude	$H_0$	2,5 m
distance to swath	$R_{GO}$	160 m
swath width	SW	240 m
radial distance to reflectors	$R_{G4}$	265 m
angular position of reflectors	$\alpha_1$	225°
	$\alpha_2$	240°
lateral distance between reflectors	$\Delta X$	15 m
length of rotorblade	$l$	6 m
angular velocity	$\omega_0$	0,2 s <sup>-1</sup>
crosssection of reflector	$\sigma$	100 m <sup>2</sup>

Table 1: Parameter of the measurement geometry.

frequency	$f_c$	1290 MHz
polarisation		VV
peak power	$P_p$	50 W
transmitted pulse length	$\tau$	200 ns
receiver bandwidth	$E_R$	5 MHz
pulse repetition frequency	$f_P$	100 Hz
range resolution	$\Delta r$	10 m

Table 2: Parameter of the SARSCAT-Measurementssystem.

Synthetic Aperture length	S	4,82 m
Range Curvature	$AR_{max}$	0,48 m
tip velocity of rotorblade	v	1,2 ms <sup>-1</sup>
Integration time	$T_{int}$	4 s
number of pulses per Aperture	$Z_H$	1200
total number of pulses	$Z_P$	9600
Poppier bandwidth	$B_{pp}$	8 Hz

Table 3: Some ROSEAR design parameters.

as a function of the angle difference  $\alpha_1$ . The absolute of the point spread function  $S_{04}$  in amplitude is the function  $S_{04}$  normalized to the maximum value  $S_{04max}$ :

$$S_{04}(\alpha_1) = \left| \frac{S_{04}(\alpha_1)}{S_{04max}} \right| \quad (31)$$

Fig. 17 shows the point spread function  $S_{04}(\alpha_1)$  with the four corner reflectors in an angular position between 225° and 240°.

With the mentioned parameters the theoretic azimuth resolution  $\sigma_{AZ}$  is with equation (25):

$$\alpha_{AZ} = \frac{\lambda}{5 \cdot L \cdot \sin(\frac{\lambda}{2})} = 1,12^\circ. \quad (32)$$

With  $R_{Q4} = 245$  m the azimuth resolution in distance is

$$\Delta x = \alpha_{AZ} \cdot R_{Q4} = 5,2 \text{ m}. \quad (33)$$

Fig. 14 shows a detail of the point spread function  $S_{ROSAR}(\alpha_z)$  between  $220^\circ$  and  $240^\circ$  to compare the attainable azimuth resolution of the ROSAR with the resolution of a rotating antenna with real array. Fig. 14a shows a photo of the illuminated scene with the four corner reflectors and two traffic signs. Fig. 15b shows the display of a rotating antenna with a real array  $S_{RAA}(\alpha)$ . This image is produced by the motion of the antenna along the circumference of the circular path. The resolution of a real array is obtained by the antenna beamwidth  $y$  [4]. The azimuth resolution is approximately 153 m and the reflectors respectively traffic signs can not be resolved. Fig. 14c shows the point spread function  $S_{ROSAR}(\alpha_z)$  of the ROSAR with an azimuth resolution of  $1,2^\circ$  and  $1,3^\circ$ , i.e.  $\Delta x$  is approximately 5.2 m. With this resolution the reflectors can be resolved, but the traffic signs with a lateral distance of 4 m can not be resolved.

#### 8. References

- [1] Klausung, H., Bartsch, N., BBSwetter, C.;  
"A mm-wave SAR design for helicopter application (ROSAR)";  
Conference Proceedings of the 16th European Microwave Conference, Ireland, Sept. 1986, pp. 317-328.
- [2] Pike, T.K.;  
"SAR Image Quality: A Review";  
DFVLR-Mitteilung (DFVLR-Mitt. 85-07), 1985.
- [3] Schwartz, M.;  
"Information Transmission, Modulation, and Noise";  
Mc Graw Hill, 1987, Chapter 2.
- [4] Moore, R.K.;  
"Radar Fundamentals and Scatterometers";  
Manual of Remote Sensing, Vol. 1 (Theory, Instruments and Techniques); American Society of Photogrammetry, 1983, Chapter 9.

#### 9. Acknowledgment

This work was performed under a joint DLR-MBB research sponsorship from 1985 to 1988. The continuing support and assistance as well as many helpful discussions by Dipl.-Ing. N. Bartsch, DLR, are gratefully acknowledged.

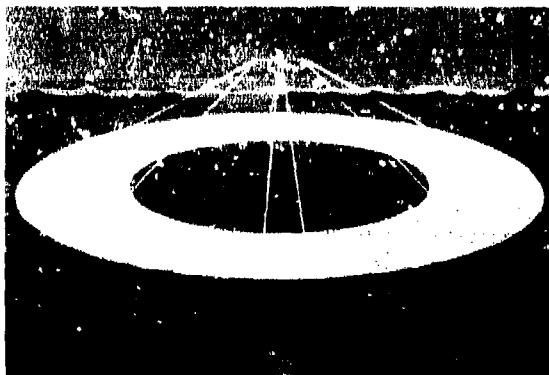


Figure 1: Basic ROFAR Configuration.

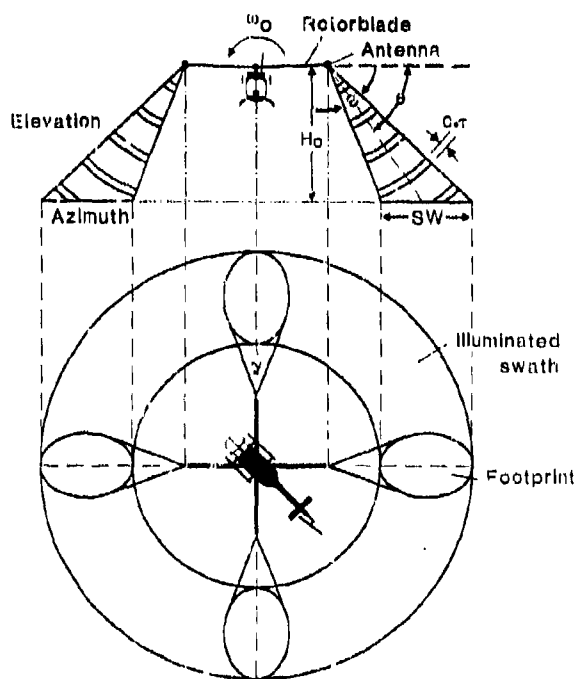


Figure 2: ROFAR Illumination Geometry.

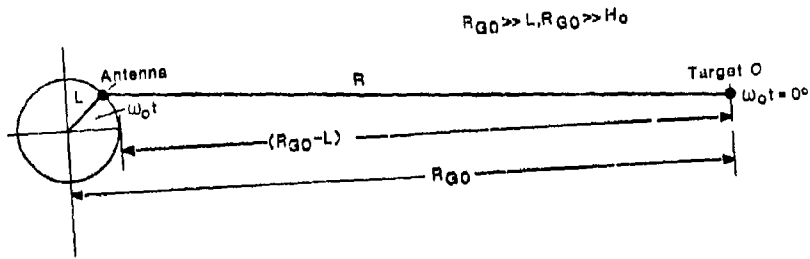


Figure 3: Single Rotating Antenna Geometry.

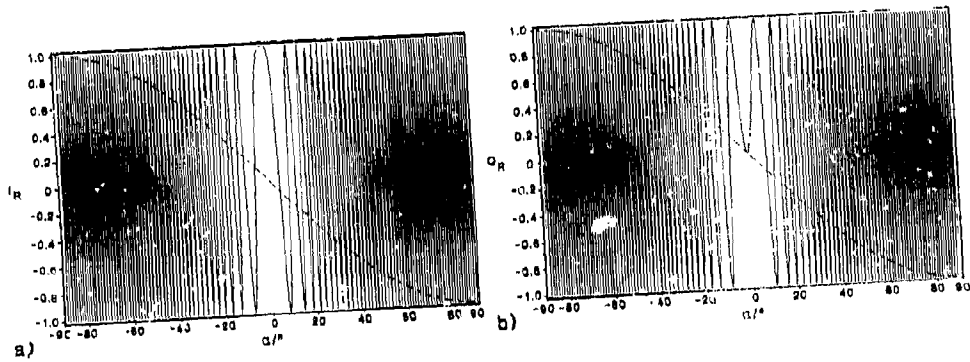


Figure 4: Received Signal  $B_R(I_R(n), Q_R(b))$ .

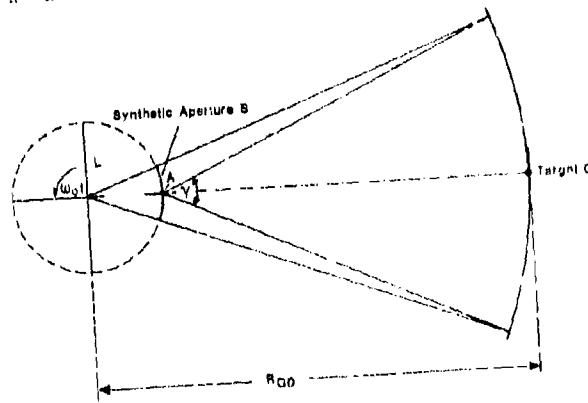


Figure 5: Circular Shaped Synthetic Aperture.

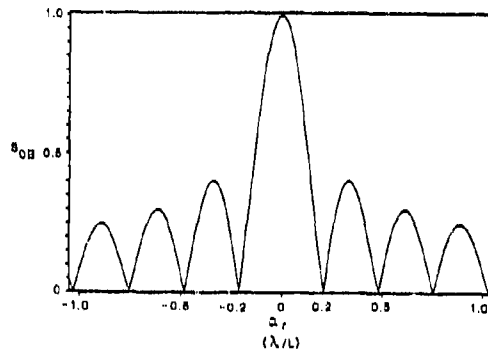


Figure 6: Point Spread Function  $h_{PB}$ .

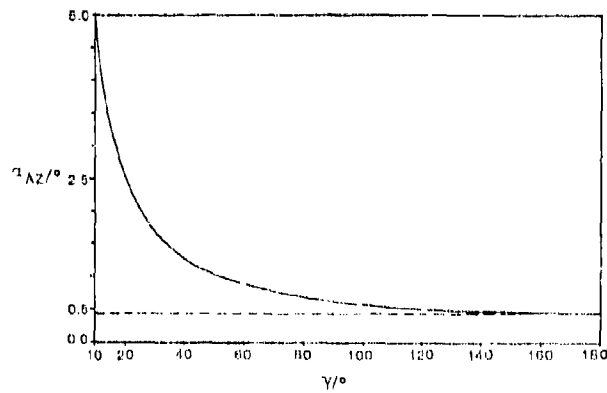


Figure 7: Angular Resolution.

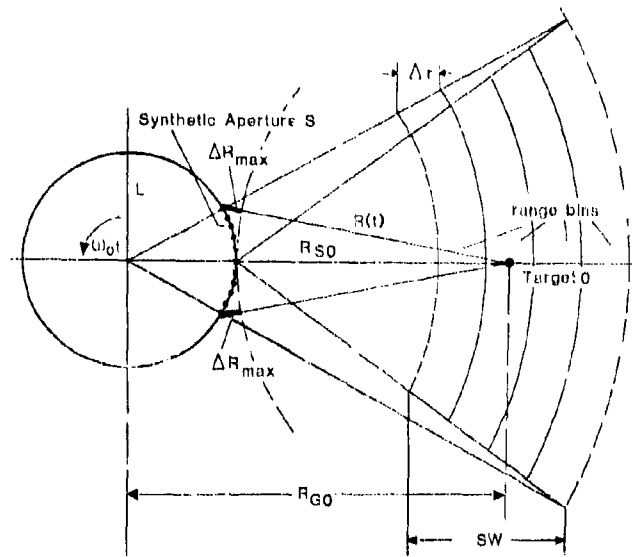


Figure 8: Range Curvature Problem.

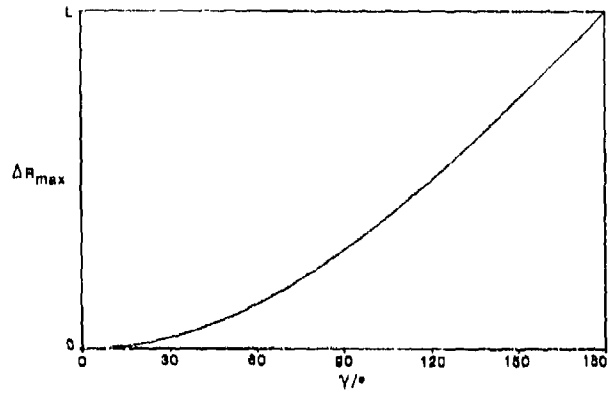


Figure 9: Range Curvature.

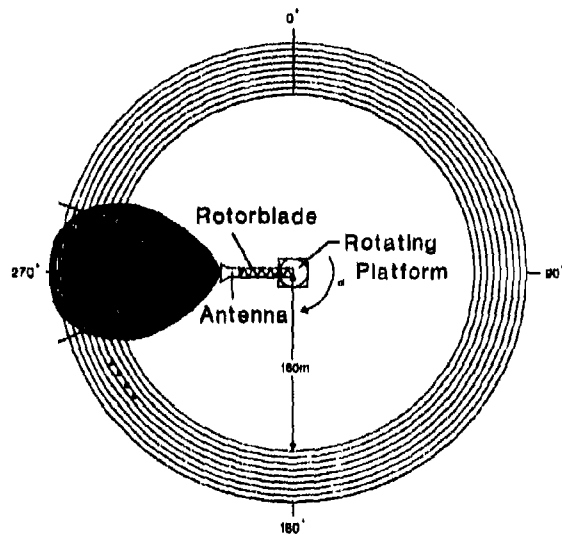
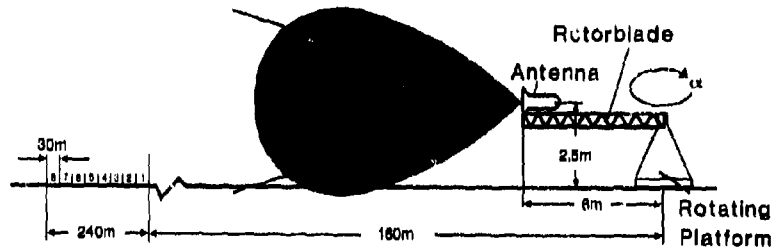


Figure 10: Measurement Configuration.

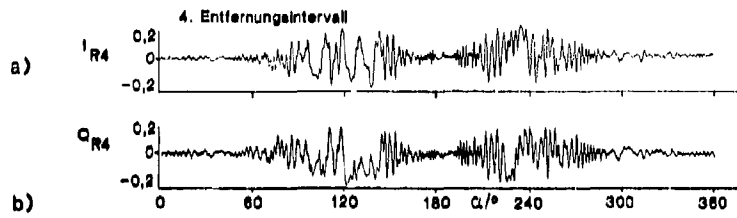


Figure 11: Received Signal  $S_{R4}$  of the fourth range bin ( $I_{R4}(a)$ ,  $Q_{R4}(b)$ ).

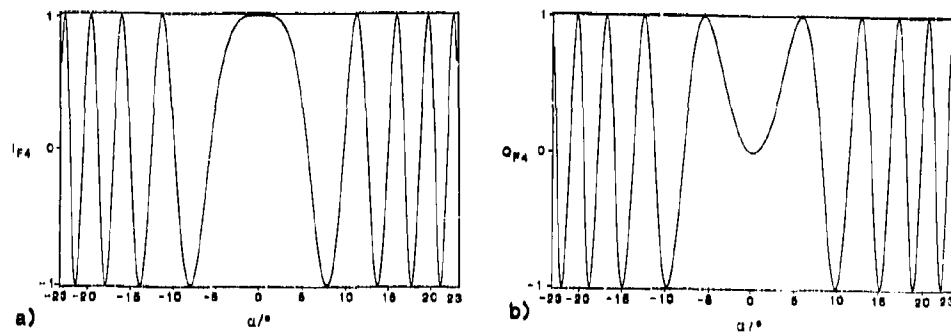


Figure 12: Reference Function  $S_{P4}$  ( $I_{P4}(a)$ ,  $Q_{P4}(b)$ ).

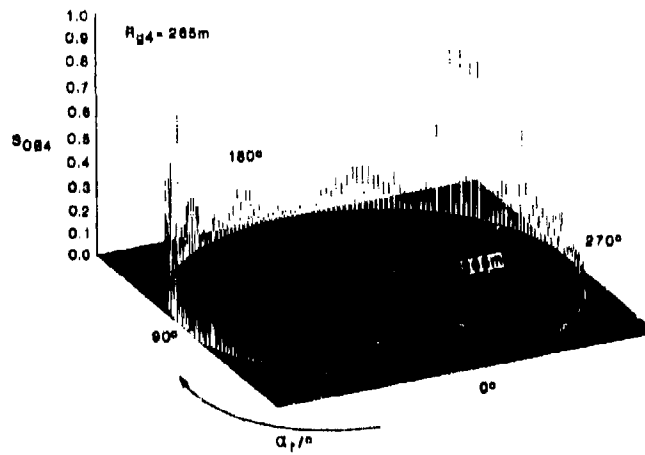


Figure 13: Point Spread Function  $S_{OB4}$ .

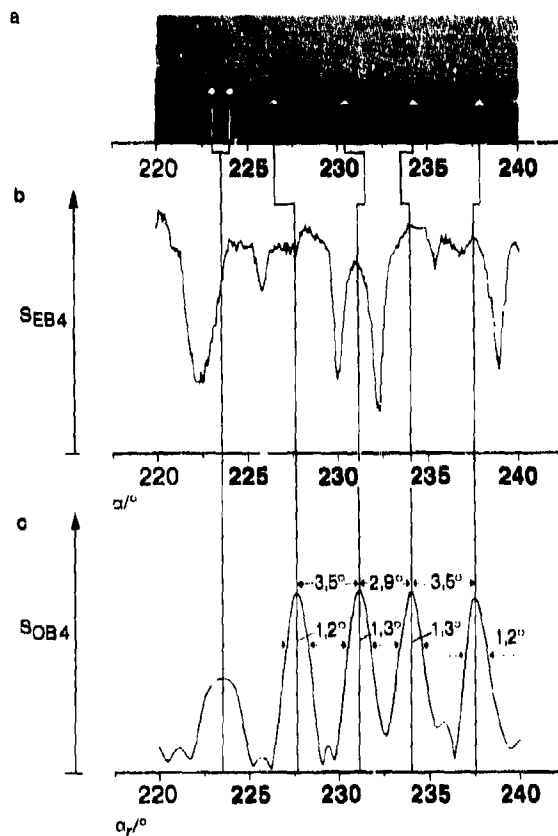


Figure 1b: Azimuth Resolution.

## DISCUSSION

**R.Klemm**

How does ROSAR perform when the helicopter is moving? Do you expect additional resolution?

**Author's Reply**

When the helicopter is moving we then have to construct several velocity individual reference functions and the signal processing will become very more complicated. An additional resolution could, in principle, be expected.

**J.Richard**

Quel type d'antenne sera implantée sur le rotor et comment sera-t-elle alimentée (par le signal RF)?

**Author's Reply**

We will use a wave-guided horn antenna at 35 GHz or 94 GHz which will be integrated in the tip of the rotorblade. The supply of the antenna will be achieved by flexible wave guides integrated in the rotorblade.

**Jacobsen**

What particular application do you have in mind with this concept?

**Author's Reply**

Helicopter pilot sight with all weather capability and high resolution. Surveillance, target detection, reconnaissance and localisation as a supplement to the optronic sensors specially in dirty battlefield and bad weather conditions. Alignment of an inertial/terminal guided missile with a RF-seeker head launched from a helicopter.



**TITLE** CAPABILITIES OF BISTATIC SYNTHETIC APERTURE RADAR  
 FOR COVERT BATTLEFIELD SURVEILLANCE

**AUTHOR** C. D. Hall

**AFFILIATION** Marconi Space Systems Limited

**ADDRESS** Anchorage Road  
 Portsmouth  
 Hampshire  
 PO5 5PU  
 ENGLAND.

AD-POO5 841

#### Abstract

The capabilities of bistatic synthetic aperture radar to provide rapid update rate, real-time covert radar surveillance to the military user are considered. The spatial resolution and sensitivity achievable from a tactical system using a small RPV-borne transmitter and a static ground based receiver are discussed and the relative advantages of two distinct types of emission modulation are examined. Finally, a number of areas requiring further study are identified.

#### 1. Introduction

Bistatic synthetic aperture radar (SAR) is a combination of the bistatic radar configuration and the high resolution processing techniques which have been developed for SAR. With this technique, motions of either the transmitter, or the receiver, or both transmitter and receiver are used to facilitate the generation of synthetic transmit and receive apertures by the processing algorithms.

The value of this technique for battlefield surveillance is its potential to provide the level of covert surveillance capability to the user which is usually associated with passive systems. These systems use natural emissions from the target and scene for the imaging process and are usually capable of high angular resolution but do not easily yield ranging data. The particular strength of the bistatic SAR technique is that it combines the covert nature of passive surveillance with the accurate ranging capability usually associated with active systems such as radars and lidars.

The specific feature of bistatic systems which provides the user with a covert surveillance capability is the potentially large separation which can exist between transmitter and receiver. This separation means that there is no guiding emission which might lead to retaliation against the user who is located at the receive site.

The transmit element is however, vulnerable and careful consideration must be given to the mitigation of the associated system vulnerability. The prime function of the transmitter is to illuminate the scene on behalf of the receive element; therefore it should be recognised that concealment of emission is not a viable approach to the mitigation of vulnerability. It is felt that a more realistic approach is to attempt to win the attrition costs on behalf of the transmitter and make the cost of its destruction unacceptably high. Particular features that promote this approach are the following:

- i) design the transmit platform around a cheap, remotely piloted vehicle (RPV) and aim for a cost which allows the platform to be regarded as throw-away. This approach aims to win the attrition cost against an anti-radar missile as the probable attack weapon.
- ii) design the platform to be small so as to be less vulnerable to artillery attack.

Finally, the general benefits provided by this type of surveillance system include:

- \* the provision of precise range data
- \* day-night operation
- \* an imaging capability of comparable spatial resolution to thermal IR
- \* excellent cloud and rain penetration - better than thermal infra-red systems
- \* a quasi "movie" imaging capability with image update rates around one frame per second

## 2. System Geometry

The particular bistatic system considered in this paper is one in which the transmitter is mounted on a cheap RPV and the receiver is stationary, and ground based. Use is then made of the platform motion in the processing algorithms associated with the receive element, to synthesize a very long transmit aperture and thereby provide the very high spatial resolution ( $\approx 8$  metres) needed for surface surveillance and the detection of tanks.

The principal elements of a bistatic radar system are shown in Figure 1, where it can be seen that the transmitter illuminates the scene which is to be observed, and signals, backscattered from the scene together with signals direct from the transmitter, are intercepted at the receiver.

The geometry associated with bistatic radar systems is more complicated than that associated with monostatic radars. In the bistatic configuration, range bins are formed on ellipsoids of revolution with foci at the transmitter and receiver locations. The range bins which lie on the scene surface therefore lie on the ellipses which are also visible in Figure 1. Each of the ellipses marks the location of a contour of constant time difference on the path transmitter-target-receiver, and so it can be seen that there is no simple relationship between time difference and range from receive location to target (as is the case with monostatic systems). Rather, there is a more complex relationship in which range and time are a function of bearing and transmitter location.

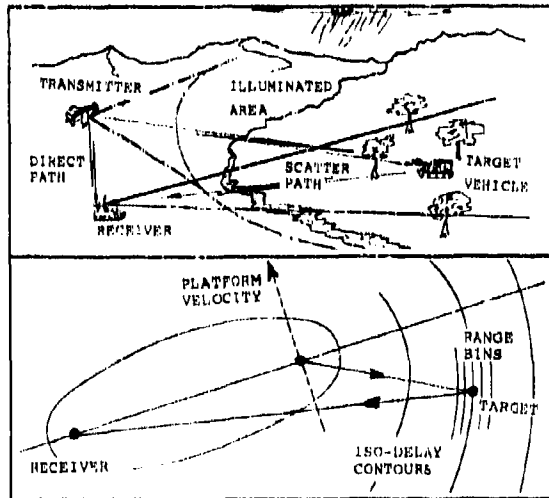


Figure 1 Elements of a Bistatic System

## 3. Spatial Resolution

It is common practice to divide the image produced by an imaging system into a two dimensional array of contiguous pixels whose spacing is of the order of the system spatial resolution. In particular, a radar image is usually arranged so that one axis of the image conforms to the direction of increasing time delay - the range direction - and the other axis, to the direction perpendicular to range - often called the azimuth direction. With the bistatic SAR system under consideration here, it is convenient to adopt the same structure and associate the range direction with the direction of the transmitter/receiver baseline. The imaging process in this case therefore uses the time difference between the direct path (transmitter to receiver), and the scatter path (transmitter to target to receiver). However, in order to completely determine the range from target to receiver, two additional pieces of information are required, range from transmitter to receiver and bearing of the target relative to the receiver.

Having thus determined the range associated with a given target return, the target is thereby located as lying within a range bin whose length can be very short but whose width is identical to that of the receive antenna beam. Suppose now that the receive beam is maintained, pointing in the direction of the target as the transmitter proceeds along its flight path. A whole sequence of returns from the target is intercepted at the receiver location, each return being associated with a different transmitter location as the platform moves along its trajectory. It can be shown that successive returns will differ in phase by a predictable amount which is characteristic of the locations of the scattering centres which produce them and is the basis of the synthetic aperture processing which enables many distinct pixel locations to be identified across each receive beam. The spatial resolution associated with the aperture which can be synthesised from these returns comes specifically from the component of motion perpendicular to the sight-line between transmitter and target. Thus, the direction of the ideal trajectory for ultimate resolution is perpendicular to the transmit/target sight-line. However, it is worth noting that this ideal condition will seldom be encountered in the field and even then, processing will be complicated by range walk, or the need to retrieve consecutive target returns from different range bins.

The consequence of this is that an analogy can be drawn showing that the angular width of the receive beam in the system, is equivalent to the angular field of view associated with a passive TV style of viewing system. The synthetic aperture processing then allows that receive beam to be sub-divided into many smaller pixels just as the TV scan mechanism identifies many small pixels in the TV picture.

In the range direction, spatial resolution is set by the bandwidth of the transmitted signal. For this example two cases are considered, one being a linear FM chirp, the other being a continuous pseudo random binary phase shift keyed sequence (P/N code). Examples showing the relative performance of systems employing linear FM chirp and PN code emissions are presented in Figure 2.

In the azimuth direction, fine spatial resolution is achieved by means of aperture synthesis techniques. It is convenient and valid to think of these techniques as permitting the synthesis of a very large transmit aperture. The system azimuth resolution is thus established by the transmit elements of the system and therefore, although sensitivity is impaired, linear spatial resolution remains constant as the receiver is moved away from the target, providing the transmitter target distance remains constant.

This section ends with some examples of the spatial resolution likely to be achieved with this type of bistatic SAR. In the range direction an emission bandwidth of 30 MHz would be sufficient to realise a range spatial resolution of around 5m. In the azimuth direction, spatial resolution  $\rho_a$  can be shown to be given by equation (1)

$$\rho_a = \frac{\lambda R_t}{L_s} \dots\dots\dots(1)$$

where  $\lambda$  = operating wavelength  
 $R_t$  = range from transmitter to target  
 $L_s$  = length of synthetic aperture

A consequence of synthetic aperture processing is that samples must be taken at specific intervals along the desired aperture. The spacing of these samples has a profound effect upon the quality of the image which can ultimately be produced by the system; in particular if the spacing between samples is too great then ambiguities will be observed in the image. These ambiguities can be regarded as resulting from diffraction grating lobes which exist as a result of the finite number of samples taken along the aperture. The desirable maximum distance between samples can be calculated by arranging that angular spacing of the grating lobes be greater than the angular width associated with the receive beam at nearest viewing range. This distance can be shown to be on the order of the dimensions of the receive antenna. Now, with a mobile transmit platform, this places a requirement on the emission modulator, that the pulse repetition frequency (or the P/N code repetition frequency) be greater than a minimum set by the ratio between the RPV platform velocity and the width of the receive antenna aperture. In the case of continuous P/N code emissions some of which can have

very long repetition intervals, the sampling requirement is transferred to the receive element where individual samples of complete range lines must be taken at a rate set by the same criterion which constrains the emission modulator.

For a typical case operating at 9.6 GHz, a synthetic aperture of length 50m would be needed to provide an azimuth resolution of 5m at a stand-off range of 8km from transmitter to target. Since an aperture of this length can be produced within a period of one second by an RPV travelling at little more than Mach 0.15, this type of system should be capable of producing images to a spatial resolution of 5m at a rate of one image per second. The individual sample rate in such a case with a receive aperture width of 1m is required to be at least 50 Hz. Although this image rate is not sufficient to give the smooth motion associated with TV images, it is quite adequate for the needs of a surveillance system intended for use against ground based vehicles.

#### 4. Sensitivity

The sensitivity of bistatic SAR systems is most usefully expressed in units of normalised radar cross section (NRCS) or  $\sigma_0$ . This unit is dimensionless and quantifies the concept, "bistatic radar cross section ( $m^2$ ) per unit area ( $m^2$ )". In attempting to quantify what is a useful system sensitivity, there is a need to know what values of  $\sigma_0$  are typical of the scenes to be viewed by the system. Now although there is a reasonably extensive base of data quantifying monostatic values of  $\sigma_0$  for the rural environments in which the system might be deployed, there is a dearth of such data quantifying bistatic measurements. A further reason favouring the particular geometry chosen for this system is that the scattering geometry at the scene is approximately monostatic so that the values of system sensitivity derived can be related to existing monostatic measurements with reasonable confidence.

System sensitivity is a function of every element of the system including transmitter, scene, and receiver. However, in the analyses conducted so far, it has been found convenient to identify an interface, located at the scene, and define there a ground irradiance associated with the transmitter. This division enables the two elements of the system, transmitter and receiver, to be studied in relative isolation so that when the receive element is analysed, the analysis can proceed on the simple assumption that the transmitter places a given illuminating power over a given area.

System sensitivity is conveniently expressed in terms of "noise equivalent  $\sigma_0$ " ( $NE\sigma_0$ ) where  $NE\sigma_0$  is identical with that value of  $\sigma_0$  which would produce the same signal at the system output as is produced there by thermal noise in the system. Using the relatively simple model of the system outlined above it can readily be shown that system sensitivity is given by equations (2) and (3) respectively for FM chirp emissions and for P/N code emissions.

The principal difference between these two expressions is the inclusion of an additional term on the top line of equation (3) which takes account of the significant uncorrelated noise component that results from the sidelobes of the autocorrelation function of the P/N coded emission. The autocorrelation function (ACF) associated with a linear FM chirp is characterised by the well known "sin x over x" function which has a sharp central peak and sidelobes which decay rapidly. This type of function provides a negligible contribution to overall system noise. However, the ACF with a continuous P/N coded emission is characterised by a single large central peak and sidelobes whose intensities are essentially constant and inversely proportional to the number of code chips contributing to the correlated signal and leads to an additional noise component which can be significant.

$$\begin{aligned} &\text{FM chirp emission} \\ NE\sigma_0 &= \frac{4\pi A_x v_t R_r^2 kT_{sys}}{P A_r R_t \lambda^2 \rho_n L_t L_r L_a} \dots\dots\dots(2) \end{aligned}$$

$$\begin{aligned} &\text{P/N code emission} \\ NE\sigma_0 &= \frac{A_x v_t R_r^2 (4\pi kT_{sys} + H \theta_r A_r \sigma_0 L_t L_r L_a M/f_0)}{P A_r R_t \lambda^2 \rho_n L_t L_r L_a} \dots\dots(3) \end{aligned}$$

where

$A_t$ = area illuminated by transmitter	$L_t$ = losses in transmit segment
$v_t$ = velocity of transmitter platform	$L_r$ = losses in receive segment
$R_r$ = range from scene to receiver	$L_a$ = atmospheric propagation
$k$ = Boltzmann's Constant	$H$ = ground irradiance ( $= P/A_t$ )
$T_{sys}$ = system noise temperature	$\theta_r$ = width of receive beam
$P$ = mean RF power generated in HPA	$\sigma_o$ = background bistatic NRCS
$A_r$ = effective area of receive antenna	$f_c$ = P/N code chip rate
$\lambda$ = operating wavelength	$M$ = No of range bins in image
$\rho_{sr}$ = system slant range resolution	

Using these relationships, it can be shown that the sensitivity associated with a system employing a quite modest transmit power is more than adequate over the ranges likely to be encountered in the battlefield. Performance data which characterize this type of a bistatic system have been calculated and are presented in Figure 2 together with typical values of signatures likely to be found in the scene, and relevant values for the system parameters. The data should be interpreted as follows. Values of system sensitivity expressed in units of  $NEC_o$  are indicated by four lines, two dashed and two full, which cover various combinations of transmitter emission modulation and atmospheric propagation conditions. The relationship between these plots of sensitivity and the regions of typical target and background signatures which are shown as hatched areas on Figure 2 is that at the range ( $R_r$ ) of interest, these features will be visible in the final image providing  $NEC_o$  is smaller than the features to be observed. It can be seen that although the performance achievable with linear FM chirp emission is significantly better than that achievable with continuous BPSK pseudo-random (P/N) code emission, the latter provides an adequate capability for observation of both targets and scene features.

The extent to which features are visible above the system thermal noise floor represented by  $NEC_o$ , is a function not only of the magnitude of the difference between feature and noise floor, but also of an artifact of synthetic aperture processing called "speckle" which is a noise component that is proportional to the intensity of the features being imaged. Speckle can be reduced by assigning each pixel in the final image to be the average of several statistically independent measurements; this process is called multi-look imaging. However, in this case, provision of the independent samples required by this process calls for an unacceptable sacrifice in spatial resolution and the decision has been taken to present a single look image on screen. In this image, although speckle will produce a substantial noise component, typically 4.8 dB for a single-look image, the difference between typical target and background features is sufficiently large that targets will still be visible.

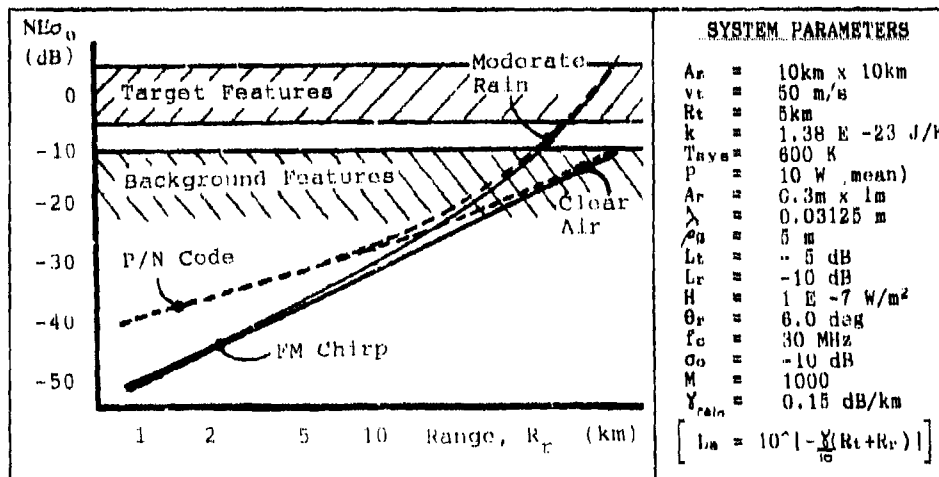


Figure 2

Performance of a Typical Bistatic SAR System

## 5. System Implementation

The system envisaged for this role consists of two major elements, transmitter and receiver. The division of activity between the two is such that the transmit element is kept very simple and contains only a stable local oscillator, an emission modulator, a modest RF power amplifier, and a simple low gain antenna of broad beam width. The RPV is likely to fly at an altitude of around 500m to 1000m and will illuminate an area between 25km<sup>2</sup> and 100km<sup>2</sup> depending on terrain limitations. The data presented in Figure 2 show that even when illuminating the larger area, excellent sensitivity can be achieved. Consequently, it is useful to point out that there is no particular requirement for the transmitter to illuminate just a small part of the surveillance zone through a high gain, steered beam. Rather the system operates using a very broad beam from a fixed low gain antenna which provides a floodlight illumination; this is essentially the microwave equivalent of the illumination provided by a searchlight or flare for night operation of visible band sensors. Thus the relatively vulnerable, transmit element of the system retains its simplicity and the more complex elements of the system are concentrated in the passive and therefore less vulnerable, receive element.

The receive element contains two low noise amplifiers (LNA), one for the scatter path through which the scene is observed, the other for the direct path along which the direct signal from the platform is received. Associated with each LNA there is an antenna, the one associated with the direct path is envisaged as being of low gain, typically being very similar in its characteristics to the transmit antenna; the antenna associated with the scatter path is a high gain, narrow beam element through which the scene is observed. (This mode of operation somewhat resembles the way in which the telescope associated with high resolution, narrow field of view visible band and IR sensors is used to observe scenes). In addition to the RF components, the receive element also contains the range correlator (for FM chirp or P/N code) and a powerful processor for transformation of the raw radar returns into a recognisable image. This processor is required to undertake a number of functions during this transformation. Before processing can commence, the current system geometry must be determined. Thereafter raw returns are transformed into a raw image, and finally the raw image is transformed into a realistic maplike projection for observation by the user.

The processing envisaged for this system differs from that associated with airborne and spaceborne SAR's predominantly in the volume of data requiring to be processed. Because both of these systems cover very wide areas at high speed and at high spatial resolution typical sample rates lie in the region of tens of millions per second. The bistatic SAR system however, is designed to operate over a much more limited region so that even when operating at ranges out to 10km, the nominal 6° azimuth beam width will generate a sample rate of only 0.2 millions per second. All the computationally intensive processing operations involved with this system are correlations and with an airborne or spaceborne SAR, these operations can conveniently be conducted in the frequency domain, making extensive use of FFT techniques. In this case however, range walk and repeated processing of images of one location using a succession of different correlation functions as the system geometry changes, means that time domain processing is more appropriate. The computation rate associated with 200,000 pixels per sec with time domain processing depends on the azimuth width of the image. In this case, the image is some 200 pixels wide, each of which is supported by two raw data samples. Thus, the correlation function for each image pixel is of length 400 samples, and the final data processing volume amounts to 160M operations (multiply and add) per second. This processing rate is large but with modern processing devices can realistically be conceived as being serviced by hardware accommodated on a few (possibly one) Double Eurocards.

The determination of system geometry has been identified as one of the critical areas which remain open for more conceptual study. Successful image formation relies on detailed knowledge of the system geometry in order to generate appropriate synthetic aperture filter functions. The accuracy required of such geometric data is still being studied but two alternative approaches to the accurate determination of transmitter location have been identified. One relies on the establishment of additional direct path receive sites in the vicinity of the receiver so that triangulation and interferometric techniques could be employed for transmitter location determination. The other relies on the

inclusion in the transmit platform of a GPSS receiver which might be used as a relay element to modulate a sub-carrier from the platform so that a full GPSS decoder at the receive element could be employed to determine the platform location. Neither of these solutions seems very attractive although each appears to provide a feasible solution if absolute precision of system geometry is shown to be a prerequisite for successful operation.

## 6. Discussion of Capabilities

The selection of operating frequency is a compromise between a number of conflicting requirements which include the following;

- \* sensitivity and spatial resolution
- \* field of view
- \* processing complexity

Primary drivers towards higher operating frequency are the desire for finer spatial resolution in order to achieve better detection and classification capabilities from the system, and the desire to operate with as small a receive antenna aperture as possible in order to aid concealment of the receive site. It can be seen from equations 2 and 3 that the sensitivity achievable decreases linearly with operating frequency. What is less clear from these equations is that for a constant angular field of view, which is given by the azimuth width of the receive beam, the receive antenna area is constrained to decrease similarly with operating frequency. Thus, the overall consequence of an increase in operating frequency is a reduction in sensitivity which is proportional to the square of frequency. There is also, however, a driver towards lower operating frequency which comes from the desire to cover wider fields of view without sacrificing sensitivity. In this situation it is possible to retain sensitivity at the expense of azimuth spatial resolution.

Finally, it is important to remember that with a synthetic aperture system, there is no inherent limitation on azimuth spatial resolution but at lower operating frequencies the time taken to form the synthetic aperture increases and this limits the rate at which full resolution images can be presented to the user. The practical constraints on the system are however, appreciable. The maximum length of aperture which can usefully be employed depends fundamentally on the time during which the system and the features observed by the system remain coherent - no useful improvement in spatial resolution can be achieved from the synthesis of an aperture over a period longer than this coherence time. The parameters which affect this coherence time include stability of system operating frequency, stability/accuracy of knowledge of transmit platform location and velocity, and ultimately, stability of the phase characteristic of features observed in the scene.

Like other ground based viewing systems, the line of sight to the target can be interrupted by features such as hills, trees and buildings present in the scene. Therefore it is important to point out that although there is an airborne element to this system, the RPV platform which carries the transmitter, a specific limitation of this system is that of terrain features which may limit the clear line of sight available between target and receiver.

The most serious limitation to the capabilities provided by this system result from the effects of target motion. A feature of synthetic aperture processing is the ambiguity existing between the doppler shifts present in returns from the scene which result from target motion and the comparable shifts which result from platform motion. These ambiguities result in the misplacing of moving features in the final image.

It is interesting to compare and contrast this bistatic system with a complete monostatic SAR on an RPV platform. The bistatic implementation makes use of a cheap, simple, RPV platform which carries only a broad beam transmitter to provide illumination for a ground based observer whereas the SAR implementation, while providing airborne observations that are less liable to terrain obscuration than ground-based observations, requires that a much larger payload be carried on the RPV. This payload would consist of a transmitter, a receiver

and a data down link, and would be substantially more complex, massive and expensive than that associated with the bistatic system. In particular, much more of the SAR system is present in the vulnerable platform area so that the attrition cost associated with its destruction moves to favour the enemy rather than the user.

## 7. Conclusions

A system concept has been described which could potentially provide an all-weather, day-night, tactical covert radar surveillance capability for the military user. The system is based on bistatic synthetic aperture radar techniques and relies for its potential cost-effectiveness, on the location of the bulk of the system components at the receive site where, because the receive site is passive, they are less vulnerable to attack. The transmitter is located on a small RPV platform and is conceived as being a throw-away item in times of hostility but could be a retrievable item during training periods. It is intended that the transmitter should be sufficiently small and cheap that its vulnerability to artillery attack would be low and its engagement by anti-radar missile, very expensive. It has been shown that this type of system has the potential to provide a near real-time imaging capability over ranges of around 10km. The spatial resolution achievable is around 5m and this when coupled with the sensitivity available from the system is sufficient to ensure that vehicles would be clearly distinguished as point targets from the background of the scene. The capabilities provided by two distinct types of emission modulation have been examined, linear FM chirp and continuous P/N code, and appreciable degradations have been shown to be associated with the P/N code type of modulation so that FM chirp is the more favoured form of illumination.

Finally, although no specific feature which renders the system non-viable has yet been identified, platform stability, platform location, bistatic SAR processing, and the effects of target motion have been identified as significant problem areas requiring further study and consideration.

## DISCUSSION

### C.J. Baker

The RPV requires motion compensation. Does this make it a vulnerable, expensive platform negating some of the advantages of the bistatic concept?

### Author's Reply

The RPV may not be compelled to carry motion compensation equipment, although certainly, correction for RPV platform motion is needed by the system. I suspect that the necessary corrections can be deduced from observations (a) made at the receive site by deploying additional receiver units in the form of an interferometer or, less desirable, because this increases the complexity of the platform, (b) by deploying on the RPV a simple GPS transponder, which enables the receive site to determine the RPV location.

Both approaches provide information which is needed to modify the synthetic aperture correlation algorithms. The difficulties associated with this task have not been studied and are expected to be significant.

### Jacobsen

What is the status of your project?

### Author's Reply

Current status of this project is conceptual.

### W. Keydel

For bistatic SAR the synchronisation between transmitter and receiver plays an important part. How do you foresee to establish this synchronisation and which accuracy do you expect?

### Author's Reply

The question quite correctly identifies the need for synchronisation between transmitter and receiver. This synchronisation is required for both ranging and aperture synthesis. Both requirements are satisfied by the information carried on the direct path. This path is the path of shortest time between transmitter and receiver and ensures that the receiver site has the potential to receive total information about the emission from the transmitter before it receives information from the target via the scatter path. This means that the accuracy achievable is limited only by the quality (link budget) associated with the direct path. At this time, we have not quantified this link. However, we felt it sufficient, at this time, to identify that the potential to completely resolve this issue already exists.

## MMW SAR ON RPV FOR BATTLEFIELD SURVEILLANCE

by

A. Farina, U. Carletti, E. D'Addio,  
C. Morabito, and R. Pangrazi  
Radar Dept. Selenia S.p.A.,  
Via Tiburtina Km. 12,400  
00131 Rome,  
Italy

AD-9005 842

SUMMARY

In this paper the remarkable capabilities and features of airborne synthetic aperture radar (SAR), operating in the millimetric wave (mmw) region, are discussed with reference to a battlefield surveillance application. The SAR system provides high resolution real-time imaging of the battlefield and moving target detection, under adverse environmental conditions (e.g. weather, dust, smoke, obscurants). The most relevant and original aspects of the system described in the paper are the band of operation (i.e. mmw in lieu of the more traditional microwave region) and the use of an unmanned platform. The former implies reduced weight and size requirements, thus allowing use of small unmanned platform. The latter enhances the system operational effectiveness by permitting accomplishment of recognition missions in depth beyond the FEBA.

An overall system architecture is described based on the onboard sensor, the platform, the communication equipment, and a mobile ground station. The relevant problem of detection and imaging of moving target is finally described.

1. INTRODUCTION

This paper describes the feasibility study of a sensor for battlefield surveillance and target acquisition. The need to penetrate in the enemy territory for several tens of kms requires, as sensor platform, the use of unmanned aircraft (UMA) such as drones and remotely piloted vehicles (RPV). Today, UMAs are equipped with electro-optical (EO) and infrared (IR) remote sensing systems. However, the performance of such systems is limited by weather condition and the presence of smoke, dust, and artificial obscurants which are present during a battle. These reasons motivate the use of radar systems which can operate all-weather.

Of course, conventional radar does not provide the same measurement accuracy resolution of the EO and IR systems. The use of synthetic aperture radar (SAR) concept allows to overcome such limitations. Briefly speaking, the SAR achieves high resolution by exploitation of the UMA motion. The movement, along the UMA path of radar antenna which is side-looking, emulates a very long synthetic antenna to which corresponds a very narrow beam along the azimuth and, consequently, a very good azimuthal resolution [1].

The use of UMAs allows to deeply penetrate into the enemy territory and to perform e.m. sensing of the interesting scene from short distances, typically 10 Km to 20 Km. In such situation, it is worth considering the use of mmw in lieu of the usual microwaves widely adopted in the majority of today radars. The following benefits accrue by the use of mmw, namely: (i) compact radar systems, and (ii) better resolutions for a given real antenna aperture area. The limitations related to greater attenuation of mmw are not very much relevant in our case because of the short range required to the radar. To sum up, the system described in this paper is a SAR operating at 35 GHz (wavelength = 8.57 mm), and installed on-board an RPV. The frequency of 35 GHz was selected in lieu of 96 GHz because of the lower atmospheric attenuation.

The remaining part of the paper is organized as follows. A detailed description of the whole system and of its operating modes is provided in Sect. 2. The main parameters and the block diagram of the radar are illustrated in Sect. 3. In Sect. 4 the radar performance are derived in clear and rain environments. Finally, the problem of detection and imaging of a moving target is afforded in Sect. 5.

2. SYSTEM DESCRIPTION

The operational requirements for the system can be summarized as follows: (a) imaging of territory areas with different e.m. reflectivity such as roads, buildings, airports, (b) detection and imaging of slowly moving (i.e. with speed up to 40 Km/h) targets such as tanks, cars, troops; and (c) operation during the day or night, in presence of mist, fog, moderate rain, smoke, and dust. The range and azimuth resolutions are required to be 5 m, while radiometric resolution should be 1.5 dB. These values allow to classify the detected targets.

The system is composed of four subsystems, namely: (i) the vehicle, (ii) the radar, (iii) the air-ground-air communication link, and (iv) the ground station. A pictorial view of the system during a mission is shown in Fig. 1.

The vehicle is 4 m long and 0.4 m of diameter. The flight can be remotely piloted or preprogrammed. The flight duration is between 1 and 2 hours. The cruise speed is 200 m/sec. Two missions are scheduled for the RPV, one having 1500 m height and the other having 10000 m height (see Fig. 2).

During the mission the RPV can penetrate more than 50 Km beyond the FEBA. The position accuracy of the RPV is 50 m, while the speed accuracy is in the order of 1%. Finally, the attitude errors along pitch,

roll, and yaw are approximately 0.1 deg/sec. These parameters play a key role in the evaluation of the actual imaging resolution. As it will be discussed later, the inaccuracy of platform positioning limits the achievable SAR resolution.

The radar payload, of approximately 50 Kg, is installed in a volume of 50 lt available in the RPV nose. The power supply, needed to the payload, is 300W, provided thru a network of 28 Vdc. A liquid cooling system is also foreseen. Two antennas of 1 mt length and 24 cm width are installed on the two RPV sides, in such a way that two swaths, symmetric to flight line, are obtained. The antenna beamwidth in elevation is 20 deg in the 1500 mt mission, while is 5 deg in the 10000 mt mission. The antenna beam off-nadir angle is 50 deg in both cases. The corresponding swath widths are 5 Km and 2.5 Km, respectively. The antenna weight is 2 Kg.

The data link subsystem allows communication between the radar and the ground station. The link is ECM safe. The up-link is narrow band. It allows to transmit to the radar command and control signals such as radiation on, setting up of working modes, etc. The same link provides control signals to the RPV frame in the remotely piloted mode. The down-link is wide-band (64 Mbit/sec). It provides to the ground station the radar raw-data related to the remotely sensed scene, and other signals concerning the radar BITE (built-in test equipment).

The ground station has three functions, namely: (i) monitoring and control of RPV flight, (ii) radar management and control, and (iii) processing of radar raw-data (holographic signal) to form the image of the scene. To these purposes, four units are installed in the station, namely: SAR processing unit, display unit with keyboard, data link interface unit and recording unit. The holographic signal (i.e. the signal scattered from the scene and stored in the radar in a range-azimuth matrix) is transmitted to ground and processed in the SAR processing unit. The display unit, which is directly connected to the data link interface, monitors and controls the RPV flight and the radar working modes through the keyboard. The display shows up the synthesized images in a real-time or off-line basis. The recording unit stores radar raw-data, processed images, and kinematic parameters of RPV flight.

The SAR processing unit provides the scene image by matched filtering of the holographic signal. Roughly speaking, the matched filtering is implemented thru a compression of the hologram along the range axis, and an additional compression of the resulting signal along the azimuth axis [1]. The range compression is implemented by correlating the hologram with the transmitted chirp signal. The azimuth compression is implemented by correlation with a reference azimuthal function. It can be shown that the function is another chirp with parameters depending on the "RPV-sensed scene" relative geometry. In the system described in this paper, the range compression is directly performed on-board, while the azimuth compression - which is computationally intensive - is implemented in the ground station. A simplified scheme of the SAR processing unit is shown in Fig. 3. The computer architecture implementing the SAR processing is a mix of dedicated and microprogrammed hardware. The main features of the computer is related to the ability of real-time processing the hologram. The computer data rate, the same of data link, is 64 Mbit/sec which derives from 2000 samples, coded with 8 bit, with a data rate of PRF = 4 KHz (see Sects. 3 and 5). The 2000 samples correspond to two real valued samples for each range cell available in the swath. The largest number of range cells is 1000 and pertains to 1500 height mission.

### 3. ON-BOARD RADAR SYSTEM

The purpose of on-board radar system is to sense the scene, by transmission of a coherent waveform, and to receive the corresponding scattered holographic signal which is stored in a range-azimuth matrix. The scheme of on-board radar is shown in Fig. 4. The main elements of the radar are briefly described in the following. The selection of radar parameters is, sometimes, a complex task which is fulfilled by resorting to a computer program. The description of such methodology is out of the scope of this paper; a detailed approach to the problem is outlined in [2].

The antenna is a slotted waveguide. The antenna is fixed to the RPV frame, thus providing the same off-nadir angle of 50 deg for both missions. As already mentioned, the elevation beamwidth has different values for the two missions. This is achieved, with the same antenna width of 24 cm, by using an illumination tapering in the low altitude mission. An improvement foreseen for second generation systems is related to the use of phased-array antennas which allow the compensation of platform attitude errors and the beam agility to spot, for instance, areas of limited surface in the controlled scene.

The RF source provides the local oscillation and the drive signals to the transmitter. The transmitted waveform is a pulse train, where each pulse is frequency modulated with a chirp code. The pulse duration is 6  $\mu$ sec and the chirp bandwidth is 40 MHz. The range resolution corresponding to the compressed pulse is 5 mt. The pulse repetition frequency of the waveform is PRF = 4 KHz; the corresponding duty cycle is 2.4%. The value of PRF is selected in such a way to contain the Doppler spectrum of the stationary scene and the echoes from the moving targets. By the relative geometry of "radar-imaged scene" the Doppler spectrum width of the stationary scene is 400 Hz. The selection of PRF = 4 KHz is motivated by the need to leave enough cleared frequency to the echoes from moving targets which will be received without frequency ambiguity (see also sect. 5).

The transmitter, which is a coherent TWT, modulates and amplifies the waveform. The TWT peak power is 300W, while the average power is 7.2W.

SAW technology is adopted to implement the chirp generator and compressor: the required compression ratio is 180. The superhot radio frequency unit amplifies and down converts, to an intermediate frequency band, the received signal. The overall receiver noise figure is 12 dB.

Finally, the video processing unit provides a coherent baseband signal, implements the A/D conversion, generates the slow time (i.e. the azimuth abscissa) and fast time (i.e. the range abscissa) axes of the holographic matrix, and sends the data to the down-link. The sampling frequency is 40 MHz, while 8 bit are used in the digital representation of the data. Table 1 provides weight, volume, and power consumption of the different radar modules. Table 2 sums up the main radar parameters for the two missions.

#### 4. RADAR PERFORMANCE

The SAR imaging capability can be expressed in terms of detection probability, for a given probability of false alarm, of the signal backscattered by a cell in the sensed scene. It is reasonable to have an almost uniform detection probability throughout the cells in the scene. Additional figures of merit are the sensor spatial resolutions (along range and azimuth), which establish the cell dimensions, and the radiometric resolution which represents the sensor capability to discriminate two adjacent cells having different reflectivity.

The range resolution is related to compressed pulse duration; it has been pointed out that such resolution is 5 m as required by system specifications. The azimuth resolution is related to the antenna length and to the number of independent looks averaged during a synthetic antenna period. The antenna length is 1 m to which corresponds a maximum azimuthal resolution of 0.5 m. Such high resolution can be traded-off with the radiometric resolution. The averaging of 10 independent looks reduces the azimuthal resolution to the required 5 m, but greatly improves the radiometric resolution to a value which is better than 1.5 dB. Such value is good enough to distinguish the different types of reflectivity pertinent to roads, airports, etc. as required by the specifications.

The detection probability is related to the ratio of the signal power-to-disturbance power. More specifically, when radar objective is to image a scene, a parameter to be evaluated is the ratio between the power reflected by a cell of the scene to receiver noise power.

Detection of a point-like target is the radar objective in another operational situation of interest. In this case, it is worth considering the ratio between the power scattered by the target to the power scattered by the cell of the scene plus receiver noise power. Such power ratios are easily evaluated by resorting to the range equation for the SAR case [2], [3], by assuming a terrain reflectivity of -25 dB, which is an average value for 35 GHz, and a reference value of 1 m<sup>2</sup> for the target RCS, it is shown that comfortable detection probabilities (PD = 0.9) are obtained for the two RPV missions.

The detection performance degrades in presence of attenuation due to atmosphere, mist, fog, rain and dust. The attenuation due to atmosphere is 0.8 dB/Km (one way), which produces a two way overall attenuation of 3.24 dB for low altitude mission. The attenuation raises to 7.2 dB for the high altitude mission. These attenuations do not impair SAR detection performance.

In presence of fog and rain the analysis is more complex. First of all, in addition to attenuation there is also a backscattering process producing a disturbance at the radar receiver input which may obscure the scene image. The deleterious effects of disturbance depend not only on the power of backscattered signal but also on its temporal correlation as compared to the SAR coherent integration interval. Secondly, the fog and rain are limited in space as shown in Fig. 5. This geometry gives rise to two cases to be investigated. In case (a),  $X_{ra} > X_c$ , where  $X_c$  is the abscissa of the considered cell (e.g. that at the middle of swath). The rain column is present in the considered cell; the processes of attenuation and backscattering are contemporary present. In case (b),  $X_{ra} < X_c$ , the rain column is between the radar and the considered cell—only the attenuation process is considered. A detailed analysis of the problem [4] gives the following results. First of all, consider the case of SAR looking at a point target; in this case the terrain reflection is considered as an additional disturbance. In the low altitude mission, it is shown that the signal-to-overall disturbance power ratio is 21 dB in absence of rain and reduces to 15 dB in presence of rain (with rate of 5 mm/hr) in the target cell. The 6 dB loss does not prevent target detection. The other case to consider refers to the imaging of terrain. Now, the useful signal is that scattered by the ground cell. When the rain is not present in the cell of interest, rain rates close to 5 mm/hr do not appreciably affect SAR imaging capabilities. The situation is worse when the considered cell is inside the rain column; even for low rain rate (e.g. 1 mm/hr) the SAR imaging capabilities are severely degraded.

#### 5. DETECTION AND IMAGING OF MOVING TARGETS

A SAR looking at a moving target having unknown kinematic parameters does not provide a good image of the same. This is because the reference azimuthal chirp, to be used in the compression process, is matched to the chirp scattered by the stationary scene while it is mismatched to the chirp scattered by the moving target.

Consider a point-like target having a radial speed with respect to SAR platform. It is shown [5] that the corresponding image of the point has the following azimuthal offset with respect to the correct position:

$$\Delta X = |R_0 v_r / V| \quad (1)$$

where  $R_0$  is the minimum slant range of target from the radar,  $v_r$  is the target speed radial component, and  $V$  the platform speed. If  $\Delta X$  is greater than the synthetic aperture, the target is lost. Additionally, a target with radial speed component may migrate through more than one range cell. A reduction of the coherent integration time, for azimuth focusing pertinent to a certain range cell, is experienced. This phenomenon produces a spread of energy throughout the range cells interested by the target migration, and a reduction of the azimuthal resolution.

Consider now a target having an azimuthal speed component. This produces a defocus in the azimuthal direction with a consequent loss of azimuthal resolution. The defocus is not appreciable if the phase error of the scattered signal is less than  $\lambda/2$  throughout the synthetic antenna. The corresponding speed azimuthal component which does not produce defocus is:

$$v_c = \frac{\rho_a^2}{2} (R_0 \lambda) \quad (2)$$

where  $\rho_a$  is the required azimuthal resolution, and  $\lambda$  is the wavelength.

In the more general case, both azimuthal and radial components of target speed are different from zero. Azimuthal defocus, energy spread along range, and azimuth offset are contemporary present. The corresponding SAR impulse response is quite different from the expected "sinX/X" type function along azimuth and range axes. Actually, it looks like an oblique parallelogram having many small peaks along the parallelogram axis in lieu of just one large peak in the true target position. Because the parallelogram shape is related to the target kinematic parameters, it is understandable that the measurement of the parallelogram axis slope gives a means to re-focus the target image [6].

Let now consider the strategies to detect and image moving targets. Detection is not easy because of the energy smeared throughout range cells. Additionally, the scattering by the stationary scene, which now acts as a clutter source, makes target detection more difficult. Once a target has been isolated from the stationary scene, it is necessary to submit the detected signal to a re-focus process to restore the azimuthal resolution pertinent to a stationary target.

To this end, the first strategy refers to a proper selection of radar PRF value. As already mentioned, it is worth to have a PRF larger than the stationary scene bandwidth; i.e.  $BD = 2V/L$ , where  $V$  is platform speed, and  $L$  is antenna length [2]. In the RPV case,  $BD$  is 400 Hz and PRF is 4 KHz. This is because the target Doppler frequency will likely be out of clutter spectrum, thus allowing the required separation of target from stationary scene. Additionally, target Doppler frequency will be unambiguous for target radial speed up to 60 Km/hr.

To understand in which way is possible to separate moving point-like targets from the stationary scene consider Fig. 6. It shows the azimuthal chirp, for a certain range cell, corresponding to the following four conditions, namely: (1) stationary point target, (2) target moving along track, (3) target moving cross-track, and (4) target having both azimuthal and radial components of speed. The mathematical expression of the azimuthal chirp for a moving target is as follows [9]:

$$f_D(t) = \frac{2V_r}{\lambda} + \frac{1}{\lambda R_0} (V_c^2 + R_0 a_r) t \quad (3)$$

where  $V_r$  is the target radial speed,  $V_c$  is the target azimuthal speed component, and  $a_r$  is the radial component of target acceleration. The quantity  $2V_r/\lambda$  is the so called target Doppler centroid, while  $(V_c^2 + R_0 a_r)/\lambda R_0$  is the target Doppler frequency rate. It should be noted that the backscattered signals from an extended stationary scene produces many azimuthal chirps all parallel to chirp (1).

A first rough approach to separate the stationary scene from moving target is to cut out the Doppler frequency spectrum  $[-0.5 B_D, +0.5 B_D]$ ; of course, a moving target represented by the azimuthal chirp (2) cannot be recovered. A Doppler filter bank, which uniformly spans the frequency intervals  $(-PRF/2, -BD/2)$  and  $(BD/2, PRF/2)$ , is a means to detect moving targets represented by azimuthal chirps as those labelled (3) and (4) in Fig. 6. This Doppler filter bank compensates for only the Doppler centroid  $2V_r/\lambda$  of eq. 3. Table 3 gives an indication of the performance that may be obtained by that channel of the bank which is matched to the target Doppler centroid. The table indicates the target Doppler centroid  $F_D$ , the azimuthal bias  $\Delta X$ , the range walk, the resolution along azimuth ( $\rho_a$ ) and along range ( $\rho_r$ ), the peak of the signal after Doppler centroid compensation and the integrated sidelobe ratio (ISLR). Two types of moving targets are considered, namely: (a) target moving cross track with  $V_c = 11$  m/s, and (b) target having the two components, along range and azimuth, of the speed. The results show that the high altitude mission suffers the highest degradations.

A more effective method to detect a moving target and to correctly estimate its position and RCS is that shown in Fig. 7. Each range line of the holographic matrix is range compressed and then corner turned. Afterwards, the processing along azimuth is implemented by means of a bank of  $(NM+1)$  filters. Each filter is implemented, in the frequency domain, as follows:

- (i) the range compressed signal is transformed by means of FFT,
- (ii) the reference signal  $h_{ij}$  is transformed by means of FFT, and
- (iii) the transformed signals from (i) and (ii) are multiplied and re-transformed in the time domain by IFFT.

The first channel is dedicated to imaging of the stationary scene; " $h_{00}$ " is the azimuthal chirp matched to a representative point of the stationary scene. The  $NM$  channels " $h_{ij}$ " are matched to the azimuthal chirps of the type of eq. (3). More in detail, index  $i$  is related to matching of Doppler centroid, while index  $j$  refers to matching of Doppler rate. The proposed processor effectively removes the azimuthal offset and the azimuthal defocus; additionally, an indication of kinematic parameters and the RCS estimation of targets is allowed. Target detection is obtained by thresholding each channel of the filter bank; threshold value can be obtained by autogate along range. The estimation of target kinematic parameters is obtained by the indexes " $ij$ " of the channel giving detection. The target Doppler centroid provides  $V_r$ , while the Doppler rate is related to the two parameters  $V_c$  and  $a_r$ . Target RCS is obtained after the envelope detector. The performance evaluation of a processing scheme similar to that presented in Fig. 7 is given in [9].

The channelized processor of Fig. 7 still suffers some limitation related to the resolution capabilities of the  $h_{ij}$  filters. Targets having close in values of Doppler centroid and Doppler frequency rate may not be distinguished by the processor. Additionally, a target with a large value of Doppler frequency rate may give rise to more than one detection in contiguous filters of the bank.

To overcome these limitations resort is made to the processing scheme depicted in Fig. 8. The processor is constituted by two channels operating on the range compressed holographic signal. The lower channel, which is quite conventional, provides the image of the stationary scene. The upper channel is dedicated to detection and imaging of moving targets. The rationale of the proposed approach is to transform the signal from a time sequence into a mixed time-frequency representation. This representation is quite useful for signal having non-stationary instantaneous frequency. The azimuthal chirp of SAR, which is a non-

stationary signal, if properly transformed provide a wedge in the  $(W, t, f_D)$  representation.  $W$  is the transformed value of the azimuthal chirp, while  $t$  and  $f_D$  are the independent variables of the transformation  $W(t, f_D)$ . A transformation which enjoys a number of features is the Wigner transform [10]. In fact, the Wigner transform of a chirp is a wedge in the transformed space or, equivalently, a line in the  $(t, f_D)$  plane. It can be shown that the line parameters are the Doppler centroid and the Doppler frequency rate of the azimuthal chirp. Looking at the Wigner transform of the range compressed hologram, we have a band of chirps around the temporal axis. Few other lines indicate the presence of moving targets. A possible way to detect moving targets is to reject the stationary scene before applying the Wigner transformation. The subsequent detection of target and estimation of Doppler parameters can be done by means of Radon transform [10] or Hough transform [8]. The Radon transform is equivalent to integrate the signal  $W(t, f_D)$  along a line in the  $(t, f_D)$  plane. The maximum value will be reached when the integration line, which is swept throughout the  $(t, f_D)$  plane, is superimposed to the target azimuthal chirp. The Hough transform is an efficient way to map a line in a point onto a transformed plane. In the present case, the Doppler centroid ( $f_{DC}$ ) and the Doppler frequency rate ( $f_D$ ) are the axes of the plane. Target detection and Doppler parameter estimation is accomplished by thresholding the Hough transform  $H_H(f_{DC}, f_D)$  to look for spikes in the transformed signal. At present, a theoretical study and simulations are going on to evaluate the performance of this novel processor.

#### 6. ONGOING RESEARCH AND CONCLUDING REMARKS

It has been shown the feasibility of a mmw SAR on-board of a RPV. The operational usefulness of such system has also been proved.

A thorough understanding of the system complexity and achieved performance need further investigations which presently are going on. They refer to the compensation of platform attitude errors, to ECM-ECCM problem, and to the simulation of the whole system.

A preliminary analysis of the effects of attitude errors on the image quality shows that the maximum allowable error along each of the three axes is 0.02°/s in order to preserve 5 mt resolution [7]. Such requirement is not fulfilled by the RPV under consideration. Two alternatives are at present under consideration: the first refers to the installation of an inertial navigation system (INS) in the RPV frame, the second considers the use of autofocus and Doppler centroid loops to adjust, at signal processing level, the image distortions [8].

The image degradations caused by ECM is another topic under investigation. In the second generation systems, where phased-array antennas are planned to use, ECCM techniques based on spatial filtering of directional jammers will be applicable. Nevertheless, the same concept can be applied to the synthetic array antenna. Such spatial filtering techniques of jammers are under investigation.

Finally, a powerful simulation tool is under development with the purpose of evaluating the system performance in presence of complex environment [8]. Briefly speaking, the simulator is able to generate several types of holograms, such as those pertaining to a moving target seen by a platform with attitude errors, and those relevant to stationary and not homogeneous scenes. The holograms are fed to another software package which emulates the on-board radar and the SAR processing module in the ground station. A better appreciation of the system geometric and radiometric resolutions will be possible.

#### 8. REFERENCES

- [1] AUSHERMAN, D.A., et al.  
"Developments in radar imaging", IEEE Trans on Aerospace and Electronic Systems, Vol. AES-20, No. 4 July, pp. 363-400.
- [2] E. D'ADDIO, A. FARINA  
"Preliminary design of a SAR for RPV", Selenia Technical Report, RT 87124-RS, 22-X-1987. Company Confidential (in Italian).
- [3] E. D'ADDIO, A. FARINA  
"Updating of design of a mmw SAR for RPV", Technical Memorandum RM ENG-PSR/ED-186, 24-VI-1988. Company Confidential (in Italian).
- [4] F. SCANNAPIECO, E. D'ADDIO  
"Evaluation of atmosphere effects on airborne SAR at 35 GHz", Selenia Technical Report, RT 88046-RS, 11-IV-1988. Company Confidential (in Italian).
- [5] G. MORABITO, E. D'ADDIO  
"Imaging of moving targets by means of an airborne SAR at 35 GHz", Selenia Technical Report, RT 88043-RS, 30-VI-1988. Company Confidential (in Italian).
- [6] A. FREEMAN  
"High resolution MTI with SAR", AGARD CP 381 Conf. Proc., October 1985 (Classified).
- [7] R. PANGRAZI  
"Effects of phase errors in SAR processing", Selenia Technical Report, RT-88078 in, VI 1988. Company Confidential (in Italian).
- [8] F. VINELLI, et al.  
"Processing of spaceborne and airborne SAR data: an experimental activity", Int'l. Conf. on Radar, April 24-28, 1989, Paris.

- [9] S. BARBAROSSA  
 "Doppler-rate filtering for detecting moving targets with Synthetic Aperture Radar", SPIE Proc., Vol. 1101, 27-28 March 1989, Orlando-Florida, USA.
- [10] E. D'ADDIO, A. FARINA, C. MORABITO  
 "The applications of multidimensional processing to radar systems", Intl. Conf. on Radar, April 24-28, 1989, Paris.

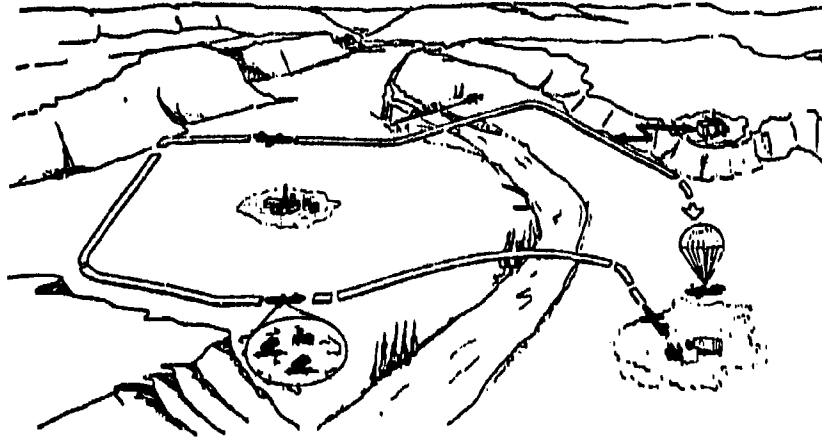


Figure 1 - Pictorial view of the system during a mission

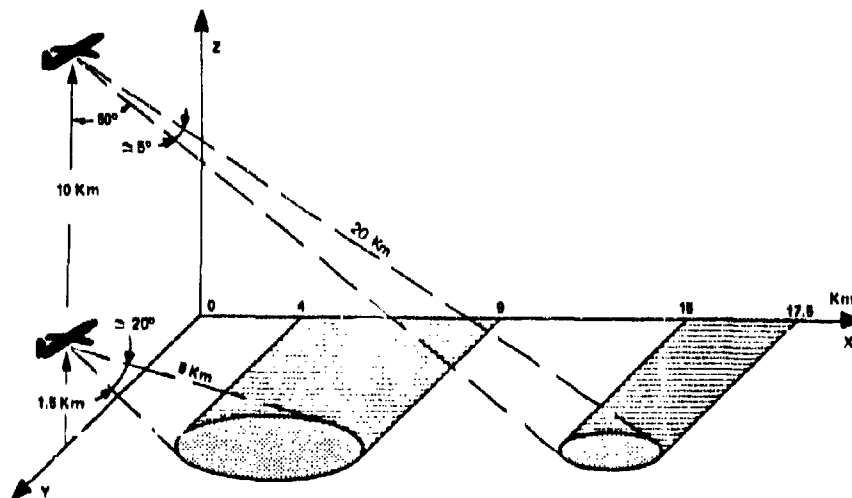


Figure 2 - Two operational modes of SAR system

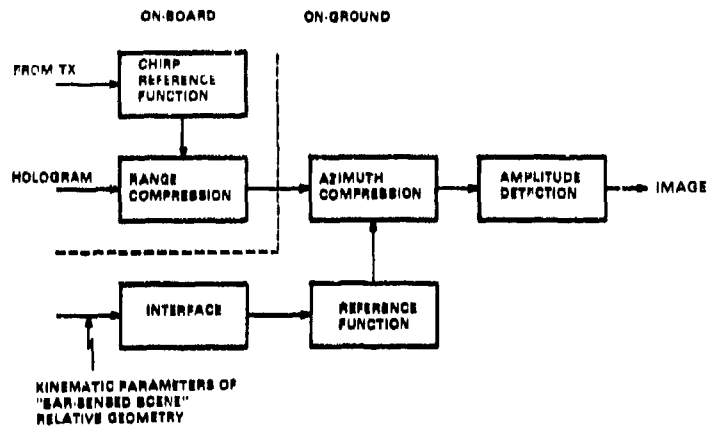


Figure 3 - SAR processing unit

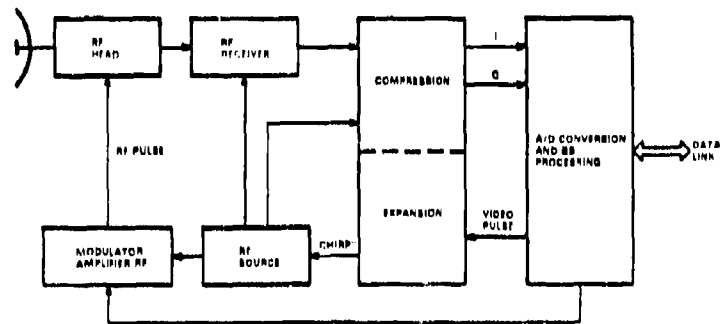


Figure 4 - Block diagram of on-board radar

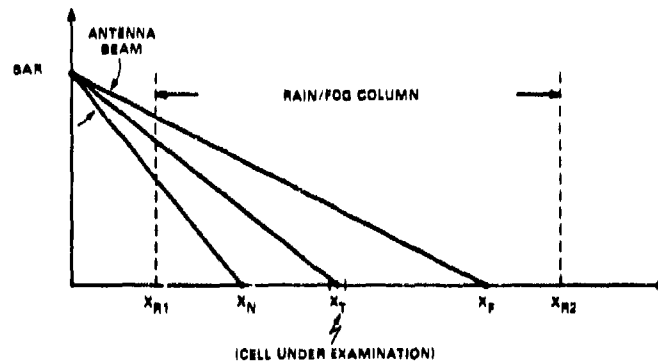


Figure 5 - Relative geometry of SAR and a rain column

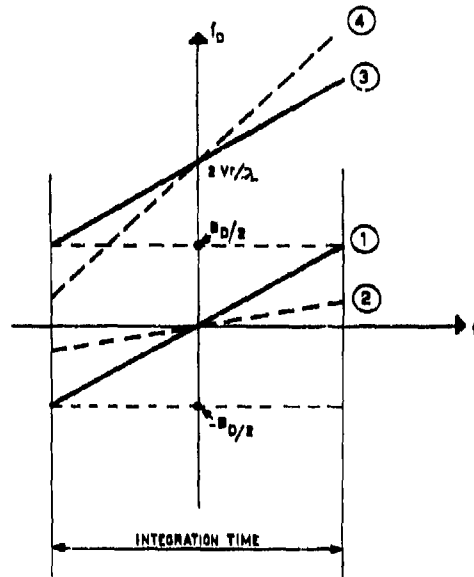


Figure 6 - Doppler frequency histories of stationary and moving point-like targets

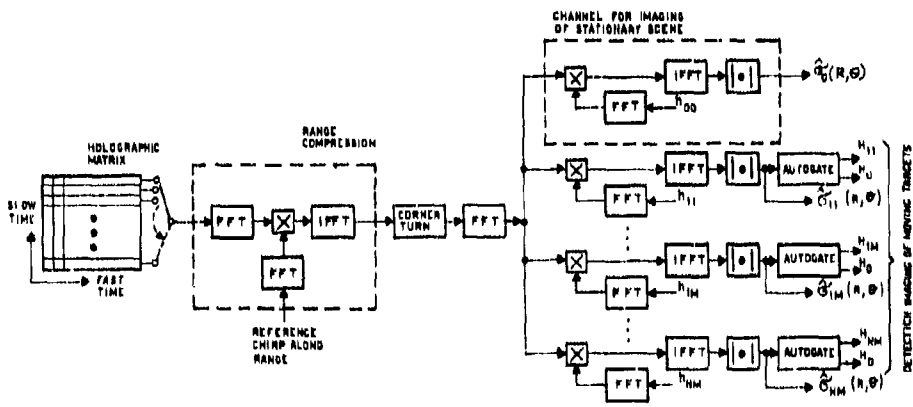


Figure 7 - Channelized processor for detection and imaging of moving targets

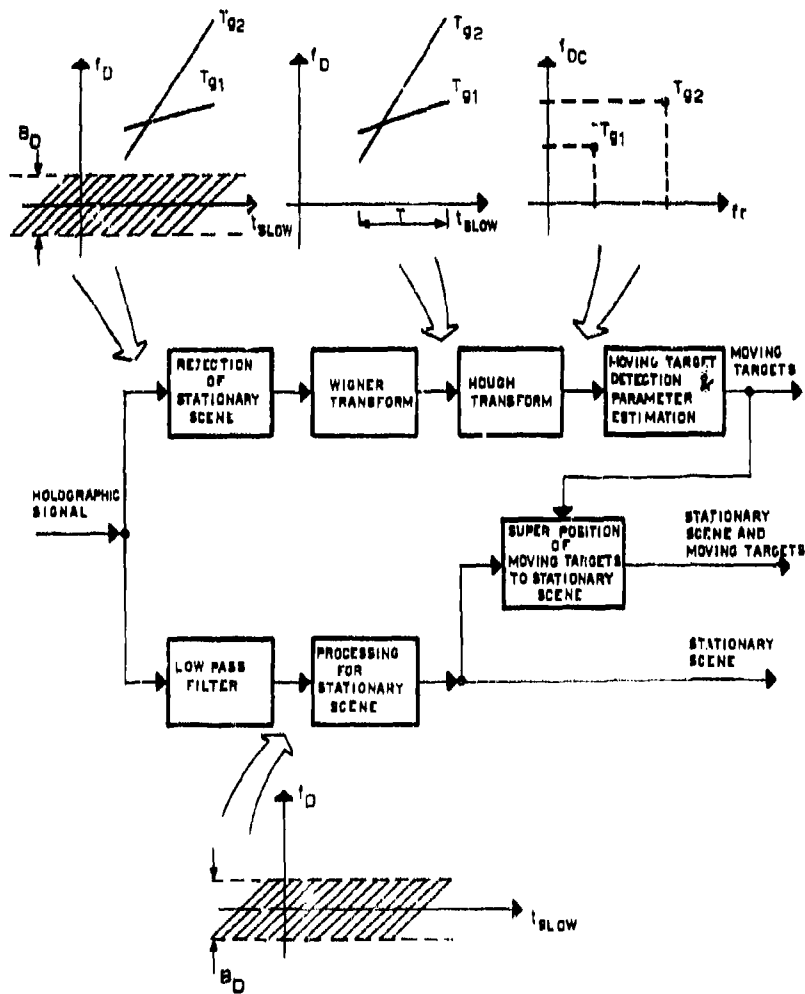


Figure 8 - Detection and imaging of moving targets by using Wigner and Hough transform

TABLE 1

UNIT	WEIGHT (KG)	VOLUME (LT)	POWER REQUIRED (W)
TRANSMITTER	32	20	350
RECEIVER	8	8	---
VIDEO PROCESSING	10	10	---
DC GENERATOR	5	5	150
PLANAR ANTENNA	2	--	---
OTHERS	5	5	---
TOTAL	62	48	500

Table 1 - Weight, volume, and power required by on-board radar units

TABLE 2

PARAMETER	H = 1500 m	H = 10000 m
RPV speed (m/s)	200	
Wavelength (mm)	8.57	
Antenna length (m)	1	
Antenna width (m)	0.24	
Antenna gain (d <sup>0</sup> )	35.7	41.8
Off nadir angle (°)	50	
Elevation beamwidth (°)	20	5
Range from scene (Km)	9	20
Swath width (Km)	5	2.5
Transmitted pulse duration (μs)	6	
Duration of compressed pulse (ns)	33	
Range compression ratio	180	
Range chirp bandwidth (MHz)	40	
PRF (Hz)	4000	
Duty cycle (%)	2.4	
Azimuthal chirp bandwidth from stationary scene (Hz)	400	
Integrated pulse number in azimuth	1542	3428
Range resolution (m)	5	
Azimuth resolution (m)	5	
Range cell number in swath	1000	500
Azimuth cell number per unit time (s)	7200	
Synthetic antenna length (m)	77	171
Number of independent looks	10	
Radiometric resolution (dB)	1.5	
Transmitted average power (W)	7.2	
Transmitted peak power (W)	300	
Bit number of A/D	8	
Rate of data link (Mbit/sec)	64	
A/D sampling frequency (MHz)	40	

Table 2 - Main radar parameters for the two RPV missions

TABLE 3

PARAMETER	REFERENCE	h = 1.500 m		h = 10.000 m	
	$V_r = 0$ $V_G = 0$	$V_r = 11$ m/s $V_G = 0$	$V_r = 7$ m/s $V_G = 7$ m/s	$V_r = 11$ m/s $V_G = 0$	$V_r = 7$ m/s $V_G = 7$ m/s
$F_D$ (Hz)	0	1762	2418	1773	2429
$\Delta X$ (m)	0	-2.4	-1.5	-2.6	1.2
Range walk	0	0	0	2	1
$\rho_r$ (m)	5	5	10	7	62
$\rho_\theta$ (m)	5	5.5	6.3	5.7	5
Peak (dB)	0	-1.4	-4.1	-4	-12
ISLR (dB)	13	10	9.8	9.5	11
[m]					

Table 3 - Performance of Doppler filter bank

**DISCUSSION****R. Klemm**

What is the minimum target speed you can detect?

**Author's Reply**

The minimum detectable target radial speed is equal to the maximum frequency of the stationary scene. Assuming an off-nadir angle of 60° and a wavelength of 0.008 m, a value of 7km/h is obtained. Concerning the minimum detectable target azimuthal speed, at present a detailed investigation is being undertaken to evaluate the capability of separating target from clutter, on the basis of Doppler rate filtering.

**W. Keydel**

Do you foresee absolute radiometric calibration? If yes, what is the accuracy?

**Author's Reply**

There are two ways of achieving the 1.5 dB radiometric calibration claimed in the paper, namely: (i) internal calibration and (ii) external calibration techniques. Both techniques are foreseen in our system. Internal calibration is based upon generation of calibration of some signals. External calibration, based on corner reflections displaced on friendly areas, is available for just one portion of the RPV mission.

**van d. Spek**

The system aims at a resolution of 5x5m. This seems just not enough for the battlefield. Could you comment on this choice?

**Author's Reply**

The resolution of 5x5m is the result of a trade-off between detection and classification and track of tanks, armoured vehicles etc., versus simplicity of hardware chirp generator, reduced processing load, and reasonable cost.



**"GENERATION PROGRAMMABLE DES IMPULSIONS MODULEES  
LINEAIREMENT EN FREQUENCE"**

par

Jacques Richard  
Jean-Marc Fallot  
Alcatel Espace  
26 av. J.E. Champollion  
BP 1187  
31037 Toulouse Cedex  
France

**RESUME**

**INTERET DE LA PROGRAMMABILITE DES IMPULSIONS GENEREES DANS LES SAR ET ALTIMETRES**

La possibilité de programmer les caractéristiques de l'impulsion émise d'un radar embarqué sur satellite sera une nécessité pour les radars futurs.

Dans un radar altimètre, une impulsion très courte permet de mesurer des distances avec une précision centimétrique au-dessus des océans mais n'est plus adaptée pour fonctionner au-dessus des glaces et des terres à cause des signaux plus faibles et du relief plus important que l'on rencontre au-dessus de ces surfaces.

La possibilité de réduire la bande du signal sur les glaces et les terres permet d'améliorer le bilan de liaison et d'élargir la fenêtre d'acquisition dans le cas d'un radar altimètre utilisant la technique "full-deramp".

Dans un SAR ou un SLAR incapable de changer les caractéristiques de son impulsion, la résolution transverse des images est inversement proportionnelle au sinus de l'angle d'incidence. Par exemple, sur des images prises entre 15° et 65° d'incidence, la résolution évolue dans un facteur 3,5. L'utilisation d'un chirp avec une bande programmable permet de résoudre cet inconvénient et, comme on peut le démontrer, sans impact significatif sur le bilan de liaison.

Cet exposé discute des diverses techniques pour programmer les caractéristiques du chirp. La plupart de ces techniques sont numériques, mais nous montrons qu'il peut être intéressant de les associer à des techniques analogiques.

**INTRODUCTION**

Le signal à générer est une impulsion modulée linéairement en fréquence dont les principales caractéristiques sont les suivantes :

- |                            |  |
|----------------------------|--|
| - Bande d'excursion        | Programmable jusqu'à quelques centaines de Mégahertz |
| - Durée                    | 10 à 50 µs voire 100 µs                              |
| - Erreurs d'amplitude      | Quelques dixièmes de dB                              |
| - Erreurs de phase rapides | 1 à 2 degrés rms                                     |
| - Erreurs de phase lentes  | Quelques degrés                                      |

Le générateur pourra, si nécessaire, corriger les erreurs de phase lentes des autres sous-systèmes du radar (exemple : celles des filtres, des amplis, etc...).

En raison de l'aspect programmabilité, on se limite à l'exposé des solutions basées sur la génération numérique.

**1 - RAPPELS THEORIQUES**

**1.1. RAPPELS SUR LA THEORIE DE L'ECHANTILLONNAGE**

Considérons un signal  $s_c(t)$  dont le spectre est à support limité :

$$S_c(f) = 0 \text{ pour } |f| > f_c$$

On montre que le signal est entièrement déterminé par la suite dénombrable des échantillons  $s(n/2T_c)$ , pris aux instants discrets  $n/2T_c$ ,  $n$  appartenant à l'ensemble des entiers.

Ce théorème permet donc de remplacer un signal  $s_c(t)$  par un signal échantillonné  $s_0(t)$ , obtenu à partir de  $s_c(t)$  par la multiplication de ce signal par une fonction d'échantillonnage  $a(t)$ .

Le cas idéal est l'échantillonnage par des distributions de Dirac :

$$p(t) = (1/2\pi c) \sum_n \delta(t - n/2\pi c)$$

Le signal  $s_c(t)$ , le signal échantillonné  $s_e(t)$  et leurs spectres sont représentés sur la Figure 1.1/A.

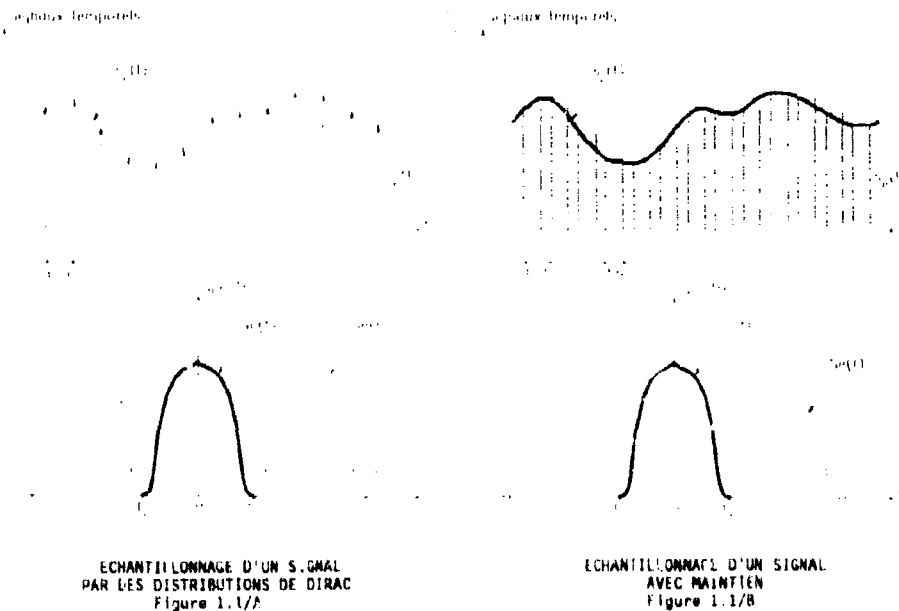
La reconstruction du signal  $s_c(t)$  à partir de  $s_e(t)$  se fait simplement par un filtre idéal passe-bas, de bande  $F_c$ . Ce filtre reconstitue le signal analogique  $s_c(t)$  par interpolation entre les échantillons ; aussi est-il appelé filtre d'interpolation.

Le cas souvent utilisé en pratique est l'échantillonnage avec maintien (voir Figure 1.1/B). Le spectre du signal échantillonné est celui du cas idéal multiplié par la fonction :

$$\frac{\sin(n T_m f)}{n T_m f}$$

La reconstruction du signal  $s_c(t)$  non distordu est obtenue par le filtre interpolateur idéal suivi d'un réseau correcteur de fonction de transfert :

$$\frac{n T_m f}{\sin(n T_m f)}$$



## 1.2. CARACTERISTIQUES D'UN CHIRP

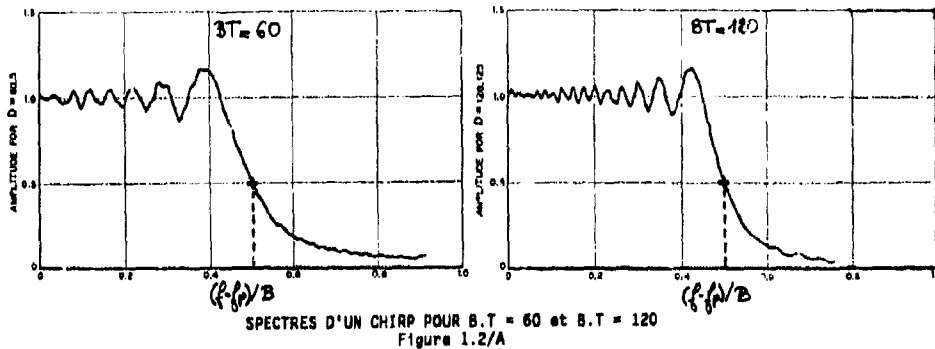
L'équation temporelle d'une impulsion chirp (onde à front de fréquence) est caractérisée par la durée  $T$  et l'élargissement  $B$  :

$$s(t) = \text{Re} \{ e^{-j\omega_0 t} \cos(\pi k t^2) \}$$

avec  $\omega_0$  : la fréquence porteuse

$k$  :  $B/T$  : la bande de la chirp

Le spectre d'un tel signal est représenté sur la Figure 1.2/A. Pour des chirps à front  $B/T$  important, l'amplitude du spectre est donnée de l'ordre de  $1/\sqrt{B}$  sur  $\pm B/2$  et décroît plus rapidement en dehors de cette portée.



## 2 - ETUDE DES SOLUTIONS

### 2.1. GENERATION SUR FREQUENCE PORTEUSE INTERMEDIAIRE

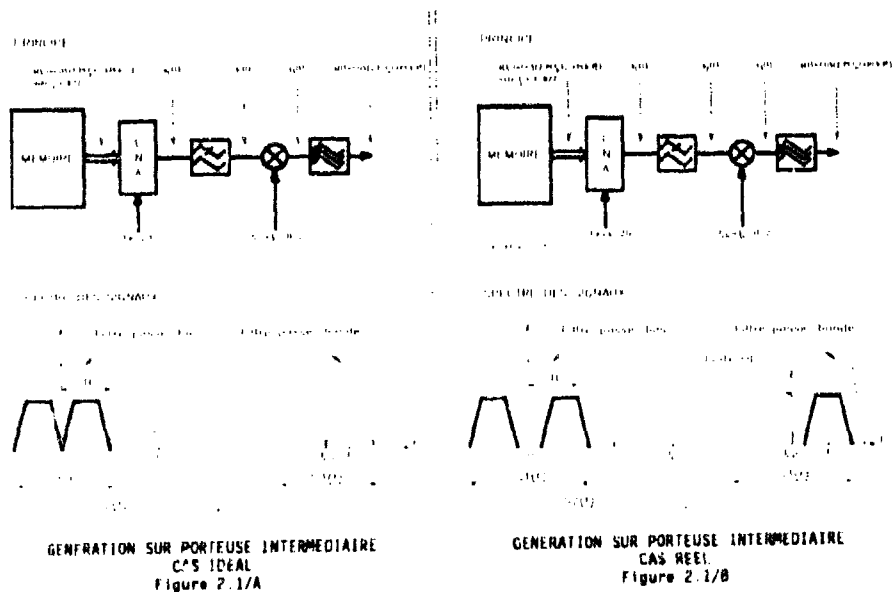
Ce type de génération consiste à générer le chirp centré sur une fréquence porteuse aussi faible que possible et à transposer ensuite le signal à la fréquence désirée par un oscillateur local. Ce principe est illustré sur la Figure 2.1/A.

Dans le cas idéal, le chirp est généré sur une fréquence de  $B/2$  où  $B$  est la bande du chirp, la fréquence d'échantillonnage est égale à  $2B$ , et la fréquence de transposition est égale à  $f_0 - B/2$  si on prend le battement supérieur, ou  $f_0 + B/2$  si on prend le battement inférieur.

En pratique, il faut prendre des marges pour faciliter les filtrages des différents parasites, comme illustré sur la Figure 2.1/B.

Ce type de génération a l'avantage de ne nécessiter la génération que d'un seul signal. Il a, par contre, l'inconvénient d'une fréquence d'échantillonnage supérieure à  $2B$  contrairement à certaines solutions se contentant d'une fréquence moitié. De plus, le plan de fréquence est complexe ; il peut même être nécessaire de réaliser une double translation de fréquence pour que le filtrage des signaux parasites soit possible.

Ce type de génération est intéressant pour les chirps à faible bande. Il ne convient pas pour les radars à haute résolution.



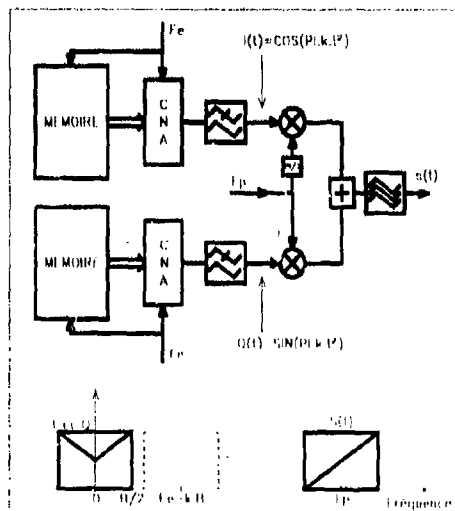
## 2.2. GÉNÉRATION DIRECTE DES VOIES VIDEO I ET Q

Une solution pour générer le signal  $s(t) = \cos(2\pi f_c t + nkt^2)$  consiste à générer les signaux  $I = \cos nkt^2$  et  $Q = \sin nkt^2$ , ces signaux étant ensuite respectivement multipliés par  $\cos 2\pi f_c t$  et  $-\sin 2\pi f_c t$  puis sommés.

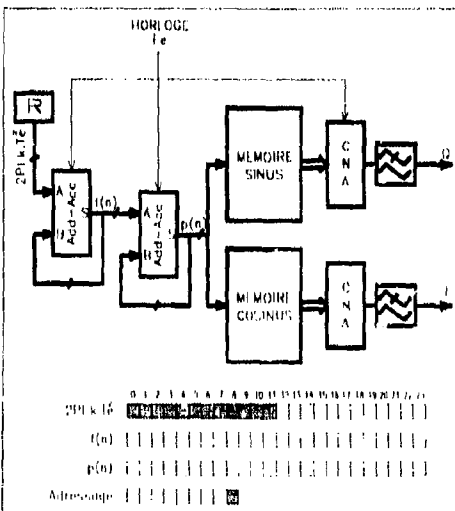
Ce principe est illustré sur la Figure 2.2/A. Les signaux ont une bande  $B/2$  ; on peut donc les échantillonner avec une fréquence  $f_e = B$ .

En pratique, il faut prendre  $f_e = kB$  avec  $k > 1$  pour faciliter le filtrage des spectres d'échantillonnage inutilisés et pour faciliter l'équilibrage en amplitude et phase des deux voies. On choisira  $k$  entre 1,3 et 1,4.

La capacité mémoire requise sur chaque voie est de  $f_e \times T$  mots.



GENERATION DIRECTE DES VOIES VIDEO I ET Q  
Figure 2.2/A



GENERATION DE LA PHASE DES VOIES I ET Q  
Figure 2.3/A

## 2.3. GÉNÉRATION DE LA PHASE DES VOIES I ET Q

Au lieu de générer les signaux  $I = \cos nkt^2$  et  $Q = \sin nkt^2$ , on peut générer le signal  $\phi(t) = nkt^2 \text{ modulo } 2\pi$  et calculer ensuite  $I = \sin(\phi(t))$  et  $Q = \cos(\phi(t))$ .

Le calcul du signal échantillonné  $\phi(nT_e)$  peut se faire avec deux additionneurs-accumulateurs ( $T_e = 1/f_e =$  période d'échantillonnage).

In effet :

$$\text{Notons : } \phi(n) = nkT_e^2 n^2$$

$$\text{On a : } \phi(n+1) = nkT_e^2 (n+1)^2$$

$$nkT_e^2 (n^2 + 2n + 1)$$

$$= \phi(n) + f(n)$$

$$\text{ou } f(n) = (2n+1) nkT_e^2$$

$$\text{De même, on a : } f(n+1) = (2n+3) nkT_e^2$$

$$f(n) + 2nkT_e^2$$

Le principe est donc d'avoir un additionneur-accumulateur pour calculer  $f(n)$  et un additionneur-accumulateur pour calculer  $\phi(n)$ . On en déduit le synoptique de la Figure 2.3/A.

Le nombre de bits requis sur les additionneurs-accumulateurs dépend de la précision de programmation que l'on désire.

Le choix de la fréquence d'échantillonnage  $F_e$  fixe la bande maximale  $B_{\max}$  du chirp que l'on peut générer :

$$B_{\max} = F_e/\alpha$$

où  $\alpha > 1$  est une marge pour faciliter le filtrage des spectres d'échantillonnage (on choisit  $\alpha$  entre 1,3 et 1,4)

On a donc :

$$\begin{aligned} 2nkT_e^2 &= 2n \frac{B}{T} T_e^2 \\ &= 2n \frac{B}{\alpha^2 B_{\max}^2} \\ &= n \frac{2}{\alpha^2 (B_{\max} T)} \frac{B}{B_{\max}} < n \frac{2}{\alpha^2 (B_{\max} T)} \end{aligned}$$

Par exemple, pour  $B_{\max} T = 3000$ , on trouve  $\alpha^2 (B_{\max} T)/2 = 2940 = 2^{11,5}$ .

Le codage de l'incrément  $2nkT_e^2$  se fait sous la forme :

$$2nkT_e^2 = n (a_0 2^0 + a_1 2^{-1} + a_2 2^{-2} + \dots + a_n 2^{-n} + \dots)$$

Si on utilise 15 bits, la précision de programmation de la bande est donnée par :

$$\frac{2}{\alpha^2 (B_{\max} T)} \cdot \frac{B}{B_{\max}} = 2^{-14}$$

Cela donne dans le cas  $B_{\max} T = 3000$ , une précision de  $B/B_{\max} = 18\%$ , ce qui est médiocre.

L'utilisation d'un additionneur-accumulateur de 24 bits permet d'atteindre dans le cas considéré 0.08%, ce qui est excellent.

La valeur maximale de  $2nkT_e^2$  vaut  $2/(\alpha^2 (B_{\max} T))$ , soit  $2^{-11,5}$ .

Le registre stockant  $2nkT_e^2$  peut donc se contenter de 12 bits de moins que les additionneurs-accumulateurs, si<sup>8</sup> on se limite aux pentes positives. Il faut autant de bits si on veut programmer des pentes négatives.

Le calcul du sinus et du cosinus peut se faire à l'aide d'une table. Une table de 256 mots ( $2^8$ ) permet un adressage par pas de  $1.4^\circ$ . Cela peut être suffisant si une mémoire rapide 512 mots de 8 bits n'est pas disponible.

La Figure 2.3/A montre la taille des divers registres utilisés.

Les composants les plus critiques sont :

- Les Additionneurs-accumulateurs 24 bits haute vitesse, et
- les Mémoires 256 ou 512 x 8 haute vitesse.

Les limites de programmabilité de cette solution et de la solution précédente ne sont pas les mêmes.

Avec la génération directe des voies I et Q, nous sommes limités en bande et en durée du chirp (en bande par la fréquence d'échantillonnage et en durée par la capacité des mémoires).

Avec la génération par la phase, nous ne sommes limités que par la bande. Il y a aussi une limite en durée (dépend du nombre de bits des additionneurs) mais cette limite est très au-delà du besoin.

#### 2.4. GÉNÉRATION DIRECTE SUR PORTEUSE

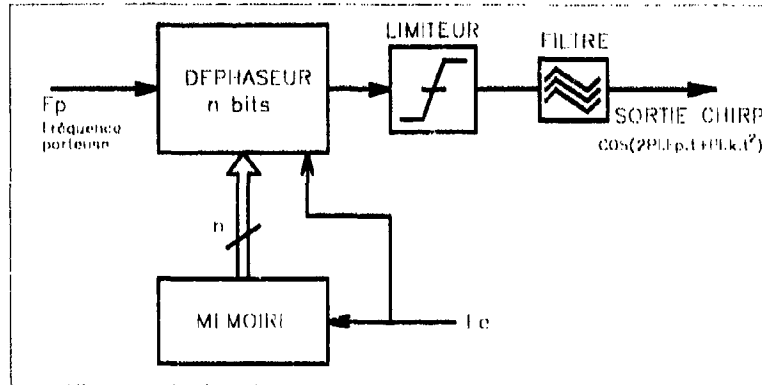
Ce type de solution utilise un déphaseur n bits. La phase  $\theta(t) = nkt^2$  est échantillonnée à une fréquence  $f_s = k \cdot 2B$  ( $k > 1$ ), puis codée sur n bits entre -n et n. La phase codée commande le déphaseur qui module donc une porteuse.

Ce principe est illustré sur la Figure 2.4/A. La fréquence porteuse peut être une fréquence intermédiaire qui serait ensuite transposée à la fréquence d'émission ou plus simplement la fréquence d'émission directement. L'aspect filtrage pourrait être déterminant dans le choix entre ces 2 solutions.

Les performances de cette solution dépendent des caractéristiques du déphaseur .

- précision de phase,
- temps de commutation,
- erreurs d'amplitude,
- parasites de commutation (synchronisation des bits).

Cette solution peut être attrayante pour un nombre de bits faible (inférieur à 4 bits environ).



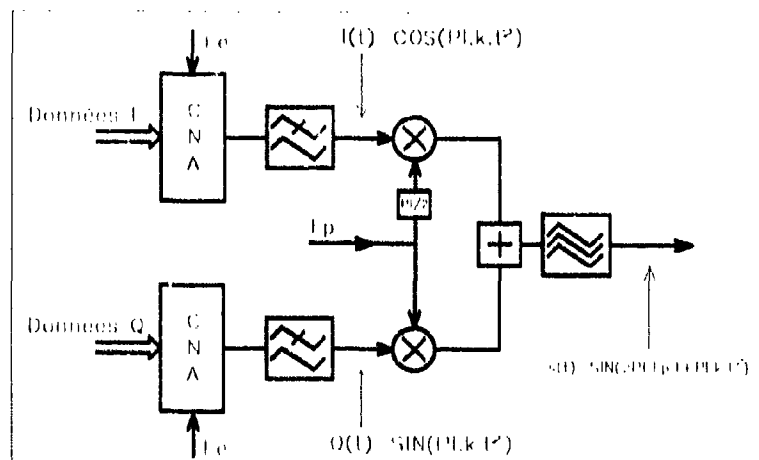
GENERATION DIRECTE SUR PORTEUSE AVEC UN DEPHASEUR  
Figure 2.4/A

### 3 - IMPERFECTIONS DES CHIRPS NUMERIQUES

#### 3.1. INTRODUCTION

Dans cette section, nous étudions les imperfections des solutions faisant appel à la génération des deux signaux vidéo I et Q utilisés ensuite pour attaquer un modulateur BLU pour la translation du chirp à fréquence intermédiaire. Le synoptique de ces solutions est rappelé sur la Figure 3/A.

On peut distinguer les imperfections dues aux convertisseurs et les imperfections dues au modulateur.



SYNOPTIQUE DES SOLUTIONS A GENERATION DES SIGNAUX I ET Q  
Figure 3/A

### 3.2. IMPERFECTIONS DUES AUX CONVERTISSEURS

Les imperfections dues aux convertisseurs sont principalement le bruit de quantification et les glitches.

Le bruit de quantification est dû à l'utilisation d'un nombre fini de niveaux pour coder le signal. Le bruit de quantification peut être divisé en un bruit d'amplitude et en un bruit de phase. Le bruit d'amplitude peut être négligé car le chirp est limité dans la chaîne émission. Le bruit de phase peut être facilement estimé.

Il vaut environ :  $\phi_{\text{rms}} = 1/(2^n \cdot \sqrt{3})$  (en radians) à la sortie du modulateur, où  $n$  est le nombre de bits de chaque convertisseur.

Par exemple, pour des convertisseurs ayant une précision de 6 bits, on obtient une erreur de phase de  $0.52^\circ$  rms (équivalent à un rapport signal à bruit de 40.8 dB).

Le spectre du bruit de quantification est pratiquement blanc dans la bande  $2F_s$  (en sortie modulateur) où  $F_s$  est la fréquence d'échantillonnage.

Les "glitches" sont les transitoires qui apparaissent pendant les changements de code. Ils sont dûs à des imperfections de synchronisation des bits de commande. Le plus important se produit au changement 1000...0 en 0111...1. Pour les minimiser, les convertisseurs doivent être munis de latches internes.

L'énergie de "glitch" garantie par les constructeurs est de l'ordre de 50 pV-s. L'impact des glitches sur le signal généré est difficile à estimer ; des simulations seraient nécessaires. (Il faut tenir compte du nombre de glitches, de leur amplitude et de leur spectre, tous ces paramètres étant fonction des changements de codes).

### 3.3. IMPERFECTIONS DUES AU MODULATEUR

Les imperfections potentielles d'un modulateur BLU sont les suivantes :

- déséquilibre d'amplitude entre les voies I et Q (dû aux CNA, aux filtres ou aux mélangeurs),
- déséquilibre de phase entre les voies I et Q (dû aux CNA, aux filtres ou aux mélangeurs),
- erreur de quadrature des Oscillateurs Locaux sur les mélangeurs,
- fuite des Oscillateurs Locaux à travers les mélangeurs,
- offset entre les voies I et Q,
- ondulation d'amplitude ou de phase dans la bande (commune aux deux voies ou en sortie FI),
- retard entre les voies I et Q.

Le signal en sortie d'un modulateur idéal aurait comme expression :  $s(t) = \sin(2\pi f_p t + nkt^2)$

La figure 3/B donne l'effet des diverses imperfections considérées en sortie modulateur. La plupart des imperfections ont pour effet de générer un chirp de pente opposée. On a également calculé les exigences sur chaque phénomène pour que les signaux parasites générés soient 45 dB sous le signal utile.

IMPERFECTION	SIGNAL IMPARFAIT	PARASITE GENERE
Déséquilibre d'amplitude	$Q=(1+a) \cdot \sin(nkt^2)$	$\frac{a}{2} \sin(2\pi f_p t - nkt^2)$
Déséquilibre de phase	$Q=\sin(nkt^2 + \phi)$	$\frac{\phi}{2} \sin(2\pi f_p t - nkt^2)$
Offset (ou fuite d'OL)	$Q=\sin(nkt^2) + c$	$c \sin(2\pi f_p t)$
Erreur de quadrature	$Q_L = \cos(2\pi f_p t + \phi)$	$\frac{\phi}{2} \sin(2\pi f_p t - nkt^2)$
Retard entre voies	$Q=\sin(nk(t+d)^2)$	$\frac{nBdt}{1} \sin(2\pi f_p t - nkt^2)$
Ondulation d'amplitude	$I=(1+a \cdot \cos \Omega t) \cos nkt^2$ $Q=(1+a \cdot \cos \Omega t) \sin nkt^2$	$\frac{a}{2} \cos(2\pi f_p t + nkt^2 \pm \Omega t)$
Ondulation de phase	$I=\cos(nkt^2 + \phi \cos \Omega t)$ $Q=\sin(nkt^2 + \phi \cos \Omega t)$	$\frac{\phi}{2} \cos(2\pi f_p t + nkt^2 \pm \Omega t)$

IMPERFECTIONS D'UN MODULATEUR BLU  
Figure 3/B

IMPERFECTION	SPECIFICATION POUR S/P > 45 dB
Déséquilibre d'amplitude	$a < 1,1\%$ (0,1 dB)
Déséquilibre de phase	$\phi < 0,6^\circ$
Offset (ou fuite d'OL)	$z < 5,6 \cdot 10^{-3}$
Erreur de quadrature	$\phi < 0,6^\circ$
Retard entre voies	$d < 36$ ps (pour B = 100 MHz)

IMPERFECTIONS D'UN MODULATEUR BLU  
Figure 3/B (suite)

#### 4 - AMELIORATION DES PERFORMANCES

##### 4.1. INTRODUCTION

Dans cette section, nous discutons des méthodes pour améliorer les performances d'un générateur de chirp numérique.

Deux méthodes sont considérées :

- utilisation d'un multiplicateur de fréquence pour accroître la bande d'un chirp,
- utilisation d'un VCO et d'un diviseur de fréquence pour accroître la bande d'un chirp tout en améliorant certaines imperfections dues à la génération numérique.

##### 4.2. UTILISATION D'UN MULTIPLICATEUR DE FREQUENCE

La bande d'un chirp "numérique" est limitée par la rapidité des circuits numériques utilisés : 20 MHz environ en technologie TTL, 100 MHz environ en technologie ECL et 300 MHz environ en technologie AsGa.

Si pour une technologie donnée, on veut encore augmenter la bande, une solution consiste à utiliser un multiplicateur de fréquence. Une multiplication par  $n$  accroît la bande d'un facteur  $n$ .

Cependant, les imperfections du chirp initial sont également multipliées par le facteur  $n$ , ce qui limite l'utilisation du procédé.

Par exemple, pour  $n=2$  les niveaux des parasites du chirp étudiés dans le paragraphe 3 remontent de  $20 \log n$ , soit 6 dB par la seule multiplication.

##### 4.3. UTILISATION D'UN VCO

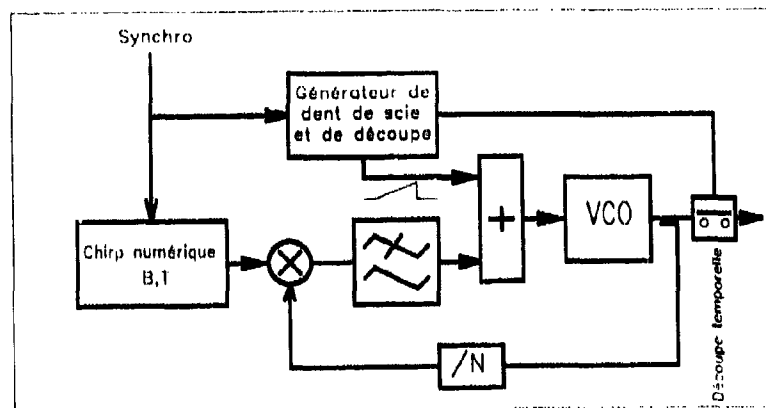
Ce procédé consiste à utiliser un VCO que l'on asservit en phase sur le chirp numérique (voir Figure 4.3/A). Le diviseur par  $N$  permet de multiplier la bande du chirp numérique par  $N$ . Le générateur de dent de scie permet, en pré-commandant le VCO, de réduire les exigences sur la boucle de phase et notamment une bande de boucle faible peut-être utilisée. La découpe permet de couper la sortie VCO en dehors du chirp utile.

Les avantages de cette solution sont déterminantes quant à la réduction des imperfections sur le chirp :

- 1) Le bruit de quantification est filtré par le filtre de la boucle de phase d'où un gain de  $B/(2b_c N)$ ,
- 2) Les chirps parasites (de pente opposée) sont filtrés par le filtre de boucle (sauf pendant une faible durée).
- 3) La fuite d'OL est également filtrée par le filtre de boucle (sauf pendant une faible durée).

L'amélioration apportée sur le bruit de quantification autorise l'utilisation de convertisseurs à nombre de bits plus faible. Le filtrage des chirps parasites par le filtre de boucle nous amène à nous demander si les 2 voies I et Q dans le générateur numérique sont encore nécessaires ou si on peut se contenter d'une seule voie ; cette question nécessiterait une étude plus détaillée.

En conclusion, les améliorations apportées par l'asservissement d'un VCO sur un chirp numérique sont attrayantes. Il n'y a pas de problème de faisabilité. L'utilisation de ce procédé (même pour  $N=1$ ) dépendra des performances qui peuvent être obtenues avec les solutions classiques.



VCO ASSERVI SUR UN CHIRP NUMERIQUE  
Figure 4.3/A

## 5 - CORRECTIONS D'AMPLITUDE ET DE PHASE

### 5.1. INTRODUCTION

Parmi les distorsions que subit le signal, certaines, peuvent ou même doivent être corrigées. Ce sont les distorsions d'amplitude résultant de l'échantillonnage avec maintien et également les distorsions d'amplitude et de phase apportées par certains filtrages critiques dans la chaîne radar.

Certaines de ces corrections pourraient être effectuées dans le traitement des échos radar, mais cette solution est plus complexe que la correction des distorsions au moment de la génération du signal.

Les corrections peuvent être faites, soit par filtre correcteur analogique, soit au niveau de la génération du chirp, soit par dispositif spécial placé en série après le générateur chirp.

Ci-après, on ne discute que les deux derniers types de correction auxquelles on peut demander une grande flexibilité.

### 5.2. CORRECTION AU NIVEAU DE LA GENERATION

Pour les générateurs de chirp basés sur la génération directe des signaux, les corrections d'amplitude et de phase sont prises en compte, dans le calcul des échantillons à stocker dans les mémoires attaquant les convertisseurs.

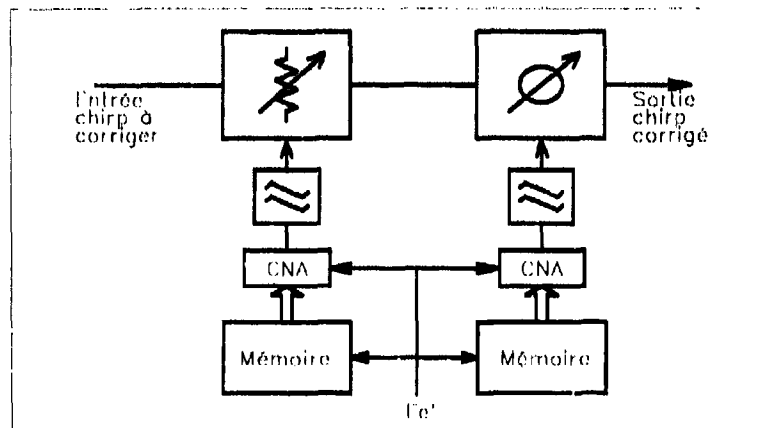
Pour les générateurs basés sur la génération de la phase, seule la correction de phase peut être prise en compte. La correction de phase se fait par changement périodique de l'incrément contenu dans le registre R de la Figure 2.3/A. Le changement d'incrément se fait à un rythme très inférieur à la fréquence d'échantillonnage, car les erreurs corrigées sont très lentes. Le nombre de bits des additionneurs-accumulateurs doit être suffisant pour que la correction soit précise.

### 5.3. DISPOSITIFS DE CORRECTION

Les corrections d'amplitude et de phase peuvent se faire en utilisant un atténuateur et un déphaseur commandables. Les amplitudes de correction sont faibles ; des composants analogiques sont donc préférables. On propose le schéma de principe de la Figure 5.3/A.

Le choix de la fréquence d'échantillonnage  $F_e$  dépend du spectre des erreurs à compenser. Par exemple, si on suppose un nombre maximal de périodes que les erreurs peuvent avoir pendant la durée du chirp de 5 et une durée d'impulsion de 30  $\mu$ s, la fréquence d'échantillonnage  $F_e$  doit être de 400 kHz.

Cela ne fait que 12 échantillons à stocker. Les circuits de commande de l'atténuateur et du déphaseur ne sont donc pas critiques.



DISPOSITIF DE CORRECTION D'AMPLITUDE ET DE PHASE  
Figure 5.3/A

## 6 - EXEMPLE DE REALISATION

### 6.1. DESCRIPTION GENERALE

ALCATEL ESPACE a réalisé une maquette en technologie ECL et AsGa dont les principales caractéristiques sont les suivantes :

- Architecture du type décrit dans le paragraphe 2.2.
- Une seule voie réalisée.
- Taille mémoire totale : 2 048 échantillons de 4 bits.
- Fréquence de fonctionnement jusqu'à 400 MHz.

### 6.2. DESCRIPTION DE L'ARCHITECTURE

Le synoptique de la maquette est présenté sur la Figure 6.2/A.

Le convertisseur numérique/analogique en technologie AsGa fonctionne à 400 MHz. Les données fournies au convertisseur sont obtenues en sérialisant les données de 8 mémoires RAM de capacité 256 x 4 en technologie ECL. La partie mémoire fonctionne donc avec une horloge de  $400/8 = 50$  MHz. Les données des mémoires RAM sont chargées à partir de mémoires PROM lentes dès la mise sous tension de la maquette.

Pour réduire la complexité, seuls 4 bits de codeage ont été utilisés.

Les composants utilisés sont les suivants :

- PARTIE CHARGEMENT

4	PROM 2K*8	:	2716
8	convertisseurs TTL ECL	:	F100124
2	convertisseurs ECL TTL	:	F100125
1	compteur diviseur	:	F100136
1	bascule	:	F100131
1	multiplexeur	:	F100171
1	OR/NOR	:	F100101

Cette partie consomme environ : 16.6W

- PARTIE ECL

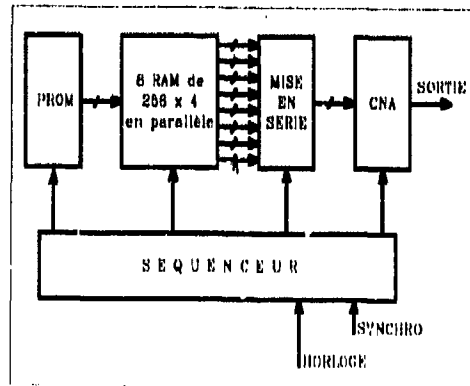
8	mémoires 256*4	:	F100422
3	drivers ; F100113	:	
3	compteurs diviseurs	:	F100136

Cette partie consomme environ : 13.5W

- PARTIE ASGA (Composants TRIQUINT)

2	sérialisateurs	:	TQ1131
1	compteur diviseur	:	TQ1112
1	CNA	:	TQ6112BV

Cette partie consomme environ : 13.6W



SYNOPTIQUE DE LA MAQUETTE  
Figure 6.2/A

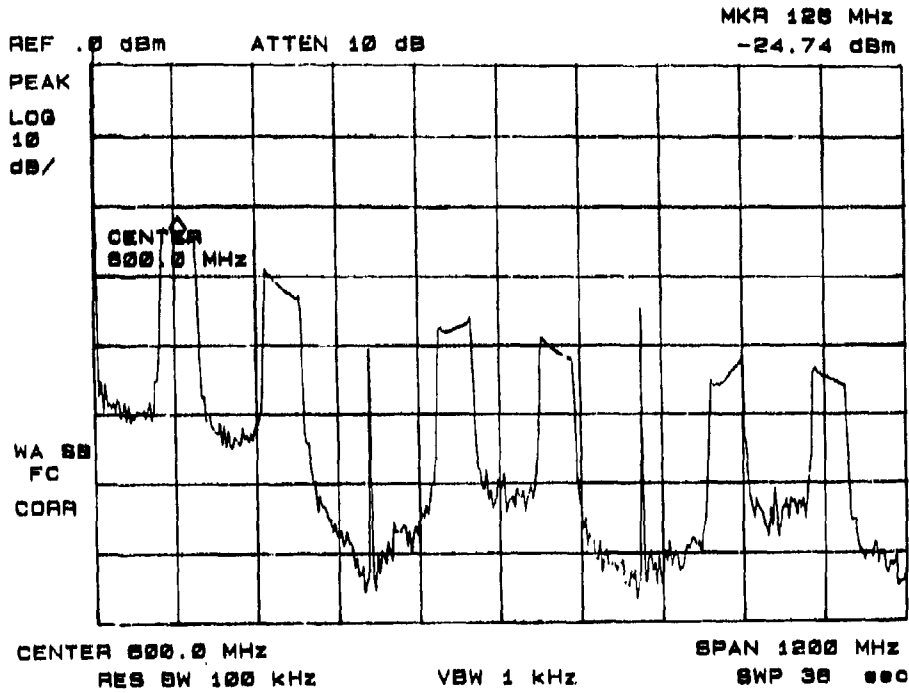
La consommation totale de la maquette est donc de 43.6W.

**6.3. EXEMPLE D'UTILISATION ET DE RESULTAT**

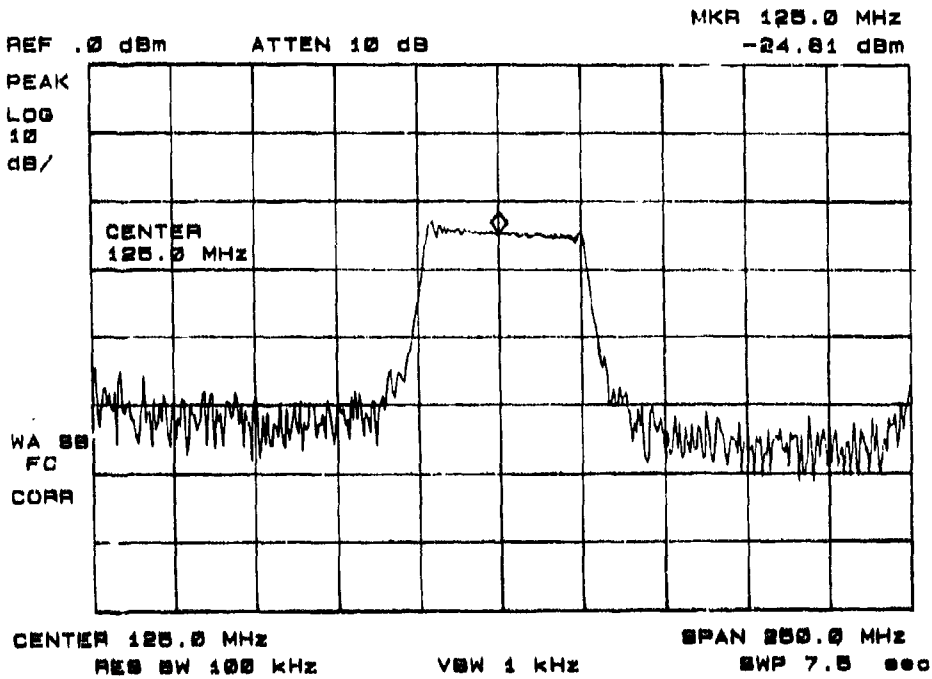
L'exemple présenté permet la génération d'un chirp centré sur 125 MHz, de bande 50 MHz et de durée 5  $\mu$ s. La fréquence d'échantillonnage est de 400 MHz.

La Figure 6.3/A montre le spectre large bande du signal à la sortie du convertisseur. Le résultat obtenu est conforme aux prédictions théoriques avec la périodicité du spectre et la modulation d'amplitude en  $\sin x/x$  résultant de l'échantillonnage avec maintien.

La Figure 6.3/B montre le spectre du signal centré sur la fréquence de 125 MHz (spectre désiré).



SPECTRE LARGE BANDE  
Figure 6.3/A



SPECTRE AUTOUR DE 125 MHz  
Figure 6.3/B

## REAL-TIME ADAPTIVE RADIOMETRIC CORRECTION FOR IMAGING RADARS SYSTEMS

Joao R. Moreira & Winfried Poetzsch

German Aerospace Research Establishment (DLR)

Institute for Radio Frequency Technology

8031 Weßling, FRG

AD-P005 843

### ABSTRACT

This paper presents a new solution of a real time radiometric image correction that also minimizes the quantization and saturation noise introduced by the process of analogue-to-digital (A/D) conversion of raw data of coherent and non-coherent imaging radar systems. The implementation of this procedure has been successfully performed with the experimental SAR System (E-SAR) of the DLR.

### 1. INTRODUCTION

In a conventional imaging radar system the backscattered signal is received, downconverted, analogue-to-digital (A/D) converted, formatted and recorded. If this radar system is flown at low altitudes, 1000m for example, the backscattered signal intensity will vary too widely within the range swath, so that a high signal dynamic range of the radar system is necessary.

The dynamic range, normally limited by the A/D-converter, can be expanded by varying the gain of the IF-section, so that the variance of the signal before the A/D-conversion remains constant and is independent of range. The choice for the value of the signal variance for a quantization with a minimum distortion has been studied by J. Max (Ref. 1) and G. Gray et al (Ref 2).

The variation of the IF-section gain compensates the range dependent decrease of the backscattered signal power. This decrease, described by the radar equation, depends mainly on the target range, type and incidence angle and on the antenna pattern. A typical gain curve for this compensation begins with a small value and increases with range.

As this gain curve cannot be exactly determined in advance, due to inaccurate information about the terrain characteristics, this paper discusses a method to generate it precisely in real-time. This method will be called radiometric image correction (RIC).

### 2. RIC-SYSTEM IMPLEMENTATION IN A SAR-SYSTEM

Figure 1 shows the implementation of the RIC-system in a Synthetic Aperture Radar (SAR) with I/Q-detection. The backscattered signal is received, downconverted and range compressed. At the IF-section the signal amplitude will be modified by the gain or correction curve. The correction curve is realized by two devices: a high speed and a low speed attenuator.

By a high speed attenuator the fast variation of the correction curve is generated (normally called sensitivity time control or STC).

By the low speed attenuator we can adjust the optimum operating point or attenuation bias for the high speed attenuator. The low speed attenuator is normally called automatic gain control or AGC.

The IF-signal is then demodulated, by the I/Q-detector for example, and A/D-converted. The RIC-system, that controls the AGC- and STC-attenuators, reads the converted raw data and calculates the signal intensity as a function of range over a given integration time. The integration time can be varied from several seconds up to some minutes.

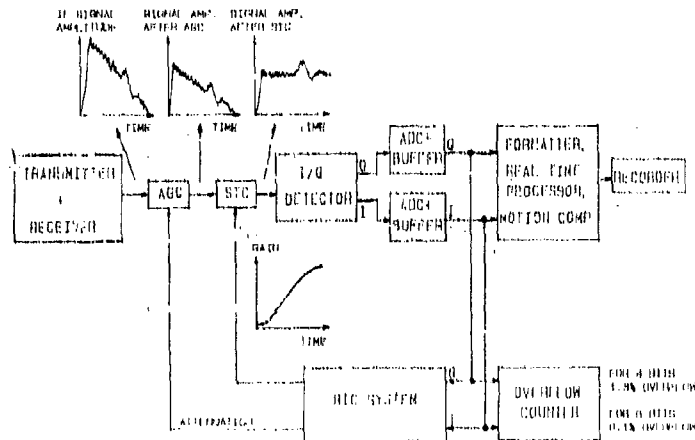


Figure 1. Implementation of the real-time radiometric image correction (RIC)

### 3. GENERATING THE STC-CURVE

Figure 2 shows the block diagram of the adaptive control system for the generation of the STC-correction curve. The whole loop consists on a STC-attenuator, the A/D-converters, a signal summation to estimate the echo signal intensity, a comparison of the estimated signal intensity with a reference level given in Ref. 1 and 2, an ideal on-off relay, an integrator and a D/A converter that generates the control signal for the analogue STC-attenuator.

The RIC-system realizes this loop for all the range bins so that we obtain a attenuation curve as a function of time or range at the control input of the STC-attenuator.

The loop parameter to be changed at each iteration "k" is the limit "d" of the ideal on-off relay. The ideal on-off relay is easy to be implemented by software and keeps the system stable with a known ripple (Ref. 3). The ripple amplitude at the output  $a(k)$  of the control system is given by the limit "d" of the on-off relay. The adaptive control will adjust the limit "d" with a large value for the first iterations so that the output converges fast to the given reference value. The limit "d" becomes smaller with the number of iterations in order to reduce the ripple amplitude. Finally we get a residual amplitude error of less than 1.0 dB.

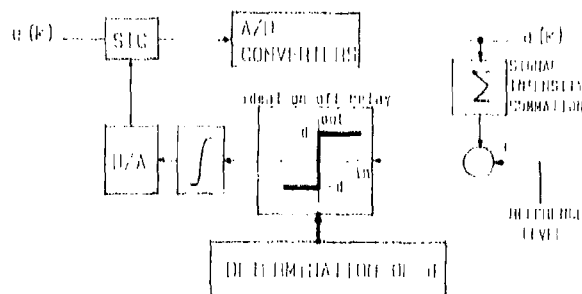


Figure 2. Nonlinear adaptive control system for the STC curve generation

### 4. GENERATING THE CORRECTION CURVE

The correction curve consists of the STC-curve and the AGC-level. A detailed block diagram of the STC-curve generation is shown in Figure 3. The algorithm can be explained as follows:

1. An initialisation of the RIC-system is made and a constant IF-section gain is programmed.

2. The calculated signal intensity curve as a function of range (see Figure 3) is filtered using moving average.
3. The adaptive control algorithm calculates the STC-curve that is also filtered using moving average. The steps "2" and "3" will be repeated until the given number of iterations of the control system is complete.
4. The operation point of the STC-attenuator is checked. If the operation point of the STC-attenuator is optimum, the AGC-level will not be modified. The operator receives a message reporting the success of the radiometric correction. The STC- and AGC-data will be recorded for later analysis. If no range compression has been made, the STC-data will be also used for calculating the weighting of the reference function for digital range compression. If the operation point of the STC-attenuator is not optimum, a new AGC-level is calculated and programmed. A new STC-curve must be derived and steps "2", "3" and "4" are repeated.

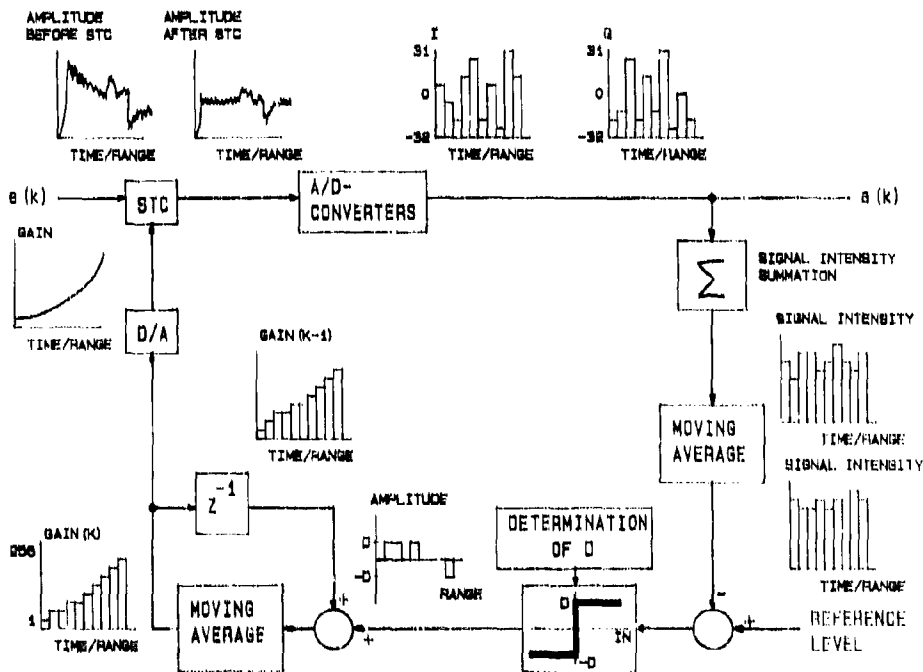


Figure 3. Detailed block diagram of the STC-curve generation.

## 5. RESULTS

The implementation of the RIC-System has been successfully performed with the experimental C-Band SAR-system during flights in October 1988. The SAR-system uses an I/Q-detection with two 6-bit A/D-converters which each run at 100MHz and have a dynamic range of 25dB at 40MHz or an effective bit number of 4 (see Ref. 4). As a system dynamic range of more than 40dB was required, a STC-attenuator with approx. 15dB range was employed. The hardware of the RIC-system consists of an interface to the A/D-converter buffers, a microprocessor system that calculates the STC- and AGC- attenuations, an 8 bit-D/A-converter for controlling the analogue STC-attenuator and a digital 7 bit-attenuator for the AGC-function (Ref. 5,6 and 7).

Figure 4 shows an example of a STC-curve generation. The aircraft (Do-228) flew in the up-down direction and on the left side of the image. Hence the left side of the image corresponds to near range and the right side corresponds to far range.

The upper part of the image is processed without STC, this means with a constant STC curve. In this case the A/D converters have a high saturation rate in near range and produce a high quantization noise

in far range. In mid range the A/D converters work with minimum conversion noise. The averaged signal amplitude is shown in the upper curve as a function of slant range.

In the middle of the image the generation of the STC-curve with 7 iterations was started. Here the RIC-system has averaged 32 range lines within 3 seconds for each iteration that corresponds to a strip in the image. The lighter strip represents the initialisation and the next strips correspond the first, second, ... iterations.

After carrying out the seven STC iterations one obtains the corrected image shown in the bottom part of the image. The lower curve shows that the averaged signal amplitude remains constant with range. The residual signal variance error of less than 1.0dB at the inputs of the A/D converters was also obtained.

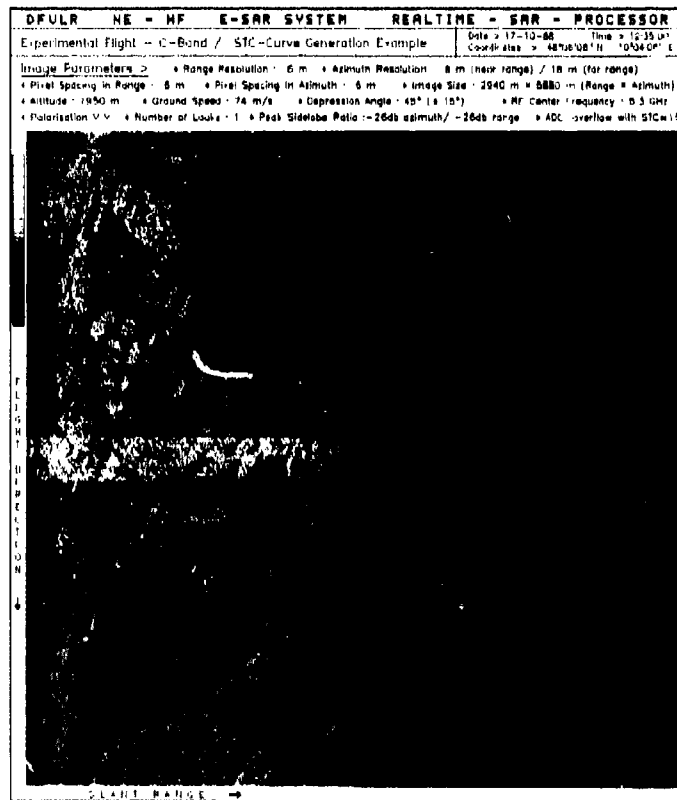


Figure 4. An example of the STC-curve generation

As the A/D-converters used have an effective number of 4 bits, we get from Ref. 2 the following conclusions:

- Optimum K. K is defined as the saturation level of the A/D-converter to the input rms voltage ratio. For a 4 bit A/D-converter we have the minimum A/D-conversion noise by  $K = 2.5$ .
- Saturation ratio. By  $K = 2.5$  we obtain a normalized quantization noise power of  $1.05E-2$ , a saturation noise power of  $0.24E-2$  and a total noise power of  $1.29E-2$ . Considering the probability density function of the radar signal before the A/D-conversion as a normal distribution, we get for  $K = 2.5$  a saturation ratio of 1.3%.

Figure 5 shows the histogram in far range of the image without STC (upper part of figure 4). The histogram was calculated from 1024 samples of the A/D-converter. The standard deviation is 7.5 and the saturation level of the A/D-converter is 32 considering 64 steps of the A/D-converter. The overflow frequency is 1 sample that corresponds to 0.1%. The ratio K for this case is 4.3. The A/D-converter has

a small excursion, works below its optimum operating point and causes a high conversion noise due to high quantization noise.

Figure 6 shows the histogram in near range of the image without STC (upper part of figure 4). The histogram was also calculated from 1024 samples of the A/D-converter. The standard deviation is 23.1 considering 64 steps of the A/D-converter. The overflow frequency is 329 samples that corresponds to 32%. The ratio K for this case is 1.4. The A/D-converter has a large excursion, works over its optimum operating point and causes a high conversion noise due to high saturation noise.

Figure 7 shows the histogram in near range of the image with STC (bottom part of figure 4). The histogram for the whole range swath is practically the same, so that we can take this example as a general one. The histogram was also calculated from 1024 samples of the A/D-converter. The standard deviation is 12.7 considering 64 steps of the A/D-converter. The overflow frequency is 14 samples that corresponds to 1.4%. The ratio K for this case is 2.5. This result matches with Ref 2, so that the A/D-converter works at its optimum operating point and causes minimum conversion noise.

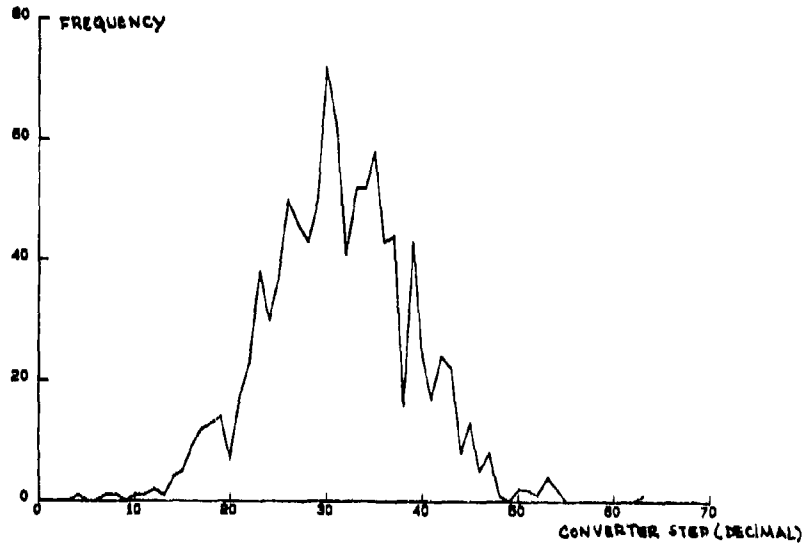


Figure 5. Histogram of the A/D-converted signal without STC in far range.

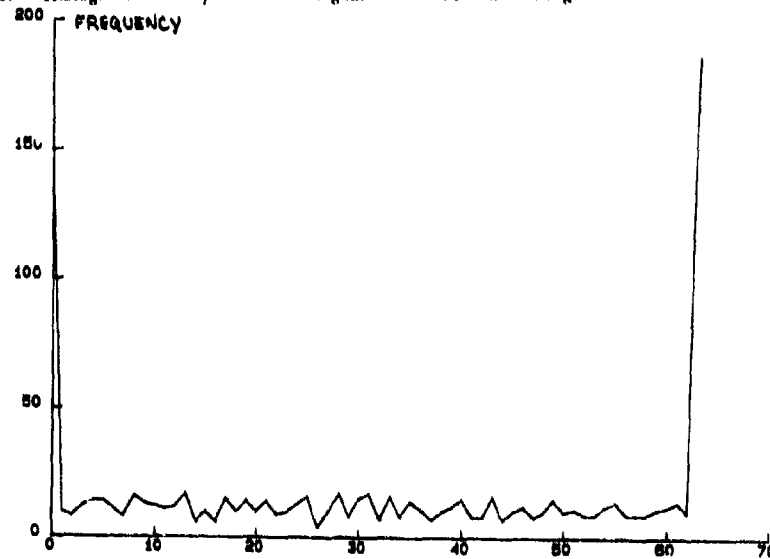


Figure 6. Histogram of the A/D-converted signal without STC in near range.

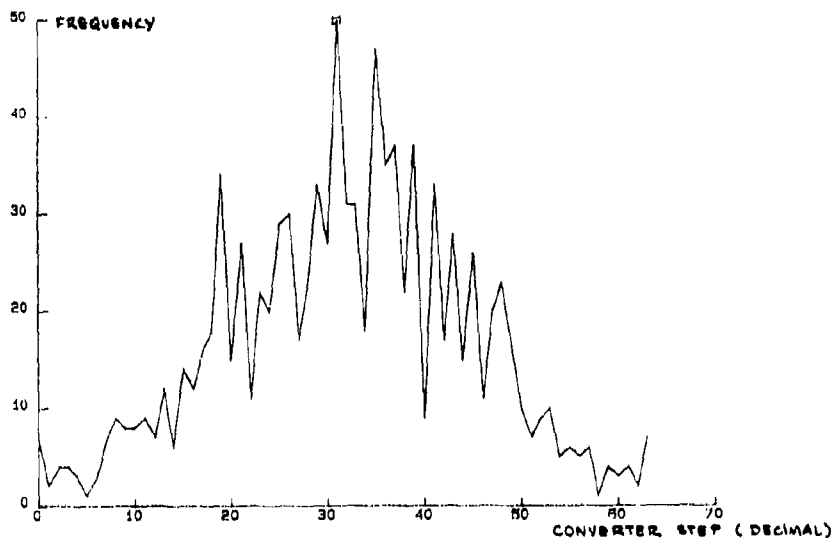


Figure 7. Histogram of the A/D-converted signal with STC in near range.

## 6. REFERENCES

- [1] Max, J.: Quantizing for Minimum Distortion. IRE Transactions on Information Theory, vol. PGIT-6, 1960.
- [2] Gray, G. et al: Quantization and Saturation Noise Due to Analogue-to-Digital Conversion. IEEE Transactions on Aerospace and Electronic Systems, Jan. 1971.
- [3] Weber, W.: Adaptive Regelungstechnik I und II. Muenchen, Wien: P. Oldenburg Verlag, 1971.
- [4] Moreira, J.: Error Analysis of SAR Hardware. European Space Agency, Technical Translation ESA-TT-1024, March 1987.
- [5] Moreira, J.: Experimentelles SAR-System; Das STC/AGC-System. DFVLR MEMO, 12.06.1986.
- [6] Spies, U.: Hard- und Software fuer das AGC/STC-System des experimentellen DFVLR SAR. DFVLR IB Nr.:551-5/87, 24.04.87.
- [7] Poetzsch, W.: Software fuer das AGC/STC-System des experimentellen DFVLR SAR. DFVLR IB in preparation.

## 7. ACKNOWLEDGEMENTS

The author wish to thank Mr. U. Spies for the hardware design and Mr. R. Horn for the interfacing with the experimental SAR.

## DISCUSSION

### N.Lannelongue

You are presenting the phase array performance as a main limitation for superresolution. Can you give us more detail in the performance requirements for the phased array (beam shape, number of cells, phase and amplitude beam calibration, residual coupling etc.)?

### Author's Reply

Required accuracy depends on separation of targets and number of channels. For the given example of 8 elements 20° phase errors can be tolerated for targets separated 1/2 beamwidth. For closer targets accuracy requirements increase rapidly.

### C.J.Baker

What is the performance of the superresolution algorithms when illuminating targets made up of many points scatterers in a residual background of correlated non-gaussian clutter?

### Author's Reply

Scattering points separated less 1/10 beamwidth do not matter. For seeker heads superresolution as a glint error reduction technique is important. Correlated non-gaussian noise affects significantly target number determination, not very much angle estimation. Field experiments with clutter will be done in the future with the FFM ELRA system.

**CONCEPT FOR A SPACEBORNE SYNTHETIC APERTURE RADAR (SAR)  
SENSOR BASED ON ACTIVE PHASED ARRAY TECHNOLOGY**

by

A. Brunner, E. Langer  
Siemens AG Munich,  
Telecommunication/Sensor Conductors  
SIR FE 25  
Landshuterstr. 2  
D-8044 Unterschleissheim  
Federal Republic of Germany

and

H. Öth, K. H. Zeiler  
DLR Oberpfaffenhofen,  
Institute for Radio Frequency Technology

AD-P005 844

Abstract

For surveillance with spaceborne remote sensing systems quite often a spatial resolution of 1 m or less is requested. In the paper a SAR concept is presented for a low flying satellite.

Assuming a peak power of 5 kW and using active phased array technology a swath width of about 30 km at an off nadir angle of 35° is considered to be reasonable. A wide swath width combined with a high resolution can only be achieved if we use a fixed antenna beam for transmitting which illuminates the whole swath width, while a very narrow antenna beam scans the swath in the manner as the reflected pulse travels from the near range to the far range across the swath width.

For the active antenna system a high efficiency of the transmit/receive-modules, low losses in the feeding network and doubly polarized radiating elements with high polarization purity are considered of utmost importance.

An antenna concept based on the slotted waveguide principle is described: for an aperture of 10 m x 2 m 38400 doubly polarized radiating elements and 3840 active phase shifter modules are proposed.

The technology of the GaAs-based modules with special respect to space requirement resulting in an economic solution of the power generation below 3 W per module is described.

Keywords

Synthetic aperture radar, SCAN-SAR, high resolution, active phased array, multi-polarization, slotted waveguide array, subarray, active T/R-module, SPDT-switch, GaAs-amplifier.

1. Introduction

Spaceborne SAR systems have gained enormous attention after the short but successful L-band SAR operation of SEASAT in 1978 /1/. Shuttle-borne SAR systems were launched the first time /2/ in 1981 (SIR-A) and a second time /3/ in 1984 (SIR-B). The next shuttle-borne SAR systems /4, 5/ are planned for 3 missions to be launched in the period between 1991 to 1994. These will be the Radar Lab Missions (SIR-C/X-SAR).

SEASAT, SIR-A and SIR-B used horizontal polarization and L-band. The swath width was approximately in the order of 100 km to 40 km and the spatial resolution around 25 m to 40 m. The main differences between the previous three projects were the off nadir angles (SEASAT 20°, SIR-A 47°, SIR-B 15° to 60° adjustable), coming from the different applications. SEASAT was ideal for oceanic research, due to the strong radar returns at 20° off nadir. SIR-A was land application oriented (enhancement of terrain structures, less sensitive against geometric layover) and SIR-B could be optimized to all disciplines (adjustable off nadir angle).

SIR-C/X-SAR will introduce new capabilities in spaceborne SAR sensors. It will incorporate multifrequency, multipolarization and variable off nadir angle. The swath width will change between 15 km and 100 km depending on the chosen parameters. Geometric resolution will be around 25 m to 30 m.

All these mentioned spaceborne SAR sensors for civil applications were limited in power, data rate, available technology and attitude control accuracy of shuttle. In the paper some ideas will be discussed how to achieve a spaceborne SAR sensor with higher spatial resolution and a reasonable swath width. The discussion will concentrate on the antenna and its distributed transmit/receive modules.

2. System Considerations for a Low Flying Satellite-borne High Resolution SAR

2.1 SCAN-SAR principle

It is a well known fact, that SAR systems have conflicting requirements with respect to high spatial resolution and of a large swath width and one usually has to make a compromise for a platform flying at a specified altitude with a given speed.

Reasons for these system limitations are, on the one hand, the need for a physically short antenna (in flight direction) for a high resolution and, on the other hand, the need to suppress range ambiguities. A short antenna illuminates a large area on the ground and, therefore, the reflected radar signals are spread over a large Doppler frequency band. The Nyquist theorem requires a sampling rate (pulse repetition frequency) larger than the Doppler frequency. For a satellite altitude of 250 km and an off nadir angle of  $35^\circ$  the real antenna aperture needed for a SAR system amounts to at least 1 m to 2 m. The resolution of 1 m (1 look processing) in azimuth leads to a real aperture length of 2 m. For the same spatial resolution in range a pulse length of 2,4  $\mu$ sec with a compression factor of 600 is necessary. This swath width would be nearly 30 km and the PRF about 8 kHz. S/N computations show that for the assumed peak power of 5 kW the antenna gain needs to be increased.

A solution to achieve this without reducing the swath width is to illuminate the whole swath in the transmit mode, but to scan in elevation (range) with a very narrow beam at the same speed as the pulse travels from the near range to far range part of the swath. In order to achieve the narrow scanning beam for reception, antenna aperture dimensions of 2 m in azimuth and 10 m in elevation are assumed. Fig. 2.1 shows a sketched configuration, fig. 2.2 the traveling wave front for the transmit and the scanning receive mode.

To simplify the system discussion the off nadir angle of the transmit antenna pattern at the mid swath position will be assumed to be constant ( $35^\circ$ )\*.

The characteristics of such a SAR system are summarized below

frequency	9,6 GHz
Antenna dimension	in range 10 m in azimuth 2 m.

Transmit pattern in elevation:

Beamforming amplitude and phase distribution in order to suppress sidelobes and to compensate for near range/far range S/N differences. Half power beamwidth approx.  $4,5^\circ$ .

Receive pattern in elevation:

No amplitude taper across the aperture, but phase steering-capability for a beam shift of  $\pm 2,3^\circ$ . The 3 dB-beamwidth is  $0,16^\circ$ .

Transmit/receive pattern in azimuth:

Constant amplitude and phase distribution, 3 dB-beamwidth is  $0,8^\circ$ .

Antenna gain, transmit mode	38 dB
receive mode	53 dB
Peak power	5 kW
Pulse length	2,4 $\mu$ s
Pulse compression factor	600
Pulse repetition rate (PRF)	8 kHz
Chirp bandwidth (RF-bandwidth)	200 MHz
Swath width single polarization	30 km
dual polarization	15 km

A/D conversion 2 bit in-phase (I) and 2 bit in-quadrature (Q). The radiometric resolution depends strongly on the back scatter coefficient  $\sigma^0$ , on pixel size and, of course, on speckle.

Fig. 2.3 shows the influence of the signal to noise ratio for 1 look, 2 looks, 4 looks and 8 looks operation.

## 2.2 Multiple polarization

The PRF is 8 kHz for each polarization. This means, for simultaneous quad-polarization operation, an interleaved 16 kHz PRF scheme will be used. Naturally the higher PRF reduced the swath width from 30 km to 15 km in order to avoid range ambiguities. Dual polarization means for example VV (transmit/receive) and VH on one pulse while on the next pulse HH and HV are selected. This quad-polarization scheme implies 1 transmit and 2 receive channels. The transmit channel is changing its polarization with each pulse, while the receive channels are vertically and horizontally polarized.

\* The electronic beam steering capability could be used for the transmit and receive pattern in order to gain a variable mid swath position (off nadir angle). This would require a flexible (matched) PRF.

In case of 1 transmit and 1 receive channel only, the interleaved pulsing scheme will be about 32 kHz for quad-polarization. In this case the swath width will be reduced to 7.5 km.

It should be mentioned that the high sampling rate in azimuth (about 4000 per sec.) results in a fairly low bit number needed for the A/D converter (2 bit for I, 2 bit for Q). Nevertheless the data rate for single polarization and swath width of 30 km (1 m resolution) results in a data rate of about 1 Gbit/s. In the case of the quad-polarization mode the data rate doubles to 2 Gbit/s (15 km swath width or 7.5 km swath width in case of 1 receive channel).

These very high data rates show the necessity of data reduction or data compression schemes. Even onboard realtime processing helps only in the case of multilook operation, not relevant here. The data rate then reduces with the inverse value of the look number.

### 3. Double Polarization Phased Array Antenna Concept

#### 3.1 Radiator element principle

The antenna aperture of 2 m x 10 m has to be filled with radiator elements about  $2/3 \lambda$  apart from each other. With a square lattice of 20 inches distance (0.64  $\lambda$  at 9.6 GHz) 50,000 radiator elements would be necessary for horizontal as well as for vertical polarization. In order to avoid 50,000 active modules with phase shifters, subarrays must be formed. Since in the azimuth plane a beam of 0.8° half power beamwidth has to be steered less than 1° several, e.g. 10 radiator elements can be fed and steered by one active module. This would lead to "only" 5000 active modules, of which everyone has to generate 1 W power in order to achieve 5 kW system peak power. Additionally the possibility of using an economic series fed 10-element-subarray is offered. A simple series fed antenna subgroup is based on the slotted waveguide principle.

A very important fact for the choice of the radiator elements is the requirement of using horizontal and vertical polarization in transmit and receive path. In this way the 4 different transmit/receive operations (horizontal/horizontal, horizontal/vertical, vertical/horizontal, vertical/vertical) yield further information about the scanned ground area. The additional information quality depends on the polarization purity of the radiator elements. Therefore rectangular orthogonally slotted waveguides with their well defined fields and currents are proposed. The second high performance factor of the slotted waveguides is their low loss behavior.

Fig. 3.1 shows the principle of the double polarization slotted waveguide array. The vertical polarization is radiated by the horizontal slots on the broadside of the rear waveguides. The coupling factor and therewith the amplitude distribution along the radiating waveguide can be adjusted by the distance of the slots from the centre line on the broadside. The horizontal polarization is radiated by the vertical slots on the small side wall of the front waveguides. These slots are derived from the alternately inclined slots in the small side wall of waveguides. Since undistorted vertical slots of that kind do not radiate, a small cylindrical post is introduced near the slot center which causes the field lines to cross the slot. The coupling factor can be set by the diameter or the depth of the post inside the waveguide. The post on the alternate side of the slots corresponds to the alternate inclination of conventional small-side slots. An inclination of the slots would reduce the polarization purity.

The slotted waveguide subarrays are resonant types and fed from the rear near one end. They are about 25 cm long and have 10 slots. This corresponds with an inside waveguide broad wall dimension of 20.0 mm, which is responsible for the waveguide wave length and the slot distance in flight direction. The waveguide distance in the orthogonal plane is about 21 mm. The feed lines of the horizontally and vertically polarized element output come from the polarization switch, which is operated electronically to select the different polarization modes.

#### 3.2 Array structure

The double polarization subarray consisting of two 10-slot waveguides is the smallest building block of the array antenna. The 20 m<sup>2</sup> array aperture therefore needs 3840 subarrays of them and 3840 active modules. That means, one module has to generate 1.3 W RF power. There are many possibilities for the feed system and the combination to subpanels. One is shown in fig. 3.2. The output of the 3840 polarization switches are attached to the 3840 active modules. It seems economic for the active module to include the polarization switch as an integrated part in the same way as it includes the transmit/receive switch for decoupling of HPA and LNA. If the co- and cross-polarization components reflected from the ground have to be received simultaneously, the active modules and the power divider system would be necessary twice, which would be bulky, heavy and expensive. The next step in combining the subarrays is a power divider for 24 modules in the elevation plane. The 24 elements cover 0.5 m out of the 10 m elevation dimension. 160 power dividers of this type are necessary. Since the sidelobe level of the elevation plane should be below -20 or -25 dB the power distribution over the aperture must be tapered. Therefore, either the 20 power dividers along the 10 m-dimension are tapered and not identical or easier they are identical and the attenuator pads in the active

modules can be set to different values. The 160 power dividers either consist of 10 different types with respectively  $2 \times 8$  identical specimens across the 2 m-dimension or they are all identical.

The next step is to feed 8 power divider outputs lying along the azimuth dimension. This nearly 2 m long power divider can be realized in one or two sections depending on the subpanel size. All twenty exemplars of these 1:20 dividers are identical and can deliver a constant amplitude distribution over the 3 m azimuth dimension with high gain, because sidelobe signals in the  $\pm 1^\circ$  direction can be suppressed by processing.

The final 1:20 divider extending over nearly 10 m in elevation also has tapered or constant energy distribution and can be constructed, for instance, in 10 separated one-meter parts which are put together by single or double RF connections.

The 160 power dividers of 1:24 type can be realized economically in series division principle. All the others must operate according to the parallel principle.

### 3.3 Beam steering

The 480 radiator element rows in the elevation plane can be individually steered by the phase shifters of the modules. Thus the  $0.16^\circ$  beam can be exactly positioned within the  $4.6^\circ$  of the swath width. In the transmit case the full  $4.6^\circ$  are covered by defocusing the phase distribution.

The  $0.8^\circ$  beam in the azimuth plane can be steered within less than  $\pm 1^\circ$  for alignment corrections by the 8 phase shifter columns along the 2 m dimension.

## 4. Active T/R-module technology

The basic requirements for active transmit/receive phased array modules (fig. 4.1) including high power amplifier, phase shifter and small signal amplifier are light weight and low power consumption. Therefore new technological solutions and mechanical design are necessary for the T/R-modules, their mechanical supports and cooling. The major drivers for the weight are not the electronic devices themselves like GaAs and Si IC's or discrete components, but the module boxes and the ceramic substrates for the thinfilm circuits with their heavy metallic base plates. In conventional designs these parts weigh 80 to 100 grammes per T/R-module not including support, feeding, controlling and cooling equipment.

Design and material of the module box must be matched to the cooling method. Heat pipes are attractive because of their effective and distributed heat extraction. They can be fully integrated in the module boxes and be designed as one-piece parts. With the optimum heat transfer of heat pipes materials with worse thermal conductivity can be used e.g. metallized ceramics for parts of the module box, to replace the heavy base plates for the hybrid circuits (fig. 4.2). These Cu-Mo-laminates or kovar sheets commonly used to provide an easy handling and assembling of the thinfilm devices, are usually 25...40/1000 inches thick and contribute about 15 to 20 grammes to every T/R-channel. For the thinfilm substrates the usual 25/1000 inches alumina is replaceable by 10/1000 inches alumina or BeO. The latter gives, in addition to the light-weight, an excellent thermal conductivity.

Considering the electronic circuits, most of the components are realizable monolithically in a well proven manner. Small-signal amplifiers SPDT-switches, phase shifters and microwave attenuators with 4...6 bit resolution are available for different frequencies up to Ku-band and higher [9].

More critical is the situation with the high power amplifiers. Though hybrid and monolithic designs with 3 to 5 Watt RF-output and with sufficiently small dimensions are in production, these components have still many problems and cause high cost.

Not less critical is the power consumption of these amplifiers, mainly at X-band and higher frequencies. Because of the low gain of high power GaAs-transistors at these frequencies, the required RF-input power is in the order of 15 to 20 % of the output power. That means 3 to 4 stages with staggered output power, until the input power of the complete amplifier is in the range of the small signal devices used for the signal processing. Despite the Power Added Efficiency of such amplifier is in the order of 20 to 25 %, the total power dissipation of a typical class A X-band amplifier is about 15...20 W for 5 W RF-output with 1 dB compression in the CW-mode. Of course, the smaller the duty factor, the less are the losses, but in practice considerable heat is generated and an uncomfortable high DC current must be managed by the power supply. To overcome this problems at SARs, a smaller RF power per module like 1 to 2 W should be preferred. Such medium power amplifiers can be realized monolithically with a good yield and much better efficiency than high power devices (fig. 4.3). This means that the power dissipation is lower and the DC-gating of the amplifier is simpler. In addition with this minor output power the DC-pulses during the duty cycle are much better to soften by buffer capacitors in the modules.

The accommodation of the active modules behind the radiator elements is easier for this SAR phased-array concept, compared to search and tracking radar phased-arrays, because of the common steering of many radiator elements by one active module. That means, there is more space for every module in the array, the module box can be larger, thus the polarization switch can be integrated (s. fig. 4.2).

An additional advantage is the smaller temperature gradient inside the module box because of the better distribution of the heat sources. That means the individual components operate at lower temperatures, the electrical data show less temperature shifts and the active SAR phased-array is more reliable.

#### References

- /1/ Bernstein, R (Editor)  
SEASAT Special Issue I, J. Geophys. Res., 87(C5), 1982.
- /2/ Cimino, J.B., and C. Elachi (Editors),  
Shuttle Imaging Radar-A (SIR-A) experiment, California Institute of Technology,  
JPL 82-77, 174 pp., 1982.
- /3/ Ford, J.P., J.B. Cimino, B. Holt and M.R. Ruzek,  
Shuttle imaging radar views the Earth from Challenger: The SIR-B experiment,  
California Institute of Technology, JPL 86-10, 135 pp., 1983.
- /4/ Üttl, H., and F. Valdoni,  
The X-SAR science plan, Deutsche Forschungs- und Versuchsanstalt für Luft- und  
Raumfahrt, Mitteilung, 85-17, 160 pp., 1985
- /5/ The Shuttle Imaging Radar-C science plan, California Institute of Technology,  
JPL 86-29, 1986.
- /6/ Jatsch, W.,  
Berechnung und Realisierung von Hohlleiter-Schlitzantennen  
ITG-Fachberichte 99, VDE-Verlag Berlin und Offenburg, 1987.
- /7/ Alexander D.K. et alii,  
A Unique Waveguide Phased Array with Independently Steered Beams  
Polytechn. Institut of Brooklyn, Phased Array Antenna Symposium 1970.
- /8/ Pettenpaul, E. et alii,  
Discrete GaAs-Microwave Devices for Satellite TV Converter Front Ends.  
SIEMENS Forschungs- und Entwicklungsberichte Bd. 13 (1984), Nr. 4
- /9/ Langer, E.,  
Integrierte GaAs-Schaltungen, Schlüsselemente für aktive Phased-arrays  
DGON, Radar Symp. 1986 Proc.

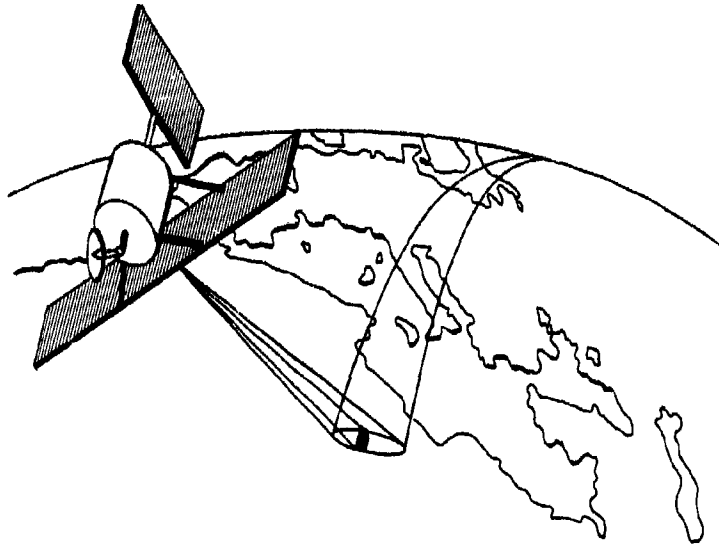


Fig. 2.1 Sketched satelliteborne SAR geometry. Indicated is the wide illuminated transmit antenna footprint and the narrow scanning receive footprint

### Travelling Wavefronts

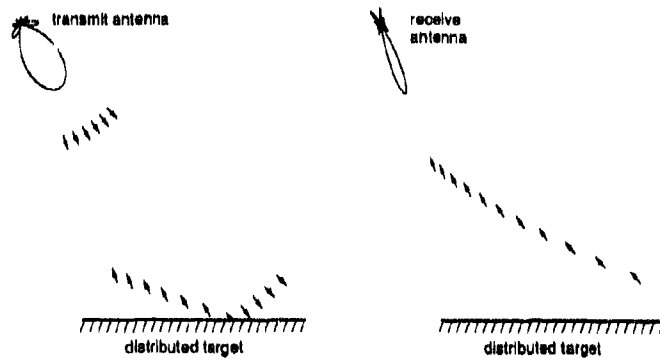


Fig. 2.2 Travelling wavefronts for the transmit and the scanning receive mode. The broad half power beamwidth of the transmit antenna and the narrow beam of the receive antenna are indicated.

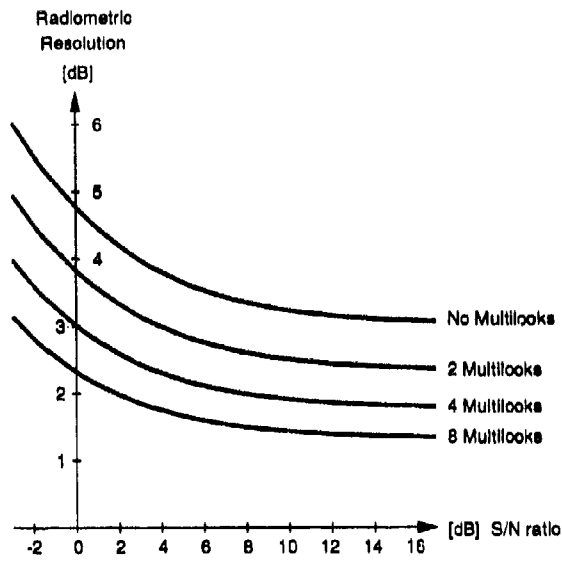


Fig. 2.3 Radiometric resolution as a function of signal to noise with the number of looks (multilooks) as a parameter

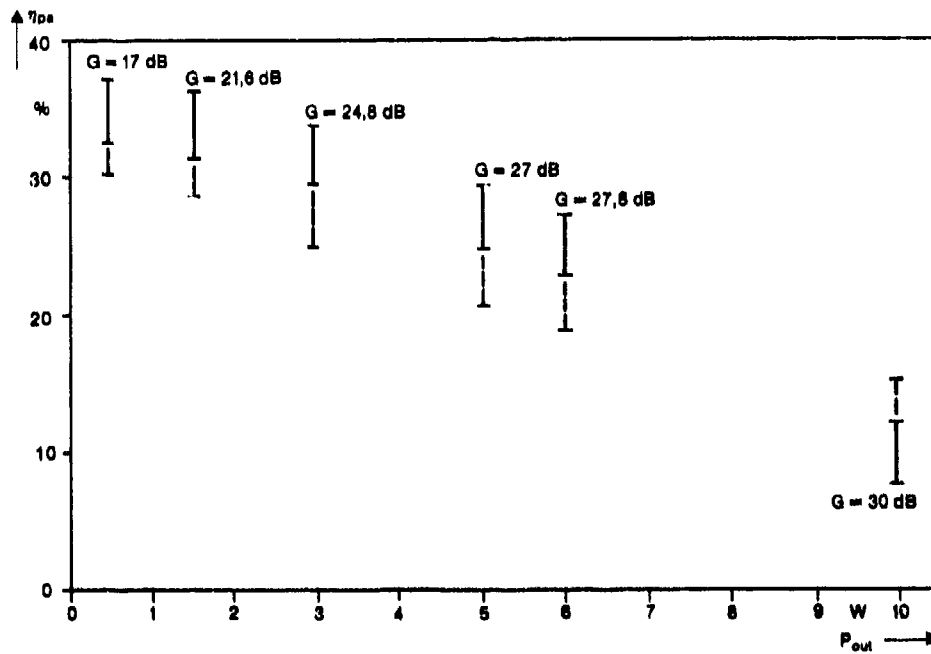
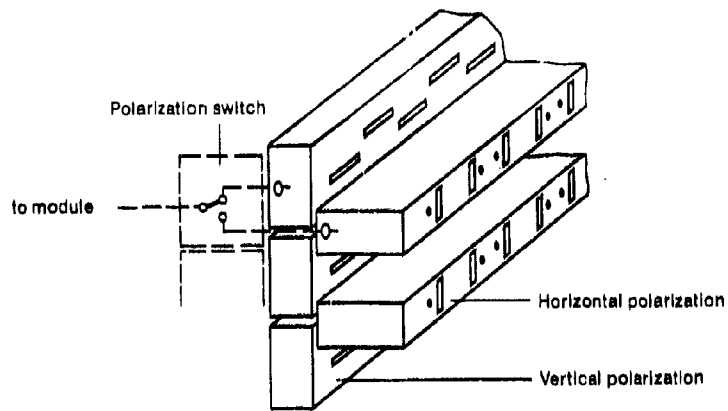
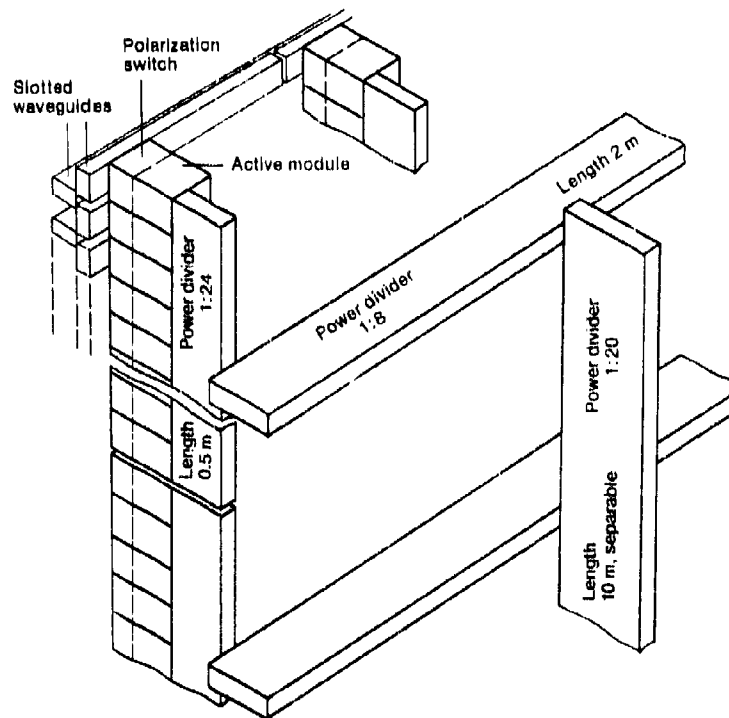


Fig. 4.3 Power added efficiency vs RF-output power of HPA related to 10 dBm RF-input power in the X-band



**Fig. 3.1. Double polarization slotted waveguide array**



**Fig. 3.2. Active array structure and feed system**

**SAR-T/R-Module**

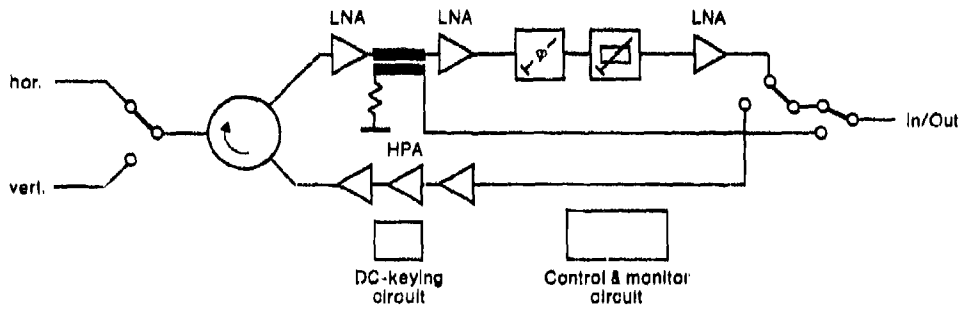


**Fig. 4.1. Block diagram**

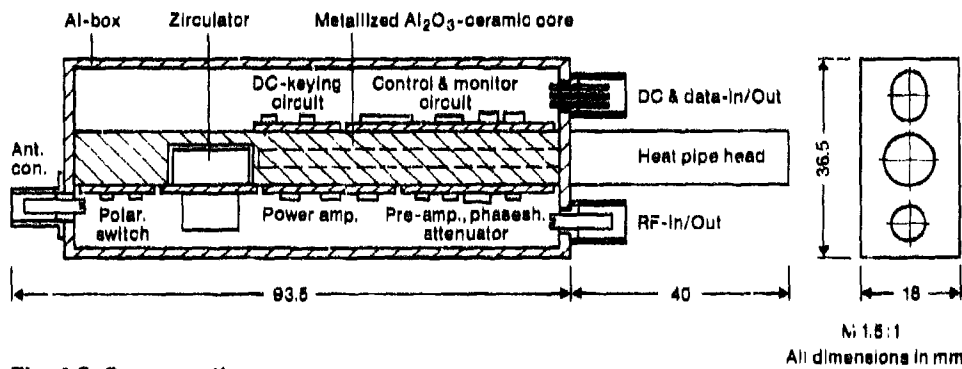


**Fig. 4.2. Cross sections**

DISCUSSION

**J. Richard**

Quelles sont les capacités maximales de pointage de l'antenne en élévation?

**Author's Reply**

From off NADIR  $35^\circ \pm 35^\circ$  that means from NADIR to  $70^\circ$  off nadir.

**N. Lancelongue**

What is the value expected for the purity of polarisation?

**Author's Reply**

Lower than -30 dB.

**I. McMillan**

Recognising that low efficiency of the PA requires low voltage and high currents, what solution have you found to the pulse storage capacitors, or, if no storage, how do you handle the ca. 100 A or so of pulse current?

**Author's Reply**

Problem is basically solved. The problem is reduced with medium output power.

**K. van Kloosten**

- (1) The amount of power to be dissipated is high and has to be radiated in space. Both front and backside are nice isolating (likely CFRP metallised waveguide). How do you think to solve this problem?
- (2) The scan volume is small and with microstrip you would be able to operate in the "dip" of the x-pol pattern with reasonable polarisation performance. Please comment.

**Author's Reply**

- (1) The total surface of the 3830 active modules is much smaller than the  $2 \times 10 \text{ m}^2$  of the array. Therefore, it is not too difficult to accommodate heat sink plates for heat radiation to space.
- (2) The antenna concept can be applied also for a larger scan volume. For a scan volume of  $\pm$  several degrees the slotted waveguide concept shows already improved cross polarization purity.

**C.J. Baker**

As you have only one receiver channel, how do you cope with the differential dynamic range of the co- and cross-polar return signals?

**Author's Reply**

Principally, this has to be done with the dynamic range of the module receivers (at the moment, there are the two co-polarizations only under discussion, and the here mentioned problem is one of the reasons for that). However, the question touches the whole complex of calibration (including STC) which is under consideration just now. Whereas external calibration for all polarizations will be done on the same way as for X-SAR/SIR-C and ERS-1 (with large test and calibration areas for instance in Oberpfaffenhofen), the internal calibration of this large array is just under discussion now.



A MOTION COMPENSATION STUDY FOR THE PHARUS PROJECT

by  
 M.P.O. Otten, M.Sc.  
 Radar & Communications Division  
 Physics and Electronics Laboratory  
 P.O. box 96864  
 2509 JG The Hague  
 The Netherlands

SUMMARY

In the PHARUS project, a polarimetric C-band SAR is being developed, which will be preceded by a non-polarimetric test system called PHARS. A motion compensation study is also part of preparatory studies for the final PHARUS design.

A SAR data simulator has been developed as a tool for the investigation of the effects of aircraft motions on the SAR image. From the SAR mapping geometry, a terrain description, the radar parameters, and detailed trajectory and attitude data of a non-maneuvring aircraft, the simulator generates raw data with a given range resolution. This can be processed, by azimuth compression, into the SAR image.

A secondary purpose of the simulation is to determine the impact of several design parameter choices, and to provide well-defined test input for SAR processing software that is being developed.

The results of test runs with real flight data have been verified theoretically, and have shown the need for motion compensation. It has also demonstrated a major advantage of simulation, in that it can take many factors into account at the same time, including for instance the SA<sup>2</sup> processing method, which is hard to do theoretically.

LIST OF SYMBOLS

A	: antenna aperture (area)
$a_{LOS}$	: line-of-sight acceleration
$B_w$	: bandwidth
$D_{as}$	: azimuth shift
$d_{la}$	: lever arm distance
H	: altitude
$F_n$	: receiver noise factor
$f_{s,eff}$	: effective sampling frequency
$\Delta f_d$	: utilized Doppler band
$\kappa$	: weighting compensation parameter
$N_{pr}$	: azimuth presampling factor
PCR	: pulse compression ratio
$P_t$	: transmitted peak power
R	: slant range
RCS	: radar cross section
$\rho_a$	: azimuth resolution
$r_r$	: (slant) range resolution
$T_a$	: integration (aperture) time
$V_{LOS}$	: line-of-sight velocity
$\phi_{err}$	: phase error
$\lambda$	: wavelength
$\theta_s$	: depression angle
$\theta_a$	: azimuth beam steering angle

AD-P005 845

## 1. INTRODUCTION

The PHARUS project (1) aims at the development of a polarimetric C-band aircraft SAR in the Netherlands, and is carried out by the Physics and Electronics Laboratory TNO (FEL), the National Aerospace Laboratory (NLR), and the Delft University of Technology (TUD). Prior to the realization phase of the project, i.e. the building of PHARUS and final software development, there is the definition phase, consisting of several preparatory studies, one of which is concerned with motion compensation. FEL and NLR collaborate on this study.

In the definition phase, a test system is also built, called PHARS, so that actual experience with most aspects of SAR can be gained before the final design for PHARUS is made.

The first phase of the motion compensation study was the development of an aircraft SAR simulation program at FEL, called SARGEN. This simulation has recently been taken into use by NLR to carry out the second phase of the study, the motion error analysis.

This paper focuses on phase one of the study, the development of the simulation program SARGEN, and some first results of simulations with 'real' flight data that were made available by NLR.

## 2. SAR SIMULATION AND MOTION COMPENSATION

Though motion compensation studies can be carried out purely theoretically, a simulation has a number of advantages.

In the first place, practically any investigation that can be carried out theoretically can also be done with a simulation. In fact, the first thing to do would be to validate the simulation with a number of theoretically verifiable test runs. However, the simulation can handle situations which soon become too complicated for theory: all types of errors can be considered, motion can be singled out and combined as desired, and real flight data can be used directly; motion variables will usually not be independent, so that considering all of them 'at the same time' is more realistic than incoherently adding up an error budget. Furthermore, the particular azimuth compression method is taken into account, secondary effects which might otherwise be overlooked will become apparent in a simulated image, and the image quality can be judged in any objective and subjective way.

Apart from a motion compensation study, a simulation can also aid the making of design choices, e.g. by determining ambiguity levels or signal-to-noise ratios, and it can generate known test input data for SAR processing software under development.

## 3. AIRCRAFT SAR SIMULATION 'SARGEN'

The primary purpose of the simulation is to study azimuth distortion and defocusing caused by aircraft motion. The necessary capabilities and permissible limitations of SARGEN have been established according to this aim. The following simulation model was considered to be adequate:

A situation is simulated where a non-maneuvring aircraft flies along a trajectory, which is perturbed by motion deviations in all directions and in attitude (roll, pitch, and yaw). The deviations are assumed to be not so large as to cause range walk, but arbitrary otherwise. A certain slant range resolution achieved by pulse compression is assumed, but the pulse compression itself is not simulated. The motion reference point may be displaced with respect to the antenna phase centre. The pointing of the antenna is arbitrary, but fixed during one simulation run. The radar PRF may be fixed or coupled to the aircraft ground velocity. An azimuth presampling factor may also be specified.

The imaged terrain may consist of any collection of point targets in a two dimensional plane, each given by a position, RCS, and phase term<sup>1</sup> (complex reflection coefficient).

Thus the output of SARGEN represents range compressed, and presampled coherent raw data, which then needs azimuth compression to form the SAR image.

Figure 1 shows a block diagram of the complete simulation, i.e. up to the final image, and the organisation of in- and output data.

<sup>1</sup> Only relevant in case of closely spaced point targets

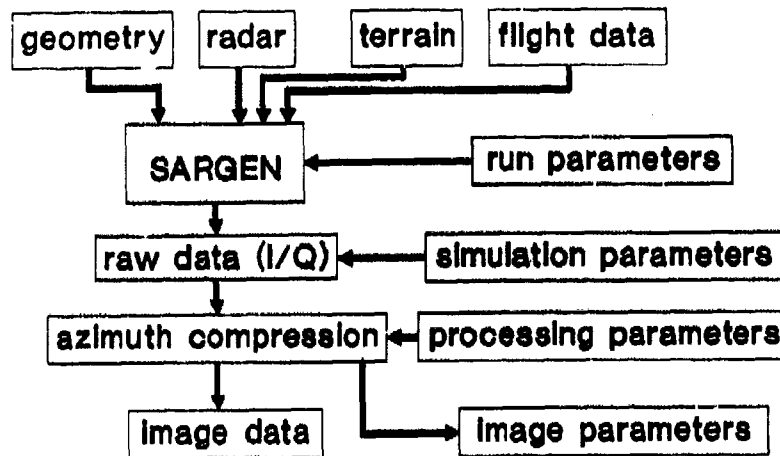


Figure 1. Simulation block diagram

The input parameters are organized in five data sets:

- geometry : parameters which describe fixed distances, like nominal altitude, distance to the imaged swath, displacement between motion reference point and antenna phase centre etc.
- terrain : description of the point target collection
- radar : wavelength, PRF, power, bandwidth, range resolution, antenna dimensions etc.
- flight data: six time sequences: three position- and three attitude variables, plus the time itself (time step is variable).
- run parameters: describes the simulation run itself, i.e. the extent in azimuth and range, and controls the selection of flight variables, and of variable or fixed PRF.

A file of raw data is generated, along with a 'summary' of the simulation parameters, some of which are necessary input for the azimuth compression (velocity, PRF, wavelength, range etc). The processing parameters specify azimuth resolution, weighting parameters, and the image format: size, pixel spacing etc., which are again summarised after processing in the image parameter file, along with the resulting number of lines and pixels.

The simulation has been implemented in the FORTRAN 77 language. Since a simulation such as this can easily become excessively time consuming, a fair amount of effort has been devoted to optimization of the computations. Nevertheless, some limitations remain: study of statistical phenomena (speckle) would require, in this set-up, collections of point targets that are too large to handle, but such investigations were not intended.

Figure 2 shows how, ideally, the simulation would be used in a set-up for motion compensation study, and how, in some cases, this may be approximated by a simpler set-up, which requires only straightforward uncompensated SAR processing. Note however that this alternative set-up presupposes that the motion that is assumed to be compensated is indeed compensated in every respect, which is not always true. For instance: phase errors may be perfectly corrected, but deterioration of the signal-to-noise ratio due to antenna misalignment cannot be undone. Such partial compensation of motion cannot be simulated in the alternative set-up. The alternative approach should therefore only be used, bearing its limitations in mind. Furthermore, since the raw data generation will often be more time consuming than the subsequent SAR processing, it may even be more practical to use the first approach, if an accurate set of flight data is available. One could generate a set of raw data using that set of flight data, after which processing can be done with motion compensation with any desired error imposed on the flight data.

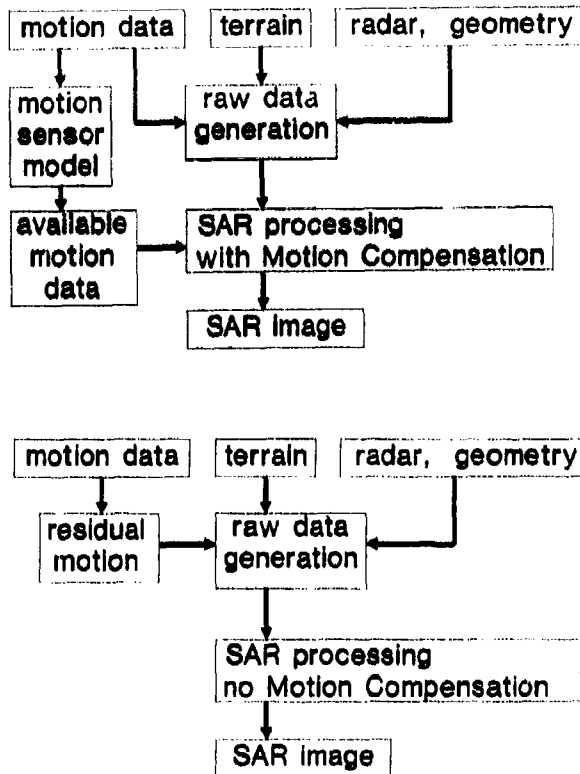


Figure 2. Simulation set-up for motion compensation study

Top: 'ideal' set-up

Bottom: simplified set-up

In principle, autofocus can also be included in a simulation cycle. However, something would have to be done about the statistical properties of the simulated data, to which autofocus algorithms are inherently sensitive. Adding speckle with the proper statistics to the image data, without simulating the underlying physical process, is therefore considered as a future extension.

#### 4. SIMULATION EXAMPLES

Some test simulations were carried out using flight data of an NLR aircraft, a Swearingen Metro II (Fairchild), which is used for Remote Sensing experiments, and which may in future serve as the SAR platform. A fictitious scene was created, described below, containing enough features to reveal any distortion, defocusing, and ambiguity:

Point targets are arranged in cross track lines, at 5 m intervals (less than the range resolution), along track lines, at variable intervals, and one 'diagonal' line. All point targets have  $RCS=1 \text{ m}^2$ , except those constituting the diagonal line, which have  $RCS=100 \text{ m}^2$ , see figure 3. The simulated trajectory is about 600 m at 104 m/s ground speed. The actual flight data are depicted in figure 4 (see figure 5 for roll, pitch, and yaw definitions). Note: the x-position (along track) is the x-position after subtraction of the nominal speed.

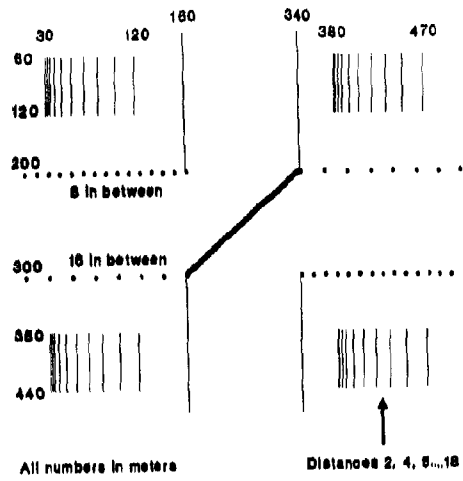
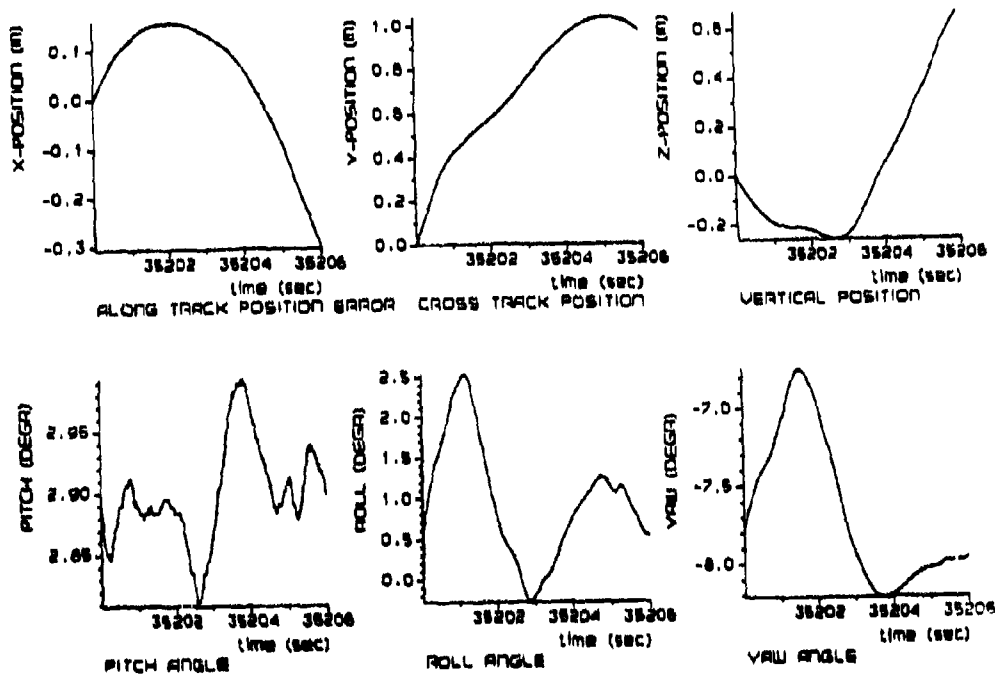


Figure 3. Simulated scene



Note: X position error =  $X - Vt$

Figure 4. Flight path data over a 6 second interval

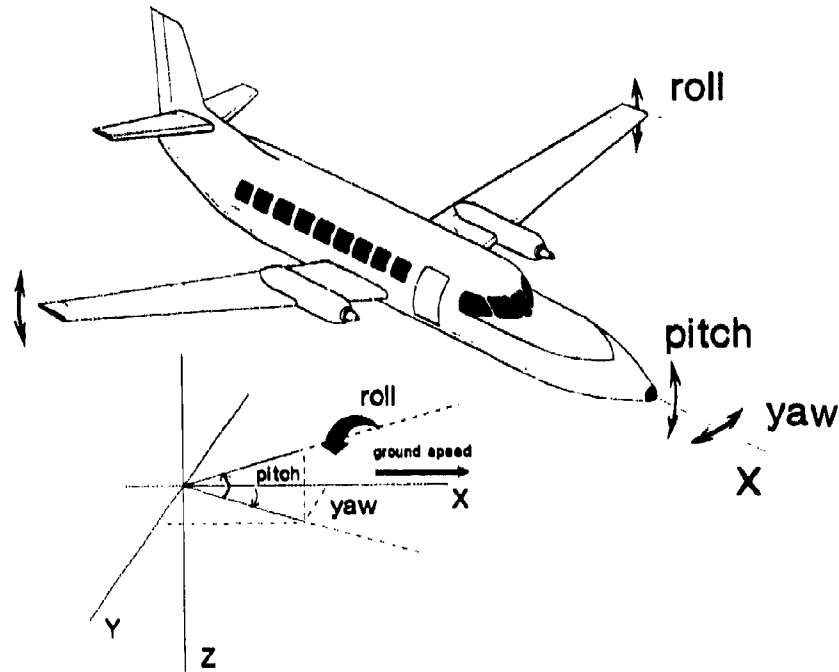


Figure 5. Roll, pitch, and yaw definitions

Top : Roll, pitch, and yaw axes of the airframe

Bottom : Relative orientations with respect to ground speed

## Other simulation parameters:

- near slant range	R = 13 km
- altitude	H = 6 km
- antenna pointing:	
depression angle:	$\theta_d = 24.4^\circ$
azimuth beam steering angle:	$\theta_a = -5.5^\circ$
except in the uncorrupted image where	$\theta_s = 0^\circ$
- wavelength:	$\lambda = 0.0588 \text{ m}$
- PRF : coupled to velocity,	PRF = 3500 Hz, at 100 m/s
- antenna aperture:	A = 0.35 m x 0.135 m
(uniform illumination assumed)	
- transmitted peak power:	$P_t = 140 \text{ W}$
- receiver noise factor:	$F_n = 2 \text{ dB}$
- bandwidth:	$B_w = 31 \text{ MHz}$
- pulse compression ratio:	PCR = 400
- range resolution	$\rho_r = 6 \text{ m}$
- azimuth presuming factor	$N_{pr} = 16$
- lever arm distance	$\underline{d}_{la} = (5.0, 1.0, -0.5) \text{ m}$

These parameters - except the lever arm distance, which is not known yet - are generally representative of the actual PHARS parameters.

The azimuth compression is carried out using line-by-line (time domain correlation) and Doppler processing ('deramping'+FFT). In both cases the azimuth resolution  $\rho_a$  is 6 m (2 pixels/resolution cell), and raised cosine weighting is applied to achieve -30 dB sidelobes.

Figure 6 shows the uncorrupted SAR image (line-by-line processed). As can be seen in the vertical line structures, the actual resolution is not as good as the theoretical 3-dB resolution. This is because a resolution cell only contains 2 pixels, so that a small dip between two point target responses cannot be seen. Around the diagonal, formed by  $100 \text{ m}^2$  point targets, a light area is visible; this is the result of the sidelobes (of the synthetic beam) rising above the noise. The maximum signal-to-noise ratio, for the  $1 \text{ m}^2$  targets, is found to be about 30 dB, after processing; in the 'uncorrupted' case, the antenna is perfectly aimed, so that the maximum gain is obtained. Since the sidelobes of the synthetic beam are about -30 dB, they do not clearly show, for the  $1 \text{ m}^2$  targets, but they do for the  $100 \text{ m}^2$  RCS targets, which of course are 20 dB higher.

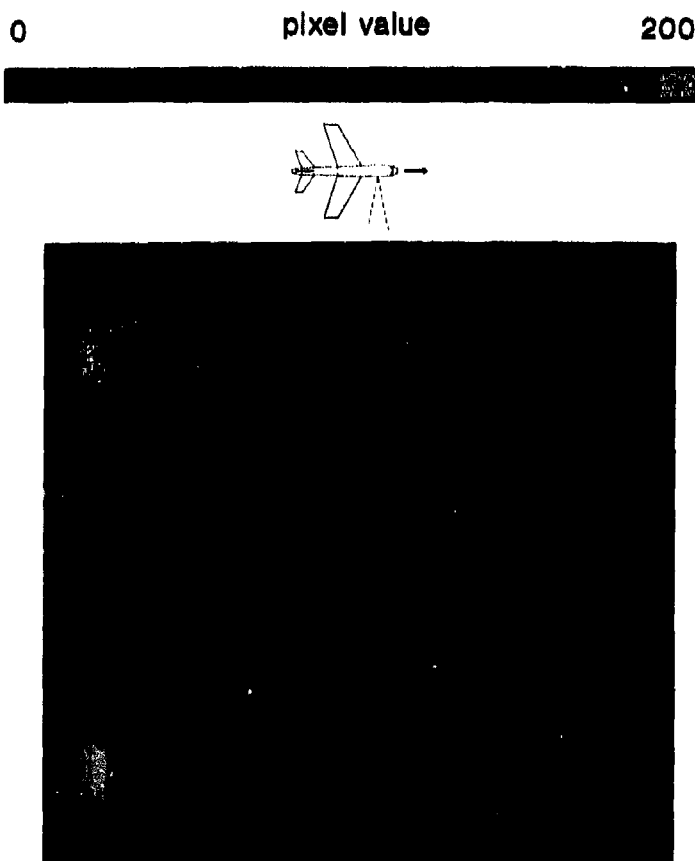


Figure 6. Uncorrupted simulated SAR image

Figure 7 shows the image that results when all motion variables as shown in figure 4 are included, and when the antenna and motion reference point coincide (no lever arm). Since the PRF is coupled to the velocity, the x-motion error is already compensated, and the beam steering angle compensates for part of the average yaw, so that there is little overall gain loss.



Figure 7. SAR image with motion errors (no 'lever arm' effect)

To get a feel of the degradation that might be expected, some approximations of image shift and defocusing can be made.

To determine azimuth shift, the linear motion components (constant velocity) in the y- and z-direction should be estimated.

The steepest part (beginning of trajectory) of the y-motion corresponds to about 0.45 m/s. The resulting line-of-sight velocity is:

$$V_{LOS} = V_y \cdot \cos(\theta_s) = 0.4 \text{ m/s} \quad (1)$$

so that the shift  $D_{az}$  at 13 km range is:

$$D_{az} = V_{LOS} \cdot R / V_x = +50 \text{ m} \quad (2)$$

The maximum z-velocity is 0.3 m/s (second half of trajectory). Along the line-of-sight this becomes:

$$V_{LOS} = V_z \cdot \sin(\theta_n) = 0.12 \text{ m/s} \quad (3)$$

yielding an azimuth shift of

$$D_{az} = 15 \text{ m} \quad (4)$$

As for defocusing: A quadratic phase error can be estimated by considering the average cross track acceleration during one aperture time ( $T_a$ ).  $T_a$  is given by:

$$T_a = \lambda \cdot R / (2 \cdot V_x \cdot \rho_n) = 0.7 \text{ s.} \quad (5)$$

( $\lambda$  is 1.1 because of the weighting).

Closer examination of the flight data (not shown here), reveals that the maximum z-acceleration averaged over 0.7 s, is about  $0.4 \text{ m/s}^2$ , in the middle of the trajectory. The averaged y-acceleration has an extremum of  $-0.45 \text{ m/s}^2$ , but this occurs at the beginning of the trajectory where the scene happens to be 'empty'. A more typical value is  $0.15 \text{ m/s}^2$ .

An average cross track acceleration along the line-of-sight of  $a_{\text{LOS}}$  yields an edge-of-aperture phase error of:

$$\phi_{\text{err}} = (2\pi/\lambda) a_{\text{LOS}} (hT_a)^2 \quad (6)$$

A commonly applied limit for this kind of error is  $\pi/4$ . The z-acceleration has a line-of-sight component of  $0.16 \text{ m/s}^2$ , so that  $\phi_{\text{err}} = 0.7\pi$ . Noticeable defocusing may be expected from this. An y-acceleration of  $0.15 \text{ m/s}^2$  leads to  $\phi_{\text{err}} = 0.6\pi$ . These values that are 'just over the limit' confirm the impression of figure 7: the defocusing is not totally destructive but clearly visible. These are, however, rough approximations. The actual motion contains higher order phase errors, which haven't been considered. Furthermore, when the azimuth compression is done line-by-line, the actual spread of a particular point target response in case of constant cross track acceleration, is determined not only by the quadratic phase error across the aperture but also by the changing orientation (linear phase component) of the aperture itself, since this has the effect of keeping the target in the synthetic beam for a longer or shorter time, depending on the direction of the acceleration. This does not apply to Doppler batch processing, where a batch of pixels is formed from one aperture.

Figure 8 shows the resulting image, when Doppler processing is applied. Reasons for the obvious differences are:

In Doppler processing, a batch of image points is formed from one batch of raw data samples. Therefore, all pixels in one batch will be influenced by the same phase errors across the aperture, and the degradation is practically the same for all pixels belonging to this batch (unless motion errors are extremely large). This causes discontinuities in azimuth from batch to batch (batch seam). It also results in occasional 'double imaging' or disappearance of parts of the scene. Furthermore, the integration length, and thus the location of the batch edges in azimuth, must vary with range. So, points at the same azimuth location, but slightly separated in range, may belong to different batches, and therefore suffer from different degradation effects: this leads to discontinuities in range as well. In general one can say that, for a given trajectory, the response to any particular point target depends on the type of processing, where for Doppler processing, this response is hard to predict. It would be even more difficult to predict, by other means than simulation, how these differences influence the performance of autofocus algorithms.

Adding the lever arm displacement, some more changes appear, see figure 9. In the left section, the yaw rate goes from positive to negative, causing a shift which also goes from positive to negative, so that the left part of the image has shrunk. For example, a yaw rate of  $-1.4^\circ/\text{s}$  gives rise to a y-velocity of  $-0.12 \text{ m/s}$ , which causes a  $-14 \text{ m}$  shift. Defocusing is hard to predict, since the variations can not be very well approximated by quadratic errors. For instance, the rather sharp change of the roll rate at two time instants, shows up as a 'breaking up' of the upper horizontal line segment in the left section, and of the diagonal in the middle.

As for gain variations: these are small, and cannot be detected visually<sup>2</sup>. There is some gain variation, however, mainly due to yaw, not exceeding 1 dB.

<sup>2</sup> Unfortunately, some apparent large scale intensity fluctuations appear, due to imperfections of the photograph.

24-10

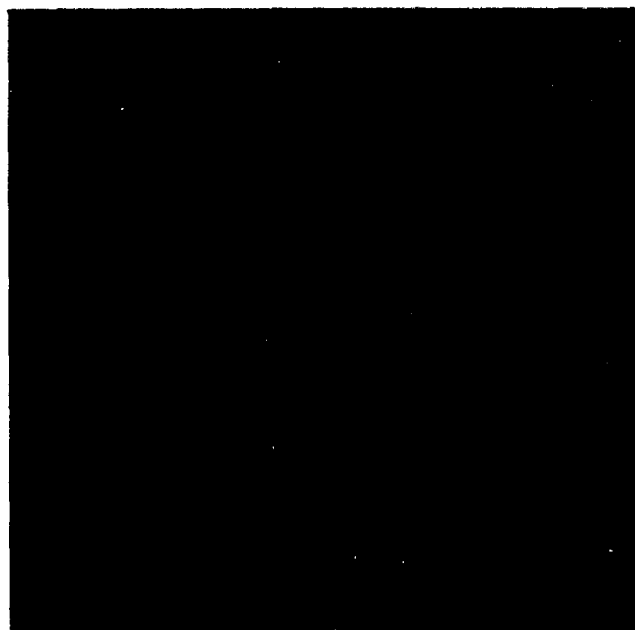


Figure 8. Doppler processed SAR image with motion errors



Figure 9. Simulated SAR image with motion errors  
including 'lever arm' displacement

The simulation may also be used to determine suitable processing parameters. For instance, when Doppler processing is applied, some frequency margin has to be taken into account to accommodate the ambiguity inherent in a discrete Fourier transform of a not strictly bandlimited signal. This margin can be manipulated by resampling between the focusing and transformation operations<sup>3</sup>. Narrowing the margin makes the computation more efficient, but increases the ambiguities. Figure 10 shows one example of a too narrow frequency margin: the FFT sampling frequency was reduced by a factor of four after the focusing operation. Note that the imaged Doppler frequency range  $\Delta f_d$  is still only a third of the effective sampling frequency  $f_{s,eff}$ !

$$\Delta f_d = V/\rho_s = 104 / 6 \approx 17 \text{ Hz} \quad (7)$$

$$f_{s,eff} = 3500 \cdot (104/100) / (16 \cdot 4) \approx 57 \text{ Hz} \quad (8)$$

Though ambiguity levels for such processing schemes could be determined analytically, this is quite difficult, among other things due to the combination of presampling before and averaging after focusing, or 'deramping' of Doppler frequencies. Presampling/averaging can be described as ordinary filter operations, but deramping cannot, since it is not time invariant. In fact, the image clearly shows that the ambiguity varies, due to the varying position in azimuth of the strong targets. In such a case, a simulation provides a quicker way of finding the answers.

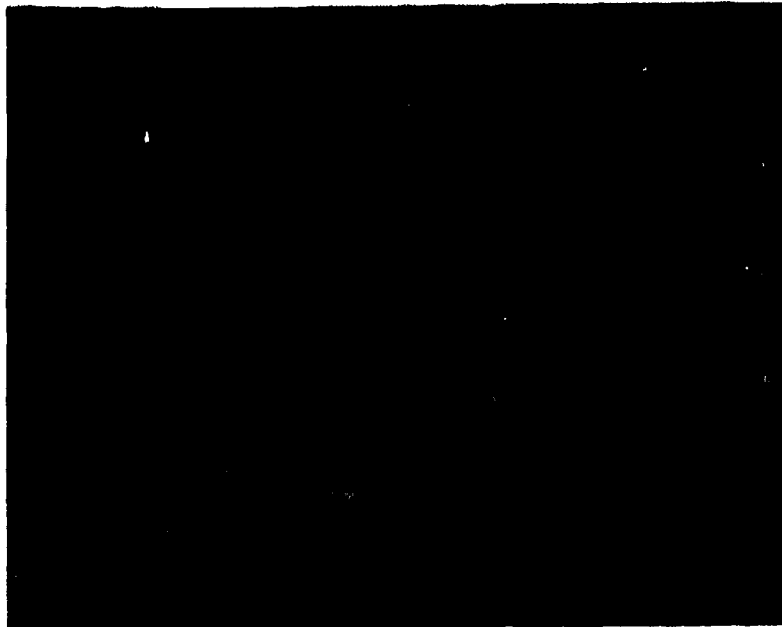


Figure 10. Ambiguities in a Doppler processed SAR image

<sup>3</sup> This yields less degradation than downsampling before focusing

## 5. CONCLUSIONS

The aircraft SAR simulation is a very useful tool for the PHARUS motion compensation study. Some simulation examples not only show the theoretically verifiable effects, but also some effects, that can be explained qualitatively, but are difficult to quantify theoretically, especially with respect to Doppler processing.

Additional advantages are the possibility to quickly determine the final impact of many design parameters, and the possibility to generate well-defined test data for SAR processing software.

Adding simulated speckle is considered as a future option, when autofocus algorithms are to be investigated using simulated data. Other extensions that are considered are FIR prefiltering, in stead of plain presuming, and in-flight beam scanning.

## REFERENCES

- [1] P. Hoogeboom  
THE PHARUS PROJECT  
Paper No.10 of the AGARD Symposium 'High resolution air- and spaceborne radar'  
May, 1989, The Hague, The Netherlands.
- [2] M.P.O. Otten  
Physics and Electronics Laboratory TNO, The Hague  
AIRCRAFT SAR SIMULATION 1.0  
report FEL-1989-44

## DISCUSSION

## G.E. Haslam

You have noted that the ambiguity level is dependent upon the processing block size. Is not this phenomenon due to the phase modulation of the spectrum under the presum filter? Please clarify.

## Author's Reply

No, the variation in ambiguity is due to down sampling being carried out before FFT-ing and after focusing to the centre of a batch. This down sampling is meant to avoid excessive redundancy, i.e. imaging a much larger Doppler frequency range than the frequency range of interest. Since the focusing is done with the full (original) sampling frequency, pixels in the middle of a batch do not suffer from increased ambiguity by subsequent integration, but pixels near the edge do. So, in fact, the ambiguity level depends on the position of a pixel in a batch. Of course, the effect depends on the reduction of the sampling frequency, which determines the FFT output frequency range.

## R.Horn

- (1) What kind of method is intended to be used for motion compensation in the PHARUS system?
- (2) Is it intended to implement real time motion compensation on board the aircraft?

## Author's Reply

- (1) The M.C. study is currently in progress: it still has to be decided what method will be required. However, it is very likely that flight path data will be recorded on tape for off-line correction, supplemented by some autofocus procedure. Requirements for the inertial unit still have to be determined, according to the outcome of this study. Also, several autofocus algorithms will be evaluated in this study.
- (2) No real-time correction is foreseen in the near future.



## A SOLUTION FOR REAL TIME MOTION COMPENSATION FOR SAR WITHOUT USING INERTIAL NAVIGATION SYSTEMS

Joao R. Moreira

German Aerospace Research Establishment (DLR)

Institute for Radio Frequency Technology

8031 Weßling, FRG

AD-P005 846

### ABSTRACT

This paper reports a new solution for real time motion compensation. The main idea is to extract all the necessary motions of the aircraft from the radar backscatter signal using a new radar configuration and new methods for evaluating the azimuth spectra of the radar signal. Hence an inertial navigation system becomes unnecessary for a lot of applications. The motion compensation parameters for real time motion error correction are the range delay, the range dependent phase shift and the pulse repetition frequency. The motions of the aircraft to be extracted are the displacement in line of sight (LOS) direction, the aircraft's yaw and drift angle and forward velocity. Results show that a three look image with an azimuth resolution of 3m in L-band using a small aircraft is achievable and the implementation of this method in real time using an array processor is feasible.

### 1. INTRODUCTION

Synthetic aperture radars (SAR) synthesize a long antenna by transmitting electromagnetic energy and coherently adding the successive reflected and received pulses in order to obtain high resolution in flight (azimuth) direction. The resolution in range direction is achieved by transmitting very short pulses or by using pulse compression. To achieve a coherent integration, called azimuth compression, it is necessary that phase errors, resulting from spurious platform motion errors, are compensated. The platform motion error is defined as the error between the actual flight path and the nominal one. For SAR systems mounted on small aircrafts the motion errors are considerably high due to atmospheric turbulence and aircraft properties. Obtaining the motion errors of the aircraft, motion compensation can be realized adjusting the pulse repetition frequency (PRF), applying a range dependent phase shift to each received pulse and delaying it. By adjusting the PRF one compensates for the aircraft forward velocity variations, so that the emissions will occur at constantly spaced intervals. Adjusting the phase and range delay one compensates for the displacement in LOS-direction.

This paper will report a method to extract the displacement in LOS-direction, the aircraft velocity, the yaw and drift angle from the radar raw data. This method is based on the analysis of the azimuth spectrum of the radar raw data. The primary condition to implement this method is the use of a wide azimuth antenna beam. This is obtained using a short fixed mounted pencil beam antenna rather than an usual long stabilized antenna (Boesswetter et al, 1983). Thus both the complex gimballing system and the clutterlock loop is avoided.

### 2. PROPERTIES OF THE AZIMUTH SPECTRUM

Consider the radar geometry of a strip mapping SAR, where  $V_f(t)$  is the aircraft forward velocity,  $V_b(t)$  the velocity error in LOS-direction,  $t$  is the time, PRF is the pulse repetition frequency,  $\theta$  the angle of the cross-flight direction to the direction of a point on the ground and  $R$  the range. The antenna points at a right angle to the nominal flight path illuminating a swath to one side of the aircraft. Due to  $V_f(t)$  and  $V_b(t)$  the transmitted pulse will have a frequency or doppler displacement of:

$$F_{\text{doppler}} = \frac{2 \cdot V_f(t) \cdot \sin \theta}{\lambda} + \frac{2 \cdot V_b(t) \cdot \cos \theta}{\lambda} \quad (1)$$

where  $\lambda$  is the wavelength of the transmitted pulse

Using the radar equation the azimuth power spectrum  $P(f)$  can be expressed as the product:

$$S(f) = k \cdot G^4(f) \cdot B(f) \quad (2)$$

where  $f$  is the frequency,  $G(f)$  the one-way antenna gain in azimuth direction and  $B(f)$  the ground reflectivity, considered real.  $G^4(f)$ , that represents the antenna pattern, can be shifted in frequency by the combination of yaw and drift angle  $\varphi$  and the velocity in LOS-direction  $V_b(t)$  as follows:

$$f_s \cong \frac{2 \cdot V_v(t) \cdot \sin \varphi(t)}{\lambda} + \frac{2 \cdot V_b(t)}{\lambda} \quad (3)$$

where  $f_s$  is the frequency shift of  $G^4(f)$ ,  $\varphi(t) = \alpha(t) + \beta(t)$ ,  $\alpha(t)$  is the yaw and  $\beta(t)$  is the drift angle of the aircraft.  $B^2(f)$ , that represents the ground reflectivity, can be shifted in frequency by the velocity in LOS-direction  $V_b(t)$  as follows:

$$f_r \cong \frac{2 \cdot V_b(t)}{\lambda} \quad (4)$$

where  $f_r$  is the frequency shift of  $B^2(f)$ .

The extraction of the motion errors of the aircraft is based on two methods. The first method analyses only the ground reflectivity part of the azimuth spectrum and is called Reflectivity Displacement Method (RDM). The second method analyses only the antenna pattern part of the azimuth spectrum and is called Spectrum Centroid Method (SCM).

### 3. THE REFLECTIVITY DISPLACEMENT METHOD (RDM)

The reflectivity displacement method analyses the frequency shift between two ground reflectivity functions of adjacent and strong overlapping azimuth spectra. It is considered, that the ground reflectivity function  $B(f)$  has a high contrast defined as:

$$K = \frac{\frac{1}{PRF} \cdot \int B^2(f) df}{\left[ \frac{1}{PRF} \cdot \int B(f) df \right]^2} - 1 \quad (5)$$

so that the antenna pattern, that has a wide beam in azimuth direction, can be considered approximately independent of frequency. The frequency shift  $V(t)$  between two ground reflectivity functions can be derived from eq. 1 and 4 and expressed as:

$$V(t) \cong - \frac{2 \cdot V_v^2(t) \cdot \Delta t}{\lambda \cdot R} + \frac{2 \cdot \dot{V}_b(t) \cdot \Delta t}{\lambda} \quad (6)$$

where  $R$  the range,  $\Delta t$  the time interval between the two adjacent azimuth spectra. The maximum bandwidth of the frequency shift function  $V(t)$  is dependent on  $\Delta t$  and is expressed, considering the sampling theorem, as:

$$BW_v = \frac{1}{2 \cdot \Delta t} \quad (7)$$

The frequency shift  $V(t)$  can be determined from the position of the maximum of the correlation between two adjacent azimuth spectra. This way gives a very accurate frequency shift due to the fact that the two adjacent azimuth spectra are strongly correlated.

As we get  $V(t)$  by this correlation, the acceleration in LOS-direction  $\dot{V}_b(t)$  must be separated from the forward velocity  $V_b(t)$ . This is done using a low and a high pass filter. The forward velocity has a very low bandwidth, for example 0 to 0.05Hz assuming a turbulence with a standard deviation of about 1m/s and a small aircraft as the Dornier Do228. The acceleration in LOS-direction has a much higher bandwidth, where only the higher frequencies are important for motion compensation, for example frequencies higher than 0.1Hz. Considering the power spectral density (PSD) of the acceleration in LOS-direction and the PSD of the forward velocity of the Do228 aircraft, we get an overlap between the two terms of eq. 6 of less than -15dB, so that both the forward velocity and the acceleration in LOS-direction can be well separated from each other. The displacement in LOS-direction is obtained integrating two times the acceleration in LOS-direction. Figure 1 shows the block diagram of the reflectivity displacement method.

The accuracy of RDM depends on the contrast  $K$  of the reflectivity function  $B(f)$ . By imaging land surface that is not homogeneous we get always a high contrast  $K$ , that implies a high accuracy of the RD method. By imaging an homogeneous source as sea or desert we get a low contrast  $K$ , that implies reduced accuracy of the RD method. The degradation of the accuracy of the displacement in LOS-direction with the decrease of the contrast  $K$  is greater than the degradation of the accuracy of the forward velocity.

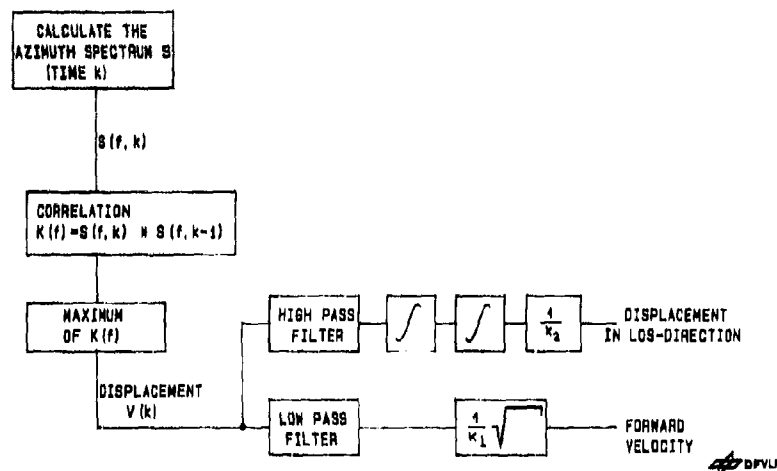


Figure 1. Block diagram of the Reflectivity Displacement Method (RDM)

#### 4. THE SPECTRUM CENTROID METHOD

This method basically determines the doppler centroid of the antenna pattern part  $G^*(f)$  of the azimuth spectrum. As the beamwidth of the antenna in azimuth direction is very wide, the method using the azimuth frequency spectrum of the processed complex imagery (Li et al, 1985) has a very low bandwidth, due to the illumination time of the antenna that is longer than 30s in L-band.

As the illumination time of the antenna is long the ground reflectivity can be determined very precisely using a Kalman filter, if the reflectivity does not change with the time very much. Extracting the ground reflectivity from the azimuth spectrum we can determine the doppler centroid with high accuracy and bandwidth. The accuracy of the ground reflectivity prediction depends on its contrast  $K$ . If  $K$  is high the ground reflectivity varies strongly with the time due to bright targets that always have a variable and not predictable reflectivity. If  $K$  is low, the ground reflectivity can be easily determined.

The doppler centroid of the calculated antenna pattern is shifted by  $\varphi(t)$  and  $V_a(t)$  according to the eq. 3.  $\varphi(t)$  is a combination of the yaw  $\alpha(t)$  and the drift angle  $\beta(t)$  of the aircraft. Yaw motion is caused by turbulence and aircraft instability and the drift angle is caused by wind. The yaw motion has a high bandwidth and the drift angle has a very low bandwidth, so that  $\varphi(t)$  has almost the same bandwidth as the velocity in LOS-direction. Thus, they have to be separated considering the geometry of the aircraft. The displacement in LOS-direction, yaw and drift angles are calculated by estimating the doppler centroid of the calculated antenna pattern in near ( $C_n(t)$ ) and far range ( $C_f(t)$ ) and evaluating the data of a high precision barometer ( $B_s(t)$ ) supported by a radar altimeter ( $H(t)$ ). The yaw motion is separated from the drift angle via a high and a low pass filter. Figure 2 shows the block diagram of the spectrum centroid method (SCM).

Finally, the SCM works with high accuracy, when the contrast  $K$  of the ground reflectivity is low. When the contrast  $K$  increases, the degradation of the accuracy of the displacement in LOS-direction and of the yaw angle is greater than the degradation of the accuracy of the drift angle.

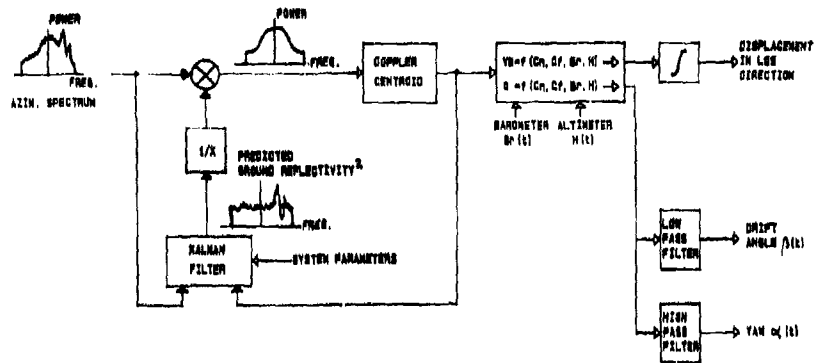


Figure 2. Block diagram of the Spectrum Centroid Method (SCM)

## 5. COMBINATION OF THE MOTION EXTRACTION METHODS

The combination of the two methods is implemented to increase the accuracy of the displacement in LOS-direction. Thus the accuracy of the displacement in LOS-direction will be almost independent of the contrast  $K$  of the ground reflectivity function. This is implemented giving different weightings to both methods according to  $K$ .

## 6. RESULTS

This motion compensation system has been successfully implemented off-line with the raw data of the Experimental SAR System of DLR (Horn, 1988). The main features, that this system has, are a high PRF and an azimuth antenna width of  $46^\circ$  in L-band and  $17^\circ$  in C-band. Figure 3 shows an example of motion compensation where the displacement in LOS-direction in near range is represented on the bottom. The main parameters for motion compensation were:

- Illumination time  $> 30s$ .
- Implementation only of the RD-method.
- Bandwidth in LOS-direction  $\approx 0.1$  up to  $1Hz$ .
- Bandwidth of forward velocity  $\approx 0$  up to  $0.05Hz$ .
- Number of range bins for the averaged azimuth spectrum : 32.
- Number of averaged azimuth spectra used : 20.
- Estimated residual error of displ. in LOS :  $8mm (1\sigma)$ .
- Estimated residual error of forw. velocity:  $0.1m/s (1\sigma)$ .

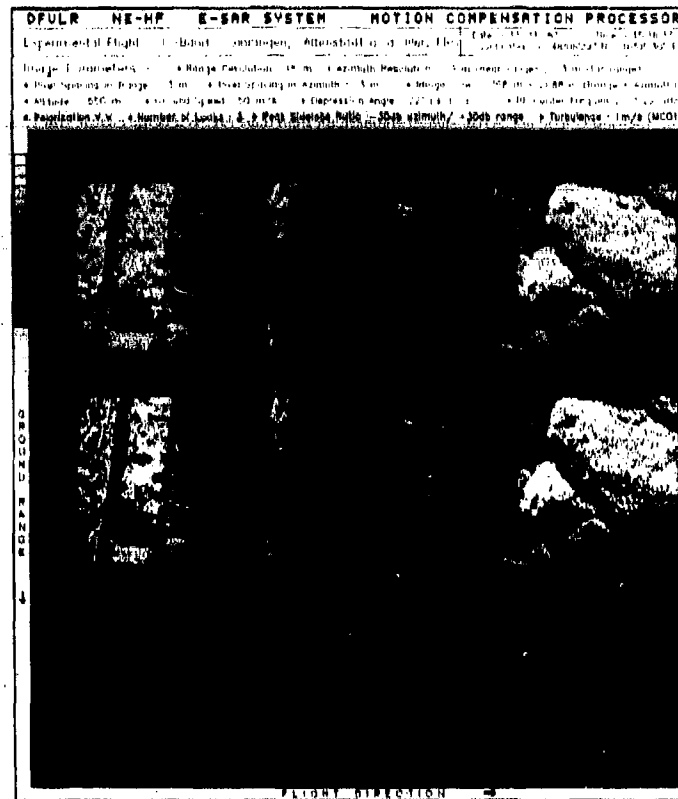


Figure 3. Example of Motion Compensation with the RD-method

## 7. REFERENCES

- [1] Boesswetter, C. and Wolfram A., "The design of an experimental synthetic aperture radar (SAR) for small aircrafts", 13th Europ. Microwave Conf., 1983.
- [2] Li F.K. et al., "Doppler parameter estimation for spaceborne synthetic aperture radars", IEEE Trans. on Geosc. and Rem. Sens., Vol. GE-23, 47-58, 1985.
- [3] Horn, R., "E-SAR - The experimental airborne L/C-band SAR system of DFVLR", IGARSS Symposium, Edinburgh, 1025-1026, 1988.

## 8. ACKNOWLEDGEMENTS

The author wishes to thank Mr. C. Dahme, Dr. K. Gruener, Mr. R. Horn, Dr. W. Keydel, Mr. A. Moreira, R. Schmid, U. Spies, M. Werner and F. Witte of DLR, Dr. C. Boesswetter, Mr. T. Pike and A. Wolfram of MBB-Ottobrunn and Dr. T. Freeman of JPL, California, whose suggestions and contributions made this work possible.

**DISCUSSION**

**J.P.Hardange**

Jusqu'à quelle fréquence de mouvements ce traitement pouvait-il être appliqué?

**Author's Reply**

I suppose that this method can be applied at higher frequencies than 0.84 Hz, as it is the case in our system, but this requires faster computing systems.

**J.Ender**

- (1) Is the correlation of consecutive azimuth spectra done with complex, amplitude or power spectra?
- (2) Could you say something about the state space of the Kalman filter predicting the reflectivity?

**Author's Reply**

- (1) We use azimuth power spectra.
- (2) No, I have to refer to Mr. Moreira.

**R. Hoogeboom**

What is the PRF in your system; does it fully cover the wide Doppler spectrum due to the large antenna beamwidth? Is there any spectral folding? Is the raw data recorded at this high PRF, or is there any data reduction?

**Author's Reply**

The PRF is 1 KHz; the Doppler bandwidth in C-Band is about 700 Hz with an azimuth beamwidth of 17 Deg. Azimuth ambiguities are well below -20 dB in the processed part of the spectrum. Presently, the data are recorded at a rate according to the 1 KHz PRF. We apply no data rate reduction.



L'IMAGERIE DES CIBLES MARINES A LA FRONTIERE  
ENTRE LE SAR ET L'ISAR

Marie PENOU  
THOMSON-CSF / RCM  
178 bd Gabriel Péri  
92242 MALAKOFF CEDEX  
FRANCE

**RESUME**

Pour disposer d'une fonction classification des cibles marines sur un radar aéroporté de surveillance maritime, THOMSON-CSF développe un système d'imagerie haute résolution. La forme d'onde utilisée permet d'obtenir une haute résolution en distance et d'effectuer un traitement cohérent qui accroît la résolution naturelle de l'antenne. Les méthodes usuelles d'imagerie synthétique SAR ou ISAR ne sont pas directement applicables puisque la cible et le radar sont mobiles. Le traitement adapté tient compte des spécificités du problème et se situe entre le traitement SAR et le traitement ISAR. D'autre part, l'image résultante est également hybride et son interprétation n'est possible que si les deux phénomènes sont pris en compte. Des améliorations de la signature ainsi obtenue sont alors envisageables pour rendre plus efficace l'identification manuelle ou automatique de la cible détectée.

**INTRODUCTION**

Les radars de surveillance maritime futurs devront permettre des traitements intelligents de l'information. En particulier, la désignation d'objectif comportera les indications de localisation, de vitesse et de cap de la cible ainsi qu'une fonction identification. Il est donc important de disposer d'une signature des cibles marines exploitable pour une classification manuelle ou automatique. L'imagerie radar haute résolution semble répondre à ce besoin. En effet, un traitement synthétique dérivé des traitements SAR et ISAR fournit dans la majorité des configurations opérationnelles une vue en perspective du navire à identifier et une analyse détaillée des composantes de l'image synthétique permet de définir des traitements d'images qui fourniront une silhouette du navire. Cette silhouette peut alors être analysée par un opérateur humain ou un processeur automatique.

**1 - TRAITEMENT SAR OU ISAR**

En imagerie radar haute résolution, deux techniques sont a priori utilisables :

- l'antenne synthétique directe ou SAR
- l'antenne synthétique inverse ou ISAR.

Dans les deux cas, l'image attendue est une projection plane où la première dimension est le résultat d'une analyse fine de la distance radar et où deux échos situés à la même distance sont séparés par effet doppler. Les deux méthodes se distinguent par l'origine des vitesses des échos, le traitement qui en est déduit et le plan de projection de l'image obtenue.

**1.1. SAR**

L'antenne synthétique directe est largement utilisée en cartographie. Les écarts de vitesse sont créés par l'avancement linéaire et uniforme du porteur radar à antenne latérale et sont liés à la position en azimut des diffuseurs. Cette technique fournit une image fine de cibles fixes avec une résolution optimale lorsque l'antenne est pointée à 90 degrés de la route avion. Le traitement adapté est une corrélation avec une fonction de référence, la réplique, qui dépend des caractéristiques de vol de l'avion (1,2). Cette réplique est calculée à partir de la centrale à inertie de l'avion ou évaluée à partir du signal reçu. Pour une résolution donnée, le temps d'intégration nécessaire croît avec la distance radar-cible.

Ce traitement appliqué à un radar de surveillance maritime à antenne latérale fournit une vue de dessus du navire à identifier dont la résolution en azimut est dégradée par les mouvements linéaires de la cible ; de plus dès que le navire présente des oscillations l'image obtenue n'est plus la vue de dessus attendue car la position des échos est modifiée par leur vitesse propre, souvent liée à leur hauteur.

### 1.2. ISAR

L'antenne synthétique inverse semble plus indiquée pour obtenir l'image d'une cible en mouvement. Son principe est bien connu dans le cas d'un radar immobile (3,4). Les écarts en vitesse utilisés pour discriminer les échos situés à la même distance du radar sont créés par les mouvements propres de la cible dont l'ampleur et la direction sont en général inconnus. Pendant le traitement, le mouvement de la cible est assimilé à une rotation de vecteur constant. Le traitement adapté est donc une simple analyse spectrale (5). L'image obtenue est une projection sur un plan contenant l'axe radar-cible et perpendiculaire à l'axe instantané de rotation(6). Cette technique n'est efficace que si la cible est animée de mouvements de rotation dont l'axe instantané n'est pas parallèle à la ligne de visée.

Par exemple, pour un navire en tangage, parallèle à l'axe radar-cible, le traitement ISAR donne une vue de côté ; c'est-à-dire une projection sur le plan contenant l'axe longitudinal du navire et ses superstructures. La résolution et le facteur d'échelle sur le deuxième axe (celui des hauteurs) sont fonction de l'ampleur des mouvements qui est a priori inconnue. De plus si le navire n'est pas parallèle à la ligne de visée qui appartient toujours au plan de projection, il est comprimé en distance d'un facteur proportionnel au cosinus de l'angle définissant la route du navire par rapport à l'axe radar/cible. Les dimensions réelles du navire (longueur et hauteur) sont proportionnelles à celles de l'image mais restent inconnues.

Pour un radar aéroporté à antenne latérale, le plan de projection de l'image obtenue par traitement ISAR est plus complexe. En effet, l'analyse spectrale est également sensible à la vitesse de l'avion et la position des échos sur l'image est donc fonction, outre leur hauteur, de leur position en azimut. La représentation du navire est en fait une perspective qui permet de connaître la longueur réelle du navire mais la hauteur vraie des superstructures ne résulte plus d'une simple homothétie sur le deuxième axe. D'autre part, la résolution sur cet axe est dégradée par l'avancement du porteur.

### 1.3. Conclusion

Dès que le radar et la cible ont des mouvements, l'image obtenue par traitement SAR ou ISAR n'est plus une projection sur un plan horizontal ou vertical mais est une représentation entre la "vue de dessus" (SAR) et la "vue de profil" (ISAR). En effet pour un radar aéroporté en antenne latérale et un navire présentant des oscillations de roulis et (ou) tangage, les deux types de traitement fournissent une vue en perspective qui donne des informations sur l'attitude, la longueur et la position des superstructures du navire. Pour interpréter l'image obtenue, il est nécessaire de comprendre tous les phénomènes à l'origine de sa formation. De plus, l'analyse des différentes sources de mouvement permet de définir un traitement synthétique adapté entre le SAR et l'ISAR qui améliore la résolution par rapport aux deux autres techniques. Il est montré dans la suite que ce traitement est une corrélation dont la réplique est calculée à partir de la centrale à inertie de l'avion et de certains mouvements de la cible évalués par pré-traitement.

## 2 - TRAITEMENT SYNTHETIQUE ADAPTE

### 2.1. Analyse des vitesses de la cible

Pour déterminer le traitement adapté, les origines possibles de vitesses des diffuseurs de la cible par rapport à l'avion sont recensées :

- l'avancement linéaire du porteur radar,
- les translations de la cible,
- les mouvements angulaires du navire (roulis, tangage, lacet).

Seules les vitesses radiales ont une influence sur la fréquence doppler des échos et donc sur la formation de l'image ; les mouvements angulaires d'axe instantané de rotation parallèle à la ligne de visée ne seront pas considérés.

Les translations de la cible sont dues à l'avancement du navire sur la surface de la mer et au pignonement. Le pignonement est en général très faible, il induit une vitesse radiale proportionnelle à la hauteur de l'écho et contribue à la part "vue de profil" de l'image.

L'avancement linéaire du navire se décompose en une vitesse tangentielle (parallèle à celle de l'avion) et une vitesse radiale. La vitesse radiale n'a pas d'incidence sur la formation de l'image puisqu'elle a une valeur identique sur tous les points situés à la même distance. Elle doit néanmoins être évaluée pour corriger les migrations en case distance qu'elle induit qui pourraient dégrader l'image.

La vitesse tangentielle du navire a un comportement identique à la vitesse du porteur. En effet, elle modifie la vitesse linéaire apparente de l'avion par rapport à la cible. C'est donc cette vitesse apparente (vitesse de l'avion moins vitesse tangentielle du navire) qui est prise en compte pour le calcul de la réplique. Cette composante permet comme dans le cas d'un traitement SAR de séparer des points situés à des azimuts différents et est à l'origine de la partie "vue de dessus" de l'image.

Les mouvements angulaires d'axe perpendiculaire à la ligne de visée et à la route de l'avion (lacet) sont en général négligeables, ils induisent également des vitesses radiales fonction de la position en azimut de l'écho et contribuent à la part "vue de dessus" de l'image. La vitesse radiale due au lacet est supposée constante durant le temps de traitement et n'est donc pas prise en compte dans le calcul de la réplique.

Enfin, les mouvements angulaires d'axe perpendiculaire à la ligne de visée et parallèle à la route de l'avion (combinaison de roulis et de tangage) ne modifient pas non plus le calcul de la réplique adaptée. Ils permettent de distinguer des échos situés à des hauteurs différentes. En effet, la vitesse radiale induite est proportionnelle à la vitesse angulaire instantanée, supposée constante pendant le temps de traitement, et à la hauteur de l'écho. Cette dernière composante des mouvements forme la partie ISAR ou "vue de profil" de l'image.

### 2.2. Traitement synthétique

Le traitement adapté est une corrélation comme dans le cas du SAR mais avec une réplique fonction des mouvements de la cible et de l'avion. La cible étant isolée, la corrélation peut être effectuée par simple transformée de fourier (7) ; c'est-à-dire que le signal reçu est multiplié par la réplique adaptée et la transformée de fourier est appliquée au résultat de cette multiplication.

La réplique est connue par un pré-traitement qui doit fournir la vitesse tangentielle de la cible. Pour ne pas dégrader l'image par des migrations en distance, la vitesse radiale de la cible doit aussi être évaluée par pré-traitement.

Le traitement proposé est donc le suivant :

- l'analyse fine en distance est effectuée (compression d'impulsion, stretch, bande synthétique, ...) pour séparer les échos en case distance (8,9).
- Sur chaque case distance, les effets des mouvements parasites de l'avion connus par les informations de la centrale à inertie et éventuellement de capteurs accélérométriques sont corrigés. Il suffit de multiplier le signal reçu par un signal dont la phase tient compte de ces parasites. Eventuellement cette phase peut inclure la vitesse uniforme de l'avion pour pré-focaliser le signal à traiter.

- Le pré-traitement ou autofocalisation du signal peut être une simple analyse spectrale de chaque case distance. En effet cette analyse donne sur chaque case la fréquence doppler de l'écho dominant. Sur la majorité des cases, cet écho à une hauteur nulle (les superstructures occupent une partie relativement réduite du navire) et donc sa fréquence est uniquement fonction de la position en azimut de la cible. Les cases où cette fréquence est modifiée par la hauteur de l'écho peuvent être éliminées. La fonction donnant la fréquence du signal en fonction de la case distance analysée est alors linéaire et sa pente est liée à la présentation du navire par rapport à la ligne de visée. Une régression linéaire sur les cases distance retenues permet donc de trouver l'orientation de l'axe longitudinal du navire par rapport à l'axe radar-cible. D'autre part la moyenne des fréquences sur l'ensemble des cases distance retenues est uniquement fonction de la vitesse radiale du navire qui peut être ainsi calculée. La vitesse tangentielle est déterminée à partir de la vitesse radiale et de la présentation du navire. D'autres méthodes d'autofocalisation sont proposées dans la littérature (10).

- La vitesse radiale est utilisée pour corriger les migrations éventuelles des échos en distance. La vitesse tangentielle de la cible détermine la réplique adaptée au signal. Le traitement de corrélation peut alors être effectué par simple transformée de fourier : focalisation fine du signal suivie d'une analyse spectrale.

Le temps d'intégration peut être dans une première étape adapté à la vitesse linéaire du porteur corrigée de la vitesse tangentielle de la cible et à la résolution cherchée puis être modifié au vue de l'image en fonction des mouvements angulaires de la cible. En effet, la résolution est limitée par la fréquence de variations des oscillations propres de la cible et cette fréquence fixe le temps d'intégration utile maximum (Annexe I). Pour améliorer la résolution, il faudrait adapter le traitement aux variations des mouvements d'oscillation du navire.

D'autre part les mouvements angulaires sont variables et l'interprétation de l'image sera favorisée si le traitement est effectué lorsqu'ils ont une amplitude importante. Pour ce le traitement est effectué sur des séquences successives du signal reçu et pour obtenir des images suffisamment espacées dans le temps (éclairage long de la cible), l'antenne est pointée sur la cible au lieu d'avoir une direction fixe comme dans le mode SAR classique. L'image où les superstructures sont le plus apparentes est retenue pour la classification (image 1).

### 2.3. Synthèse

Le mode d'utilisation du radar est proche de l'ISAR. L'antenne est pointée sur la cible pour disposer d'un temps d'éclairage supérieur à celui fixé par l'ouverture naturelle de l'antenne. Pour bénéficier du mode SAR, l'antenne doit néanmoins être dépointée par rapport à la route avion de sorte que la ligne de visée soit proche de la perpendiculaire à la route avion.

Le traitement adapté est dérivé du traitement SAR puisque c'est aussi une corrélation, le calcul du signal de référence nécessite en outre une autofocalisation du signal reçu. Les contraintes de traitement sont proches du mode ISAR : la résolution obtenue sur l'image et le temps de traitement sont liés aux mouvements propres de la cible. En particulier, la distance radar-cible n'a pas d'incidence sur le temps d'intégration qui est limité par les variations de roulis et/ou tangage.

Enfin pour s'adapter aux variations des oscillations du navire, plusieurs images sont obtenues à des instants successifs correspondant à différentes amplitudes du vecteur instantané de rotation. Ainsi, il est possible de sélectionner l'image la plus adaptée à une identification.

## 3 - INTERPRÉTATION DE L'IMAGE

L'image obtenue est une perspective dont l'angle de projection dépend de l'importance des oscillations du navire. En effet le premier axe correspond à la distance radar et la situation des points brillants sur le deuxième axe, qui correspond à la fréquence doppler des échos, est fonction de leur position en azimut et de leur hauteur puisque ces deux facteurs contribuent à la vitesse radiale d'un écho.

Expression de la vitesse radiale d'un écho au premier ordre :

$$V_r = - \frac{V^2 t}{D} - \frac{VY}{D} + \omega H$$

avec :

$V_r$  : vitesse radiale du diffuseur  
 $H$  : hauteur du diffuseur  
 $Y$  : position en azimut du diffuseur  
 $V$  : vitesse relative du porteur par rapport à la cible (vitesse réelle de l'avion moins vitesse tangentielle de la cible)  
 $D$  : distance avion-cible  
 $\omega$  : vitesse angulaire de la cible projetée sur la route avion

La position de l'écho sur le deuxième axe est obtenue par une analyse spectrale et est égale à sa fréquence doppler qui est donc donnée, après focalisation (suppression du terme dépendant du temps), par :

$$f_d = - \frac{2 VY}{\lambda D} + \frac{2 \omega H}{\lambda}$$

avec :

$f_d$  : fréquence doppler du diffuseur  
 $\lambda$  : longueur d'onde du signal émis

L'image du navire peut être interprétée comme une homothétie de la projection orthogonale du navire sur un plan contenant l'axe radar-cible et perpendiculaire au vecteur instantané de rotation qui a une composante sur l'axe défini par la route avion,  $\omega$ , et une composante sur l'axe des hauteurs,  $V/D$ . Le facteur d'échelle définissant l'homothétie est la norme du vecteur instantané de rotation. Cette représentation est difficilement exploitable puisque le plan de projection et le facteur d'homothétie dépendent du terme  $\omega$ , inconnu.

Les paramètres de vol de l'avion et la vitesse tangentielle de la cible étant connus, le terme  $V/D$  l'est également. La représentation est alors modifiée pour que la position des échos sur le deuxième axe soit donnée par :

$$Y + aH \quad \text{avec} \quad a = \frac{\omega D}{V}$$

La représentation du navire est alors une projection sur un plan horizontal. Cette projection n'est plus orthogonale et l'angle de la projection est défini par le coefficient  $a$ . En effet  $a$  représente l'angle du vecteur suivant lequel s'effectue la projection avec la normale au plan de projection. Le plan de projection étant connu et parallèle à la surface du navire, la perspective obtenue donne la longueur réelle du navire et son orientation par rapport à la ligne de visée. Selon l'importance du coefficient  $a$ , dont la connaissance est liée à celle des oscillations propres du navire les superstructures paraissent plus ou moins dilatées. Elles le seront d'autant plus quand le radar est loin du navire.

Si la cible n'a pas de vitesse angulaire l'image obtenue est une simple vue de dessus (projection orthogonale :  $a = 0$ ) sur laquelle la longueur et la largeur du navire peuvent être mesurées. Ces indications ne permettent qu'une classification "grossière" de la cible.

Dès que le navire a des mouvements de roulis et/ou de tangage, les superstructures du navire apparaissent ( $a \neq 0$ ). Quand le bateau est perpendiculaire à la ligne de visée l'image est plus difficilement exploitable car les superstructures sont projetées sur l'axe du navire et ne peuvent donc pas y être situées.

Enfin quand le navire a des mouvements et que sa route n'est pas parallèle à celle de l'avion (ce qui est vrai dans la majorité des cas), la perspective obtenue devient exploitable pour la classification. En effet la ligne des points de hauteur nulle donne la longueur réelle du navire. D'autre part les superstructures sont situées de façon exacte sur l'axe de navire et sont proportionnées entre elles. Cette signature peut être analysée par un opérateur humain.

Pour simplifier l'interprétation de la signature, l'orientation du navire étant déterminé par le traitement d'autofocalisation, la perspective peut être redressée sans perdre les informations de longueur et de position des superstructures (image 2). Si les superstructures sont particulièrement dilatées (cas d'une distance radar-cible élevée), un facteur d'échelle peut alors être appliqué au deuxième axe de l'image. Cette contraction de l'image permet d'améliorer la résolution et de présenter une silhouette mieux proportionnée.

AMELIORATION DE L'IMAGE ET PERSPECTIVES

Le mode opérationnel proposé permet d'obtenir une séquence d'images où l'angle de la perspective présentée évolue avec la vitesse angulaire du navire. Cette évolution se traduit par des dilatations et des contractions des superstructures du navire. En suivant, leur hauteur apparente sur la suite des images et en modélisant les mouvements de roulis et de tangage, les variations de la vitesse angulaire instantanée de chaque image peuvent être évaluées. Les traitements d'image doivent permettre dans un premier temps d'améliorer la finesse des échos. Ils devraient aussi localiser les échos de hauteur nulle qui ne subissent pas de modification sur la séquence d'images puisqu'ils ne sont pas sensibles à l'angle de projection. Le but est d'obtenir une silhouette compacte du navire sur laquelle il ne restera plus qu'à évaluer un facteur d'échelle pour connaître la hauteur vraie des superstructures. Néanmoins, même si la silhouette obtenue n'est pas proportionnée, elle fournit une signature identifiable par un opérateur ou par un système automatique de reconnaissance de formes.

REFERENCES

- 1 - M. LUCAS, "Synthetic Aperture Imaging Airborne Radar"  
IEEE International Radar Conference, 1985
- 2 - A.B.E. ELLIS, "The processing of Synthetic Aperture Radar signals"  
GEC Journal of Research, Vol. 2, N° 3, 1984
- 3 - J.J. WALKER, "Range Doppler imaging of rotating objects"  
IEEE Trans. AES, January 1980
- 4 - C.C. CHEN, H.C. ANDREWS, "Target-Motion-Induced Radar Imaging"  
IEEE Trans. AES, January 1980
- 5 - Y.W. CHEN, R.S. BERKOWITZ "Inverse Synthetic Aperture Radar Imaging techniques for Sea-surface targets"  
Proceedings of IGARSS'87 Symposium, Ann Arbor, May 1987
- 6 - M.J. PRICKETT, "Principles of Inverse Synthetic Aperture (ISAR) Imaging"  
IEEE EASCON, Arlington, September 1980
- 7 - M. SACK, I.D. CUMMING "Application of efficient linear FM matched filtering algorithms to Synthetic Aperture Radar processing"  
IEEE Proceedings, Vol. 132, N° 1, February 1985
- 8 - W.J. CAPUTTI, "Stretch : a time transformation technique"  
IEEE Trans. AES Vol. 7, N° 2, March 1971
- 9 - D.R. WEHNER "High Resolution Radar"  
Artech House, 1987
- 10 - K.H. WU, M.R. VANT, "A SAR focussing technique for imaging targets with random motion"  
NEACON, pp 289 - 295, 1984



Image 1 :

5 images obtenues à des instants successifs

- sur la deuxième et troisième vue, les mouvements angulaires ne sont pas suffisamment importants pour fournir une image caractéristique du navire. Leurs variations rapides perturbent la représentation.
- Sur les trois autres vues, les superstructures sont apparentes et permettent avec l'information sur la longueur du navire (mesurable sur l'image), de classer le navire.



Image 2a :

Image en perspective du navire

- donne la longueur et l'orientation du navire

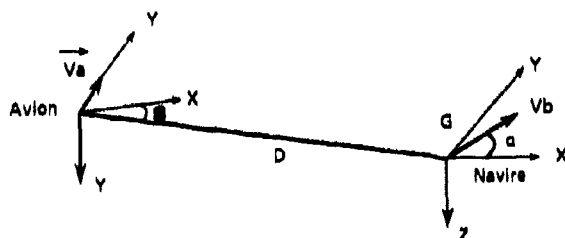
Image 2b :

Image précédente redressée

- permet de placer les superstructures sur l'axe longitudinal du navire
- donne aussi la longueur réelle du navire
- la comparaison avec la silhouette du navire montre que les superstructures ne sont pas à l'échelle

**ANNEXE**

## TEMPS D'INTEGRATION - RESOLUTION



$\vec{V}_a$  : vitesse avion

$\vec{V}_b$  : vitesse du navire

$\alpha$  : angle entre la route du navire et la ligne de visée

$S$  : site ( $S \approx 0$ )

$D$  : distance avion / cible

$G$  : centre de gravité du navire

$\Omega_r$  : vitesse angulaire de roulis

$\Omega_t$  : vitesse angulaire de tangage

$\Omega_l$  : vitesse angulaire de lacet ( $\Omega_l \approx 0$ )

Soit un point M du navire :  $\vec{GM} \begin{bmatrix} X \\ Y \\ H \end{bmatrix}$

$X$  : position du point sur l'axe radar/cible

$Y$  : position en azimut

$H$  : hauteur du point

La vitesse radiale du point M par rapport à l'avion est la somme de 3 termes :

- la vitesse radiale du navire :  $V_b \cos \alpha$

- la vitesse radiale induite par l'avancement relatif du porteur :

$$-\frac{(V_a - V_b \sin \alpha)^2 t}{D} - \frac{(V_a - V_b \sin \alpha)}{D} Y$$

- la vitesse radiale induite par le roulis et le tangage

$$(\Omega_r \sin \alpha + \Omega_t \cos \alpha) H$$

où  $\Omega_t \sin \alpha + \Omega_r \cos \alpha$  est la composante du vecteur instantané de rotation sur l'axe (OY), la composante sur l'axe (OX) n'ayant pas d'incidence sur la vitesse radiale du navire par rapport à l'avion.

La fréquence doppler du point M est donc :

$$f_d = \frac{2}{\lambda} \left[ -\frac{V^2 t}{D} - \frac{VY}{D} + \Omega H \right] + \frac{2}{\lambda} V_r$$

où :

$$V = V_a - V_b \sin \alpha$$

$$\Omega = \Omega_t \sin \alpha + \Omega_r \cos \alpha$$

$$V_r = V_b \cos \alpha$$

Après correction du terme dépendant du temps  $\left[ \frac{2 V^2}{\lambda D} t \right]$ , et du terme constant  $\left[ \frac{2 V r}{\lambda} \right]$

l'analyse spectrale de la case distance considérée donne :

$$fd = - \frac{2 V Y}{\lambda D} + \frac{2 H}{\lambda} H$$

La résolution sur  $fd$  est égale à  $\frac{1}{T}$  où  $T$  est le temps d'intégration si  $H$  est constant pendant l'intégration.

Si  $H$  varie, la fréquence doppler du point  $M$  dépend du temps, soit :

$$fd(t) = - \frac{2 V Y}{\lambda} + \frac{2 H(t) H}{\lambda}$$

$$\text{avec } H(t) = \theta_t \omega_t \cos(\omega_t t) \sin \alpha + \theta_r \omega_r \cos(\omega_r t) \cos \alpha$$

où :

$\theta_t$  : angle maximum de tangage

$\theta_r$  : angle maximum de roulis

$\omega_t = \frac{2\pi}{T_t}$  ;  $T_t$  : période de tangage

$\omega_r = \frac{2\pi}{T_r}$  ;  $T_r$  : période de roulis

$$\text{d'où } fd(t) = - \frac{2 V Y}{\lambda D} + \frac{2 H}{\lambda} \left[ \sin \alpha \theta_t \omega_t + \cos \alpha \theta_r \omega_r \right] \\ + \frac{2 H}{\lambda} \left[ \frac{\theta_t \omega_t^3 t^2}{2} \sin \alpha + \frac{\theta_r \omega_r^3 t^2}{2} \cos \alpha \right]$$

La résolution sur la fréquence pour un temps d'intégration  $T$  est donnée par le maximum de :

$$\frac{1}{T} \text{ et } \frac{2 H}{\lambda} T^2 \left[ \frac{\theta_t \omega_t^3 \sin \alpha + \theta_r \omega_r^3 \cos \alpha}{2} \right]$$

La résolution est optimale et vaut  $\frac{1}{T}$  lorsque  $T$  vérifie :

$$\frac{1}{T} = \frac{2 H}{\lambda} T^2 \left[ \frac{\theta_t \omega_t^3 \sin \alpha + \theta_r \omega_r^3 \cos \alpha}{2} \right]$$

si  $H_m$  désigne la hauteur maximale du navire, le temps d'intégration optimal est donné par :

$$T = \left[ \frac{\lambda}{H_m \left[ \theta_t \omega_t^3 \sin \alpha + \theta_r \omega_r^3 \cos \alpha \right]} \right]^{1/3}$$

La résolution sur la hauteur obtenue est alors  $\Delta H$

$$\text{avec } \frac{2 \Delta H}{\lambda} (\theta_t \omega_t \sin \alpha + \theta_r \omega_r \cos \alpha) = \frac{1}{T}$$

$$\text{soit } \Delta H = \frac{\lambda}{2 (\theta_t \omega_t \sin \alpha + \theta_r \omega_r \cos \alpha)} \left[ \frac{H_m (\theta_t \omega_t^3 \sin \alpha + \theta_r \omega_r^3 \cos \alpha)}{\lambda} \right]$$

APPLICATION NUMÉRIQUE ( $\alpha = 45^\circ$ )

TYPE DE NAVIRE	VALEUR DE ROULIS ET TANGAGE	TEMPS D'INTEGRATION OPTIMAL	RESOLUTION MAXIMALE SUR LA HAUTEUR
PETIT NAVIRE (longueur $\leq 50$ m)	Mer forte $T_t = 5$ s $\theta_t = 20^\circ$ $T_r = 8$ s $\theta_r = 5^\circ$	0,16 s	0,3 m
	Hauteur maximale : 15 m		
GROS NAVIRE (longueur $\approx 100$ m)	Mer moyenne $T_t = 5$ s $\theta_t = 10^\circ$ $T_r = 8$ s $\theta_r = 5^\circ$	0,20 s	0,5 m
	Hauteur maximale : 50 m		
	$T_t = 13$ s $\theta_t = 10^\circ$ $T_r = 8$ s $\theta_r = 5^\circ$	0,24 s	0,6 m

## DISCUSSION

**C.J. Baker**

What are the cross and down range resolutions of your measurements?

**Author's Reply**

La résolution en distance radar est de 3 m. Sur deuxième axe, elle est certainement meilleure, elle est liée à la vitesse angulaire du navire qui est inconnue mais certainement importante, vu la hauteur apparente du mât.

Problem in ISAR Processing with Range Resolution  
by Stepped Frequency Bursts

Gerd Krämer, Research Establishment for Applied Science, FGAN - FHP  
Neuenahrer Str. 20, D 5307 Wachtberg-Werthhoven, Germany

AD 4005 847  
Abstract

If a target image is reconstructed from an ISAR measurement by immediate application of the Discrete Fourier Transform, the image becomes blurred with increasing distance from its center. It is shown that with an ISAR sensor applying stepped frequency bursts, samples of the 2-dimensional Fourier Transform of a 2-dimensional scatterer density are measured and how a target image can be reconstructed.

1. Introduction

In this paper, the generation of a target image based on rotative motion of a target is considered. If the target is moving on a known trajectory, it is assumed that its motion relative to the radar can be decomposed into a radial motion of a reference point superimposed by a rotative motion. If the target is moving with fixed orientation in space on a straight trajectory, the axis of rotation is orthogonal to the plane spanned by the position vectors of initial and end point of the target trajectory segment on which the processing of the ISAR image is based.

It is assumed that the radar transmits pulse bursts consisting of impulses with rectangular envelopes of width  $T$  whose carrier frequencies increase from impulse to impulse by a constant amount  $f$ . The  $m$ -th transmitted pulse burst is described by

$$s_m(t) = \sum_{k=0}^{M-1} \text{rect}\left(\frac{t-kT_m - mT_B}{T}\right) e^{j(2\pi(f_0 + kf_A)t + \phi_{mk})} \quad (1-1)$$

where

$$\text{rect}(x) = \begin{cases} 0 & \text{if } |x| > \frac{1}{2} \\ 1 & \text{otherwise} \end{cases} \quad (1-2)$$

denotes the rectangular impulse envelope and complex notation has been used because signal processing in I and Q components is assumed throughout the following. The time interval between adjacent impulses within one burst is denoted  $T_T$ , the distance of impulses with equal carrier frequencies in adjacent bursts is denoted  $T_B$ .

Let the signal delay due to the reflection of the radar signal by a scattering center at the reference point be denoted by  $t_0$ . Neglecting attenuation and RCS, the signal received from that scattering center would be given by

$$s_{rm}(t) = \sum_{k=0}^{M-1} \text{rect}\left(\frac{t-kT_T - mT_B - t_0}{T}\right) \cdot e^{j(2\pi(f_0 + kf_A)t + \phi_{mk})} e^{-j2\pi(f_0 + kf_A)t_0} \quad (1-3)$$

The received impulses are downconverted into I and Q components which are integrated over the impulse duration time  $T$ . It is assumed that the integration gate extent  $T$  is large compared to the delay variation due to the distance of the individual target scattering centers so that all contributions are integrated with negligible loss.

If the amplitude of the integrator output resulting from the scattering center under consideration is denoted  $a_0$ , the complex valued response on the  $k$ -th impulse of the  $m$ -th burst is given by

$$s_{0km} = a_0 e^{-j2\pi(f_0 + kf_A)t_0} \\ = a_0 e^{-j2\pi f_0 t_0} e^{-j2\pi f_A t_0 k} \quad (1-4)$$

The complex numbers obtained from the integrator may be corrected by multiplication with  $e^{j2\pi k f_A t_0}$  to provide for the reference on the scattering center with delay  $t_0$ .

It is now assumed that a scattering center is displaced in range by some distance  $y$  and in crossrange by some value  $x$  with respect to the reference point and that it is rotating with angular velocity  $\omega$ . Then in analogy to Eq. (1-4) the complex numbers obtained at the integrator output are given by

$$S_{1km} = a_1 e^{-j2\pi f_0 (t_0 + \frac{2}{c} y \cos \omega (kT_1 + mT_B) + \frac{2}{c} x \sin \omega (kT_1 + mT_B))} \\ \cdot e^{-j2\pi f_0 (t_0 + \frac{2}{c} y \cos \omega (kT_2 + mT_B) + \frac{2}{c} x \sin \omega (kT_2 + mT_B))} \cdot k \quad (1-5)$$

By applying the correction with  $e^{j2\pi f_0 k t_0}$  it follows

$$S_{1km} = a_1 e^{-j2\pi f_0 (t_0 + \frac{2}{c} y \cos \omega (kT_1 + mT_B) + \frac{2}{c} x \sin \omega (kT_1 + mT_B))} \\ \cdot e^{j2\pi f_0 k t_0} (y \cos \omega (kT_1 + mT_B) + x \sin \omega (kT_1 + mT_B)) k \quad (1-6)$$

To allow for a perfect imaging of the scattering centers by twofold application of the Discrete Fourier Transform on the complex numbers obtained, restrictions have to be applied to target size and rotation speed. Let  $NI$  denote the number of impulses per burst, see Eq. (1-1), and  $NB$  denote the number of bursts to be processed. Then if

$$\frac{2f_0}{c} y (1 - \cos \omega ((NI-1)T_1 + (NB-1)T_B)) \ll 1 \\ \frac{2f_0}{c} x \sin \omega (NI-1)T_1 \ll 1 \\ (NI-1)f_0 \ll f_0 \quad (1-7)$$

$$\frac{2(NI-1)f_0}{c} x \sin \omega (NI-1)T_1 + (NB-1)T_B \ll 1$$

it follows from Eq. (1-6), approximating the sine by a linear function,

$$S_{1km} \approx a_1 e^{-j2\pi f_0 (t_0 + \frac{2f_0}{c} y)} \cdot e^{-j2\pi \frac{2f_0}{c} k x T_B} \cdot e^{-j2\pi \frac{2f_0}{c} y \cdot k} \quad (1-8)$$

from which  $x$  and  $y$  can be imaged by taking the Discrete Fourier Transform with respect to  $k$  and with respect to  $m$ . If the restrictions in Eq. (1-7) are not fulfilled, however, combination and  $k^2$  terms appear which result in a blurring of the image increasing with the target dimensions in range and crossrange  $1/\lambda$ . In the following, possibilities to avoid image blurring will be investigated.

## 2. Generation of the radar echo

It is assumed that the distribution of the scattering centers which shall be imaged can be described by a 2-dimensional scatterer density function  $s(x,y)$ . This can be thought of as being a projection of the target scattering centers into a plane orthogonal to the axis of rotation. In the case of isolated scattering centers,  $s(x,y)$  contains Dirac pulses. It is further assumed that throughout the whole data collection time for one ISAR image the same scattering centers contribute to the generation of the echo signals.

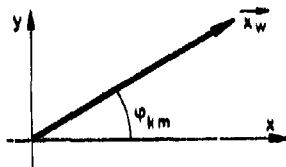


Fig. 1 Unit vector in wave propagation direction in target coordinate system

It is further assumed that within the target dimensions the radar signals can be described by plane waves. The coordinate system  $x,y$  in which the scatterer density is described is assumed to be orthogonally oriented with respect to the axis of target rotation, its origin is taken as the reference point. Let  $k_w$  in Fig. 1 denote the unit vector in wave propagation direction in the target coordinate system  $x,y$  pertaining to the  $k$ -th impulse of the  $m$ -th burst and let  $t_0$  denote the signal delay corresponding to the reference point.

With  $\vec{x}_w = (\cos\phi_{km}, \sin\phi_{km})$  (2-1)

it follows for the component of the integrator output signal for the k-th impulse of the m-th burst resulting from the element  $s(x,y) \cdot dx dy$  in analogy to Eq. (1-4), neglecting an amplitude factor common for all received impulses,

$$d g_{km} = s(x,y) dx dy e^{-j2\pi(f_0 + kf_A)(t_0 + \frac{2}{c}(\vec{x} \cdot \vec{x}_w))} \\ = e^{-j2\pi(f_0 + kf_A)t_0} s(x,y) e^{-j2\pi(f_0 + kf_A)\frac{2}{c}(\vec{x} \cdot \vec{x}_w)} dx dy \quad (2-2)$$

with  $\vec{x} = (x,y)$

and  $(\vec{x} \cdot \vec{x}_w)$  indicating the dot product

$$(\vec{x} \cdot \vec{x}_w) = x \cos\phi_{km} + y \sin\phi_{km} \quad (2-3)$$

To calculate the total output signal, Eq. (2-2) has to be integrated over the scattering density, thus

$$g_{km} = e^{-j2\pi(f_0 + kf_A)t_0} \iint s(x,y) e^{-j2\pi(f_0 + kf_A)\frac{2}{c}(x \cos\phi_{km} + y \sin\phi_{km})} dx dy \quad (2-4)$$

Introducing the 2-dimensional Fourier Transform of  $s(x,y)$

$$S(u,v) = \iint s(x,y) e^{-j2\pi(ux + vy)} dx dy \quad (2-5)$$

it can be seen that  $g_{km}$  of Eq. (2-4) equals

$$g_{km} = e^{-j2\pi(f_0 + kf_A)t_0} S\left(\frac{2}{c}(f_0 + kf_A) \cos\phi_{km}, \frac{2}{c}(f_0 + kf_A) \sin\phi_{km}\right) \quad (2-6)$$

Thus, except for the factor  $e^{-j2\pi(f_0 + kf_A)t_0}$ , which is held constant by tracking the reference point, by the ISAR sensor samples of the 2-dimensional Fourier Transform of the scatterer density are measured. During the transmission of the NB bursts consisting of  $N_I$  impulses each the target orientation changes by some angle  $\Delta\phi$ . If the x-axis of the target coordinate system is arbitrarily placed in the bisector of the angle  $\Delta\phi$ , the samples in the 2-dimensional frequency plane  $u,v$  are located in a sector symmetrical to the  $u$ -axis as shown in Fig. 2.

Since the samples are located in a bounded area of the  $u,v$ -plane which does not include the origin, they can be regarded as a description of a 2-dimensional bandpass signal.

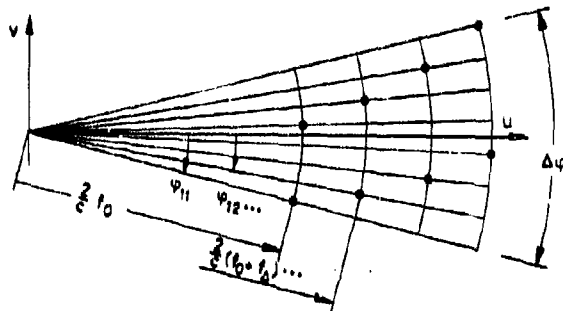


Fig. 2 Location of sample points in  $u,v$ -plane

Consider a 2-dimensional transfer function restricting the input on a rectangular area of width  $\Delta u$  and  $\Delta v$ , respectively, centered at  $(u_0, 0)$ ,

$$H(u,v) = \text{rect}\left(\frac{u-u_0}{\Delta u}\right) \text{rect}\left(\frac{v}{\Delta v}\right) \quad (2-7)$$

with  $\text{rect}(x)$  according to Eq. (1-2). The corresponding 2-dimensional impulse response is given by

$$h(x,y) = \Delta u \Delta v \text{sinc}(\pi \Delta u x) e^{-j2\pi u_0 x} \text{sinc}(\pi \Delta v y) \quad (2-8)$$

with

$$\text{sinc}(x) = \begin{cases} 1 & \text{if } x = 0 \\ \frac{\sin \pi x}{\pi x} & \text{elsewhere} \end{cases} \quad (2-9)$$

Restricting the Fourier Transform  $S(u,v)$  of the scatterer density  $s(x,y)$  on the rectangle by multiplication with  $H(u,v)$  from Eq. (2-7) corresponds to the 2-dimensional convolution of  $s(x,y)$  with  $h(x,y)$  from Eq. (2-8), denoted

$$g(x,y) = s(x,y) \otimes h(x,y) \quad (2-10)$$

Thus, if two distinct scattering centers exist according to

$$s_1(x,y) = \delta(x) \delta(y) + \delta(x-x_0) \delta(y-y_0) \quad (2-11)$$

it follows with Eq. (2-10)

$$g_1(x,y) = h(x,y) + h(x-x_0, y-y_0) \quad (2-12)$$

Since as a first approximation  $h(x,y)$  from Eq. (2-8) is restricted on the interval  $|x| < 1/(2\Delta u)$ ,  $|y| < 1/(2\Delta v)$ , the two scattering centers can be distinguished if

$$|x_0| < \frac{1}{\Delta u} \text{ or } |y_0| < \frac{1}{\Delta v} \quad (2-13)$$

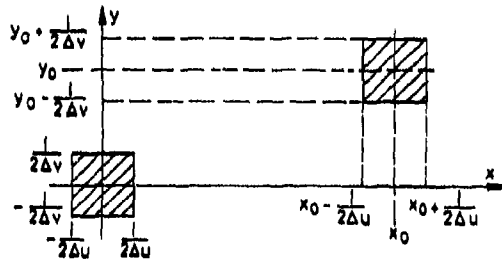


Fig. 3 Reconstructed scatterer density

The equivalent 2-dimensional low pass signal of

$$G(u,v) = S(u,v)H(u,v)$$

with  $H(u,v)$  from Eq. (2-7) is given by shifting the Fourier Transform to the origin resulting in

$$G_L(u,v) = S(u+u_0, v) \text{rect}\left(\frac{u}{\Delta u}\right) \text{rect}\left(\frac{v}{\Delta v}\right) \quad (2-14)$$

and therefore

$$g(x,y) = \int_{-L}^L s(x,y) e^{-j2\pi u_0 x} \int_{-L}^L \Delta u \Delta v \text{sinc}(\pi \Delta u x) \text{sinc}(\pi \Delta v y) \quad (2-15)$$

It is intended to reconstruct the scatterer density of a target from the equivalent 2-dimensional equivalent low pass signal pertaining to the section of the 2-dimensional Fourier Transform as measured by the ISAR sensor. To perform the reconstruction by application of the Discrete Fourier Transform, the sampled function in the sector of the  $u,v$ -plane according to Fig. 2 has to be resampled in a rectangular lattice  $1/L$ . Possibilities for the resampling are currently under investigation in the FHP. To distinguish two scattering centers according to the definition underlying Eq. (2-13) and Fig. 2, as well as the definition of  $u$  and  $v$  according to Eq. (2-6), they have to be separated by

$$|x_0| > \frac{1}{\Delta u} = \frac{1}{(NI-1) \frac{\lambda}{2A}} \quad (2-16)$$

in range or

$$|V_0| \frac{1}{\Delta V} = \frac{2}{c} f_0 \cdot 2 \tan \frac{\Delta \varphi}{2} \approx \frac{2}{c} f_0 \cdot \Delta \varphi \quad (2-17)$$

in crossrange. It follows thus from Eq. (2-17) for the necessary angular change

$$\Delta \varphi > \frac{c \Delta V}{2 f_0} \quad (2-18)$$

**Reference**

/1/ D. R. Wehner, High Resolution Radar, Artech House, ISBN-0-89006-194-7



A FAST ISAR-IMAGING PROCESS AND  
ITS INHERENT DEGRADING EFFECTS ON IMAGE QUALITY

by

K.-H. Bethke  
D. Röde

Institut für Hochfrequenztechnik  
Deutsche Forschungsanstalt für Luft- und Raumfahrt (DLR)  
D-8031 Oberpfaffenhofen  
F.R. Germany

AD-POOS 848

**SUMMARY**

A method for a fast two-dimensional inverse synthetic aperture radar (ISAR) imaging process is presented. A coherent short pulse radar is used to sample amplitude and phase of the backscattered field from a continuously rotating object. This is being done while a narrow range gate is sweeping in range steps of 15 cm across the target plane at a typical speed of 150 m/s. Applying fast synthetic aperture radar (SAR) principles, in an off-line process for each range cell an acceptable good cross-range resolution can be obtained when processing angle intervals of less than 30°. The influence of analytical approximations as well as the effect of moving scattering centers through several range resolution cells during the process interval can cause severe image degradations. Two methods for partial and complete compensation of those effects under the aspect of minimum loss in processing speed have been developed and will be presented here.

**1. INTRODUCTION**

By processing radar echoes from geometrical complex shaped objects it is possible to reconstruct the spatial distribution of the scattering centers in form of two-dimensional images. The field of radar echoes can be described as a linear superposition of high frequency signals mainly backscattered from independent spot reflectors. The exact determination of the two-dimensional radar signature is the best prerequisite for identification of unknown objects passing the radar beam. However, these intentions can be affected by process inherent errors which can result in image smearing effects and in systematically decreasing RCS values.

Two-dimensional radar imaging independently requires the resolution in range, the radar line of sight, and in cross-range, the azimuth direction. Range resolution is obtained from the time-delay information of the radar echoes. That can be achieved either by using wideband multifrequency signals where time-delay sorting is realized via FFT algorithms or by using a gated short pulse radar, in which case the range resolution is determined by the echo pulse duration. In order to obtain the cross-range resolution, a relative motion between radar sensor and target is necessary. Coherent data sampling of amplitude and phase of the received signals is necessary for high resolution imaging. For this, amplitude and phase values either obtained in the frequency domain by varying the signal frequency or in the time domain by transmitting short pulses at a constant frequency have to be recorded as a function of aspect angle. With the aid of the synthetic aperture radar (SAR) principle a synthetic pencil-like antenna beam can be generated in an off-line process evaluating the recorded coherent data samples. The cross-range resolution, given by the width of the synthetic aperture antenna beam, is determined by the aperture length which is equivalent to the processed angle interval. That provides a two-dimensional image of the projection of the spatial distribution of the scattering centers onto a plane normal to the rotation axis. A detailed survey about SAR or ISAR (inverse synthetic aperture radar) methods is given in [1] - [4].

Fast imaging techniques are needed for time and cost effective investigations of the backscatter behaviour of scaled models or original targets in the real world identification problems. On the other hand, airborne intelligence and reconnaissance also require fast imaging techniques. In each case, the guarantee for a simple and reliable image interpretation requires, that degrading effects on image quality resulting from the image process itself have to be known and to be removed as far as possible.

The experiments described in this paper have been conducted with a short-pulse Doppler-radar. This has the advantage of range resolution in real time by sweeping the delay time for the receiver gate continuously or stepwise, as it was done here at a considerable velocity. In an off-line process fast SAR principles were applied to generate radar images for small-angle looks with processed angle intervals of less than 30°. Scaled targets of small size are usually mounted on styrofoam-columns standing on ground-based turntables and they are homogeneously illuminated by the stationary radar so that the generated relative motion between the radar sensor and target is a circular one. Because of the equivalence to the relative motion generated by a moving radar and a stationary target as it is the usual situation that we find in SAR technique all experiences made in ISAR imaging can be transferred to SAR imaging and vice versa. This also holds true for the case of a ground stationed radar and a moving object with a transverse velocity component as it is given in the cases of observing and following a passing aircraft with the radar beam or eventually observing even a straight line flying aircraft intersecting a fixed radar beam [5].

The most significant image degrading effects resulting from the usual ISAR processing of coherent raw data in the time domain are discussed. These effects mostly depend on the motion of scattering centers through resolution cells, especially, if the coherent integration time is longer than the transit time of a scattering center through one range cell. In those cases the effective synthetic aperture is shortened and signal contributions of a single scattering center will appear in neighbouring range cells so that the calculated RCS is decreased and the imaged scattering center is smeared out over several resolution cells. A similar effect in cross direction can be observed resulting from certain approximations relevant for the

fast imaging process. Two methods for partial and complete compensation for these image degrading effects are briefly presented. Both methods have been developed under the aspect of fast image processing.

## 2. EXPERIMENTAL SETUP

The system used here was a gated coherent short pulse radar, which covers the frequency range between 8 and 18 GHz. The receiver gate width as well as the transmitter pulse length could be adjusted from 1  $\mu$ s down to 0.8 ns. This apparatus is used for ground-based high resolution RCS-measurements of academic objects, scaled models or original targets.

In order to obtain high resolution in range, a constant receiver gate width and transmitter pulse length of about 1 ns is used. In most practical cases this adjustment is sufficient for imaging targets with maximum object dimension down to about 1 m. For a two-dimensional image generation of the spatial target reflectivity distribution at a fixed frequency the delay time of the receiver gate is repeatedly swept in steps of 1 ns, corresponding to a depth of  $\Delta y = 15$  cm for each range cell, whereby the sweeping time here was fixed to 40 ns. 40 range steps were used during each sweep which is equivalent to an image depth of 6 m. This adjustment required an amplitude and phase sampling of the backscattered signal at every millisecond.

Most of the RCS-measurements which are performed at outdoor-ranges suffer from ground reflexions. This effect can be suppressed by installing radar fences at proper positions inside the measurement range [6]. Figure 1 shows a typical measurement range for smaller scaled targets as it was used for this work. The targets had been mounted on a continuously rotating styrofoam column and were homogeneously illuminated by the ground-based stationary radar. The range sweeps were triggered by the angular decoder every 0.1° at a fixed rotational speed of 1°/sec. The effective speed of the moving range gate was chosen to 150 m/sec, only limited by the maximum available video bandwidth of 3 kHz.

## 3. FAST ISAR-PROCESSING

To obtain cross-range resolution typical SAR principles will be used. This is possible, because only a relative motion between radar sensor and target is required, so that the SAR principles also hold in the inverse case of a stationary radar and a moving object. Due to the rotational target motion, for each range cell a synthetic aperture can be generated on part of a circle around the target, as depicted in Figure 2, with an equidistant spacing of the aperture elements of 0.1°, corresponding to the data sampling triggered by the angular decoder. The maximum cross-range dimension  $D$  in object space that can be imaged without any aliasing artifacts is determined by this angular increment  $\delta\theta$  via the relation

$$(1) \quad \delta\theta = \frac{\lambda}{2D}$$

where  $\lambda$  denotes the signal wavelength.

The typical SAR or ISAR principle is to focus and to steer in each range cell a narrow synthetic antenna beam across the target plane via compensation of signal phase differences resulting from different signal pathlengths between a target point to each aperture element. This can be realized stepwise for every resolution cell at a constant range by a coherent superposition of the received complex signals sampled every 0.1°, after preceding phase corrections demanded by the focusing process have been applied.

In a rectangular coordinate system - where  $y$  denotes the range coordinate - the phase of a backscattered signal from a point located at  $(x, y)$  in the object space and measured relative to the transmitted signal is given by

$$(2) \quad \varphi(x', y') = -\frac{4\pi}{\lambda} \left[ R_0 + 2(y_i \cos \theta_n - x_i \sin \theta_n) + \frac{r_{iA}^2}{R_0} \right]^{\frac{1}{2}}$$

where  $x'_i$  and  $y'_i$  are the coordinates in an object fixed coordinate system defined by the coordinate transformation

$$(3) \quad \begin{aligned} y' &= y \cos \theta_n - x \sin \theta_n \\ x' &= y \sin \theta_n + x \cos \theta_n \end{aligned}$$

for clockwise rotating the target by an angle of  $\theta_n = n \delta\theta$  ( $n = \text{integer}$ ) [7];  $R_0$  denotes the distance from the radar sensor to the center of rotation and  $r_{iA} = \sqrt{x_i^2 + y_i^2}$  is the radial distance between a point  $(x_i, y_i)$  on the object and the rotation axis. A so-called direct method will focus and steer the synthetic beam according to the relation

$$(4) \quad A(x_A, y_A) = \frac{1}{N} \sum_{n=0}^{N-1} V(\theta_n, y_i) \exp[-j\varphi(x'_i, y'_i)],$$

where  $A(x_A, y_A)$  is the reconstructed average signal strength backscattered from a target point located at  $(x_A, y_A)$ ;  $N$  gives the number of data samples which is equivalent to the process angle  $\Delta\theta$

$$(5) \quad \Delta\theta = N \delta\theta$$

and  $V(\theta_n, y_i)$  denotes the received complex signal in the  $i$ -th range at the angle  $\theta_n$ .

In order to limit the computational burden, however, the number of multiplications, required for forming and steering a synthetic antenna beam, can be significantly reduced, if  $R_0 \gg r_{iA}$  and furthermore if the process angle can be confined to values  $\Delta\theta < 30^\circ$ , so that the approximations  $\sin \theta_n \approx \theta_n$  and  $\cos \theta_n \approx 1$  can be applied. With these approximations Eqs.(2) and (4) yield

$$(6) \quad A(x_k, y_l) \approx \frac{1}{N} \exp\left[ +j \frac{4\pi}{\lambda} \left( R_0 + y_l + \frac{y_l^2}{2R_0} \right) \right] \sum_{n=0}^{N-1} V(\theta_n, y_l) \exp\left[ -j2\pi \frac{2\theta_n}{\lambda} x_k \right],$$

where all angle invariant phase terms are written outside the summation and will be neglected subsequently because they carry no angular information so that Eq.(6) reduces to

$$(7) \quad A(x_k, y_l) \approx \frac{1}{N} \sum_{n=0}^{N-1} V(\theta_n, y_l) \exp\left[ -j2\pi \frac{2\theta_n}{\lambda} x_k \right],$$

which has the form of a digital Fourier-transform [7]. Therefore, the cross-range resolution in each range cell can be obtained by using Fast Fourier Transform (FFT) algorithms. Fast data sampling in combination with fast software algorithms fulfil the conditions for a speedy two-dimensional image generation. It is a further advantage of this method that the knowledge of an exact position of the rotational center in respect to the range coordinate is not required, because the phase corrections in Eq.(7) do not include the range coordinate  $y_l$ . The method described in this paper can be used for groundtruth ISAR imaging and, in principle, for imaging of moving targets, which also have a transverse velocity component, or for imaging of ground-based targets observed from an aircraft.

However, the process of a stepwise range gate sweep across the target under test as well as the applied approximations when deriving the image algorithm can yield significant focusing errors, which cause an increasing blurring of the picture in its peripheral area in case that object dimensions and process angle are large. Because large process angles are required for a fine cross-range resolution which is determined by the cross-range cell size  $\Delta x$  via the relation

$$(8) \quad \Delta x = \frac{\lambda}{2\Delta\theta},$$

a high resolution of scattering centers and an exact determination of RCS-values will be limited, if no further error correcting measures are being taken.

#### 4. IMAGE DEGRADING EFFECTS

The typical degrading effects are demonstrated for a case where the field of 20 independently scattering point reflectors of equal cross-section with a mutual distance of about 1 m had been simulated. A subsequent analysis with the algorithm of Eq.(7) created the image displayed in Figure 3. The receiver gate length and the transmitter pulse length are both assumed to be 1 ns, and the other parameters are  $\Delta y = 15$  cm (depth of a range cell),  $\lambda = 3$  cm,  $\Delta\theta = 5.5^\circ$  and  $R_0 = 600$  m.

There are two dominant effects, which cause these degradations. The degradations in range direction mainly result from the approximation  $\cos \theta \approx 1$ . This approximation can safely be used for process angles of less than about  $5^\circ$ . If we reformulate the approximations used for deriving Eq.(6) by taking into account higher orders we arrive at:

$$(9) \quad \frac{4\pi}{\lambda} y_l (1 - \cos \Delta\theta/2) \ll \pi.$$

If we use the left hand side of Eq.(9) to calculate the phase error arising from Eq.(7) for a point scatterer located at  $(x=0, y=6m)$ , we obtain a deviation from the ideal value of about  $165^\circ$ , which means, that the phase corrections performed on signals at the edge of the aperture is insufficient and will result in a nearly antiphase condition compared to the phase-corrected signal from the aperture center.

The second dominant effect on image quality is the migration of a scattering center through more than one range cell during the processing time. That so-called range walk reduces the effective aperture width and hence the resolution quality, especially for scattering centers at larger cross distances. For the range cell including the rotational center Figure 4 shows an experimental result of the sampled signal amplitude shape originating from a point scatterer moving on a circle of the radius  $r = 1$  m during the angular interval of  $\Delta\theta = 51.2^\circ$ . The receiver gate width and the transmitter pulse length again were both 1 ns. As a first result, we observe the expected triangle amplitude shape, as a consequence from the convolution of the receiver gate with the received echo pulse, which means, that the sampled echo amplitude in each range cell strongly depends on the location of a scattering center in the image plane. As a second result, one can see that if the process interval is considerable larger than the transit time of scattering center through a resolution cell, the scattering centers are only detectable across a limited angular interval which is smaller than the process interval. Hence, the effective width of the synthetic aperture is limited and the cross-range resolution becomes independent from the size of the angular process interval. In Figure 4 the measured width of the foot print from the sampled point reflector echo given by the product  $r \cdot \theta_e$  ( $\theta_e$  = effective aperture length) extends about 40 cm which is equivalent to 2.6 ns, whereas a width of  $y_{conv} = 30$  cm would be expected corresponding to the convolution of two rectangular functions each of 1 ns. The reason for this deviation is, that the receiver gate and the transmitter pulse do not exhibit any longer a well defined rectangular but a more gaussian pulse shape if these low gate and pulse lengths are reached. In order to avoid ambiguous definitions the measured convolution result shown in Figure 4 is taken to define the range filter function (range gate) used for all other image results presented in the following chapters.

Several intermediate steps of the amplitude change depending on the scatterers lateral position are displayed in Figure 5. For cross-range locations  $x > x_{conv}$  where  $x_{conv}$  is defined by

$$(10) \quad x_{conv} = \frac{y_{conv}}{\Delta\theta},$$

the effective aperture will be shortened. At the same time, the maximum signal contribution of a point reflector will also appear in neighbouring range cells, as depicted in Figure 6. So, the range walk effect causes a decrease of the reconstructed average signal amplitude, a decrease in range resolution and according to Eq. (8) for  $x > x_{conv}$  a decrease in cross-range resolution. Defocusing effects the signal amplitudes as is shown in Figure 7, where for the same parameters as in Figure 3 the envelope of the amplitude maxima of all reconstructed unit point reflectors at any position in the image plane is calculated for two relevant cases of object size. It is emphasized, that these calculations only hold for point-like scatterers with a maximum cross dimension of less than  $\Delta x$ . For cross dimensions greater than  $\Delta x$  a special treatment is necessary due to the extended backscatter pattern [7].

It is a general technique in SAR and ISAR imaging to weight the aperture signals  $V(\theta_{nt}, y)$  before data processing, according to Eq. (7), with a window function, in order to reduce the side lobe levels of imaged scattering centers [8]. The use of windows can remarkably reduce degrading effects, because especially at the edges of the synthetic aperture, where the focusing errors are largest, the signals  $V(\theta_{nt}, y)$  will be mostly damped and therefore the influence of phase correction errors will be reduced too [7]. The result is illustrated in Figure 8. But nevertheless, there still exist significant image degradations, especially, if maximum target cross dimension is greater than  $2 x_{conv}$ .

The dominant image degrading effects caused by an incorrect focused aperture are typical when processing time domain raw data in ISAR/SAR techniques, and they are also present in processing frequency domain data. In order to obtain reliable results either for an exact interpretation of the two-dimensional radar images under the aspect of camouflage work or for the identification of typical target signatures under the aspect of target classification and target identification the dominant degrading effects have to be known and compensated for.

### 5. COUNTER MEASURES

In this paper two techniques for limiting or even compensating image degradational effects are briefly presented. These techniques have been developed under the aspect of a fast image processing. Both techniques require the knowledge of the range gate number including the rotational center and the knowledge of typical signal shape for a point scatterer as a consequence of the range walk, which gives the spatial filter form of the range gate, as shown in Figure 4. As an example some results have been calculated with the parameters displayed in Figure 3.

#### AMPLITUDE CORRECTIONS

The first presented method is an amplitude-corrective measure as described in more detail in [7]. Approximating the signal shape of  $V(\theta_{nt}, y)$  by a simple triangular function for equal lengths of receiver gate and transmitter pulse, as indicated in Figure 4, one can derive an analytical description for the amplitude behaviour of a moving target point reflector depending only on its lateral position. Using a Hamming window as weighting function the amplitude dependence of the reconstructed signals  $f_x$  on the cross-range coordinate  $x$  results in

$$(11) \quad f_x = \begin{cases} 0.54 - 0.177 \frac{|x|}{x_{conv}} & \text{for } |x| < x_{conv} \\ 0.27 \frac{x_{conv}}{|x|} + 0.0466 \frac{|x|}{x_{conv}} (1 + \cos 2\pi a) & \text{for } |x| \geq x_{conv} \end{cases}$$

where the dimensionless value  $a$  is defined as

$$(12) \quad a = \frac{1}{2} \left( 1 - \frac{x_{conv}}{|x|} \right)$$

As another result of [7] the amplitude dependence  $f_y$  on the range coordinate  $y$  can be approximated by

$$(13) \quad f_y = 0.65 + 0.35 \cos\left(\frac{\pi}{2} \frac{|y|}{y_{max}}\right)$$

where  $y_{max}$  is defined by

$$(14) \quad y_{max} = \frac{B}{\Delta\theta} \Delta x = \frac{4\lambda}{(\Delta\theta)^2}$$

So, the envelope  $f_{xy}$  of the reconstructed two dimensional resolution function maxima of all reflector positions in the image plane, as shown in Figure 8, can be approximated very well by the product of  $f_x f_y$ . If the function  $f_{xy}$  is once known, it is very easy to compensate the amplitude degradation by simply multiplying the reconstructed signal amplitudes  $A(x, y)$  with the inverse function  $f_{xy}^{-1}$ . The computational effort is small, so that there is no significant loss in processing speed. The effect of this countermeasure is demonstrated in Figure 9. Here, the reconstructed signal amplitudes of unit point scatterers are nearly equal after applying amplitude corrections, so that a reliable quantitative interpretation of the calculated RCS-values is possible, as long as the cross dimension of the individual imaged scattering center is less than  $\Delta x$ . Although the degradations on image resolution are not affected, the amplitude corrective measure is sufficient for many situations of practical relevance, especially, if the maximum lateral object position  $|x|$  is less than or slightly above  $x_{conv}$  as is demonstrated in Figure 10. If the object dimension  $D$  is much larger than  $2 x_{conv}$ , as in case of a real aircraft [10], at the mentioned RF-parameters the loss in resolution will be significant as is shown for the imaging of simulated pairs of unit point reflectors in Figure 11.

#### THE FOCUSED APERTURE

In order to enhance the resolution, the synthetic aperture must be correctly focused in the image plane, that means, the motion through resolution cells has to be compensated for. Already twenty years ago, Brown and Fredericks [11] derived for pulse doppler radar measurements a fundamental method, which consists of taking the Fourier transform of range

sweep data, followed by a gentle distortion of this range transform plane, and that followed by a two-dimensional Fourier transform resulting a correct focused image. If no optical transformation devices are used, such methods cost some computational effort and consequently cause a loss in speed for the image generation mainly due to an additional two-dimensional Fourier transform.

Another method suggested here, is a special tracking technique, where point reflectors will be traced through several range cells, if required. This method is supplemented by a single preprocessing phase correction replacing the phase approximation outlined in Section 2, where phase contributions of the  $y_1 \cos \theta_n$  term have been neglected. The additional phase correction is described by

$$(15) \quad V''(\theta_n, y_1) = V(\theta_n, y_1) \exp \left[ -j \frac{4\pi}{\lambda} y_1 \cos \theta_n \right]$$

which, however, now requires a knowledge about the location of the rotational center.

For compensation of range walk effects, scattering centers can be traced through several range cells if the processing time is larger than the time needed for the scattering center to move through a resolution cell. In those situations the maximum detectable signal strength will also appear in neighbouring range cells. The example in Figure 12 displays the signal strength versus aspect angle in three neighbouring range cells for a point reflector crossing the  $l$ -th range cell during the angular interval  $\Delta\theta$ . The phase of the backscattered signal only depends on the distance between the radar sensor and the current location of a scattering center. The signals in the neighbouring range cells ( $\pm 1$ ) sampled at equal aspect angles therefore are in phase to those of the  $l$ -th range cell as long as the motion of the scattering center in range direction during the time interval between the signal samples in neighbouring range cells is negligible. Hence, it is possible to use those signals for coherent extension of the analysable angular interval which in turn leads to a larger effective aperture. This can be achieved, for instance, by replacing all those fractions of the signal samples in the  $l$ -th range cell at a given aspect angle by signal contributions of neighbouring range cells, where the amplitudes of the latter ones are larger. For the above mentioned parameter set this will happen if the signal amplitude of a point reflector becomes less than 60% of its maximum.

Figure 12 displays an example of this coherent signal extension. The location of the scattering center at half of the process angle interval  $\Delta\theta/2$  is assumed to be at the center of the  $l$ -th range cell and the total migration path  $\delta y$  in range direction during the process interval is assumed to be  $2\Delta y$  ( $\Delta y$  = depth of a range cell). Here signal amplitudes larger than 60% of its maximum are only extended on half of the interval  $\Delta\theta$ . In order to reduce the hereby resulting image quality degrading range walk effects the signal values given by the dashed areas can be coherently combined to form a focused synthetic aperture in the  $l$ -th range cell. In cases where the migration path  $\delta y$  is larger than  $3\Delta y$  the angular interval, during which the signal amplitude exceeds the 60%-mark, is limited to less than  $\Delta\theta/3$  and therefore signal contributions of a point scatterer in five and more neighbouring range cells have to be included in the signal extension process, as shown in Figure 13. However, the triangular shape of the signal envelope resulting from this tracking procedure will cause an increase of sidelobe level for scattering centers even if Hamming windows are used in the imaging process. The enhanced sidelobe level can be further reduced if one allows an controlled coherent overlapping of sampled data sections from neighbouring cells in order to smooth the signal shape as outlined in [9]. The scattering centers will be imaged then only with negligible distortions and with reliable quantitative RCS values.

Applying this tracking technique at each step of steering the focused beam, much more computer time will be consumed, because the fast FFT algorithms can not be applied for this direct method. Therefore, in cross-range direction the image plane is divided in strip like zones running parallel to the range coordinate. Now, for each zone an individual tracking procedure is applied which results in an optimal focused aperture in every range cell arranged for a point reflector at the center of each zone. If the cross range extension of a zone is such dimensioned, that differences in range walk inside each zone remain small, then for all points the same tracking arrangements may be applied as for the position at the center of the zone. Therefore, the usual fast image algorithm based on FFT-algorithms can again be applied to achieve a zone-wise undistorted cross-range resolution, whereby only the reconstructed data inside each single zone are taken into account to construct the final focused image [9]. The increase of computational effort is limited by the number of zones, because each zone requires the application of one FFT. The number of zones depends on the maximum object dimension and on the length of the processed angle interval. The definition of the zone widths is somewhat arbitrary. For the parameter values given above, the definition

$$(16) \quad R_m = (m + 0.5) \frac{\Delta y}{\Delta\theta}, \quad m = 1, 2, 3, \dots$$

has been found useful, where  $\pm R_m$  denotes the boundaries of the zones in cross-range direction. Compared to the method suggested by [11], it is a further significant advantage, that a correct focused aperture is obtained by processing pure time domain raw data, so that no further data manipulations with inherent unknown effects as caused by applying additional fore- and backward transformations do exist.

The two examples for correct focused images in Figures 14 and 16 demonstrate the efficiency of this method. Figure 15 shows the experimental setup corresponding to Figure 16. The image of Figure 16 is processed with an unusually large process angle of  $51.2^\circ$  in order to realize a migration path for the outer point scatterer through more than 6 range cells.

## 6. CONCLUSIONS

In this paper a combined hardware/software method for generating fast two-dimensional ISAR images has been presented. The one-dimensional RCS-profiles versus range are produced in real time with the aid of a gated coherent short pulse radar. Small-angle looks are sufficient to obtain high cross-range resolution using fast SAR principles. It was shown that an incorrect focusing of the synthetic aperture can cause severe degradations on image quality. The main mechanisms

for these effects are identified and two compensating countermeasures have been presented. Examples of processed images from simulated and experimental data demonstrated the capabilities of these methods.

#### 7. REFERENCES

- [1] Walker, J.L., "Range-Doppler Imaging of Rotating Objects", IEEE Trans. on Aerosp. and El. Syst., Vol. AES-16 (1980), No 1, pp. 23-53
- [2] Mensa, D.L., "High Resolution Radar Imaging", Dedham M.A.: Artech House, 1982
- [3] Ausherman, D.A.; Kozma, A.; Walker, J.L.; Jones, H.M., "Developments in Radar Imaging", IEEE Trans. on Aerosp. and El. Syst., Vol. AES-20 (1984), No 4, pp. 363-400
- [4] Wehner, D.R., "High Resolution Radar", Norwood, MA: Artech House, Inc. 1987
- [5] Chen, C.C.; Andrews, H.C., "Target-Motion-Induced Radar Imaging" IEEE Trans. on Aerosp. and El. Syst., Vol. AES-16 (1980), No 1, pp. 2-14
- [6] Bethke, K.-H., "Investigation of Signal Degradation by Scattering and Its Suppression in Near-Ground Radar Cross-Section Measurements", ESA-TT-967 (1986)
- [7] Bethke, K.-H., "Ein schnelles zweidimensionales Radarabbildungsverfahren für rotierende Objekte und eine Analyse der Abbildungsqualität", DFLVR-FB-88-51, (1988), will be published as a ESA Technical Translation: "On a Fast Two-dimensional Radar Imaging Process for Rotating Targets and an Analysis of its Image Quality", ESA-TT-???(1989)
- [8] Harris, F.J., "On the Use of Windows for Harmonic Analysis with the Discrete Fourier-Transform", Proc. IEEE, Vol. 66 (1978), No. 1, pp. 51-83
- [9] Bethke, K.-H., "Fokussierte zweidimensionale Radarabbildung durch kohärente Signalverarbeitung im Zeitbereich", DLR-FB-89-??, (1989) to be published; will also be published as a ESA Technical Translation: "Focused Two-Dimensional Radar Imaging Using Coherent Time Domain Signals", ESA-TT-???(1989)
- [10] Roads, B., "Stealth Technologies and Their Experimental Verification Part II", AGARD FMP-symposium on Improvement of combat performance for existing and future aircraft, Treviso 14.-17.4.1986
- [11] Brown, W.M.; Fredericks, R.J., "Range-Doppler Imaging with Motion Through Resolution Cells", IEEE Trans. on Aerosp. and El. Syst., Vol. AES-5 (1969), No 1, pp. 98-102

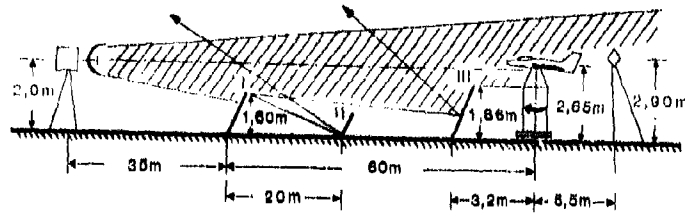


Figure 1. Typical geometry of the outdoor measurement range.

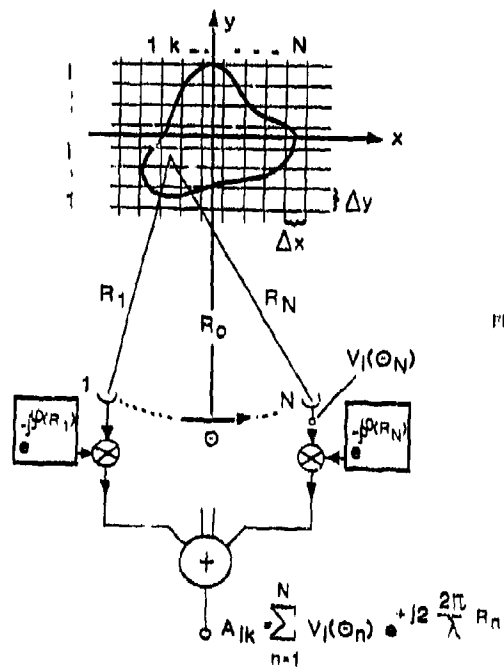


Figure 2. SAR principle: Focusing the synthetic aperture on to a resolution cell located at  $(x_k, y_k)$  by compensating different pathlengths.

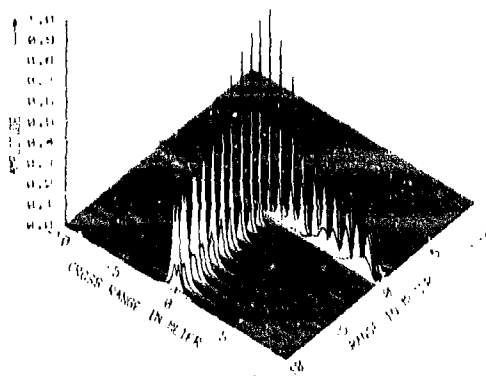


Figure 3. Two-dimensional image of simulated unit point scatterers  $\Delta\theta = 5.5^\circ$ ,  $\lambda = 3\text{cm}$ ,  $y_{\text{cell}} = 40\text{cm}$ ,  $\Delta y = 1.5\text{cm}$ ,  $R_0 = 600\text{m}$

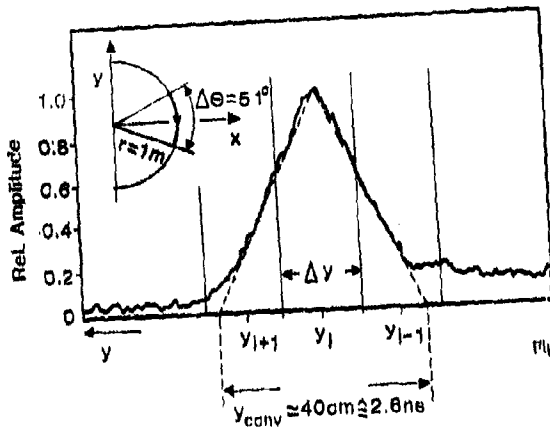


Figure 4. Echo signal shape for a moving point scatterer. Receiver gate width and the transmitter pulse length both are about 1 ns.

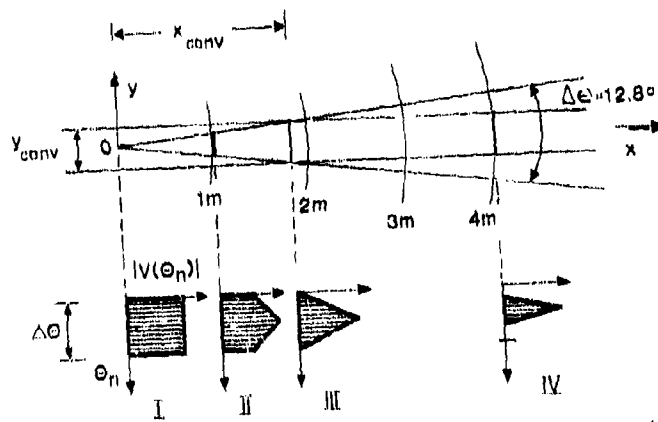


Figure 5. Principle relationship between amplitude shape of a single point reflector and its lateral distance from the rotational center.

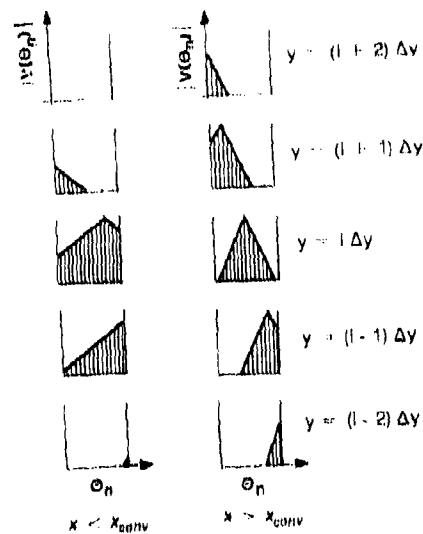


Figure 6. Examples for the propagation of echo signal contributions from one single point reflector through several range cells, depending on the lateral distance.

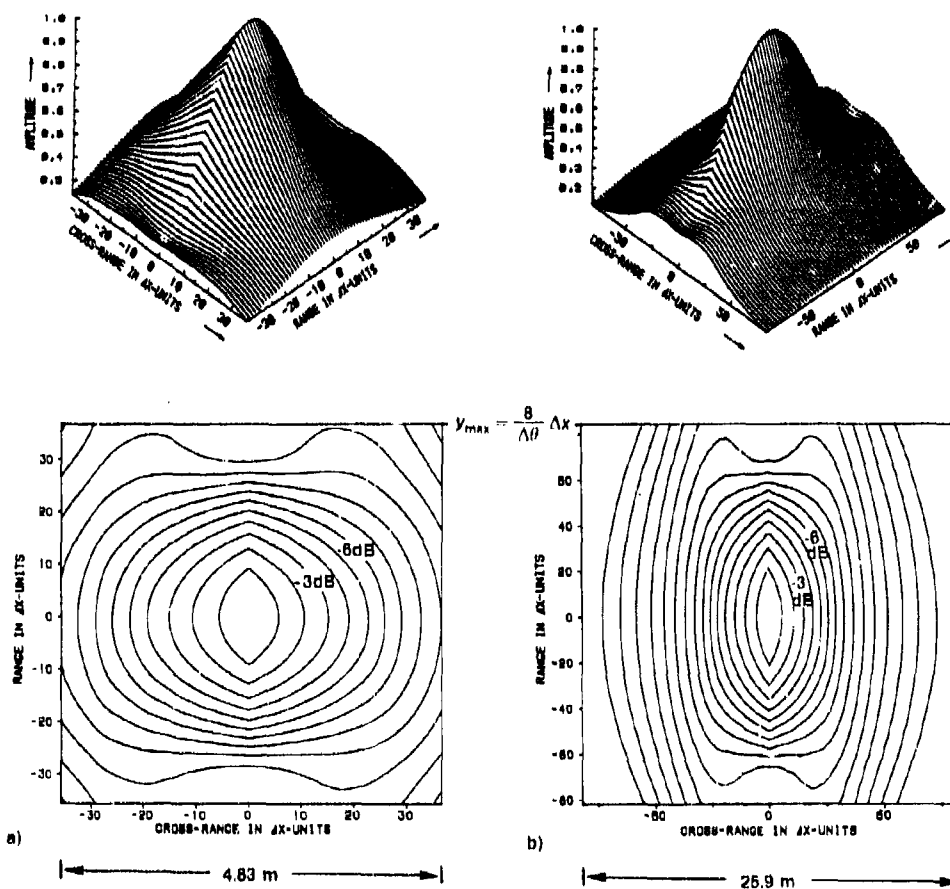


Figure 7. Envelope of reconstructed maximum signal amplitudes calculated for a point reflector at any position in the image plane. Amplitude of this surface depends on focusing errors and range walk effect;  $y_{\text{max}} = 40\text{cm}$ ,  $\lambda = 3\text{cm}$ , a)  $\Delta\theta = 12.8^\circ$  ( $\Delta x = 6.7\text{cm}$ ), b)  $\Delta\theta = 5.5^\circ$  ( $\Delta x = 15.6\text{cm}$ ).

31-10

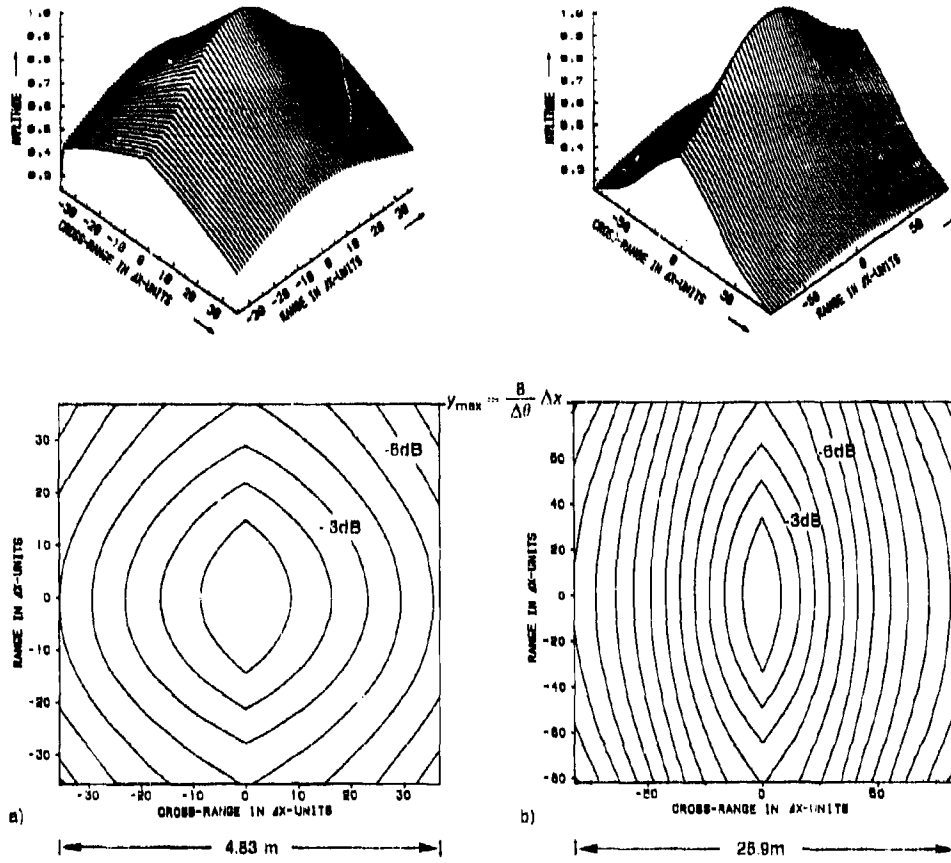


Figure 8. Improved imaging conditions when using a Hamming window for a preprocessing signal weighting, otherwise the same parameters as in Figure 7.

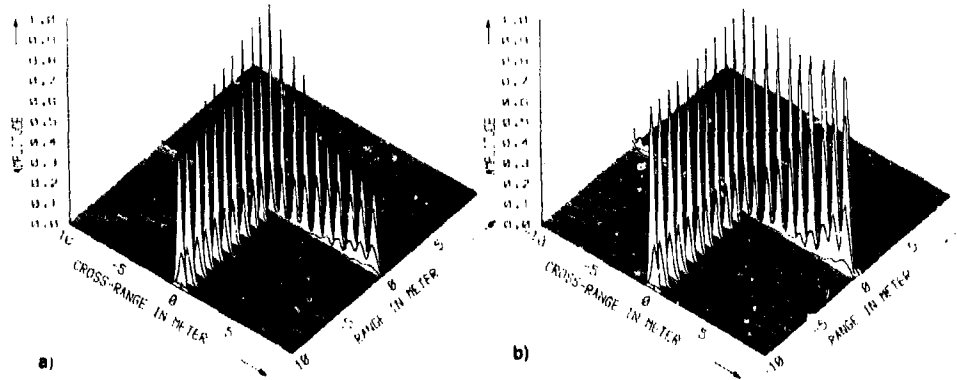


Figure 9. Two-dimensional image of simulated unit point scatterers when a) using a Hamming window for a preprocessing signal weighting and b) additional applied amplitude corrections; see also Figure 3.

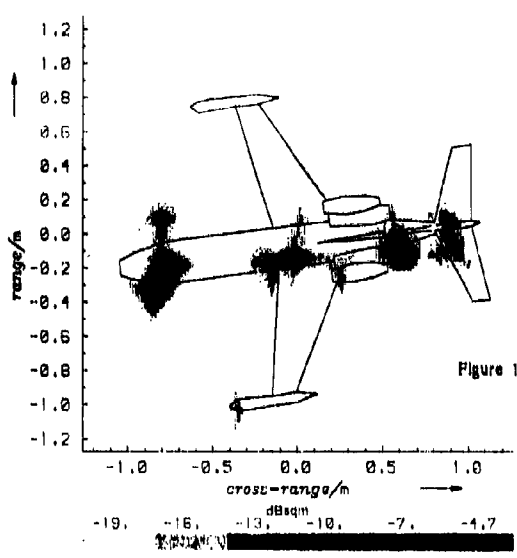


Figure 10. Imaged scattering centers of a scaled aircraft model,  $\lambda = 3\text{cm}$ ,  $\Delta\theta = 12.8^\circ$ .

Figure 11. Limited resolution capability when using only amplitude corrective measures, demonstrated for pairs of (4.5cm-distance) simulated point reflectors,  $\lambda = 3\text{cm}$ ,  $\Delta\theta = 5.5^\circ$ .

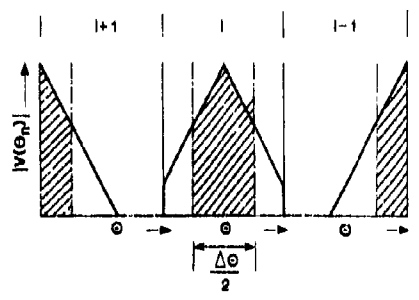
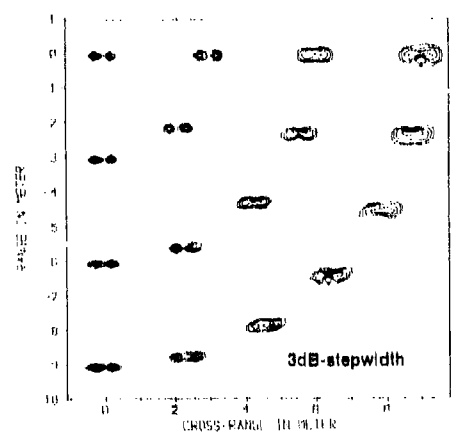


Figure 12. Sampled signal amplitudes of a point scatterer centered at the  $l$ -th resolution cell shown for three adjacent range cells. During the process interval  $\Delta\theta$  the scatterer moves over a pathlength of  $\Delta y = 2\Delta y$  in range direction.

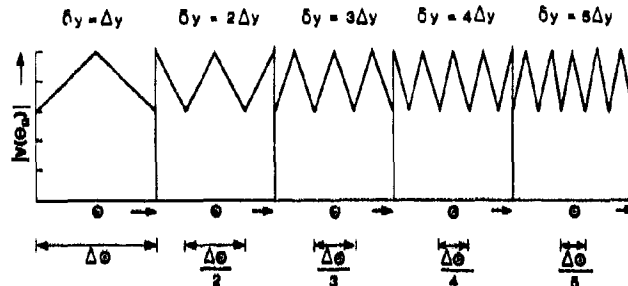


Figure 13. Resulting signal shapes after applying the tracking procedure, shown for different point scatterer migration path lengths  $\delta y$  during the process interval.

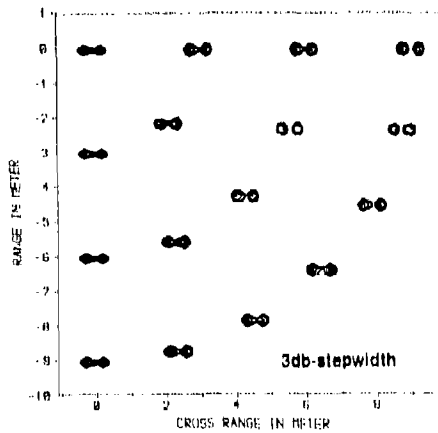


Figure 14. Correct focused image of simulated pairs of point reflectors. The same arrangement as in Figure 11.

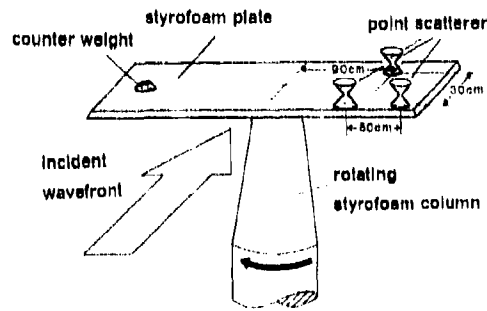


Figure 15. Experimental setup for imaging point reflectors.

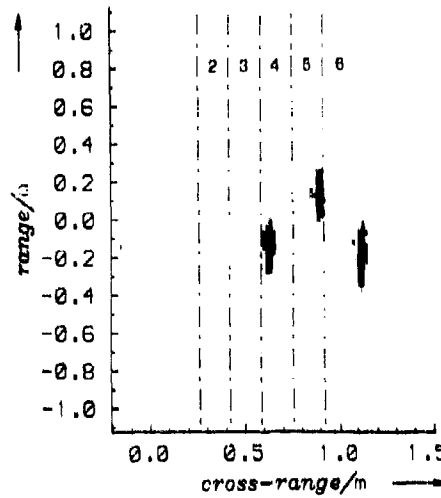
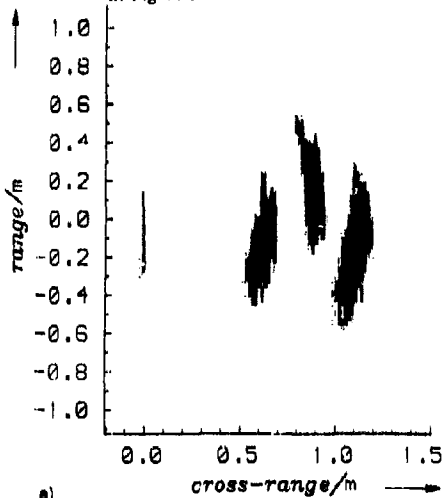


Figure 16. Imaged point reflectors in an arrangement as shown in Figure 15. Heavy blurring caused by significant range walk,  $\lambda = 3\text{cm}$ ,  $\Delta y = 15\text{cm}$ ,  $y_{\text{scan}} = 40\text{cm}$ ,  $\Delta\theta = 51.2^\circ$ ; a) for only Hamming data weighting, b) for correct focusing.

RADAR OBSERVATIONS OF A FORMATION OF TWO FIGHTERS  
A CASE STUDY FOR ISAR IMAGING

Frits Willems  
TNO Physics and Electronics Laboratory  
P.O. Box 96864  
2509 JG The Hague  
The Netherlands

AD-P005 849

**SUMMARY**

This paper reports on a study of ISAR imaging of a formation of two fighters. The observations are interpreted in terms of relative motions of the two aircraft by use of model study and computer simulation.

**0. INTRODUCTION**

ISAR is an acronym for Inverse Synthetic Aperture Radar. This is a technique to obtain high cross range spatial resolution of a flying target. The tangential translation is used to synthesize a large radar aperture. The aim of ISAR is to resolve the individual radar highlights of the target.

The target is assumed to be a collection of highlights on a rigid body. Each highlight contributes to the radar return. The contribution is a function of radar reflectivity and distance to the antenna. By processing coherently recorded radar returns it should be possible to estimate the flight path of each individual highlight. The flight path of a highlight can be described by the path of the center of motion (CM) of the target and pitch, yaw and roll of the highlight. The problems which arise in the estimation of the velocity, pitch, yaw and roll of the target are addressed in this paper.

In order to discriminate between the contributions of the different motions to the ISAR processing we made a model study. The results of this study have been verified by computer simulations and applied to radar data of a formation of two fighter aircraft which was observed under controlled conditions.

**1. MODEL STUDY**

The target is modeled by a collection of  $L$  discrete highlights on a rigid body. The  $n^{\text{th}}$  radar echo can then be written as,

$$e_n = \sum_{i=1}^L a_i e^{i\pi} \frac{e}{\lambda} r_{ni} \quad (1)$$

with

- $n$  = number of radar echo
- $i$  = number of highlight
- $a_i$  = radar reflectivity of the  $i^{\text{th}}$  highlight
- $r_{ni}$  = distance of the  $i^{\text{th}}$  highlight to the radar at the  $n^{\text{th}}$  radar return
- $\lambda$  = wavelength of the radar

We constrain ourselves to the 2 dimensional description of the target geometry for the sake of simplicity. We describe the target in a plane which includes the radar and the flight path of the target. Figure 1 gives the geometry in which the radar and CM are moving with respect to the origin of the grid. The origin is the center of ISAR processing (CP).

The distance to the radar of a single highlight can be written as,

$$r_{ni} = \left[ R_n^2 + (x_{ni}^2 + y_{ni}^2) + 2 R_n (x_{ni} \sin(\theta_n) + y_{ni} \cos(\theta_n)) \right]^{\frac{1}{2}} \quad (2)$$

with

- $r_{ni}$  = distance of the  $i^{\text{th}}$  highlight to the radar at the  $n^{\text{th}}$  radar return
- $R_n$  = distance of the radar to CP in the  $n^{\text{th}}$  radar return
- $x_{ni} = m_0 \cos(\alpha) + d_1 \cos(\phi_n) + c \cos(\beta) n \Delta t + \frac{c}{2} \cos(\gamma) (n \Delta t)^2$

$$y_{n1} = m_0 \sin(\alpha) + d_1 \sin(\phi_n) + c \sin(\beta) n \Delta t + \frac{a}{2} \sin(\gamma) (n \Delta t)^2$$

$m_0$  = distance of CM to CP at  $n = 0$   
 $c$  = velocity of CM relative to CP  
 $a$  = acceleration of CM relative to CP  
 $\Delta t$  = pulse interval of the radar  
 $\alpha, \beta, \gamma, \theta_0$  and  $\phi_0$  are indicated in figure 1

Under the assumption of  $R_n^2 \gg x^2 + y^2$ ,  $\theta_n = \omega_1 n \Delta t$  and  $\phi_n = \omega_2 n \Delta t$  we make a Taylor expansion up to the second order of Eq. (2) around  $n = 0$  ( $t = 0$ ).

$$r_{n1} = R_n + m_{0r} + d_{1r} + \left[ c_r + m_{0cr} \omega_1 + d_{1cr} (\omega_1 + \omega_2) \right] (n \Delta t) + \left[ \frac{a_r}{2} + c_{cr} \omega_1 + d_{1cr} \omega_1 \omega_2 - d_{1cr} \cos(\phi_0 - \theta_0) \omega_2^2 \right] (n \Delta t)^2 \quad (3)$$

With

$$\begin{aligned}
 m_{0r} &= m_0 \sin(\theta_0 + \alpha) & m_{0cr} &= m_0 \cos(\theta_0 + \alpha) \\
 d_{1r} &= d_1 \sin(\theta_0 + \phi_0) & d_{1cr} &= d_1 \cos(\theta_0 + \phi_0) \\
 c_r &= c \sin(\theta_0 + \beta) & c_{cr} &= c \cos(\theta_0 + \beta) \\
 a_r &= a \sin(\theta_0 + \gamma) & a_{cr} &= a \cos(\theta_0 + \gamma)
 \end{aligned}$$

Next we investigate four special cases of Eq. (3):

- a/ A target stationary to CP  
(CP = CM,  $m = 0$ ,  $c = 0$ ,  $a = 0$ ,  $\omega_1 = 0$ )
- b/ A target rotating around CP  
(CP = CM,  $m = 0$ ,  $c = 0$ ,  $a = 0$ )
- c/ A target translating with a uniform velocity with respect to CP  
( $a = 0$ ,  $\omega_2 = 0$ )
- d/ A target accelerating uniformly with respect to CP  
( $\omega_2 = 0$ )

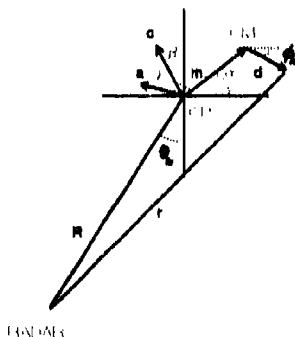


Fig.1

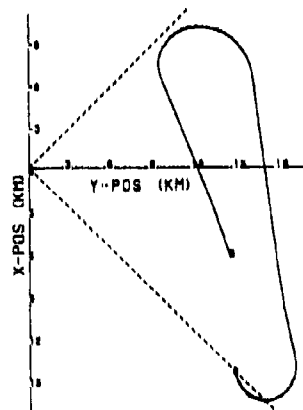


Fig.2

Figure 1. The geometry of a target moving with respect to CP. The geometry is a projection of the target onto the plane spanned by the flight path and the radar. The relative velocity ( $c$ ) and relative acceleration ( $a$ ) vector of the target at CM are also plotted. The symbols are explained in the text.

Figure 2. The flight path of the formation. B indicates the beginning and E the end of the run. The radar is positioned at  $(0,0)$ . The dashed lines indicate the field of view of the phased array radar.

### 1.1 A STATIONARY TARGET

For a stationary target the radar return can be written as

$$e_n = \sum_{i=1}^L a_i e^{j \pi j} \frac{e}{\lambda} \left[ R_n + d_{1r} + d_{1or} \omega_i n \Delta t \right] \quad (4)$$

If the phase history of CM is known we can reduce Eq.(4) to

$$e_n' = \sum_{i=1}^L a_i' e^{j \pi j} \frac{e}{\lambda} \left[ d_{1or} \omega_i n \Delta t \right] \quad (5)$$

with

$$a_i' = a_i e^{j \pi j} \frac{e}{\lambda} d_{1r}$$

A DFT symmetric around  $n = 0$  of Eq.(5) gives

$$E_k = \Delta t \sum_{i=1}^L a_i' \sum_{n=-N/2}^{N/2} e^{j \pi j} \left[ \frac{e}{\lambda} d_{1or} \omega_i \Delta t - \frac{\lambda}{N} \right] n \quad (6)$$

$E_k$  is a linear combination of  $L$  sinc functions. The main lobes do not overlap when  $N$  is sufficiently large. The power spectrum  $P_k (= E_k E_k^*)$  has  $L$  peaks in that case. The strength of the  $i^{\text{th}}$  peak is  $|a_i'|^2 (= |a_i|^2 = a_i a_i^*)$  at  $\frac{\lambda}{N} = \frac{e}{\lambda} d_{1or} \omega_i \Delta t$ .

The frequency axis gives a measure for the cross range of the target

$$d_{1or} = \frac{\lambda}{e} \frac{h}{\omega_i \Delta t N} \quad (7)$$

The angular velocity of the target is approximated by

$$\omega_i \approx \frac{V_0 \cos(\theta_0)}{R_0} \quad (8)$$

with

- $V_0$  = velocity of the target at  $n = 0$
- $R_0$  = distance of the target at  $n = 0$
- $\theta_0$  = aspect angle of the target at  $n = 0$

This derivation shows that the power spectrum of motion compensated radar returns can be used to produce a cross range image of the target if the phase history of CM is known and pitch, yaw and roll can be neglected.

### 1.2 ROTATING TARGET

During short time intervals pitch, yaw and roll motion of a target can be described by uniform rotation  $\omega_s$  around CM. The motion compensated radar returns can then be written as:

$$e_n = \sum_{i=1}^L a_i' e^{j \pi j} \frac{e}{\lambda} \left[ d_{1or} [\omega_i + \omega_s] n \Delta t - \left[ d_{1r} \omega_i \omega_s + d_{1r} \cos(\phi_0 - \theta_0) \omega_s^2 \right] (n \Delta t)^2 \right] \quad (9)$$

We investigate the DFT of Eq.(9) as the power spectrum has proven to be a useful tool to examine the ISAR image of a stationary target.

$$E_k = \Delta t \sum_{i=1}^L a_i' \left\{ \sum_{n=-N/2}^{N/2} e^{j \pi j} \left[ \left[ \frac{e}{\lambda} d_{1or} [\omega_i + \omega_s] \Delta t - \frac{\lambda}{N} \right] n - \frac{e}{\lambda} \left[ d_{1r} \omega_i \omega_s + d_{1r} \cos(\phi_0 - \theta_0) \omega_s^2 \right] (n \Delta t)^2 \right] \right\} \quad (10)$$

The term between accolades in Eq.(10) is a discrete form of a Fresnel integral - defined Fresnel sum in the rest of the text - which is discussed in the appendix. The DFT of Eq.(9) is a sum of  $L$  blurred sinc functions with

$$d_{\text{cor}} = \frac{\lambda k}{2(\omega_1 + \omega_2) \Delta t N} \quad (11)$$

The blurring is proportional to the second order term in Eq. (9). We can make an estimate of this term by taking typical values for  $\lambda$ ,  $d$ ,  $\omega_1$  and  $\omega_2$ . The observations are made in C band so  $\lambda = 0.05$  m. With  $V = 200$  m s<sup>-1</sup> and  $R = 15$  km we get  $\omega_1 \approx 0.01$  rad s<sup>-1</sup>. The RMS angular velocity of a typical fighter<sup>1</sup> is  $\leq 3$  deg s<sup>-1</sup> so  $\omega_2 \leq 0.05$  rad s<sup>-1</sup>. The typical size of a fighter is  $20$  m so  $d \leq 10$  m. The second order term is  $\leq \delta$  ( $= 10 \cdot 0.05^2 \approx \pi / 0.05$ ). The results in the appendix indicate that for a one second integration interval the blurring of the peaks in the ISAR image can be neglected for values of the second order term  $\leq 5$ .

### 1.3 TARGET WITH UNIFORM VELOCITY

In the case of a rigid body of  $L$  highlights translating uniformly with respect to CP the motion compensated radar return can be written as:

$$e_n = \sum_{l=1}^L a_l' e^{2\pi j \frac{n}{\lambda} \left[ \left[ c_r + m_{\text{cor}} \omega_1 + d_{\text{cor}} \omega_1 \right] n \Delta t + c_{\text{er}} \omega_1 (n \Delta t)^2 \right]} \quad (12)$$

The DFT of Eq. (12) has the form

$$E_k = \Delta t \sum_{l=1}^L a_l' \sum_{n=-N/2}^{N/2} e^{2\pi j \left[ \left[ \frac{2}{\lambda} \left[ c_r + (m_{\text{cor}} + d_{\text{cor}}) \omega_1 \right] \Delta t - \frac{k}{N} \right] n + c_{\text{er}} \omega_1 (n \Delta t)^2 \right]} \quad (13)$$

Eq. (13) is a series of Fresnel sums. Each Fresnel sum is symmetric around

$$\frac{k}{N} = \frac{2}{\lambda} \left[ c_r + (m_{\text{cor}} + d_{\text{cor}}) \omega_1 \right] \Delta t$$

The position of the  $l^{\text{th}}$  highlight in the spectrum is shifted compared to the stationary target (cf. Eq. (7)). This shift is proportional to the line of sight velocity difference between the translating target and CP. The cross range velocity component causes a blurring of the peak in the power spectrum if  $2\pi \frac{2}{\lambda} c_{\text{er}} \omega_1 \leq \delta$  for a 1 second integration interval. With  $\omega_1 \approx 0.01$  rad s<sup>-1</sup> and  $\lambda = 0.05$  m blurring occurs when  $c_{\text{er}} > \frac{\delta \lambda}{2\pi \omega_1} \approx 2$  m s<sup>-1</sup>.

### 1.4 LINEAR ACCELERATING BODY

The case of the accelerating body is almost analogous to the previous case. When  $c_n = c_a + a n \Delta t$  the second order term in Eq. (12) can be written as:

$$\frac{2}{\lambda} \left[ \frac{a}{2} + c_{\text{cor}} \omega_1 \right] \quad (14)$$

The blurring of the ISAR image given by Eq. (14) depends on the magnitude and sign of  $a$ , and  $c_{\text{cor}}$ .

### 1.5 ISAR IMAGE

The power spectrum can be used to make a radar image of a target if the phase history of CM is known. A bad estimate of the phase history of CM shows-up as blurring of features in the power spectrum as is discussed above for both a uniformly translating and an accelerating target. The offset in the power spectrum due to the velocity term in the first order term of Eqs. (12 & 13) is of no importance in the processing of a single target as we are only interested in relative sizes of the target. When the velocity in Eqs. (12 & 13) is large compared to  $V$  (the velocity of CP) the angular velocity  $\omega_1$  will be wrongly estimated causing a bad scaling of the ISAR image (c.f. Eq. (7)). The scaling of the target is also influenced by the internal rotations of the target.

## 2. RADAR OBSERVATIONS OF A FORMATION OF TWO FIGHTERS

The results of the model study have been used to interpret the radar echoes of a formation of two fighters. By analyzing subsequent intervals we can estimate the motion of one of the airplanes in the frame of the other one. The analysis is illustrated with some computer simulations.

### 2.1 OBSERVATIONS

A formation of two fighters of the Royal Dutch Air force flew some predefined tracks in view of our instrumentation radar in the fall of 1987. We asked the pilots to keep the formation inside a box with the size of 75 m in the x, y and z direction. One of the flown tracks is shown in figure 2. The track is plotted in the coordinate system of the radar.

The formation is observed with an experimental phased array radar. The radar parameters are: C band; 1000 pulses per second; a bandwidth of 1MHz.

### 2.2 MOTION COMPENSATION

The results of the processing of a part of the first leg is discussed below. The flight path of CM can be approximated by a straight path for this part of the track. The distance of CP to the radar ( $R_n$ ) can be expressed as:

$$R_n = \left[ R_0 + (V n \Delta t)^2 + 2 R_0 V \sin(\theta_0) n \Delta t \right]^{\frac{1}{2}} \quad (15)$$

if  $V = V_0 + A n \Delta t$  and  $R_0 \gg V n \Delta t$  then

$$R_n \approx R_0 + V_0 \sin(\theta_0) n \Delta t + \left[ \frac{V_0^2 \cos^2(\theta_0)}{2 R_0} + \frac{A \sin(\theta_0)}{2} \right] (n \Delta t)^2 \quad (16)$$

The motion compensation is performed by multiplying each radar return with a correction factor  $\exp(-j\phi_n)$ . This factor has the form

$$\exp(-j\phi_n) = \exp(-j [ A1 (n \Delta t)^2 + A2 n \Delta t ]) \quad (17)$$

With

$$A1 = \left[ \frac{V_0^2 \cos^2(\theta_0)}{2 R_0} + \frac{A \sin(\theta_0)}{2} \right] \frac{4\pi}{\lambda} \quad (18)$$

$$A2 = V_0 \sin(\theta_0) \frac{4\pi}{\lambda} \quad (19)$$

The parameters  $A1$  and  $A2$  can be estimated by a second order fit to the phase data of the coherently recorded echo returns. When short intervals of a straight flight path are processed the contributions of the individual highlights can be regarded as noise on the second order phase fit. This procedure for motion compensation is described by Berland (1984)<sup>2</sup>

### 2.3 COMPUTER SIMULATION

We have simulated radar returns for a formation of two targets. Each target consists of three highlights along the body axis with a spacing of 5 m. The amplitude ratio of the three highlights are 1 : 0.75 : 0.45 from nose to tail. The two targets are lined-up with a relative distance  $m_0$ . The parameters for four simulations are given in table I.

$R_0$ ,  $V_0$  and  $\theta_0$  are the parameters for the target at CP.

TABLE I

	$R_0$ km	$V_0$ m s <sup>-1</sup>	$\theta_0$ °	$N \Delta t$ s	$c_0$ m s <sup>-1</sup>	$\alpha$ m s <sup>-1</sup>	$m_0$ m
a	15	200	30	2	0	0	50
b	15	200	30	2	-1	0	50
c	15	100	30	2	1	0	50
d	15	200	30	2	0	1	50

Table I. Parameters used in the computer simulation

The radar parameters used in the simulations are the same as the parameters of the instrumentation radar.

The ISAR images plotted in figure 3 are Hanning tapered power spectra of the motion compensated radar returns. The frequency axis of the images are scaled with Eq. (7). The velocity, range and aspect angle used in the scaling are estimated from the processing of the radar returns.

A comparison of images 3a, 3b and 3c shows that the measured distance between the aircraft is very sensitive to differences in the range velocity. Image 3d demonstrates that the accelerations indeed show-up as a significant widening of the highlight features. The peak power decreases due to the widening. The limited spacing of the highlights compared to the width of the blurred main lobes introduces significant contributions of cross-terms of overlapping main lobes to the image of the accelerated target in figure 3d. The cross terms cause the distortion of the image.

#### 2.4 DATA PROCESSING

We have analysed 27.6 seconds of the first leg ranging from  $t = 7.0$  to  $t = 34.6$  s. This interval is divided in intervals of 1 second. Between  $t = 7.0$  and  $t = 19.5$  s the intervals overlap 0.5 s and between  $t = 19.5$  and  $t = 34.6$  s the intervals are adjacent.

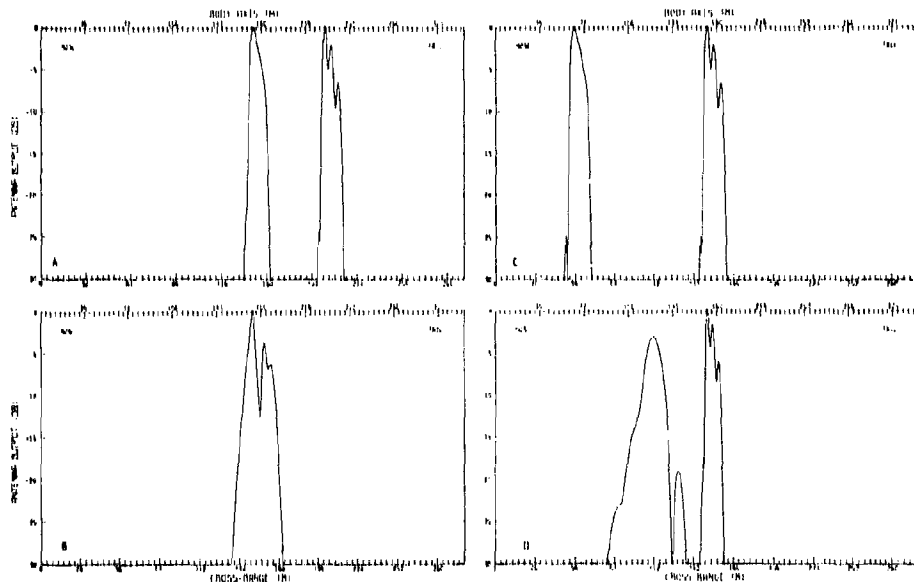


Figure 3. ISAR images obtained from computer simulated radar data. The parameters of the four images are given in table I.

We applied the motion compensation method of Ferland (1984) to the radar returns in each interval. The method gave  $A1$  and  $A2$  for CM of one of the aircraft. The tapered power spectra of the motion compensated radar returns showed two targets in most of the intervals. In the intervals between  $t = 19.5$  and  $t = 16.5$  s images of the targets overlapped. The results for eight intervals are given in figure 4. The images are lined-up on the leading aircraft. The aircraft at CP is always positioned in the middle of the individual image. Note that CP is not always at the same aircraft. The effects discussed in the model study clearly manifest in the images. One observes a rapid change in the observed cross range distances of the two aircraft. The widening of the image and decrease of peak power of the incorrectly motion compensated aircraft is clearly observable in some images.

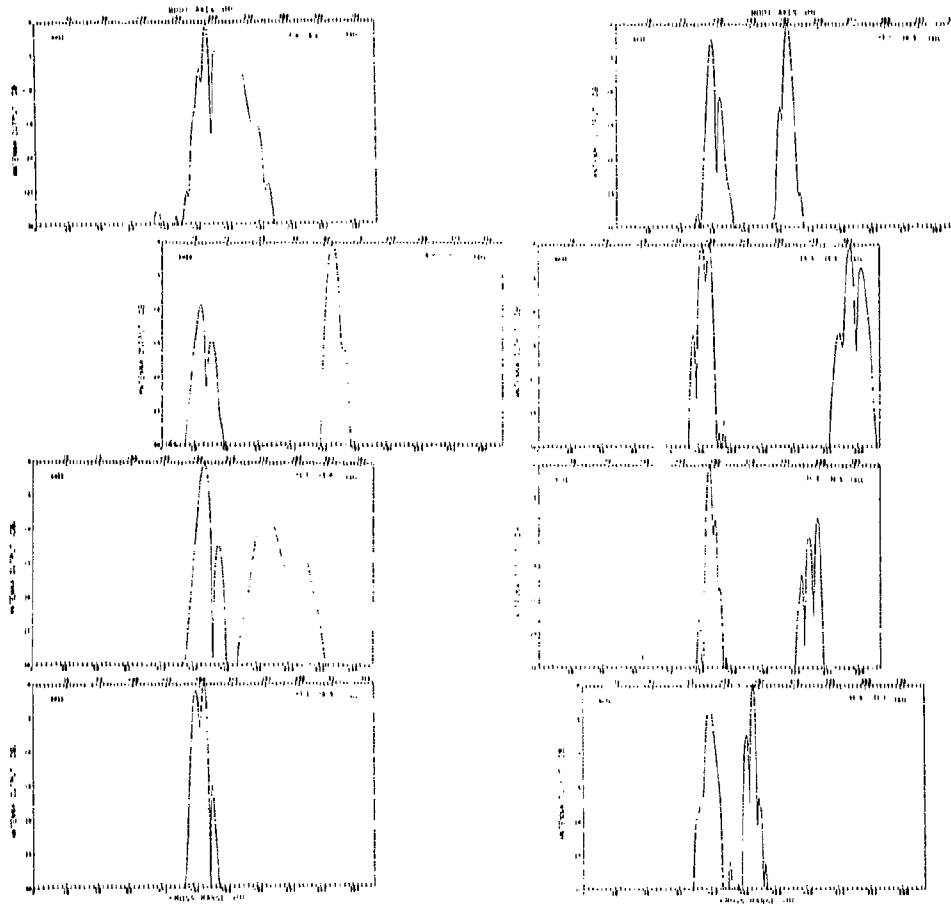


Figure 4. ISAR images of the formation for eight processing intervals. The start and end time of each interval are given in the plot. The aspect angle  $\theta$  is  $-36.5^\circ$  for  $t = 7.5$  s,  $-37.0^\circ$  for  $t = 9.5$  s,  $-36.0^\circ$  for  $t = 12.5$  s,  $-36.0^\circ$  for  $t = 16$  s,  $-35.0^\circ$  for  $t = 20$  s,  $-33.9^\circ$  for  $t = 25$  s,  $-31.1^\circ$  for  $t = 32$  s,  $-30.5^\circ$  for  $t = 34$  s.

In order to estimate the phase history of the not motion compensated aircraft we proceeded as follows.

- 1/ Use the 'CLEAN' method<sup>3</sup> to remove the aircraft at CP in the frequency domain.
- 2/ Apply an inverse Fourier transform to get 'CLEANED' radar returns.
- 3/ Multiply the 'CLEANED' radar returns with the inverse motion compensation factor  $\exp(+j\theta_n)$  (see Eq. (17)) of CP.
- 4/ Use the motion compensation method to estimate the phase history parameters of the second aircraft ( $A_1^i$  and  $A_2^i$ ).

With the help of Eq. (19) and  $A_1^i$  and  $A_2^i$  we can estimate  $c_r$ .

$$\begin{aligned} A_2^i - A_1^i &= \Delta V_0 \sin(\theta_0) \frac{4\pi}{\lambda} \\ &= c_r \frac{4\pi}{\lambda} \end{aligned} \quad (20)$$

Eq. (18) gives

$$A_1^i - A_2^i = \left[ \frac{\Delta A}{2} \sin(\theta_0) + \frac{[V_{0_1}^2 - V_{0_2}^2]}{2 R_0} \cos^2(\theta_0) \right] \frac{4\pi}{\lambda} \quad (21)$$

where

$V_{0_1}$  = velocity at  $n=0$  of the aircraft with phase history coefficients  $A_1^i$  and  $A_2^i$ .

$V_{0_2}$  = velocity at  $n=0$  of the aircraft with phase history coefficients  $A_1^i$  and  $A_2^i$ .

$\Delta A$  = acceleration difference between the two aircraft.

with  $V_{0_1}^2 - V_{0_2}^2 = 2 \Delta V_{cr} V_0$  we write Eq. (21) as

$$A_1^i - A_2^i = \left[ \frac{\Delta A}{2} + \frac{c_{cr} V}{R_0} \right] \frac{4\pi}{\lambda} \quad (22)$$

The uncertainty in the estimation of  $A_1^i$  and  $A_2^i$  equals  $(2\pi / T^2)$  and  $(2\pi / T)$ , respectively (Kerland 1984).  $T$  is the length of the processing interval ( $T = 1$  s in our case). The error in the estimation of  $c_r$  follows from,

$$\Delta c_r = \Delta A_2 \frac{\lambda}{4\pi} \quad (23)$$

With  $\Delta A_2 = 2\pi$

$$\Delta c_r = \frac{\lambda}{2} = \pm 0.025 \text{ m s}^{-1}$$

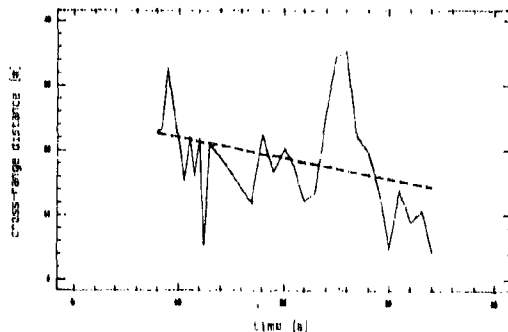


Figure 5. The cross range distance as function of time. A linear fit to the data is also plotted. The correlation coefficient of the fit is 0.8 for 20 data points.

If we use the subsequent estimated values of  $c_r$  to derive  $a_r (= \Delta c_r / \Delta t$  see Eq. (25))  $\Delta a_r = \pm 0.025 \text{ m s}^{-2}$ . When  $c_{cr}$  is derived with help of Eq. (22) we estimate  $\Delta c_{cr}$  as

$$\Delta c_{cr} = \left[ \frac{\lambda \Delta A l}{4 \pi} + \frac{\Delta a_r}{a} \right] \frac{R_0}{V_0} \quad (24)$$

With  $\Delta A l = \pm 2 \pi$ ,  $\Delta a_r = \pm 0.025 \text{ m s}^{-2}$ ,  $\lambda = 0.05 \text{ m}$ ,  $R_0 = 15 \cdot 10^3 \text{ m}$  and  $V_0 = 200 \text{ m s}^{-1}$  this results in  $\Delta c_{cr} = 23 \text{ m s}^{-1}$ . This is a large error. Another possibility to estimate  $c_{cr}$  is by use of the measured distance between the aircraft. The distance  $l$  of the centers of motion of both aircraft is (c.f. Eq. (14))

$$l = \frac{c}{\omega_i} + m_{cr} \quad (25)$$

The distance  $l$  can be obtained from the ISAR images. The distance  $l$  gives us  $m_{cr}$  as  $\omega_i$  and  $c_r$  are known. A regression analysis on the values of  $m_{cr}$  derived from processing successive intervals gives an estimate of  $c_{cr}$ . The blurring of the ISAR images introduces an uncertainty in the measured values of  $l$ . The cross range distance  $m_{cr}$  is derived from an averaged value of  $l$  measured with CP on aircraft 1 and CP on aircraft 2. This gives a 10 error of 10 m. The derived values of  $m_{cr}$  are plotted in figure 5 together with a linear fit. Due to the large individual errors there is no use for a higher order regression analysis. With the obtained slope we get  $m_{0cr}(t=7.5 \text{ s}) = 22.75 (4.0) \text{ m}$  and  $c_{cr} = -0.35 (0.2) \text{ m s}^{-1}$ .

From Eq. (24) we derive  $\Delta a_r = 10.05 \text{ m s}^{-2}$  since  $\Delta c_{cr} = 20.2 \text{ m s}^{-1}$ ,  $\Delta A l = \pm 2 \pi$ ,  $\lambda = 0.05 \text{ m}$ ,  $R_0 = 15 \cdot 10^3 \text{ m}$  and  $V_0 = 200 \text{ m s}^{-1}$ . The error in  $a_r$  is probably a little larger as we have ignored systematical deviations from a linear time dependence for  $c_{cr}$ . The assumptions underlying the derivation of  $a_r$  with Eq. (22) have been tested by correlating  $a_r$  with  $\Delta c_r / \Delta t$ .

$$\frac{\Delta c_r}{\Delta t} = \frac{c_r [l + l] - c_r [l - l]}{l[l + l] - l[l - l]} \quad (26)$$

Where

$l(i)$  = the time halfway the  $i^{\text{th}}$  observation interval

The slope of the correlation is 0.8 and the correlation coefficient is 0.8 for 20 points. These results justify the use of the linear regression of  $m_{cr}$  and Eq. (22) to derive  $a_r$ . In view of the larger error in  $a_r$  when using Eq. (22) we applied the more straightforward Eq. (26) to estimate  $a_r$ .

## 2.5 RESULTS

The methods described in the previous section are used to derive the cross range and the range distance between the two aircraft as function of time.

cross range distance

$$m_{cr} = m_{0cr} + c_{cr} (t - t_0) \quad (27)$$

with

$$\begin{aligned} m_{0cr} &= 22.75 \text{ m} \\ c_{cr} &= -0.35 \text{ m s}^{-1} \\ t_0 &= 7.5 \text{ s} \end{aligned}$$

range distance

$$m_r = m_{0r} + \sum_n c_{nr} \Delta t \quad (28)$$

With

$$\begin{aligned} m_{0r} &= \text{range distance at } t = 7.5 \text{ s} \\ c_{nr} &= \text{range velocity in the } n^{\text{th}} \text{ time interval} \end{aligned}$$

Due to the limited range resolution  $m_{or}$  is only known to about 75 m. In order to illustrate the relative motion in the formation we assume  $m_{or} = 60$  m. In figure 6 we have plotted the derived relative positions in the formation of the two aircraft in the frame of the rear aircraft with the help of Eqs. (27 & 28). The direction of the flight in figure 6 is consistent with figure 2. The range axis is positive in the direction of the radar. Due to overlap of both aircraft in the ISAR images between  $t = 13$  and  $t = 17$  s no direct information on the relative position could be extracted in this time interval. From the fact that the images overlap we deduce  $c_r < 0$  m s<sup>-1</sup>. The overlap gives values of  $t$  close to 0 (see Eq. (25)) for  $13 \leq t \leq 17$  s. This gives

$$\frac{c_r}{\omega_t} = -m_{or} \quad (29)$$

At  $t = 13$  s  $m_{or} = 21$  m and  $\omega_t = 0.011$  rad s<sup>-1</sup> which gives  $c_r = -0.22$ . This value of  $c_r$  is assumed between  $t = 13$  and  $t = 17$  s. It should be emphasized that the choice of  $m_{or}$  is arbitrary. With the choice of  $m_{or}$  of 60 m the two aircraft are approaching each other. This seems a sound assumption as it is likely that we have observed the two aircraft in the process of forming a formation.

### 3. CONCLUSIONS

Knowledge of the phase history of the center of motion of a target is a prerequisite for high quality ISAR processing. Inaccuracies in the estimates of velocity and acceleration of the center of motion and rotation around the center of motion cause blurring and wrong scaling of the image. Wrong scaling is due to a misfit of the first order term and blurring is due to a misfit in the second order term of the phase history of radar highlights. The first order term is dominated by the range velocity and rotation around the center of motion while the second order term is dominated by the cross range velocity and the range acceleration. These effects are illustrated in ISAR images of a formation of two aircraft.

In the case of a formation each of the two airplanes can be taken as reference point for processing. Here with it is possible to derive the relative range velocity between the two aircraft with which we are able to estimate the cross range distance between the two aircraft. The cross range distance as function of time gives an estimate of the relative cross range velocity between the aircraft with which the range acceleration can be estimated. The so derived range acceleration is consistent with the range acceleration obtained by the time derivative of the range velocity. With the derived cross range distance and range velocity we can reconstruct the relative motion of the two aircraft in the formation. Only the zero point of the relative range distance is unknown.

In the description of the relative motions in the formation given above, each aircraft is implicitly assumed to be a single point scatterer. In case of a single aircraft observed with high range resolution radar it should be possible to use a similar approach to estimate iteratively the parameters describing the phase history of each individual highlight. These parameters could then be used to derive linear accelerations and rotations during the processing interval leading to a model of the target.

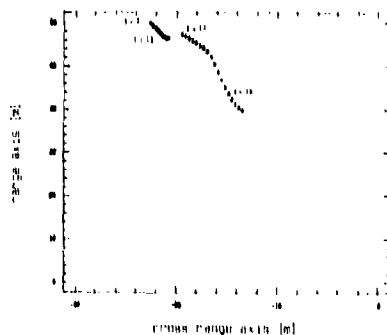


Figure 6. The position of the center of motion of the leading aircraft in the frame of the trailing aircraft. The center of motion of the rear aircraft is located in (0,0). The time increases from top left to bottom right.

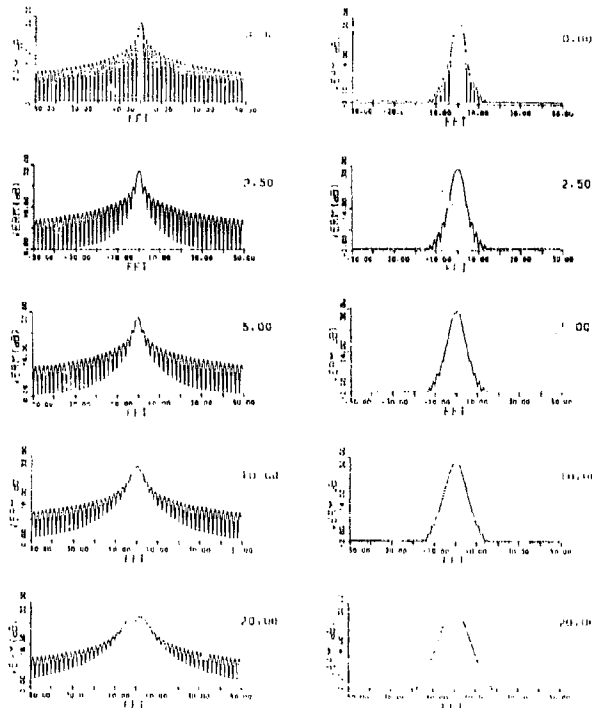


Figure A1. The uniformly and Hanning tapered Fourier transform of Eq.(A2). The left column represents the results with the uniform taper and the right column with the Hanning taper. The values of the parameter  $\alpha$  are indicated. The integration interval runs from  $-0.5$  to  $+0.5$ . The vertical axis gives the power in dB. The highest value in each plot is scaled to 30 dB. The horizontal axis gives the number of the FFT channel.

#### REFERENCES

- <sup>1</sup>Dunn, J., H. and Howard, D., D., *RADAR Handbook*, ed. Skolnik, M., I., 1970, McGraw-Hill, p. 28-18
- <sup>2</sup>Eerland, K., K., *International Conference on Radar*, Paris, 1984, p.618 - 623
- <sup>3</sup>Schwartz, U., J., *Mathematical-Statistical Description of the Iterative Beam Removing Technique (Method CLEAN)*, *Astronomy and Astrophysics*, 05, 1978, p.345 - 356

## APPENDIX FRESNEL INTEGRAL

An integral with second order complex exponential powers is called a Fresnel integral. One form of the Fresnel integral is given by

$$F(x) = \int_{-x}^{+x} e^{j [a t^2 + x t]} dt \quad (A1)$$

When  $x$  is replaced by  $x'$  ( $= -x/2\pi$ ) Eq. A1 represents the Fourier transform with a uniform taper of the function

$$f(t) = e^{j a t^2} \quad (A2)$$

The power function of  $F(x)$  is defined as

$$P(x) = F(x) F^*(x)$$

$$P(x) = \frac{\pi}{2a} \left\{ \left[ C \left[ \frac{\pi x + a \pi}{\sqrt{a}} \right] - C \left[ \frac{\pi x - a \pi}{\sqrt{a}} \right] \right]^2 + \left[ S \left[ \frac{\pi x + a \pi}{\sqrt{a}} \right] - S \left[ \frac{\pi x - a \pi}{\sqrt{a}} \right] \right]^2 \right\} \quad (A3)$$

with

$$C(x) = \sqrt{\frac{x}{\pi}} \int_0^x \cos(t^2) dt$$

$$S(x) = \sqrt{\frac{x}{\pi}} \int_0^x \sin(t^2) dt$$

Eq. (A3) is symmetric around  $x = 0$ . The power function approaches a squared sinc function if the parameter  $a$  goes to zero. The main lobe of the power function flattens and widens for increasing absolute values of the parameter  $a$ . The widening and flattening is illustrated in figure A1. In this figure we have plotted the uniformly and Hanning tapered Fourier transforms of Eq. (A2). The Hanning taper is used in general to suppress side lobes in the power spectrum. The figure is scaled to the maximum of each feature.

The values of parameter  $a$  are 0.0, 2.5, 5.0, 10.0 and 20.0 respectively and  $\pi = 0.5$ . The difference between the jagged uniformly and smooth Hanning tapered plots is striking. Full width at half maximum (FWHM) is defined as the width of the main lobe at the minus 3 dB point. From figure A1 it is clear that FWHM is increasing with increasing  $a$ . The ratio of the width of the response to the width of the squared sinc function ( $a = 0$ ) is  $\approx 1.25$  when  $a = 10$ . This means that the power function gets significantly blurred for values of  $a$  larger than 5.



## 1D-ISAR Imaging of Manoeuvring Aircraft

J. Ender

Forschungsinstitut für Funk und Mathematik (FFM) der FGAN  
 Neuenahrer Str. 20, D-6307 Wachtberg-Werthhoven, F.R. Germany

## SUMMARY

Most operating radar systems don't provide sufficient range resolution to resolve flying targets in range direction. Nevertheless, high cross range resolution can be obtained by 1-D ISAR imaging. This procedure will be successful only, if the target motion is compensated with a high accuracy. In this paper, a motion compensation technique is introduced based on Kalman forward-backward-smoothing on radar position estimates together with spectral information. An iterative error correction procedure (autofocus) yields a cross range image with sufficient resolution. Correct scaling and estimation of the imaging axis direction are derived from the flight path by a simple orientation model.

Some experimental investigation of this kind of ISAR-processing was done with the ELRA phased array at Werthhoven, FRG. Echo sequences of targets of opportunity were recorded and off-line processed. With the autofocus procedure coherence times up to 6 sec could be achieved providing resolution cells in the magnitude of 1 m. Images during straight flight periods as well as along curved flight paths were generated. The reliability of the information given by the signatures was examined by comparison of images of the same aircraft at different positions and different flight manoeuvres, but at the same aspect angle.

## 1. INTRODUCTION

Radars without broadband equipment cannot achieve any target resolution in the range direction. Nevertheless, ISAR-methods promise sufficient cross range resolution as a tool for classification. Compared to 2D-methods, which have been investigated intensively ([1],[2],[3]), the information content of 1D-ISAR signatures is limited. But, at least, the target dimensions as well as a few dominating scattering centers can be identified. 1D-ISAR is not a subset of 2D-ISAR, since customary motion compensation techniques like the isolated-scatterer-track-method [2] cannot be applied. On the other hand, the amount of data is much smaller, so the computational effort can be concentrated on procedures with maximum available performance.

If the flight path of the target and its orientation relative to the radar are known in the magnitude of  $\lambda/8$ , 1D-ISAR is a rather simple procedure, consisting of a motion compensation part (phase correction according to the distance between the antennas phase center and a target fixed point) followed by spectrum analysis.

The main problem is to get exact knowledge of translational and rotational motion. Due to this, the first ISAR-experiments were restricted to rectilinear flight sections [4]. A filterbank over all possible velocity vectors made focusing possible. But for other flight manoeuvres this method is no longer feasible. Ordinary position estimates provided by the radar are too rough for this purpose. Analysis of the complex echo sequence alone eventually permits the generation of high resolution spectra but does not give any relation to the target concerning imaging axis and scaling. So we tried to put position estimates and spectral information extracted from the echo sequence together into a Kalman filter. Since a continuous estimate of the flight path is needed, we used a technique developed at the FFM by H.J.Mieth [7] combining forward-backward smoothing and interpolation.

Imaging axis and scaling are determined by the momentaneous angular velocity vector. The latter can be derived from the flight path, if some elementary rules of aircraft motion are taken into account. This model is restricted to ordinary manoeuvres of wing aircraft and does not extend to rotorcraft or land and sea vehicles.

The experiments with the ELRA phased array indicate, that this procedure yields reliable results in the most cases. Difficulties arise in the transition stage from straight flight to curved flight and in the landing phase, where irregular motion and clutter inference prevent focusing.

## 2. MODEL OF ORIENTATION

In the case of manoeuvring targets vector notation seems to be appropriate. Consider two cartesian coordinate systems, the first one  $(x,y,z)$  being ground fixed with its origin in the antennas phase center and the  $z$ -axis directed to zenith, the second one  $(x',y',z')$  fixed to the airplane with its origin in the targets center of gravity (Fig. 1).

The target motion in six degrees of freedom is described by the translational part  $R(t)$  (motion of the center of gravity measured in the radar coordinate system) and the rotational part given by an orthogonal matrix  $M(t)$ . A target fixed point at position  $r'$  (aircraft coordinates) is transformed to ground coordinates by

$$r(t) = R(t) + M(t)r'$$

The only reliable information about the orientation is given by the target track. The dynamic behaviour of the aircraft may be simplified by the following two conditions (Fig. 2):

AD-P005 850

- (i) the nose of the airplane always points in the direction of motion
- (ii) the roll angle is determined by the component of the resulting acceleration vector perpendicular to the motion axis (balance of power)

Using these conditions, the matrix  $M(t)$  can be expressed by  $R(t)$  and its first and second time derivatives  $\dot{R}(t)$  and  $\ddot{R}(t)$ . In the following, the scalar product is denoted by " $\cdot$ ", the vector product by " $\times$ ", the transpose of a matrix or vector by " $^T$ ", and obvious time dependencies are omitted.

With  $u_x = R / |R|$   
 $g$  = gravity acceleration vector  
 $z = (\ddot{R} + g) \cdot u_x u_x - (\ddot{R} + g)$   
 $u_z = z / |z|$ ,

the orientation matrix can be written as

$$M = (u_x, u_z \times u_x, u_z)$$

$R$ : translation  
 $M$ : rotation

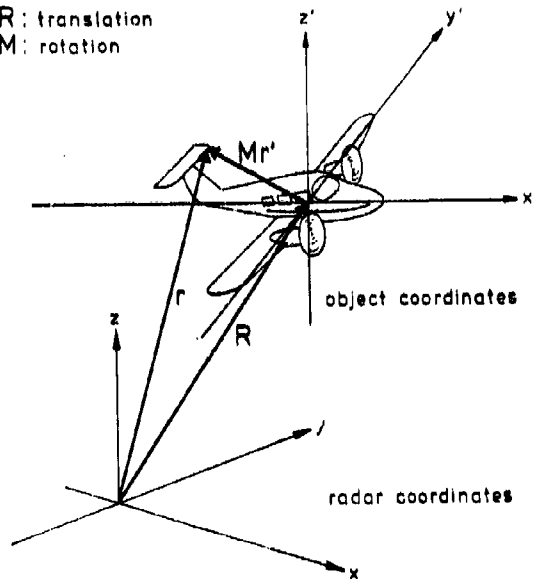
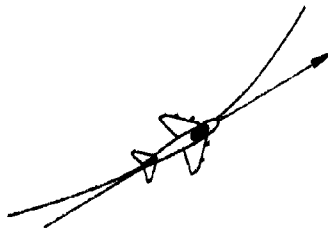


Fig. 1: Coordinate systems

condition (i)



condition (ii)

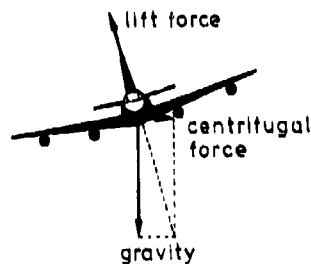


Fig. 2: Orientation model

## B. IMAGING EQUATIONS

If an estimate  $\hat{R}$  of the translational part of motion is available, the motion compensated phase history of one scatterer at point  $r'$  is given by

$$\begin{aligned} \phi &= -2B(|R + Mr'| - |R|) = -2B(|R| - |\hat{R}| + R^T Mr' / |R|) \\ &= -2B(\epsilon - u^T r'), \end{aligned}$$

where  $\epsilon$  denotes the motion compensation error,  $u = -M^T \hat{R} / |M^T \hat{R}|$  the unit vector in target coordinates pointing to the Radar and  $B = 2R/\lambda$  the wave number.

A Fourier analysis of the signal containing the component  $a \cdot \exp(j\phi(t))$  will give an response at the momentaneous Doppler frequency

$$\Omega = -2B\dot{\epsilon} + 2B\dot{u}^T r'$$

Imaging axis and scale are determined by the first time derivative of the unit vector  $u$ , the linear part of the motion compensation error causes a shift of the spectrum. The length of the Fourier transform window - determining the resolution - is limited by the nonlinearity of phase, that means, the second time derivatives of  $\epsilon$  and  $u$ . During the integration time the phase deviation from a linear function of time should not be greater than  $\pi/2$ . In practice, the contribution of the motion compensation error to the quadratic term is more severe than the contribution of  $\dot{u}$ . As a consequence, a better estimation of the flight path is more important than a

reduction of nonlinearities caused by the rotation. This can, for instance, be achieved by nonequidistant resampling.

#### 4. ESTIMATION OF FLIGHT PATH AND MOTION COMPENSATION VIA MIETH'S ALGORITHM

In contrast to motion compensation techniques which take their information only from phase and doppler histories we intended to relate it to the observed track. In this way it is possible to get a simultaneous estimate of imaging axis and scaling.

Let  $Z_n = Z(\nu at)$  be the sequence of complex video samples,  $R(t_n)$  independent position measurements taken at the times  $t_n$ . If a Gauss-Markovian dynamic flight model is assumed, an appropriate track estimate based on  $R(t_n)$  is given by the *Rauch-Tung-Striebel* algorithm [6] (Kalman forward-backward-smoothing). The sequence of smoothed state vectors can be interpolated continuously in an optimum sense by *Mieth's* algorithm [7].

If the vector of measured data is extended by the radial velocity, determined by the momentaneous Doppler frequency based on spectral analysis of the motion compensated sequence  $Z_n$ , the accuracy of the filtered flight path is increased by a high degree. It is not necessary, that the data for Doppler analysis are taken at central times  $t_n$  forming a common vector; instead of this, the two kinds of measurements can be timed independently and fed into the filter. The absence of the just missing component has to be taken into account by setting the corresponding elements of the inverse measurement covariance matrix to zero.

#### 5. ADDITIONAL TOOLS

##### Removal of velocity ambiguity.

Since the PRF used in the experiments is rather low (500 Hz), the feedback of radial velocities has to take care of the Doppler ambiguities. These are removed by the following procedure: 1. To reduce noise, the complex samples are smoothed by a moving window adapted to the momentaneous Doppler frequency. 2. The phase differences of successive smoothed data are tracked beyond the  $2\pi$ -limits and summed up ("phase unwrapping"). 3. The phase increment over the recorded time interval is compared to the corresponding range increment. The integer number of blind velocities are computed, which have to be added to the unambiguous Doppler estimates.

##### Estimation of variances

The track filter needs the measuring covariance matrix, which contains position and velocity components. The variances of position measurements are estimated simply by a line fitting over some neighbouring points. The radial velocity variances are set equal to the resolution cell of the momentaneously used Doppler filter length, multiplied by a fixed factor 2 to 5, with regard to possible remaining motion compensation errors.

#### 6. COMPLETE IMAGING PROCEDURE

The off-line processing of the recorded data is done in several steps (see Fig. 3); not all details are discussed in the paper: first, the complex offset for each sample section with a fixed antenna look direction is compensated. In the next step, local variances of the position measurements are estimated and values exceeding pre-defined tolerances are removed. A first filtering is done with the track measurements only (without phase information). After applying a phase unwrapping procedure described in section 5, the Doppler ambiguity is eliminated by storing the integer multiples of blind velocity for each point of measurement.

Now the iteration begins: By aid of *Mieth's* interpolation formula, the continuous range history is developed and used for a first motion compensation. The sections of the partitioned compensated echo sequence are Fourier transformed with a double overlapping Hamming weighted FFT of predefined window length.

By comparison to a threshold which is adjusted relative to the maximum spectral power, the global frequency band occupied by the spectrum of the motion compensated signal is determined. A low pass filtering according to this bandwidth, followed by Nyquist resampling, reduces the amount of data.

The motion compensation error appears in the spectra as a temporal variation of the center frequency. Depending on the stage of resolution, different methods for the estimation of the error frequency history are chosen: At the first stage, no resolution of target scattering centers is present. In this case, the center frequency is estimated as weighted mean. If some degree of resolution has been reached, the time development of error frequency is determined by searching those shifts of consecutive spectra, for which maximum correlations are achieved. According to experience, a correlation of thresholded logarithmic values yields better results than correlation of power spectra.

The error frequency sequence serves as an estimate of the difference between true radial velocity and that radial velocity proposed by the previous motion compensation. The latter is corrected by that amount and fed back to the track filter.

In the following iteration, the motion compensation is performed with much higher accuracy, since the track filter is fed with high precision radial velocity values. Accordingly, quadratic and higher order phase error terms are reduced and the Fourier time base can be increased without spectral blurring effects. Because of the higher spectral resolution the following error estimate is more precise than the previous one, such that a new track filtering is worth while.

The process is stopped, when no further focussing is possible. This is the case, if the Fourier resolution cell becomes smaller than the remaining fast varying part of the motion compensation error.

At this stage, the estimate of the flight path has reached its maximum accuracy. According to the orientation and imaging equations (sections 2 and 3) the momentaneous imaging axis and scaling factor are calculated for each ISAR image.

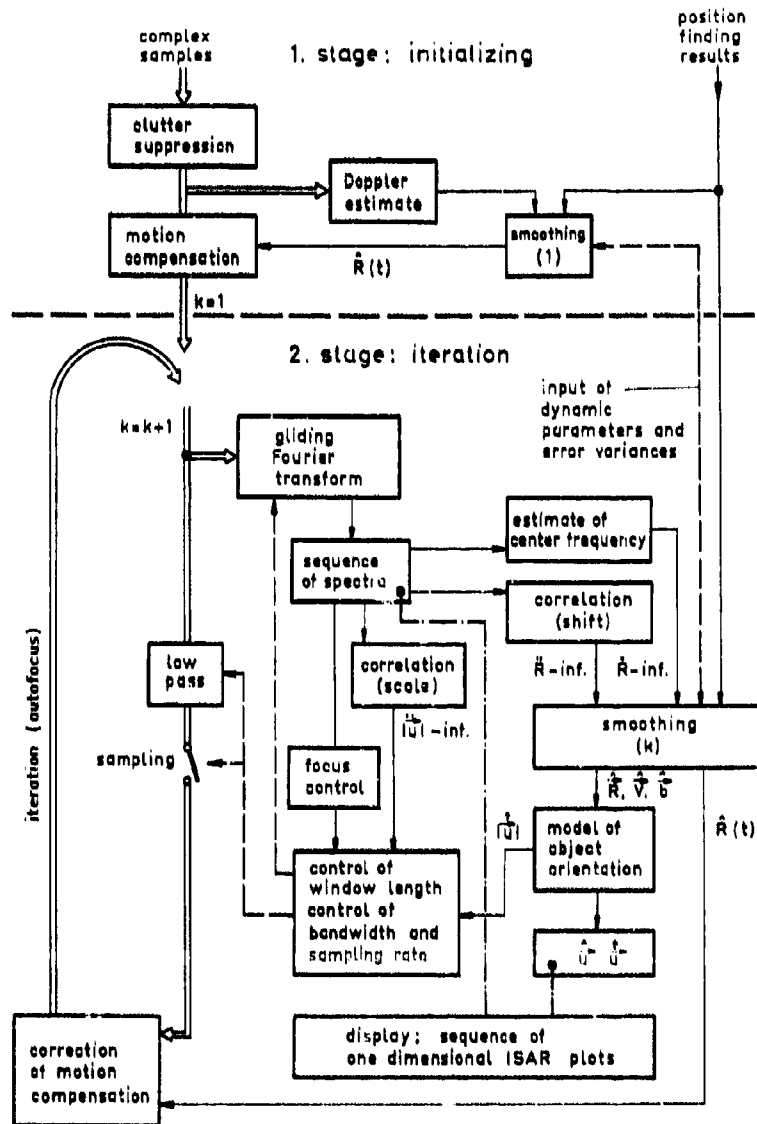


Fig. 3: ISAR processing

## 7. EXPERIMENTAL RESULTS

The experimental investigation in this kind of ISAR-processing was done with the ELRA phased array radar at Werthhoven, FRG. ELRA (experimental electronically steerable radar) operates at a wavelength of 11 cm (S-band) at a maximum bandwidth of 1 MHz. The beam direction is steered by 8 bit phase shifters, which are controlled by a phase calculator. Sum and difference beams are available as digital 10 bit I and Q video signals. For a detailed description see [8], [9].

The recording is done in the following manner: first, ELRA is operated in the search mode only (10  $\mu$ sec pulses). If the search results indicate a promising target, the ISAR mode is switched on. In this mode, a continuous sequence of 1  $\mu$ sec pulses is transmitted at a fixed PRP of 600 Hz. Simultaneously, the antenna gets every 0.1 to 0.2 sec a new steering command in order to track the target. Now the echo sequence within a range window centered at the maximum response can be stored together with the position finding results in a RAM memory. When this is full (after about 10 minutes), the data can be transferred to tape, which is exploited later by a GPC.

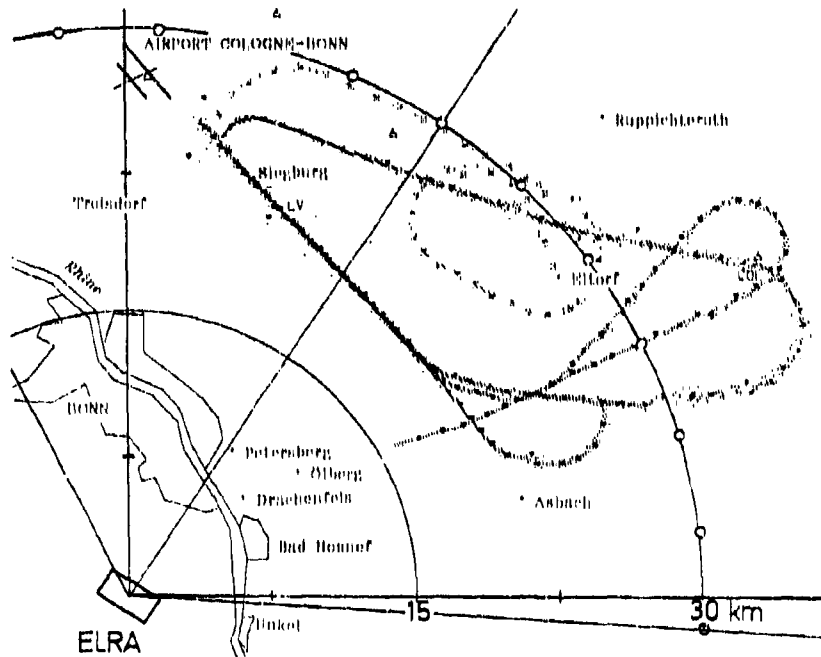


Fig. 4: Raw track

Fig. 4 shows the raw track (without any filtering) of a repeated approach to the Cologne airport. This target of opportunity was found out to be a Boeing 787. The flight path (mean distance ca. 80 km) consists of many straight and curved sections presenting a variety of different aspect angles and imaging vectors.

After the first motion compensation a sequence of Doppler spectra is obtained, more or less centered at zero frequency (fig. 5). The resolution is not yet sufficient to get a reflectivity structure of the target. On the other hand, the Doppler signature consisting of a spectrum of turbine frequencies, comes forward quite well. In the next iteration these responses, which don't belong to the target motion induced relative Doppler, will be filtered out by a digital low pass.

After some iterations (2 to 4) the final resolution is achieved (fig. 6). Normally, we obtain a resolution cell of 1 to 2 meters depending on distance and signal to noise ratio. In fig. 6 the resolution is about 1 meter.

Due to the model of orientation, aspect vector, imaging axis and scale are computed for each ISAR-image. This information gives a basis for computer drawings of the aircraft from the right viewpoint with the correct scaling. These drawings are superposed to the ISAR-signatures in order to recover scattering parts causing special responses.

Since the accuracy of range history was increased in the course of iterations by a high degree, the track accuracy after the last filtering is much better than in the beginning, which is shown in fig. 7 at a processed part of the flight path.

Due to the variety of flight manoeuvres given by the track in fig. 4, it was possible to compare different situations, where aspect and imaging vectors of the same direction promise similar ISAR-plots. As a test of reliability, in fig. 8 two such situations are opposed. The two parts of the flight path have in common, that the forward edge of the radar nearer elevator passes the direction orthogonal to the line of sight at the center of integration time. If this edge is assumed to be a linear uniform reflector, the time behaviour of the echoes should be like a  $\sin x/x$ . In the frequency (image) region a rectangular response with geometrical correspon-

dence to the projected elevator edge should be observed. Apart from some ripple, which is induced probably by the finite time window, a certain agreement with the expected pattern can be stated.

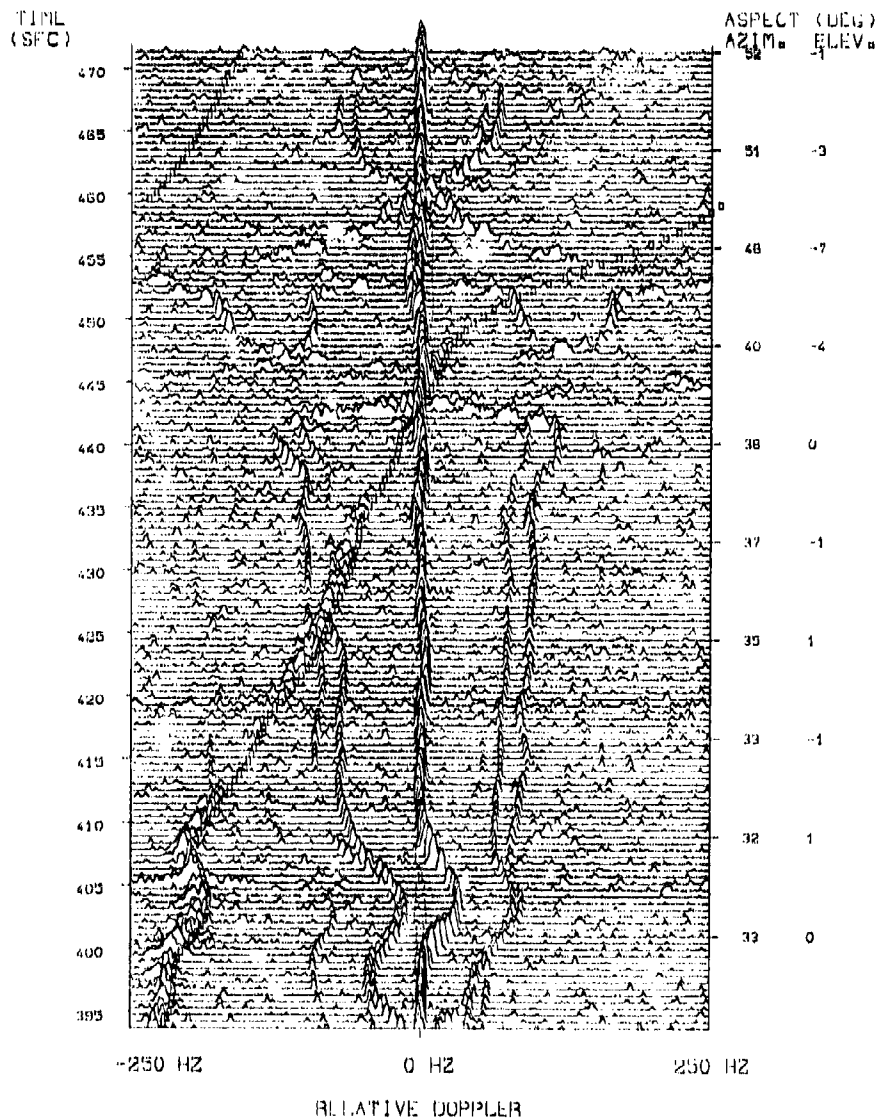


Fig. 6: Doppler spectrum after first motion compensation

By the right side of some ISAR-plots in fig. 6 additional framed plots are mounted for comparison. These are results achieved by the FBL-TNO, The Hague, Netherlands, with the PUCAS phased array, using an imaging procedure, which takes into account slight variations from a straight line flight by polynomial fitting [10]. The aircraft was also a Boeing 707, observed at the same azimuth aspect angle but at a different wavelength during a different flight manoeuvre.

**B. CONCLUSIONS**

33-7

We introduced a technique of motion compensation suitable for the generation of 1D-ISAR plots of aircraft. The experimental results with the ELRA phased array indicated that this procedure yields reliable results in the case of airliners on straight and curved flight paths. Military targets were not observed.

The computation was done off-line taking a processing time of some hours per minute recorded data. Nevertheless, it seems possible to organize the processing scheme in a pipelined manner to get a quasi on-line image generation.

1D-ISAR images contain at least the information about the target dimensions; beyond that, a few strong scatterers may be recovered. A sequence of ISAR plots at different aspect angles allows to identify stable scatterers and to eliminate artifacts. In this way, 1D-ISAR could serve together with other information as a classification tool for radars without high range resolution capability.

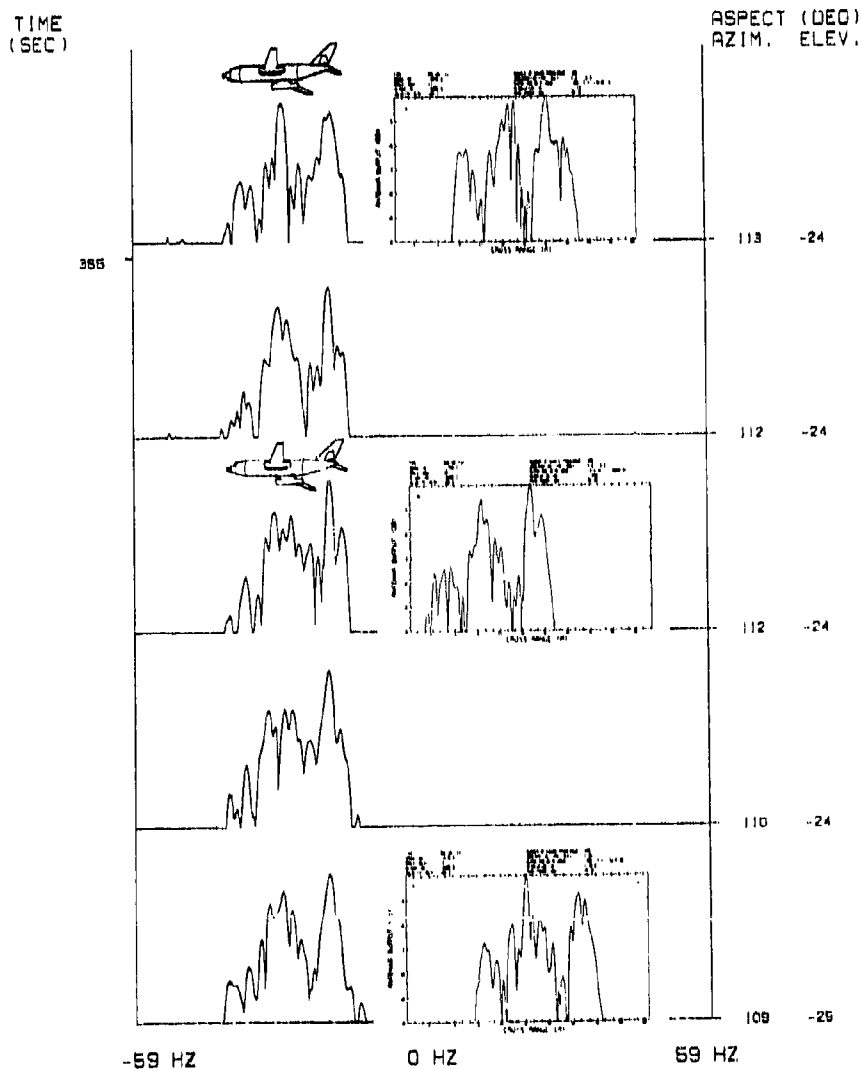


Fig. 8: Final ISAR-plots

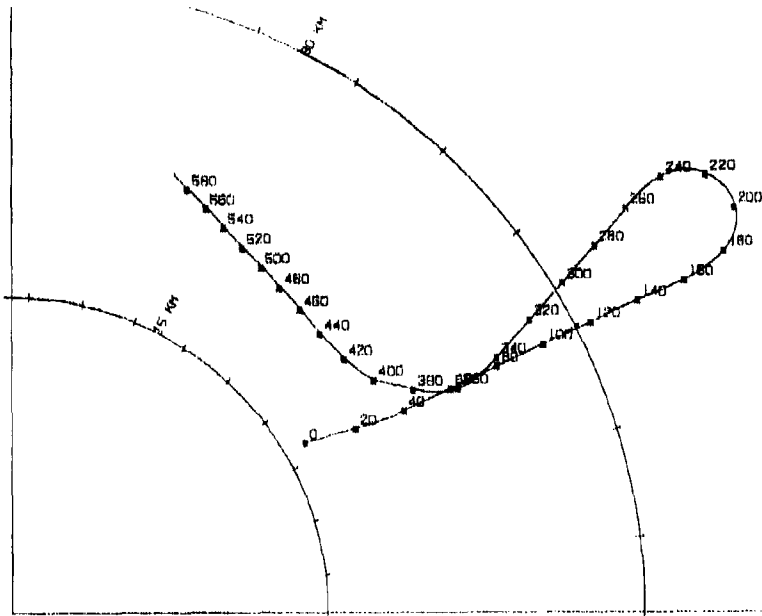


Fig. 7: Pinal flight path estimate

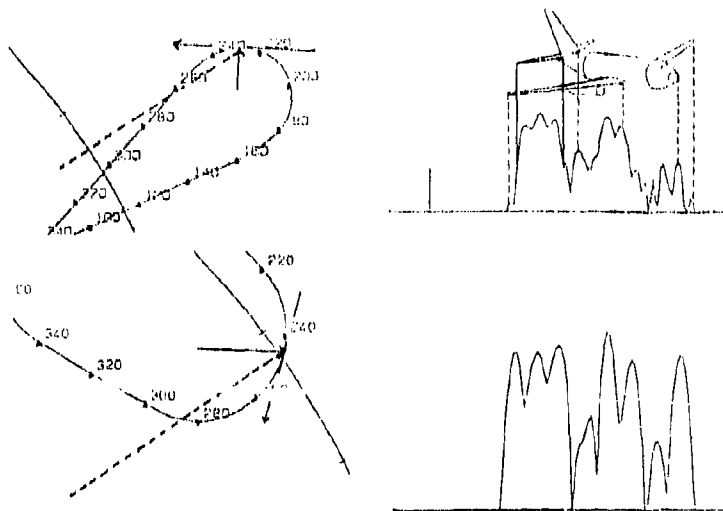


Fig. 8: ISAR-plots at different manoeuvres

#### LITERATURE

- [1] M.J. Prickett, C.C. Chen, "Principles of inverse synthetic aperture radar (ISAR) imaging", 1980 NASCON record, pp. 840-845
- [2] C.C. Chen, H.C. Andrews, "Target-motion-induced radar imaging," IEEE Trans Vol. AEB-16, No. 1, Jan 1980, pp. 2-14

- [3] G. DiKe, R. Wallenberg, "Inverse SAR and its application to aircraft classification," IEEE Intern. Radar Conf. 1980, pp.161-167
- [4] W.D. Wirth, "High resolution in azimuth for radar targets moving on a straight line," IEEE Trans. AES-16, No.1, Jan. 1980, pp. 101-104
- [5] H.E. Rauch, F.Tung, C.T. Striebel, "Maximum likelihood estimates of linear dynamic systems," AIAA Journal, Vol.8, no. 8 (1968), pp. 1445-1450
- [6] W.D. Wirth, "Solid state multifunction phased array," AGARD conference on multifunction radar for airborne applications.
- [7] H.J. Mieth, "Verfahren zur Rekonstruktion des kontinuierlichen Flugzustandes aus diskreten Radarmeldungen," Internal report of the FFM, Oct. 1988
- [8] W. Sander, "Experimental phased-array radar ELRA: antenna system," IEE proc. pt. F, vol. 127, no. 4, Aug. 1980
- [9] W.D. Wirth, "Signal processing for target detection in experimental phased-array radar ELRA," IEE proc. pt. F, vol. 128, no. 6, Oct. 1980
- [10] K.K. Berland, "Application of inverse synthetic aperture radar on aircraft," Internat. radar conf. Paris 1984, communication C-10, pp. 618-620

#### DISCUSSION

J.Dorey

I think that Fourier-Fresnel transforms would be better than FFT+Kalman filtering. What is your opinion?

Author's Reply

I agree with you, that these methods should be investigated. Nevertheless, it will neither achieve a compensation of phase terms of higher than second order, neither will it contribute to an accurate estimate of aspect, imaging axis and scale.



## RADAR TARGET IMAGE BY ISAR CASE STUDY

by

S. Murini, S. Pardini, F. Prodi  
 Radar Dept. Selenia S.p.A.  
 Via Tiburtina Km 12,400  
 00131 Rome,  
 Italy

AD-P005 851

## SUMMARY

This paper describes target imaging based on ISAR techniques. It consists of two parts: theoretical topics and experimental results. The former illustrates the suite of processing functions needed to obtain the target image starting from the radar echoes. Key processing steps include motion compensation and reconstruction of the reflectivity function. The second part of the paper illustrates an experimental set-up based on a currently available tracking radar, a data recorder and off-line processing facilities. A high cross-range resolution image of a MB-339 aircraft has been obtained by processing recorded radar echoes from a Selenia X-band tracking radar.

## 1. INTRODUCTION

In this paper a radar imaging technique based on the spatially coherent processing of radar returns will be described /1,2/. This technique is well established in literature and, in some sense, has many similarities with other imaging techniques such as spotlight SAR, image reconstruction from projections, etc. The technique considered in this paper is generally referred to as ISAR (Inverse Synthetic Aperture Radar). A high resolution image of radar target is obtained by coherently processing echoes relative to different aspects radar-target.

In the first section of this paper the theoretical bases /1/ of the imaging technique will be described. ISAR processing consists of baseband conversion, motion compensation, and the reconstruction of the reflectivity function. The last step is performed by means of an Inverse Fourier Transform of the motion compensated signal. It will be noted, in particular, that the depth of field of the reconstructed image depends on the couple of coordinates  $(X, Y)$  employed to represent the motion-compensated signal.

The second part of the paper describes an experimental set-up based on a currently available tracking radar, a data recorder, and off-line processing facilities. A cross-range high resolution image of an MB-339 aircraft has been obtained by processing the recorded echoes from Selenia X-band tracking radar. From the reconstructed profile it has been possible to obtain a rough estimate of target extension on the cross-range dimension. Finally, a reliable estimate of the radial and tangential components of target velocity have been obtained by the motion compensation algorithm.

## 2. THEORETICAL TOPICS

In the ISAR system considered in this paper, (fig. 1), the radar is located in the origin  $O$  of the reference axes  $\xi\eta$ . The target is represented as a bidimensional object which moves in the plane  $\xi\eta$ . The reference coordinates  $xy$ , with origin in  $T$ , are fixed to the target. The transmitted and received signals  $s_T(t)$  and  $s_R(t)$  are expressed in their analytical forms:

$$s_T(t) = A_1(t) \cdot \exp[j2\pi f_0 t] \quad (1)$$

$$s_R(t) = A_2(t) \cdot \exp[j2\pi f_0 t] \quad (2)$$

where  $A_1(t)$  and  $A_2(t)$  are bandlimited signals. It will be assumed that the transmitted signal is one of the waveforms typically employed in radar applications, i.e.: the monochromatic pulse or chirp. Initially the transmission of a noncontinuous waveform will be considered. The expression of  $s_R(t)$  is obtained from  $s_T(t)$  assuming that the electromagnetic properties of the target can be described by a complex function  $f(x, y)$ , defined on the coordinates  $xy$  of the target. Signal  $s_R$  is then down converted, motion compensated, and expressed in function of a suitable couple of variable  $XY$ . The motion compensated signal  $s_R^M(X, Y)$  is well approximated by the bidimensional Fourier Transform of  $f(x, y)$ . The reflectivity function, that is the target image, can then be reconstructed by means of an Inverse Fourier Transform of  $s_R^M(X, Y)$ .

## 2.1 THE SCATTERING MODEL

The scattering model is based on the physical and geometrical diffraction theory. This model refers to the notion of ideal point scatterers, equivalent scatterers, and the reflectivity function /1,3,4,5/. The point scatterers are corners, edges, and, in general, parts of the targets whose bending radius is smaller than the wavelength. For an aircraft these parts may be the edges of the wings, of the impennage, or the nose.

Referring to fig. 2, the ideal  $i$ -th point scatterer with coordinates  $(X_i, Y_i)$  is such that the received signal  $s_{Ri}$  is related to the transmitted signal  $s_T$  as follows:

$$s_{Ri} = A_i \cdot s_T(t - \tau_i) \quad (3)$$

where  $A_i$  is the complex reflectivity of the  $i$ -th scatterer and  $\tau_i$  is the propagation delay, given by:

$$\tau_i = \frac{R(x_i, y_i)}{c} \quad (4)$$

$c$  is the light speed and  $R(x_i, y_i)$  is target range.

When the point reflector is in motion, Eq. (3) becomes:

$$s_{Ri}(t) = A_i \cdot s_T[t - \tau_i(t)] \quad (5)$$

where  $\tau_i(t)$  is well approximated by /6/:

$$\tau_i(t) \approx \frac{2}{c} R(t, x_i, y_i) \quad (6)$$

When the target consists of a collection of ideal point scatterers, it is very tempting to describe the received signal  $s_R(t)$  as a superposition of the contributions of all the scatterers:

$$s_R(t) = \sum_{i=1}^{N_d} A_i \cdot s_T[t - \tau_i(t)] \quad (7)$$

where  $N_d$  is the number of scatterers. This representation ignores, however, the interactions that exist between scatterers. These interactions give rise to multiple scattering and masking. These effects are very sensitive to the angle of arrival of incident wave. To overcome these difficulties, it will be assumed that the scatterers appearing in Eq. (7) are an equivalent set such that this expression is a good approximation of the received signal. The equivalent set is also comprehensive of all the system parameters that are involved in scattering. These parameters are typically the wavelength, the polarization, and the angle of incidence of the transmitted waveform. In practice the value assumed by the latest parameter depends on time, as the target is generally in motion. This fact would ask, in theory, for a time varying model of scattering. According to this model, the reflectivity coefficients  $A_i$  or the coordinates  $(x_i, y_i)$  should be time dependent. In many applications, like that considered in the next section, the variation of aspect angle is limited to few degrees. In this case backscattering can be described by Eq. (7).

Eq. (7) may be generalized to a continuous distribution of scatterers as:

$$s_R(t) = \int_A f(x, y) \cdot s_T[t - \tau(t, x, y)] dx dy \quad (8)$$

where  $f(x, y)$  is the complex reflectivity function defined over the target relative to a set of coordinates  $xy$  fixed to the target.  $\tau(t, x, y)$  is the propagation delay relative to point  $(x, y)$ .  $A$  is indicatively the target domain extension. The reflectivity function, relative to the equivalent set of point reflectors, is given by:

$$f(x, y) = \sum_{i=1}^{N_d} A_i \delta(x-x_i) \cdot \delta(y-y_i) \quad (9)$$

In general, we can observe that:

- the way of associating  $f(x, y)$  with the physical and geometrical characteristics of the distributed target is not simple. In particular the domain  $A$  does not coincide necessarily with target domain extension.
- $f(x, y)$  depends on parameters such as frequency, polarization and on aspect angle of incident wave.

## 2.2 SIGNAL PROCESSING

With reference to Fig. 1 indicate with:  $R(t)$  the distance of point  $T$  from target,  $\varphi$  the angle between the radial direction  $OT$  and the  $\xi$  axis,  $\theta$  the angle between the axes  $\xi$  and  $x$ . The position of target on the plane  $\xi\eta$  is determined by  $\varphi$ ,  $\theta$  and  $R$ . Axes  $u, v$  are aligned respectively with cross-range and range directions.

Suppose the radar transmits a continuous wave with frequency  $f$ :

$$s_T(t, z) = \exp(j2\pi ft) \quad (10)$$

By substitution of Eq. (10) into Eq. (8), and approximating range delay  $\tau(t, x, y)$  by means of Eq. (6), the received signal  $s_R(t, z)$  becomes:

$$s_R(t, z) = \exp(j2\pi ft) \int_A f(x, y) \cdot \exp[-j \frac{4\pi R}{c} R(t, x, y)] dx dy \quad (11)$$

where  $R(t, x, y)$  is the distance of point  $P(x, y)$  from radar at time  $t$ . In particular  $R(t) = R(t, 0, 0)$  is the distance of reference point  $T$  from radar.

The baseband converted signal  $s_b^*(t, z)$  is obtained by down mixing the signal  $s_R(t, z)$  with a coherent local oscillator with frequency  $f$ :

$$s_b^*(t, z) = s_R(t, z) \cdot \exp(-j2\pi ft) = \int_A f(x, y) \cdot \exp[-j\varphi(t, x, y)] dx dy \quad (12)$$

where:

$$\varphi(t, x, y) = \frac{4\pi R}{c} R(t, x, y) \quad (13)$$

is the phase history relative to the point  $P(x, y)$ .

Motion compensation consists in removing the phase relative to a point fixed to the target from the phase of signal  $s_R^1$ . It can be supposed, without loss of generality, that the reference point coincides with T. Motion compensated signal is then given by:

$$s_R^1(t, \xi) = s_R(t, \xi) \cdot \exp[-j\phi(t)] \quad (14)$$

where  $\phi(t) = \phi(t, 0, 0)$  is the phase history relative to reference point. By substitution of Eq. (12) in Eq. (14), signal  $s_R^1$  is expressed as:

$$s_R^1(t, \xi) = \int_A f(x, y) \cdot \exp[-j\phi^1(t, x, y)] dx dy \quad (15)$$

where:

$$\phi^1(t, x, y) = \frac{4\pi R}{c} [R(t, x, y) - R(t)] \quad (16)$$

Motion compensation requires a precise tracking of some reference point fixed to target. However the standard deviation of the estimate error of target range must be of the order of one wavelength, in order to obtain a satisfactory reconstruction of target reflectivity. As this goal is difficult to achieve in practical systems, an alternate approach must be devised. In /7/ a technique which gives a parametric estimate of the phase of reference point has been proposed. Motion parameters have been estimated directly from received signal by maximization of a suitable correlation function. As this maximization gives the focus of reference point, this technique is referred to as autofocusing. In /8/ such technique has been applied in the hypothesis of straight line motion. In this case motion parameters have been estimated by means of an efficient iterative algorithm.

To understand the importance of motion compensation in ISAR processing, compare expressions (13) and (16). Though analogous in the form, they are quite different in substance. In fact, while the former depends functionally on absolute phase  $\phi(t, x, y)$  of point P, the latter depends on  $\phi^1(t, x, y) = \phi(t, x, y) - \phi(t)$ , which is now the phase of point P but relative to the reference point T(0,0). As target size is negligible compared to target range, the condition  $|\phi^1| \ll |\phi|$  is practically verified. In general  $\phi^1$  can be approximated by the following bilinear form:

$$\phi^1 \approx xX + yY \quad (17)$$

where (X, Y) is a couple of variables obtained by the couple (t, \xi) thru a proper transformation T: (t, \xi) \to (X, Y). Approximation (17) is supposed verified for (x, y) \in A and (X, Y) \in D, where D is the supporting domain of  $s_R^1$  on plane XY.

By substitution of Eq (17) into Eq (15), signal  $s_R^1$  is now approximated by the bidimensional Fourier Transform of f(x, y), i.e.:

$$s_R^1(X, Y) \approx \int_A f(x, y) \cdot \exp[-j(xX + yY)] dx dy \quad (18)$$

Eq. (18) represents the basic result of ISAR technique and, for this reason, is called *imaging equation*. The reflectivity function may be reconstructed by means of an Inverse Fourier Transform of  $s_R^1(X, Y)$ :

$$\hat{f}(x, y) = \frac{1}{4\pi^2} \int_D s_R^1(X, Y) \cdot \exp[j(xX + yY)] dXdY \quad (19)$$

where  $\hat{f}(x, y)$  is the reconstructed reflectivity function.

The resolution properties of reconstructed image depend on the extension of domain D, which is essentially related to tracking angle and to bandwidth available in the received signal.

Furthermore we note that approximations given by Eqs. (17) and (18) are generally verified on a bounded domain on plane (XY). In this domain the reflectivity function, reconstructed by means of Eq. (19), will be well focalized. The extension of this domain, which defines the depth of field of reconstructed image, depends on the particular couple XY employed to represent signal  $s_R^1$ . Depth of field has been evaluated /9-12/ for two typical representations of signal  $s_R^1$  which are commonly referred to as rectangular and polar format of data. In the first case samples of signal  $s_R^1$  are available on a rectangular grid on plane XY. Samples of  $\hat{f}(x, y)$  may be then efficiently obtained by means of a bidimensional IFFT (Inverse Fast Fourier Transform) of  $s_R^1$  samples. The rectangular format is considered when target motion is straight. In this case the depth of field may be adequate to represent small targets (like missiles or small aircrafts). In the polar format the  $s_R^1$  samples are represented on a polar grid of plane XY, thus preventing from the direct application of the IFFT algorithm to recover reflectivity function. Therefore, some interpolation algorithms prior to the inverse transform are needed to obtain the samples on a Cartesian grid /13/. The depth of field associated to polar format is practically adequate for all typical ISAR applications. Polar format will be analyzed in detail in the next paragraph.

### 2.3 THE POLAR FORMAT

In this paragraph it will be shown that polar format derives directly from straight iso-range approximation.

With reference to fig. 3, indicate with (u, v) the coordinates of the point P in the reference coordinates (u, v). The distance of P from the radar is:

$$R(t, u, v) = [(R(t) + v)^2 + u^2]^{1/2} \quad (20)$$

As target size is small compared to target range,  $R(t, u, v)$  may be approximated by:

$$R(t, u, v) \approx R(t) + v \quad (21)$$

The error  $\epsilon_R = R(t, u, v) - [R(t) + v]$  associated to the above approximation is given by:

$$\epsilon_R = \frac{u^2}{R(t, u, v) + R(t) + v} \quad (22)$$

This error vanishes when target range approaches to infinity. According to approximation (22), the curved iso-range contours of fig. 3 are considered straight for a limited region in u dimension.

By substitution of Eq. (21) in Eq. (16) the phase  $\phi''$  is well approximated by:

$$\phi'' = \frac{4\pi f}{c} v \quad (23)$$

Coordinates u, v are related to coordinates xy by the following relations:

$$\begin{aligned} u &= y' \cos(\delta) - x' \sin(\delta) & (24) \\ v &= x' \sin(\delta) + y' \cos(\delta) & (25) \end{aligned}$$

where  $\delta = \theta - \theta_0$  is the angle between axis x and v. It defines the orientation of target with respect to radar. After substitution of Eq. (25) in Eq. (23), the latter may be expressed in the bilinear form (17), if variables (X, Y) are related to variables (t, f) by:

$$T_2: \begin{cases} X = \frac{4\pi f}{c} \cos(\delta) \\ Y = \frac{4\pi f}{c} \sin(\delta) \end{cases} \quad (26)$$

where X and Y depend on time through  $\delta$ . By means of transformation  $T_2$ , the signal  $s''_R$ , available on a rectangular domain D of plane tf, is represented on a polar domain of the plane XY.

#### 2.4 SYSTEM RESOLUTION

The reconstructed reflectivity function  $\hat{f}(x, y)$  may be considered the response of a linear system to the reflectivity function.

$$\hat{f}(x, y) = F[f(x, y)] \quad (27)$$

Impulse response  $h(x, y, x_0, y_0)$  of F is the reconstructed image of a point reflector located in  $P(x_0, y_0)$ . This response may be easily obtained by Eqs. 15, 16, 19 after substituting in the former  $f(x, y) = \delta(x - x_0) \delta(y - y_0)$ :

$$h(x, y, x_0, y_0) = \int_D \exp[-j\phi''(x, y, x_0, y_0)] \exp[j(xX + yY)] dx dy \quad (28)$$

where  $\phi''(x, y, x_0, y_0)$  is the motion-compensated phase relative to point  $(x_0, y_0)$  and expressed by means of variables (X, Y).

It will be now assumed that the motion-compensated phase  $\phi''$  may be exactly expressed in the bilinear form (17). In this case F is a space invariant transformation whose impulse response  $w(x, y)$  is given by:

$$w(x, y) = \int_D \exp[j(xX + yY)] dx dy \quad (29)$$

$\hat{f}(x, y)$  can be then expressed as a bidimensional convolution of  $f(x, y)$  and  $w(x, y)$ :

$$\hat{f}(x, y) = f(x, y) \otimes w(x, y) \quad (30)$$

$w(x, y)$  is typically the shape of a lobe centered in point  $P(0, 0)$ . The width of this lobe in a certain direction gives the resolution attainable in the same direction. From Eq. (29) it can be deduced that system resolution depends on the shape of domain D in which signal  $s''_R$  is represented.

Impulse response will be now evaluated for some typical domains, or windows, obtainable with the polar representation of data.

When the transmitted signal is monochromatic, the window is the arc of circle shown in fig. 4. The arc aperture is given by the variation of the aspect angle  $\delta = \theta - \theta_0$  during the observation time. For a pure rotational and translational motion of target this variation is due to a variation respectively of  $\theta$  and  $\theta_0$ . The window obtained by means of a finite number of frequencies  $f_c$  is reported in fig. 5. The arc radius relative to the i-th frequency is given by  $4\pi f_i / c$ . The window relative to a continuous frequency bandwidth is illustrated in fig. 6.

The impulse response by a translatory motion will be now evaluated. The geometry of this motion, (fig. 7), has been derived from fig. 1 assuming that the axis  $\eta$  bisects the angle described by the segment OP during the observation time  $T_0$ . Furthermore the coordinate system xy is now parallel to system  $\xi\eta$ .

Suppose that a large bandwidth is transmitted. In this case the motion compensated signal is represented, by means of Eq. (26), in the annular region of plane XY (fig. 8). This window is approximated by the rectangular window:

$$w_r = \begin{cases} 1 & \text{for } |x| \leq X_A \text{ and } |y| \leq Y_A \\ 0 & \text{elsewhere} \end{cases} \quad (31)$$

where:  $Y_1 = Y_c - Y_A$ ,  $Y_2 = Y_c + Y_A$ ,  $Y_c = 4\pi f_m / c$ , and:

$$X_A = \frac{4\pi f_m B}{c} \sin(\Delta) \quad (32)$$

$$Y_A = \frac{2B}{c} B \quad (33)$$

$B$  and  $f_m$  are respectively the medium band frequency and the available bandwidth. Impulse response  $w_r$ , (fig. 9), is then given by:

$$w_r(x, y) = \frac{X_A Y_A}{\pi^2} \exp(j \frac{4\pi f_m}{c} y) \cdot \text{sinc}(X_A \cdot x) \cdot \text{sinc}(Y_A \cdot y) \quad (34)$$

Resolutions  $r_x$ , (cross-range), and  $r_y$ , (down-range), are determined by the occurrence of the first zero in the sinc function:

$$r_x = \frac{\pi}{X_A} = \frac{\lambda_m}{4 \cdot \sin \Delta} = \frac{\lambda_m}{2\theta_{01}} \quad (35)$$

$$r_y = \frac{\pi}{Y_A} = \frac{c}{2B} \quad (36)$$

These resolutions correspond approximately to -4 dB mainlobe width of sinc function.

It will be now assumed that the signal  $s'_k$  is uniformly sampled in both time and frequency dimensions. In this case the samples of  $s'_k$  are represented on the polar grid of fig. 10. These samples are then suitably interpolated /13/ on a rectangular grid of plane XY, (fig. 11). Samples  $\hat{f}_{pq}$  of reconstructed reflectivity function are then obtained by means of an IFFT of interpolated samples.

In the discrete case impulse response  $w'_r$  is well approximated by:

$$w'_r(x, y) = \frac{1}{4\pi^2} \exp(j \frac{4\pi f_m}{c} y) \frac{\text{sinc}(X_A \cdot x)}{\text{sinc}(\frac{X_A}{N} \cdot x)} \frac{\text{sinc}(Y_A \cdot y)}{\text{sinc}(\frac{Y_A}{M} \cdot y)} \quad (37)$$

In this case system resolutions are still given by Eqs. (35), (36). Furthermore the number  $N$  and  $M$  of samples, acquired respectively in cross-range and down range dimensions, must satisfy the following conditions:

$$C_x = N \cdot r_x \geq L_x \quad (38)$$

$$C_y = M \cdot r_y \geq L_y \quad (39)$$

where  $L_x$  and  $L_y$  are target extensions, respectively in cross-range and down-range. Assuming  $r_x = r_y = 1$  m,  $L_x = L_y = 50$  m, conditions (38) and (39) are verified respectively when  $N \geq 50$  and  $M \geq 50$ .

It can be observed that a good cross-range resolution may be achieved with a relatively small value of observation angle  $\theta_{01}$ . When  $\lambda = 3$  cm,  $\theta_{01} = 1^\circ$ , it gives, for instance, a cross-range resolution  $r_x < 1$  m. The observation time necessary to describe this angle depends, in general, on target motion. Assuming that target range  $R_0 = 10$  Km and target velocity  $v_t = 200$  m/s, an observation time  $T_0 = 1$  s is sufficient to obtain a processing angle  $\theta_{01} = 1^\circ$ .

Among translational motions, the rectilinear and uniform ones represent a good approximation of real target motion.

## 2.5 ANALYSIS OF TRANSMITTED SIGNAL

System resolution is strictly related to the extension  $D$  of the domain where motion compensated signal  $s'_k$  is represented. In the previous chapter we saw that this domain coincides with an arc when the transmitted signal is monochromatic. More complex domains may be obtained gathering the informative content given by different frequencies. The same domains may be obtained by means of a large bandwidth signal. In this case it must be proved, however, that the received signal, suitably acquired and processed, may be expressed in the form (19). This has been proved /1/ for the following typical signals: monochromatic pulse, multifrequency pulse, burst of monochromatic pulses, and chirp.

## 3 EXPERIMENTAL RESULTS

The feasibility of technique described in section 2 has been verified by an imaging experiment performed with a conventional tracking radar /14,15/. The radar echoes have been acquired by means of a general purpose setting-up. A high resolution image of the MB 339 aircraft has been obtained by off-line processing the stored echoes.

### 3.1 THE EXPERIMENTAL SET-UP

The sensor employed in the experiment was a X-band tracking radar of Selenia. Radar echoes were acquired by means of a general purpose setting up while the aircraft was flying a pre-programmed path. The acquisition set-up is shown in fig. 12. According to flight plan, the aircraft was expected to fly the

straight path AB with uniform speed  $v_a=130-150$  m/sec. Both length of trajectory AB and distance  $R_0$  are about 10 Km. When trajectory is run along, the aircraft turns, flies back along the same trajectory, and so on for about 15 times. Radar PRT is staggered with a mean value of 260  $\mu$ s. The baseband converted echoes are acquired by the W.R. (Waveform Recorder) HP 5180A. The W.R. works in the following way: the input signal is sampled with the clock (internal or external) frequency. When a trigger (internal or external) is present at input, each sample is stored sequentially into a record as a ten bit word. The capability of the record may be set up to one of the following values: 512, 1 K, 2 K, 4 K, 16 K words. Data recording ends when the record is full. At this time the record may be transferred to a buffer of the HP 9000/300 HP P.C. (Personal Computer). The acquisition of a new record begins later with the next trigger, and so on. In the experiment, the W.R. was set up with the greatest capability of 16 k words. External clock and external trigger were generated by means of the timing circuitry, which consists of a pulse generator and a burst generator. When the buffer is full, is stored in the hard disk. As this transfer ends, the computer controls the acquisition of a new buffer, and so on. During the target flight, azimuth, elevation, range, doppler and speed were recorded by the operator at the radar-console. Target trajectory was automatically plotted by means of the data available from the data-processor.

The timing for the acquisition of the radar pulses is reported in fig. 13: 16 pulses are acquired in each sweep, 8 for channel A, 8 for channel B. In this way one record contains the samples of 1024 sweeps. It is then possible to make a rough evaluation of the resolution obtained by coherently processing one record. The observation time  $T_0$  is given by:

$$T_0 = 1024 \cdot \text{PRT} \approx 0.26 \text{ s} \quad (40)$$

The flight plan foresees that target velocity  $v_a$  and target range  $R_0$  assume the following values:  $R_0=10$  Km and  $v_a=150$  m/s. If during the observation interval  $T_0=[-T_0/2, T_0/2]$  target trajectory is approximately tangential with respect to the radar, the processing angle  $\theta_{e1}$  is given by:

$$\theta_{e1} \approx \frac{v_a \cdot T_0}{R_0} = 39 \cdot 10^{-4} \text{ rad} \quad (41)$$

The cross-range resolution is then given by:

$$r_x \approx \frac{\lambda}{2\theta_{e1}} = 3.6 \text{ m} \quad (42)$$

This resolution, limited by the observation time  $T_0$ , may be sufficiently good to resolve some target scatterers.

### 3.2 SIGNAL PREPROCESSING

Signal processing of data stored in each record have been performed by means of HP 9000/300 P.C. Signal processing consists of the motion compensation and reconstruction of the reflectivity function.

Data preprocessing consists of the following steps:

- select from each sweep of the record a suitable complex sample,
- undersampling the data available from step a),
- estimate and subtract the bias from the samples obtained in step b).

### 3.3 FREQUENCY ANALYSIS

The frequency analysis has been made for each record as modulus of the FFT of the pre-processed samples  $b_k$ . Each spectrum obtained in this way has been represented in the ambiguous interval  $[0, v_0]$ , where  $v_0=37.6$  m/s is the blind speed relative to the PRF=3.845 KHz and to the wavelength  $\lambda=3$  cm. The maximum value of one spectrum gives an ambiguous estimate of target radial velocity. In fig. 14-17 the spectral analysis relatives to four consecutive records are reported. The non-ambiguous radial velocity relatives to these records are given respectively by: -45.7, -45.1, -43.9, -43.2 m/s (the radial velocity is conventionally negative when the target is approaching to the radar).

### 3.4 MOTION COMPENSATION

Motion compensation consists of removing the phase term  $\varphi(t)=4\pi R(t)/\lambda$  relative to the reference point. This term is not generally known and is estimated by means of a parametric technique [7]. Target motion has been approximated as rectilinear and uniform as:

- the aircraft is expected to fly according to this type of motion
- the observation time  $T_0=0.26$  s is sufficiently short to neglect the effects of unintentional pilot maneuvers or of atmospheric effects like wind gust, change of the external pressure, and so on.

In this case the reference point phase  $\varphi(t)$  is approximated by the second order Taylor polynomial with respect to  $t=0$ :

$$\varphi(t) \approx \alpha + \beta t + \gamma t^2 \quad (43)$$

where:

$$\alpha = \frac{4\pi f_0}{c} R_0 \quad (44)$$

$$\beta = \frac{4\pi f_0}{c} v_t \quad (45)$$

$$\gamma = \frac{2\pi f_0}{c} \frac{v_r^2}{R_0} \quad (46)$$

and  $R_0$  is target range,  $v_r$  and  $v_t$  are the radial and tangential velocities at  $t=0$ .

The coefficients  $\beta$  and  $\gamma$  have been estimated by maximization of the following correlation function:

$$F(\beta, \gamma) = \frac{1}{N} \left| \sum_{k=1}^N b_k \exp\{j(\beta t_k + \gamma t_k^2)\} \right| \quad (47)$$

by means of the algorithm developed in /8/. In Eq. (47)  $t_k = (k-1)T_{\text{PRT}}$  are the time instants of  $b_k$  and  $N$  is the number of available samples. The motion compensated samples  $b_k'$  are then evaluated as:

$$b_k' = b_k \exp\{j(\hat{\beta} t_k + \hat{\gamma} t_k^2)\} \quad k=1, N \quad (48)$$

where  $\hat{\beta}$  and  $\hat{\gamma}$  are the estimates of  $\beta$  and  $\gamma$ . Eq. (47) has been typically evaluated with  $N=64$  samples  $b_k$  obtained by means of a suitable undersampling in the preprocessing step.

Let us now spend some considerations on motion parameter estimates. A rough estimate  $\hat{R}_0$  has been obtained by means of association of the processed record with the plotted trajectory. The estimate  $\hat{v}_x$  has been obtained by spectral analysis. The estimate  $\hat{v}_t$  of tangential velocity may be easily derived from Eq. (46) as:

$$\hat{v}_t = \left( \frac{\hat{\gamma} \lambda \hat{R}_0}{2R} \right)^{1/2} \quad (49)$$

The tangential velocities estimated for the records considered in 3.3 are approximately given by  $\hat{v}_t = 120$  m/s.

### 3.5 PROFILE RECONSTRUCTION

Let us now see how the cross-range profile of the aircraft may be reconstructed by means of motion compensated samples  $b_k'$ . At first a simple relationship between cross-range profile and bidimensional reflectivity function  $f(x, y)$  will be found.

The wing span and length of M339 aircraft, employed in the experiment, are approximately of 10 m. Because of the short value of the wavelength and the short observation time corresponding to a small variation of aspect angle, the motion compensated samples may be represented on Fourier domain according to the rectangular format. In this case, Eq. (16) may be approximated by /10/:

$$\phi' = \frac{4\pi f}{c} \left( \frac{v_x t}{R_0} x + y \right) \quad (50)$$

After substitution of Eq. (50) in Eq. (15), signal  $s_R'$  may be approximated by:

$$s_R'(t) = \int_{x_1}^{x_2} f_1(x) \exp\{-j \frac{4\pi f}{c} \frac{v_x t}{R_0} x\} dx \quad (51)$$

where  $f_1(x)$  is aircraft cross-range profile, given by:

$$f_1(x) = \int_{y_1}^{y_2} f(x, y) \exp\{-j \frac{4\pi f}{c} y\} dy \quad (52)$$

and  $x_1, x_2$  and  $y_1, y_2$  are the bound of target extension, respectively in the cross and down range dimensions.  $f_1(x)$  may be considered as a sort of projection of reflectivity function on cross-range direction.

By means of the following transformation:

$$x = \frac{4\pi f}{c} \frac{v_x}{R_0} t \quad t \in [-T_0/2, T_0/2] \quad (53)$$

$s_R'$  is expressed as Fourier transform of  $f_1$ :

$$s_R'(X) = \int_{x_1}^{x_2} f_1(x) \exp\{-jxX\} dx \quad (54)$$

$s_R'(X)$  is defined in the interval  $[-X_A, X_A]$ , where  $X_A$  is obtained by substitution of  $t=T_0/2$  in Eq. (53). The reconstructed profile  $\hat{f}_1(x)$  may be obtained by means of an Inverse Fourier Transform of  $s_R'(X)$ :

$$\hat{f}_1(x) = \int_{-X_A}^{X_A} s_R'(X) \exp[jxX] dx \quad (55)$$

The data  $b_k'$  has been obtained by means of a uniform sampling in time. Furthermore the relationship between time and spatial frequency  $X$ , defined by Eq. (53), is linear. Consequently the  $N$  samples  $b_k'$  are represented on a uniform grid of the interval  $[-X_A, X_A]$ . The samples  $\hat{f}_1$  are then reconstructed by means of an FFT of samples  $b_k'$ .

$$b_k' \xrightarrow{\text{FFT}} \hat{z}_k \quad (56)$$

The distance between two neighbouring pixels on the axis  $x$  is given by the estimate  $\hat{z}_k$  of cross-range resolution:

$$\hat{z}_k = \frac{\pi}{k} = \frac{1}{2} \frac{\lambda R_0}{v_t T_0} \quad (57)$$

where  $\hat{R}_0$  and  $\hat{v}_t$  are the range and tangential velocity estimates. In practise the IFFT is preceded by a zero padding of the samples  $b_k'$  in order to have four pixels for every resolution cell in the reconstructed profile.

In figs. 18, 19 the modulus of the reconstructed profile, before and after motion compensation, have been shown. It is evident that motion compensation induces a compression of the reconstructed spectrum. The reconstructed profile is affected by two peaks which are separated by about 7 m. It is not a simple task to associate these peaks to some parts of the aircraft. It can be noticed however that the separation between the two peaks corresponds approximately to the aircraft cross-range projection length.

Consider now the estimated resolution. It is determined by the occurrence of zeroes in the sinc function. This corresponds approximately to the -4 dB width of mainlobe of this function. It can be indeed verified that -4 dB mainlobe width of both the peaks of fig. 21 is approximately equal to the estimate  $\hat{z}_k=5.1$  of the cross-range resolution. This value has been obtained substituting in Eq. (57) the estimate  $\hat{R}_0=10.7$  Km, deduced from the plotted trajectory, and the estimate  $\hat{v}_t=121$  m/s, obtained by Eq. (49).

#### 4 CONCLUSIONS

In the first section the coherent spatially processing of radar returns has been described. The target electromagnetic properties may be described by the reflectivity function, defined in the reference coordinates  $xy$  fixed to the target. This function depends on the physical and geometrical characteristics of target. Furthermore this function takes into account system parameters like wavelength, polarization and orientation of radar with respect to target. It has been shown that the received signal, suitably processed and represented on the Fourier domain  $X,Y$ , may be interpreted as the Fourier Transform of the reflectivity function  $f(x,y)$ . It has been also noted that motion compensation represents a crucial step in ISAR processing. The depth of field of the reconstructed image depends on the particular couple  $(X,Y)$  employed to represent the signal  $s_k(X,Y)$ . In particular the polar format is adequate to image all ISAR targets. It has been then considered that resolution depends, in general, on signal bandwidth and on the processing angle.

In the second section the results of a radar imaging experiment have been discussed. This experiment was made by using a conventional tracking radar to reconstruct the cross-range profile of an aircraft. It has not been possible, however, to establish a correspondence between the real and the reconstructed profile. One reason of this fact could be that the available cross-range resolution, approximately equal to 6 m, is too poor to resolve some distinct reflectors. Furthermore, as range resolution has not been achieved, reflectors aligned in range result practically overlapped (see Eq. 52) in the reconstructed profile. Notwithstanding the above-mentioned limits, a meaningful cross-range compression of signal spectrum has been obtained by motion compensation. Finally a reliable estimate of radial and tangential velocities have been obtained by motion compensation.

#### REFERENCES

- /1/ A. Cantoni, G. Corsini: "The Spatially Coherent Processing of Radar Returns", RT 84SEL/3, Istituto di Elettronica e Telecomunicazioni, Università di Pisa, September 1984.
- /2/ D.L. Mensa: "High resolution radar imaging", Artech House: Inc. 1981.
- /3/ D.C. Munson, J.D.O'Brien, W.K. Jenkins: "A tomographic formulation of spotlight-mode synthetic aperture radar", Proc. IEEE, vol. 21, 8, pp. 917-923, August 1983.
- /4/ C. Elachi, T. Eicknell, M.L. Jordan, C. Wu: "Spaceborne synthetic aperture imaging radar: applications, techniques and technology", Proc. IEEE vol. 70, n. 10, pp. 1174-1209, October 1982.
- /5/ W.M. Brown: "Walker model for radar sensing of rigid target fields", Trans. of IEEE AES, vol. AES-16, 1, pp. 104-107, January 1980.
- /6/ F. Prodi: "Analysis of the error induced on impulse response by the approximation of range delay", Promemoria SELENIA FR/PROG/AS - Pisa 85/02 - February 1985 (in Italian).
- /7/ M.K. Herland: "Application of inverse synthetic aperture radar on an aircraft", Proc. International Radar Conference, pp. 618-623, Paris, 1984.
- /8/ F. Prodi: "An algorithm for motion compensation in ISAR systems", RT 87SEL/1, Istituto di Elettronica e Telecomunicazioni, Università di Pisa, April 1987 (in Italian).
- /9/ F. Prodi: "Depth of field in ISAR systems", RT 88SEL/1, Istituto di Elettronica e Telecomunicazioni, Università di Pisa, January 1988 (in Italian).
- /10/ F. Prodi: "Depth of field achievable by rectangular format of data: case of not transversal motion", RT 88SEL/2, Istituto di Elettronica e Telecomunicazioni, Università di Pisa, January 1988 (in Italian).

- /11/ G. Corsini, L. Quiriconi: "Analysis of depth of field for the spatially coherent processing of radar returns", RT 878EL/3, Istituto di Elettronica e Telecomunicazioni, Università di Pisa, July 1987 (in Italian).
- /12/ F. Prodi: "Depth of field achievable by polar format of data: case of not transversal motion" October 1988 (in Italian).
- /13/ G. Corsini, E. Dalle Mese, A. Vaccarelli: "Reconstruction of the reflectivity function in ISAR systems", RT 888EL/4, Istituto di Elettronica e Telecomunicazioni, Università di Pisa, July 88 (in Italian).
- /14/ F. Prodi: "Conception of an experiment of imaging based on the ISAR technique", RT 878EL/4/, Istituto di Elettronica e Telecomunicazioni, Università di Pisa, July 1987 (in Italian).
- /15/ F. Prodi: "Results of an experiment of radar imaging based on the ISAR technique", Rapporto Tecnico SELENIA 87123, July 1988 (in Italian).

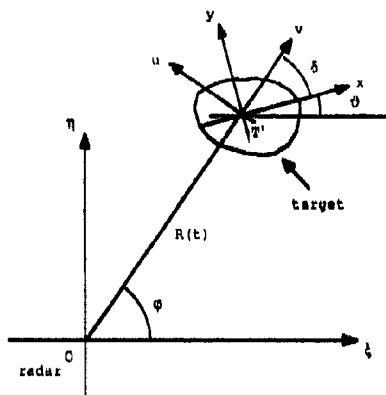


Fig. 1: Geometry of system

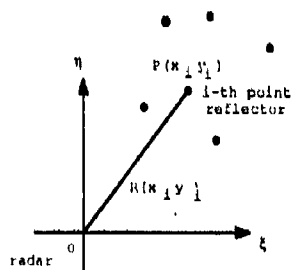


Fig. 2: Point reflectors of a target

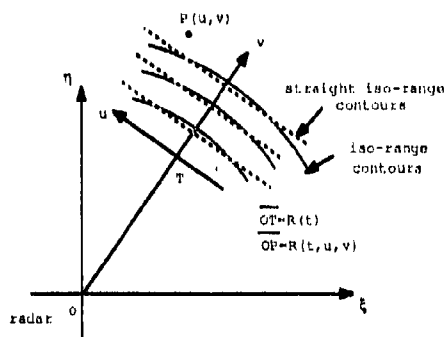


Fig. 3: Straight iso-range approximation

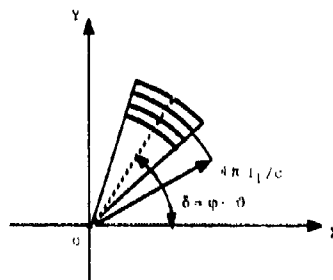


Fig. 4: Arc window (one frequency)

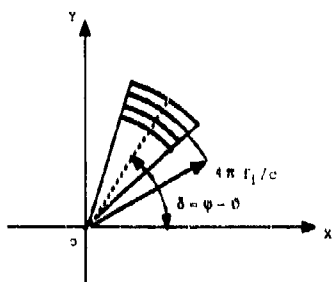


Fig. 5: Arc window (many frequencies)

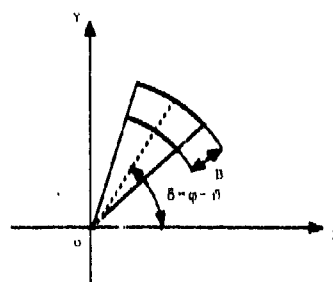


Fig. 6: Annular window

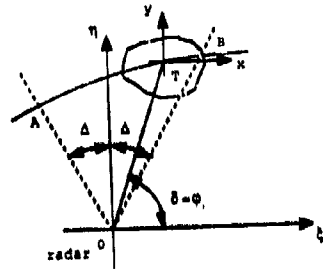


Fig. 7: System geometry (translatory motion)

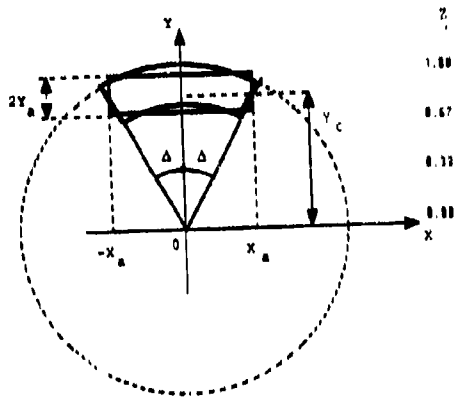


Fig. 8: Rectangular window

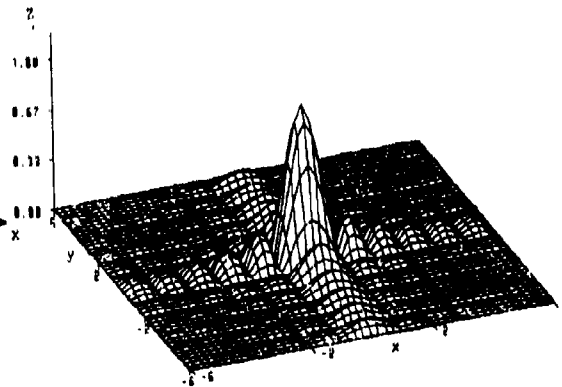


Fig. 9: Impulse response (rectangular window)

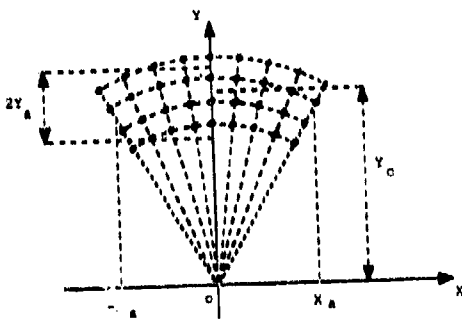


Fig. 10: Polar grid

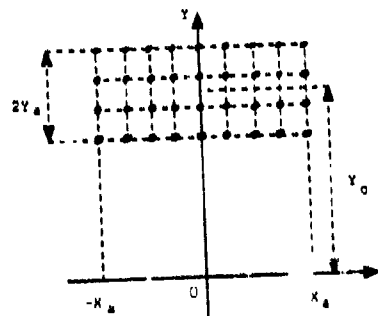


Fig. 11: Rectangular grid

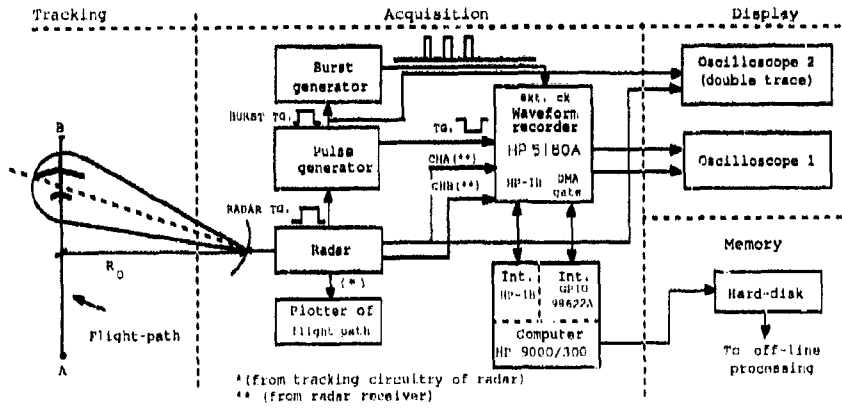


Fig. 12: Experimental set-up

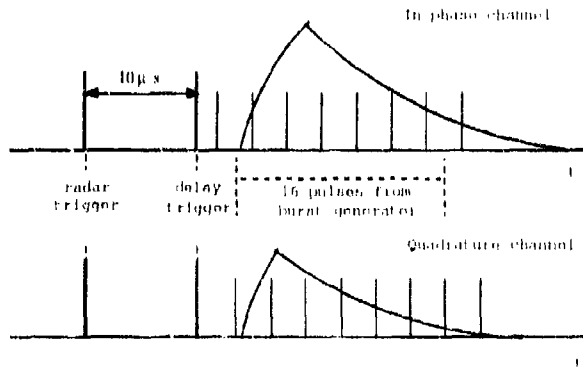


Fig. 13: Pulse acquisition

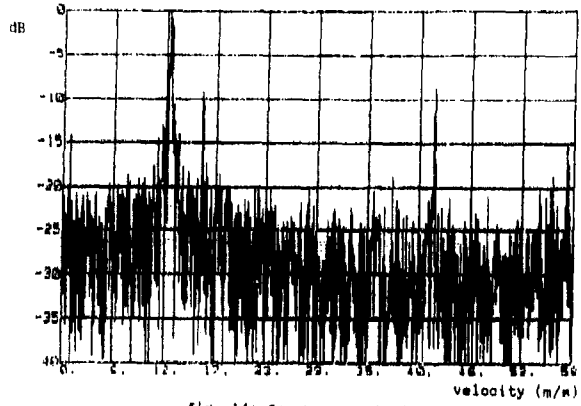


Fig. 14: Spectrum analysis (record 1)

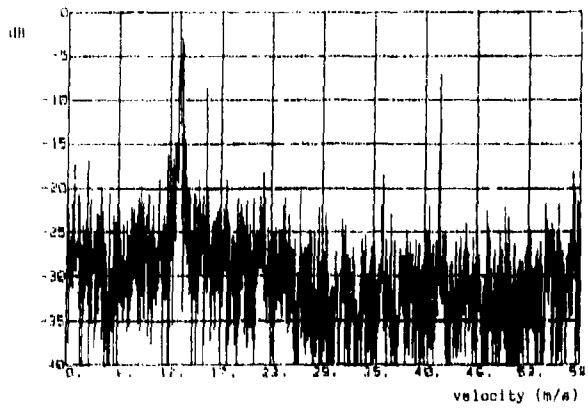


Fig. 15: Spectrum analysis (record 2)

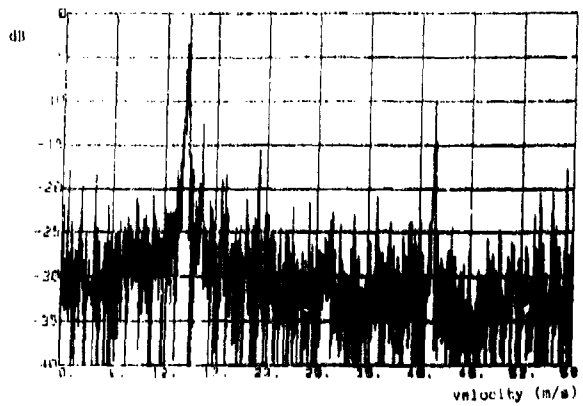


Fig. 16: spectrum analysis (record 3)

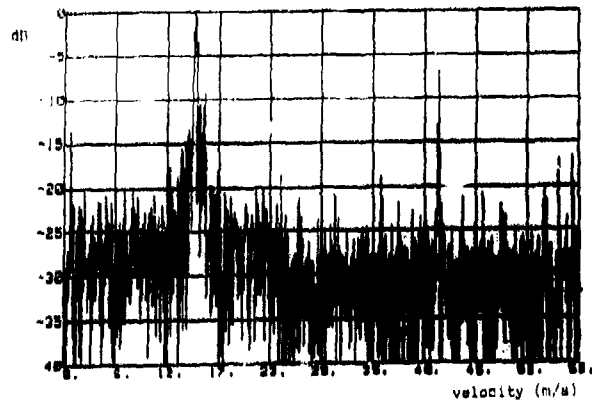


fig. 17: Spectrum analysis (record 4)

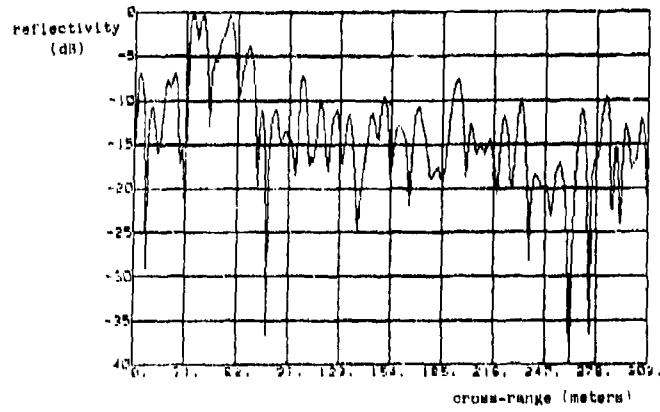


fig. 18: Reconstructed profile before motion compensation

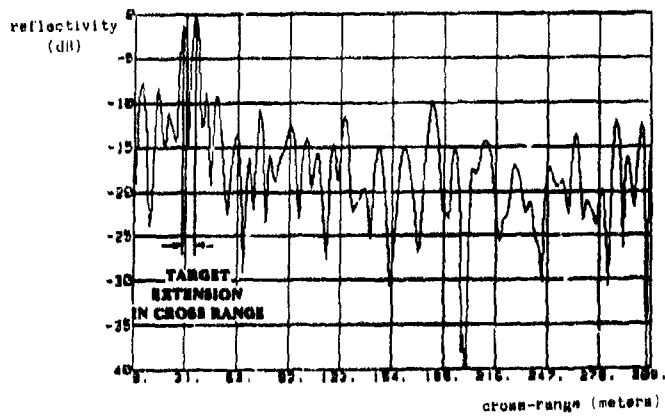


fig. 19: Reconstructed profile after motion compensation



AD-POOS 852

**(UN)AIRBORNE DOPPLER RADAR FLIGHT EXPERIMENTS FOR THE DETECTION OF MICROBURSTS**

Hans-J. C. Blume, C. D. Lytle, W. R. Jones, E. M. Bracalente  
 NASA Langley Research Center  
 Hampton, Virginia 23665-8225

and

C. I. Brill  
 Research Triangle Institute  
 Raleigh, North Carolina 27709-2194

**(UN)ABSTRACT**

(UN)In the interest of aviation safety, NASA and the Federal Aviation Administration (FAA) are jointly conducting research to determine the applicability of airborne, coherent Doppler radar techniques to detect early microburst in wind shear conditions during aircraft takeoff and landing. If early detection of these severe wind shear conditions can be demonstrated, avoidance maneuvers can be exercised and significantly reduce the probability of aircraft disaster. Researchers have developed a computer model of the radar which predicts its response when viewing a simulated microburst against the simulated clutter background of an airport, the so-called radar-microburst-ground clutter model.

(UN)Studies employing this model revealed that Doppler radar can accurately detect microburst ahead of the aircraft in time for pilot evasive response, but flight experiments will be required for complete performance evaluation of the system.

(UN)An experimental X-band (9.35 GHz) radar is being developed for future flight experiments to verify the simulation modeling results. This instrument will measure the radial (horizontal) component of wind velocity by Doppler return from atmospheric moisture and raindrops. It will utilize special signal processing techniques to control the radar gain on a bin-to-bin (or pulse-to-pulse) basis to enhance the microburst detection characteristic. Other circuitry will correct the radar response by removing the aircraft forward motion. The processed output signal is a measure of wind velocity along the radar pointing vector.

(UN)A description of the experimental radar, recording equipment, and its installation on the NASA 515 (Boeing 737) aircraft is presented. The flight experiments to be conducted are also described. They are subdivided into three phases. The first phase is directed toward the measurement of ground clutter data by flying landing approaches into typical airports in clear weather. The second phase addresses the detection of wind shear conditions by excluding ground clutter returns flying toward convective storms at altitudes above 700 meters excluding ground clutter returns. The third phase will involve approaches to airports, during severe convective storm activity, to evaluate the ability of the radar concept to detect rain reflectivity and provide wind shear data and warning criteria in the presence of ground clutter.

**(UN)I. Introduction**

(UN)Low-altitude microburst wind shear is recognized as a major hazard during takeoff and landing of aircraft. Microbursts are relatively small, intense downdrafts which spread out in all directions upon striking the ground. When such wind shear is encountered at low altitudes during landing or takeoff, the pilot has little time to react correctly to maintain safe flight (Fig. 1). In the United States during the period 1984 to 1985, there were 26 major civil transport aircraft accidents for which wind shear was a direct cause or a contributing factor. Four incidents caused 826 fatalities and over 200 injuries. As part of its integrated wind shear program, the FAA, jointly with NASA, is sponsoring a research effort to develop airborne sensor technology for detection of low-altitude wind shear during aircraft takeoff and landing. A primary requirement for an airborne forward-looking sensor or system of sensors is to be capable of detecting both heavy ("wet") and light ("dry") precipitation microbursts. One sensor being considered for this application is a microwave Doppler radar operating at X-band or at higher frequencies. Since absolutely clear air produces no radar return at microwave frequencies, except very slight scattering from gradients in the index of refraction on the scale of the radar wavelength, the emphasis in the present research is on those microbursts containing at least some liquid water.

(UN)Previous experiments<sup>1</sup> and studies have demonstrated, in a limited way, the capability of airborne Doppler radars to detect the presence of wind shear. However, for aircraft landing and takeoff applications, the problems of severe ground clutter, rain attenuation, and low reflectivity levels must be solved. To consider these problems, a Microburst/Clutter/Radar simulation program has been developed to aid in the evaluation and development of Doppler radar concepts. The simulation program incorporates windfield and reflectivity data bases derived from a high resolution numerical wind shear model<sup>2</sup>, clutter maps derived from airborne Synthetic Aperture Radar (SAR) backscatter data, and various airborne Doppler radar configurations and signal processing concepts. The program simulates the operation of a Doppler radar located in an aircraft approaching a runway, receiving signal returns from a wind shear microburst and an airport clutter environment. The results of the Microburst/Clutter/Radar simulation program are presented later in this paper. Preliminary study results have demonstrated the feasibility of using airborne Doppler radars to detect wind shear, but further detailed studies will be required, including future flight experiments, to completely characterize their capabilities.

**(UN)II. Requirements for Wind Shear Detection**

(UN)A preliminary set of performance requirements<sup>3</sup> have been established for design of forward-looking wind shear sensors. The sensors' primary requirement is to detect severe microburst wind shear during final approach to landing (Fig. 1) or during takeoff and to provide as a minimum 15 to 40 seconds (approximately 1 to 3 km) warning to the pilot. Advisory information on wind shear conditions 50 to 100 seconds (4 to 8 km) in front of the aircraft is also desired. The sensor or sensor system must be able to detect wind shear caused by both heavy and light precipitation microbursts. The sensor must measure the average horizontal wind speeds every 150 to 300 meters out to a range of 6 to 8 km along the flight path and a small sector (approx. 20°) on either side of the aircraft (A/C) with approximately 1 meter per second (m/s) accuracy. These primary requirements have been established as minimum guidelines for developing sensor design requirements and evaluating potential concepts. The requirements to provide other information and capabilities, such as vertical wind speeds, rain reflectivity, wind turbulence, microburst signature recognition, and various display capabilities are being developed.

## (UN)III. Simulation With the Radar-Microburst-Ground Clutter Model

(UN)Airborne weather radars operate in an allocated frequency band around 9.3 GHz and utilize solid state transmitters of about 100 watts. They are presently in use to display rain reflectivity and wind turbulence advisory information to the pilot in relatively high altitudes. It is of interest to assess airborne Doppler radar concepts for wind shear detection operating in this frequency band utilizing relatively low powers. Space limitation in the nose radome of passenger aircraft limit the maximum antenna size to about 30-36 inches (.76 - .91 m) in large aircraft and about 18-20 inches in smaller aircraft. This makes it more important, from a resolution and sensitivity standpoint, to operate at the higher frequencies. It is desirable to keep transmitter power requirements low so that solid state transmitters can be considered. Other radar parameters such as Pulse Repetition Frequency (PRF), and pulse width are chosen to minimize velocity and range foldover problems and to provide acceptable range resolution. Table 1 lists the radar parameter values being considered in the simulation study which represent state-of-the-art airborne Doppler radar hardware implementation capability.

(UN)Table 1. Radar parameters used in simulation analysis

A/C range from runway	5 & 7 km
A/C ground velocity	77 m/s
A/C glide slope	3°
Frequency	9.3 GHz
Antenna Dia.	.76 m (30 in.)
Antenna edge illum	-10 dB
Rain Reflectivity	10 dBz
Pulse width	1 $\mu$ -sec.
PRF	5000 units
Ant. tilt angle	0 & 2°
Ant. azimuth angle	0 & 45°

(UN)Antenna patterns simulated include a generic parabolic antenna with side and aperture illumination taper specified by input data, and a flat plate array antenna with a pattern representative of those found in the current generation of X-band airborne weather radars.

(UN)The microburst model is a detailed, numerical, convective cloud and storm model that calculates the time history of the development of a microburst. The model uses a nonhydrostatic, compressible, and unsteady set of governing equations which are solved on a three-dimensional staggered grid. The computation can be initiated from observed data and generates realistic wind fields that compare favorably with observed data such as that obtained in the JAWS study<sup>5</sup>. For the radar simulations to date, a 4x4 km lattice of 40x40 meter grid spacing increments (two-dimensional axisymmetric version) have been generated at selected time periods. Output parameters include the radar reflectivity factor (dBz), wind velocity components, temperature, equivalent potential temperature, pressure, and moisture content (water vapor, ice, cloud droplets, rain, snow, and hail/graupel). The model developed under NASA sponsorship is described in detail in references 2 and 5.

(UN)For the radar simulation cases discussed in this paper, a typical "wet" microburst is selected and used to investigate radar performance at a particular instant of time. Figure 2 shows the reflectivity factors and velocity field of the axisymmetric "wet" microburst used in the radar simulation. The "wet" microburst data are taken at 11 minutes after initiation of the microburst calculation and resemble an axisymmetric version of the August 2, 1986, Dallas-Ft. Worth storm<sup>6</sup>.

(UN)The ground clutter model used for the present simulation cases is a high-resolution X-band SAR map of the Willow Run, Michigan, airport area provided by the Environmental Research Institute of Michigan (ERIM).

(UN)The SAR image files produced by ERIM provide calibrated Normalized Radar Cross Section (NRCS) data with a resolution of 20 m. Figure 3 shows a high resolution (3 m) SAR image of Willow Run airport, from which these data were derived, and the runway BR used in the simulation runs. In the simulations, the aircraft is positioned at a selected distance from the runway touchdown point on a 3° glide slope.

(UN)A problem with the use of existing SAR data is associated with the variation of cross section with depression angle. These data were taken at depression angles ranging from approximately 18° to 50°, whereas for the operational airborne radar simulated the depression angles of interest are approximately 1° to 20°. To partially account for this difference, ERIM supplied an empirical depression-angle correction function that corrects the NRCS to the angle seen by the airborne radar.

(UN)The simulation program is a comprehensive calculation of the expected output of an airborne coherent Doppler radar system viewing a low-level microburst along or near the approach path of the aircraft. Inputs to the program include the radar system parameters and large data files that contain the characteristics of the ground clutter and the microburst. For more details see reference 7. The ground clutter data file consists of high-resolution (20 m) calibrated SAR data of selected airport areas. The microburst data files provide reflectivity factors, x, y, and z wind velocity components, and other meteorological parameters with a resolution of 40 meters. This data base is generated by a numerical, convective cloud model<sup>2</sup> driven by experimentally-determined initial conditions and represents selected time periods of the microburst development.

(UN)For each range bin, the simulation calculates the received signal amplitude level by integrating the product of the antenna gain pattern and scattering source amplitude and phase over a spherical-shell volume segment defined by the pulse width, radar range, and ground plane intersection. The amplitude of the return from each incremental scatterer in the volume segment is proportional to either the square root of the normalized cross-section of the ground clutter (from the clutter map) or the square root of the reflectivity factor of the water droplets in the microburst (from the microburst data base).

(UN)Path attenuation for each incremental scatterer is determined by integrating the path losses over the transmission path. Empirical formulas<sup>8</sup> are used to determine the incremental path losses from the liquid water content of the microburst. Aircraft ground velocity is assumed to be known accurately so that derived Doppler frequencies can be referenced to a value of zero corresponding to that velocity.

(UN)To examine the expected radar performance in specific situations, several cases have been simulated using the baseline system parameters given in table 1, the microburst model of figure 2, and the ground clutter map from the Willow Run airport area (fig. 3). Figure 4 plots the Signal-to-Noise Ratio (SNR) and Signal-to-Clutter Ratio (SCR) vs. radar range for a "wet" microburst that would be seen by the radar at a distance of 7 km from the runway touchdown point with the antenna tilted up 2° from the projected aircraft path. The microburst axis is located on the projected path 2 km from the touchdown point. The calculated reflectivity factor of the water droplets along a line corresponding to the projected aircraft path is also plotted in figure 4 for comparison to the simulated radar measurements. For this case, the SNR and SCR are high over the entire region of the microburst, with a minimum value of SCR = 10 dB occurring at approximately 3 km from touchdown. This minimum value is due to high clutter power from an urban area at this location. The SNR exceeds 20 dB over the range, with approximately 18 dB difference between the near side and far side of the microburst due to path attenuation and geometrical factors.

(UN)A two-pole, high-pass Butterworth filter was used to filter the Inphase (I) and Quadrature (Q) pulses to suppress ground clutter. The 6 dB frequency response cutoff point is located at a Doppler frequency, relative to the aircraft ground velocity, corresponding to a radial component of wind velocity of 3 m/s, and the filter has two zeros at zero Doppler frequency. The effect of the clutter filter can be seen in figure 5, which is a plot of the Doppler spectrum in a range bin 4 km from the radar, calculated with and without the clutter filter. For simulated velocity measurements, a processing threshold of 4 dB is used (i.e., the pulse-pair and spectral averaged velocities are set to zero if the radar received power is less than 4 dB greater than the noise threshold.)

(UN)Figure 6 shows the calculation of the radial component of wind velocity derived from both pulse-pair and spectral averaging algorithms operating on 128 simulated I and Q pulses from the radar. This figure also plots, for comparison, the "true" wind speed, defined as the velocity component along the center line of the antenna beam. It should be noted that the true velocity, as defined, will always differ somewhat from the radar-measured velocity because the true velocity is measured along a line (the antenna center line), whereas the radar system measures a weighted (by reflectivity and antenna pattern) average of the velocity over a finite volume of the microburst.

(UN)The simulated velocity measurements are within 2 m/s of the "true" velocity for velocities greater than 5 m/s and indicate clearly the potentially hazardous wind shear associated with the microburst. To relate the wind shear hazard to the aircraft, a measure called the F-factor or hazard index has been defined by Bowles.<sup>3</sup> This index is defined by the equation:

$$F = \frac{W_x}{g} \cdot \frac{W_h}{V} \quad (1)$$

where  $\dot{W}_x$  is the rate of change of the component of wind velocity along the aircraft path,  $g$  is the acceleration of gravity,  $W_h$  is the vertical component of wind velocity and  $V$  is the aircraft velocity. Values of  $F$  greater than 0.1 to 0.15 are considered hazardous to jet transport aircraft depending on aircraft type, configuration, and range of gross weights.<sup>3</sup>

(UN)Although a forward-looking radar sensor cannot directly measure the vertical wind component, the radial velocity component is measured directly. The first term in the equation for the F-factor can be derived from radar measurements of radial velocity as follows:

$$\text{Let } W_x = V \frac{\delta W_r}{\delta R_r} \quad (2)$$

then

$$F_R = \frac{V}{g} \frac{\delta W_r}{\delta R_r} \quad (3)$$

where

$\delta W_r$  = change in radial velocity between adjacent range bins

$\delta R_r$  = distance between range bins

$F_R$  = the radial component of the hazard index

(UN)This radial term is calculated in the simulation from the velocity measurements as shown in figure 6 by averaging velocity differences over five range bins, which results in outputs as shown in figure 7. The radial term of the hazard factor reaches a maximum value of 0.1 for this microburst and both pulse-pair and spectral averaging algorithms give good measurements of the factor.

(UN)The radar simulation program can simulate an azimuth scan mode and generate simulated displays of several variables of interest. Figure 8 shows a black and white copy of a simulated (color) display of radial wind velocity for the "wet" microburst with the baseline set of radar parameters. Figure 9 is a simulated plot of the radial term of the F-factor and clearly indicates that a potential wind shear hazard lies on the aircraft path. These displays should not be interpreted as recommended displays for the aircrew, since the specific method of alerting the crew to a hazard requires extensive study, which is presently underway, and will most likely consist of a warning light or alarm which may be supplemented by displays of additional information to aid the aircrew's decision-making process.

#### (UN)IV. Experimental Doppler Radar

(UN)Detection of microbursts in weather and the presence of ground clutter begins with the transmission of radar pulses which will be reflected by raindrops and the ground surface. The radar operates in the approved weather radar band at 9.33 GHz. This frequency was selected because it represents a good compromise between precipitation penetration distance by the radar pulses and the amount of reflected signal from raindrops for good signal processing.

(UN)The radio frequency (RF) section of the wind shear/microburst radar detector is shown as a block diagram in figure 10. The reference frequency sources generate frequencies of 784.0, 186.7, 78.4, and 13.9 MHz. The frequencies 784 MHz and 13.9 MHz combine to 777.9 MHz with the up-converter. The buffer-amplifier serves also as a frequency-clamp correction device. The 777.9 MHz continuous wave is shaped into pulses with the pulse circuit. The transmitter pulse width is selectable from 1 to 10 microseconds. The pulse repetition rate can be changed from 150 to 10,000 p/second. The power multiplier (x 12) converts the frequency up to 9.33 GHz. The transmitter output power of approximately 200 W is applied to the duplexer which couples it to the antenna port.

(UN)The duplexer also provides the receiver section with the reflected signals. The 784 MHz signal from the reference sources is multiplied by twelve in the multiplier and injected into the first local oscillator with the output frequency of 9170 MHz. The local oscillator converts the received signal down to the first intermediate frequency (IF) 186.7 MHz with the first mixer. The second local oscillator (182.8 MHz) converts the first IF down to the second IF (13.89 MHz), and the third local oscillator (13.89 MHz) provides the signals for the Inphase and Quadrature mixing to obtain the I/Q outputs. These I/Q channels are the inputs to the processor and display of rain intensities.

(UN)The information on these I/Q channels is not sufficient to evaluate the weather condition above the runway during landing approach or during takeoff. The RF portion below the dotted line in figure 10 represents the wind shear detector system of the Doppler radar. The first IF of the radar receiver is split into two signals. One signal is converted down to 30 MHz with the mixer. The local oscillator (136 MHz) is obtained by using the reference frequency 76.4 MHz and converting it, after amplification with the frequency synthesizer, to 136 MHz. The frequency synthesizer also compensates the Doppler effect due to forward motion of the aircraft. The control signal is derived from the Inertial Navigation System (INS). After the synthesizer, the local oscillator signal is filtered with a band pass filter of 40 MHz band pass and, after amplification, provided to the mixer. Following the mixer, a variable attenuator provides the Automatic Gain Control (AGC). The AGC is generated in the digital bin-to-bin AGC processor. The IF passes through a filter with 7 MHz bandwidth and is amplified before it is supplied to the I/Q mixer. The 30 MHz local oscillator frequency is generated in the frequency synthesizer, filtered (bandwidth = 40 KHz), and amplified. The I/Q channel outputs are provided with programmable low-pass filters. The filters are controlled from the control computer to adjust the pass band to the pulse width. The second channel coming from power divider represents the AGC drive. After passing through the filter (7 MHz bandwidth) and being amplified in the logarithmic amplifier, the AGC is low pass filtered and sent to the digital bin-to-bin AGC processor (Fig. 11).

#### (UN)V. Experimental Signal Processing and Data Recording System

(UN)The experimental system is comprised of a sensor (previously described), a signal processing system, and a data recording system described here. The X-band radar detector (see block diagram, Fig. 10) provides analog I and Q signals from the weather target from which the radial component of horizontal wind velocity is measured. The radar also supplies a logarithmic output (LOG) representing the radar receiver's signal strength when the I and Q measurements were made. In order to distinguish the weak weather return from the strong ground clutter, such as is present during a landing approach, the radar receiver has, in addition to the instantaneous dynamic range of approximately 65 dB (1 MHz bandwidth), a second dynamic tracking range of about 65 dB. The 65 dB dynamic tracking range assures that the detector of the bin-to-bin AGC operates in the linear portion of the system. This is achieved in this system by a very unique AGC system. The fundamental principle of this AGC system is given in the diagram of figure 11. The receiver window for example is divided into 200 range bins with a pulse rate of 5000 pulses per second and a 1 microsecond pulse width. A smaller, movable data range window covers 64 of these bins at any one time span between two pulses. The I, Q, and LOG signals within each of these 64 range bins (bin resolution) are stored in the buffer storage in a matrix fashion where the transmitter pulses P<sub>1</sub> to P<sub>128</sub> designate the proper sample location for the received bin values I, Q, and LOG. The average value of the received signal strength (LOG) for each bin is then computed in the AGC processor and used to reset the AGC value independently for the specific bin over the next group of 128 transmitted pulses. Each storage buffer that implements this is configured in two groups such that one can accept data while the other is being read out to the data recording system in a ping-pong fashion of operation that permits time for recording full radar output data within the selected bin window of 64 bins. This provides the capability to store 100 percent of the data produced by the radar sensor within the 64-bin window. Two buffer-storage devices are used to obtain two ping-pong buffer outputs. The first supplies the digitized data to the data display processor and the second supplies the data to the data recorder.

(UN)The AGC value obtained from the AGC processor in this manner allows the receiver to be set to its optimum value for distinguishing the weak return in the presence of strong ground clutter, i.e., optimizing the signal-to-noise ratio in clutter condition. The digitally-computed AGC values are used to control the radar system gain by setting digitally-controlled attenuators located in the receiver chain of figure 10.

(UN)The recording system is a 14-track, high speed, high storage capacity system that is capable of storing all sensor output information along with necessary experiment and housekeeping data. The system is capable of about 1 hour of flight data recording between changes of its 14-inch diameter tape reels, at which time approximately 3.6 Gbytes of data have been recorded.

(UN)The signal processing and recording equipment are packaged in one 60-inch high, double wide, 18-inch rack unit shown in figure 14. All equipment is designed, assembled, and aircraft qualified at NASA according to requirements for the flights aboard the Boeing 737 aircraft.

#### (UN)VI. Aircraft Installation

(UN)In order to make use of an existing X-band weather radar, the antenna and pedestal are shared by the cockpit and the test station located in the aft section of the fuselage as shown in figure 12. The waveguide switch provides connection either to receiver/transmitter unit no. 1 for the weather indicator in the cockpit, or to the receiver/transmitter unit no. 2 of the research sensor system. The research sensor system comprises (besides the standard indicator and control panel) the system interface together with the flight test system. The flight test includes the test control computer, the I-Q detectors, the bin-to-bin AGC, the aircraft INS, and the system clock. The flight data recording system is shown in figure 13. The sensor data, such as I, Q, and AGC, and the aircraft inputs, such as INS attitude, aircraft speed, position, housekeeping, and data system control information, are converted from analog to digital data and formatted. The record electronics provide the necessary control and data flow to the airborne digital recording system. The functional diagram of figure 13 shows the data flow and the operations in a simplified form.

(UN)The location of the experiment components and equipment inside the Boeing 737 (NASA 515) is indicated in figure 14. The flat plate antenna is installed in the nose cone protected by a radome with low losses (smaller than .5 dB) one way. The receiver/transmitter unit no. 1 is installed in the nose cone compartment in front of the cockpit and, because of lack of space, the receiver/transmitter unit no. 2 is located in the cockpit. The weather radar control unit and indicator are located in the cockpit near the pilot. The wind shear/microburst experiment station and the digital tape recorder are placed in the aft section of the fuselage. The experiment station consists of the control computer, data processing equipment, and the wind shear data display unit.

(UN)The flight experiment setup for the final performance demonstration is shown in figure 15. As shown in figure 15, the RF waveguide switch makes the antenna available either to the pilot (weather indicator) or to the experimentalist in the aft section of the aircraft (microburst detector). The experimentalist operates the control computer and adjusts the system interface to optimum performance by selecting pulse width, pulse repetition rate, AGC level, signal-to-noise ratio, and other parameters. The data are recorded by the flight recorder and, in addition, a wind shear signal processor is provided which will drive the displays located in front of the experimentalist and the pilot. For the experiment, the display is a standard commercial weather radar indicator. If implemented as a practical system, the type of display would be subject to coordination between FAA, the pilots and the engineers.

(UN)The installation of the microburst detector system in the Boeing 737 aircraft and a complete system checkout will be completed by the end of 1990. The planned flight experiments subdivide the wind shear radar flight program into three phases.

(UN)Phase I will initially establish the basic radar operation in the installed configuration. After aircraft flight testing of the system (shakedown), Phase I is mainly dedicated to ground clutter measurements and validation of previous measurements of clutter at previously targeted airports with the SAR by ERUM. The target airports are located in Philadelphia, Ann Arbor, and Denver. A local clutter measurement of opportunity, when the weather is clear, will be at Wallops airfield on the Delmarva Peninsula. The clutter measurements are important to validate the capability to synthesize computer clutter models for many different airports and to determine the expected SCR for different ground coverage around airports such as grass, trees, buildings (suburban and industrial), and parked aircraft. Special attention will be directed toward the clutter signatures of moving clutter objects such as trains, automobiles, or taxiing aircraft. The estimated time frame for these flights will be November 1990 to September 1991.

(UN)Phase II is directed toward the detection of wind shear conditions in weather fronts at altitudes above 700 meters where ground clutter is not a factor. The objectives of Phase II are the characterization of radar parameters over the operational range for as many as possible atmospheric conditions to support the analytical data base of the aforementioned simulation model. Another objective is the evaluation of the capability of the wind shear radar to detect wind shear by measuring solely the horizontal windspeed component. These flights will be conducted in the vicinity of the Denver airport and Wallops airfield between August 1991 and March 1992.

(UN)Phase III includes a series of tests for several evaluations such as recording the radar's response during landing approaches at airports during severe convective storm activities and data analysis at the ground processor station from recorded data. One objective of Phase III is the collection of composite radar signal and clutter data to support the development of real-time processing algorithms. These flight experiments and data analysis are planned for August 1991 until July 1992 at the Denver airport and Wallops airfield. Another objective is to define the radar's ability to provide the wind shear detection and warning function in terms of the wind shear hazard factor and its presentation of the hazard index to the aircraft crew, i.e., real-time demonstration of radar capability for wind shear detection. At later stages of the program, it also includes the onboard processing and display of wind shear conditions to the experimentalist and the pilot. The performance demonstration flights will take place at Denver and Wallops and are planned for June 1992 until August 1994 and include a detailed data analysis.

(UN)The Phase III experiments are flights of opportunity because wind shear development is very dependent on weather conditions such as migration of cold fronts into masses of warm air or vice versa. These conditions appear frequently at Denver airport in spring, summer, and fall months and at limited frequency at Wallops during the summer months. Other locations of frequent wind shear and microburst activities are Dallas, Houston, and Miami.

#### (UN)VIII. Concluding Remarks

(UN)A preliminary tradeoff and assessment study was conducted to evaluate the performance of airborne Doppler radar sensors to detect hazardous microburst wind shear during aircraft landing. Using a preliminary set of performance requirements for the design of forward-looking sensors, a baseline set of radar parameters was developed for use in assessing wind shear detection performance using a radar simulation program. A description was given of the simulation program, which includes excellent models of microburst wind fields, realistic clutter maps of airports, and accurate models of Doppler radar operation and signal processing.

(UN)Simulations were conducted with a specific airport, selected instantaneous microburst conditions, and the baseline radar parameters. These simulations show that in realistic situations, forward-looking airborne radar sensors have the potential to detect wind shear and provide information to the aircrew that will permit escape or avoidance of hazardous shear situations.

(UN)For the Doppler radar sensor configuration, analyses of computer simulation studies show that wind shear can be detected accurately 10 to 60 seconds in front of an aircraft approaching a hazardous microburst positioned in the flight path of the landing aircraft. This is accomplished using a bin-to-bin AGC, clutter filtering, limited detection range (64 bins), and suitable tilt management of the antenna. The sensor is highly effective for the "wet" microburst where high signal-to-noise ratios and high signal-to-clutter ratios are obtainable due to a large reflectivity level.

(UN)The experimental radar consists of a modified Doppler weather radar. Its first IF is used to provide the signals for processing of the Inphase and Quadrature information and for the LOG amplifications and detection of the envelope of the IF amplitude. The detected signal serves as the drive for the AGC and controls the digitally-programmed attenuators for the bin-to-bin adjustment of path losses.

(UN)The signal processing and data recording is achieved with analog to digital conversion. A matrix buffer-storage device provides a smooth data flow to the recording system by using a ping-pong control. Two buffer-storage devices deliver the digitized signal in parallel to the high-speed recorder and to the wind shear signal processor. The signal processor is planned to indicate the hazard index with displays to the pilot and the experimentalist. The experimental radar is in the process of being installed in the Boeing 737 aircraft (NASA 315).

(UN)The planned flight schedule subdivides the wind shear radar flight program into three phases. Phase I includes the shakedown flight and ground clutter measurement/recording at the Philadelphia, Ann Arbor, Denver airports, and Wallops airfield during clear weather conditions. Phase II is directed toward wind shear measurements from convective storms above 700 meters without ground clutter. The flights will be conducted in the vicinity of the Denver airport and Wallops airfield. During Phase III, convective storm wind shear data in the presence of ground clutter will be collected. These data will be used to evaluate the capability of suppressing the strong clutter signal. Finally performance demonstration flights will be conducted at the Denver airport and Wallops airfield by August 1994.

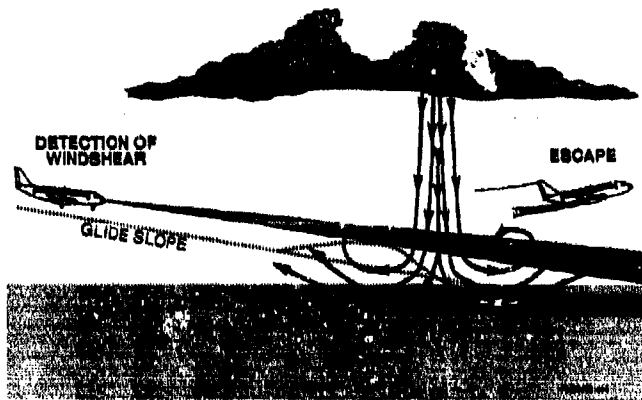
(UN)During the scheduled experiments, data analysis and news release publications will inform industry and the public of progress in the field of wind shear/microburst detection capability using Doppler radar.

## (UNIX) References

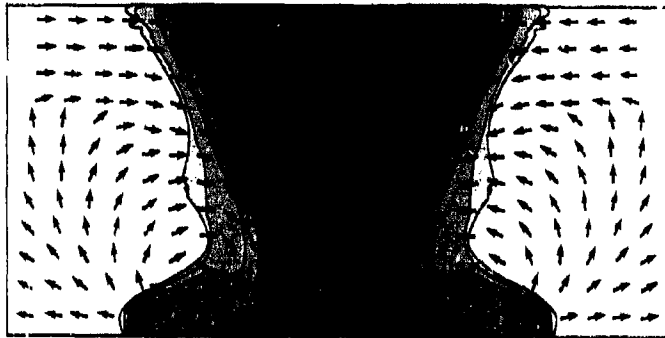
1. Staton, L. D.: Airborne Doppler Radar for Wind Shear Detection. Presented in Windshear/Turbulence Inputs to Flight Simulation & Systems Certification Workshop. NASA CP 2747. July 1987.
2. Proctor, F. H.: The Terminal Area Simulation System Vol. I: Theoretical Formulation. NASA CR 4046; DOT/FAA/PM-88/50, I. April 1987.
3. Bowles, R. L. and Targ, R.: Windshear Detection and Avoidance: Airborne Systems Perspective. Presented at 16th Congress of the ICAS, Jerusalem, Israel. August 28-September 2, 1988.
4. Doviak, R. J. and Zrnic, D. S.: Doppler Radar and Weather Observations. Academic Press, Inc. 1984.
5. Proctor, F. H.: The Terminal Area Simulation System Vol. II: Verification Cases. NASA CR 4047; DOT/FAA/PM-88/50, II. April 1987.
6. Bowles, R. L.: Windshear Modeling: DFW Case Study. Presented at Windshear Detection Forward-Looking Sensor Technology Conference. NASA CP 10004; DOT/FAA/PS-87/2. October 1987.
7. Bracalente, E. M.: Airborne Doppler Radar Detection of Low Altitude Windshear. Presented at AIAA/NASA/AFWAL Sensors and Measurement Technologies Conference. Atlanta, Georgia. September 7-9, 1988.

## Acknowledgement

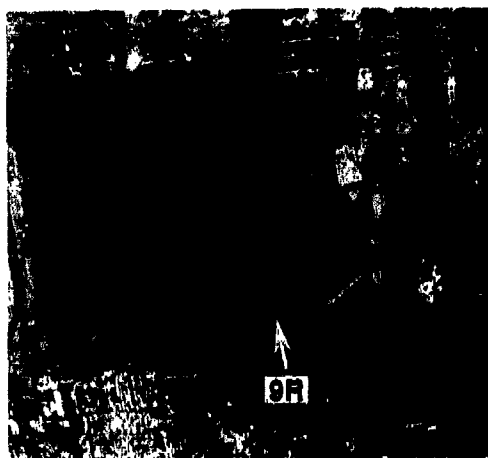
The authors wish to thank L. D. Staton, S. D. Harrah, D. L. Sullivan of the NASA Langley Research Center; J. H. Schrader of Research Triangle Institute; V. E. Dehnore, C. L. Manor, and C. C. Chan of Planning Research Corporation, and K. K. Macauley of Hewlett-Packard for their discussions, suggestions, and art contributions for this publication.



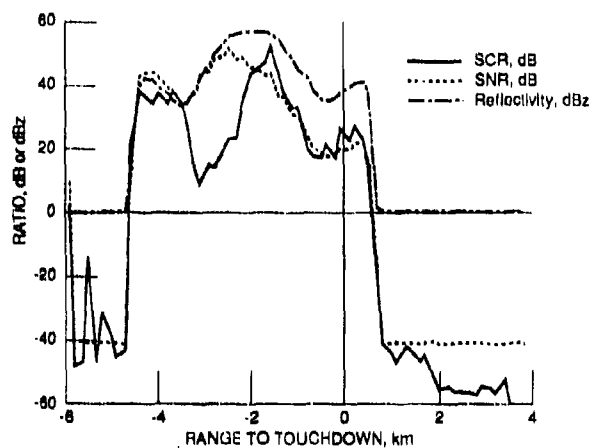
(UN) Fig. 1 Sketch illustrating the microburst wind shear hazard for an approaching aircraft, being probed by a radar beam. Potential impact path is shown if escape or avoidance maneuver is not activated.



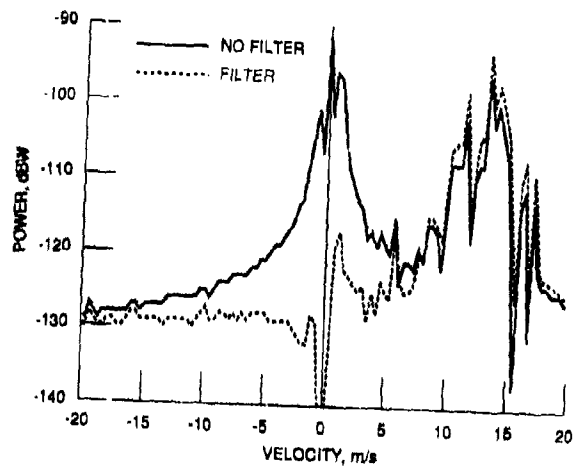
(UN) Fig. 2 Reflectivity contours and velocity field for the asymmetric "wet" microburst model used for initial radar performance simulations studies.



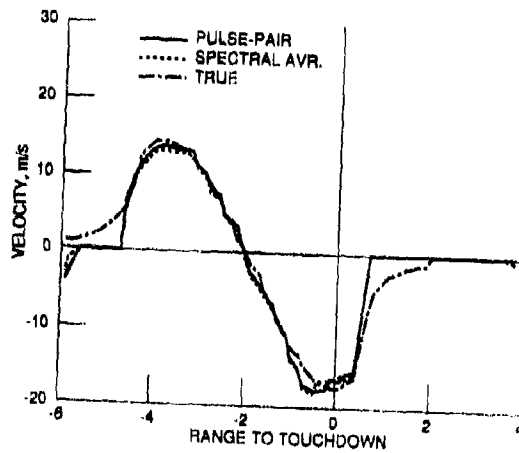
(UN) Fig. 3 High resolution SAR image of the Willow Run, MI, airport area. NRCS map, produced from this image data base, is used to calculate the ground clutter return in the radar simulation program.



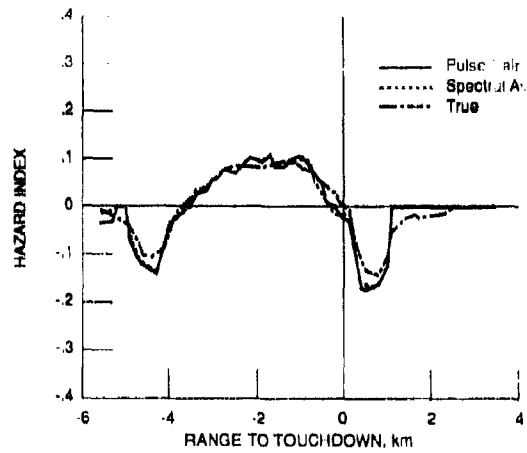
(UN) Fig. 4 Plot of calculated SNR, SCR, and reflectivity factor vs range to touchdown for the "wet" microburst. Aircraft located -7 km from touchdown on 3° glide slope, radar antenna (Ht = 2°, microburst centered on projected flight path - 2 km from the touchdown point, freq. = 9.3 GHz.



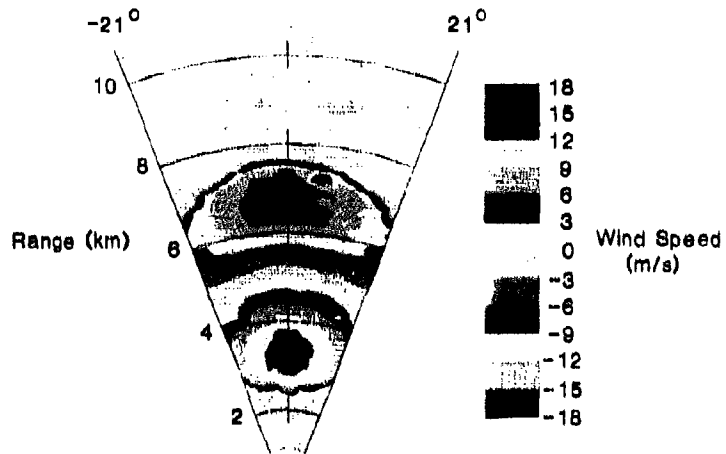
(UN) Fig. 5 Plot of Doppler spectrum from radar range bin 4 km from touchdown, prior to wind velocity estimation, showing effect of 2-pole filter used to suppress ground clutter.



(UN) Fig. 6 Radar wind velocity measurement vs. range to touchdown; same conditions as in figure 4. In this plot, positive velocities represent headwinds.

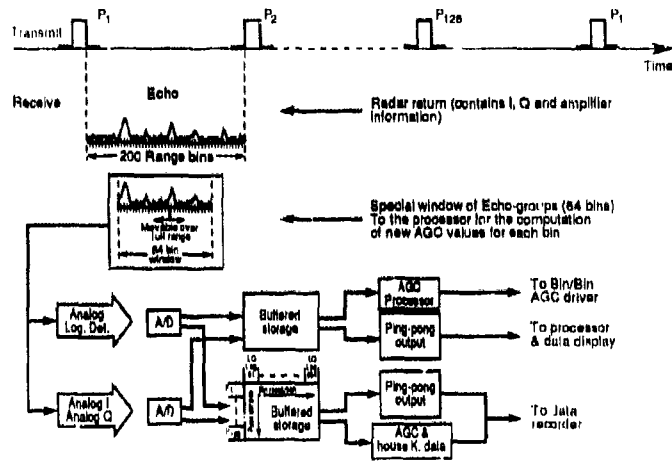


(UN) Fig. 7 Hazard Index vs. range to touchdown derived from the velocities shown in figure 6. Index is calculated from average velocity differences over 5 range cells (780 m).

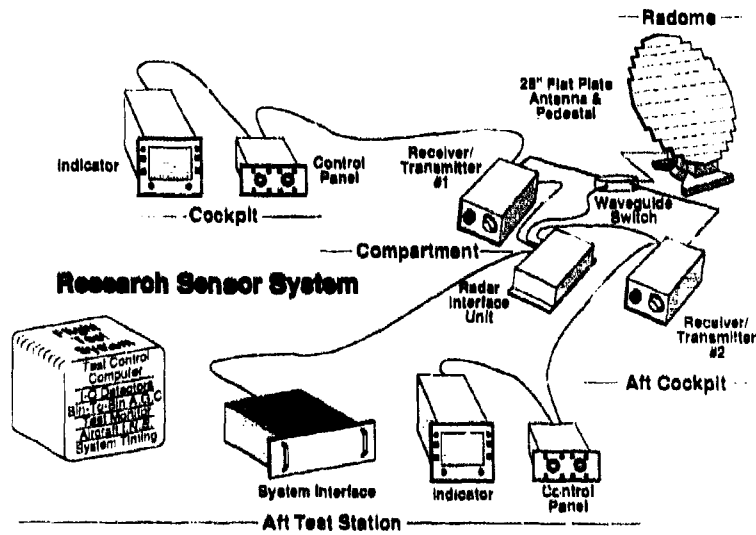


(UN) Fig. 8 Range-azimuth display of wind velocity contours for the "wet" microburst, baseline radar parameters, and conditions listed in Fig. 4. The large head to tail velocity and wind direction change is clearly shown.

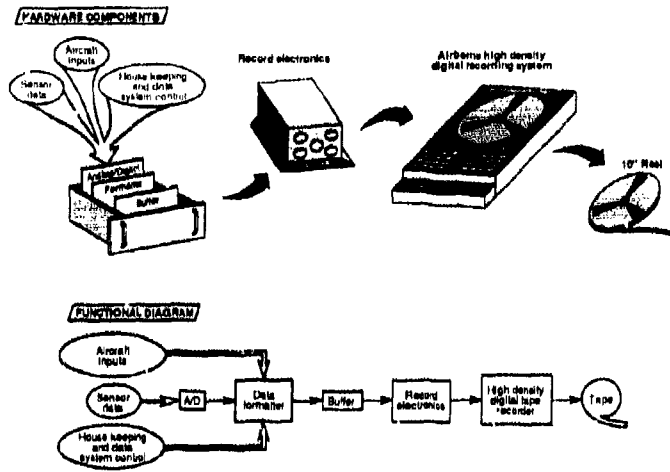




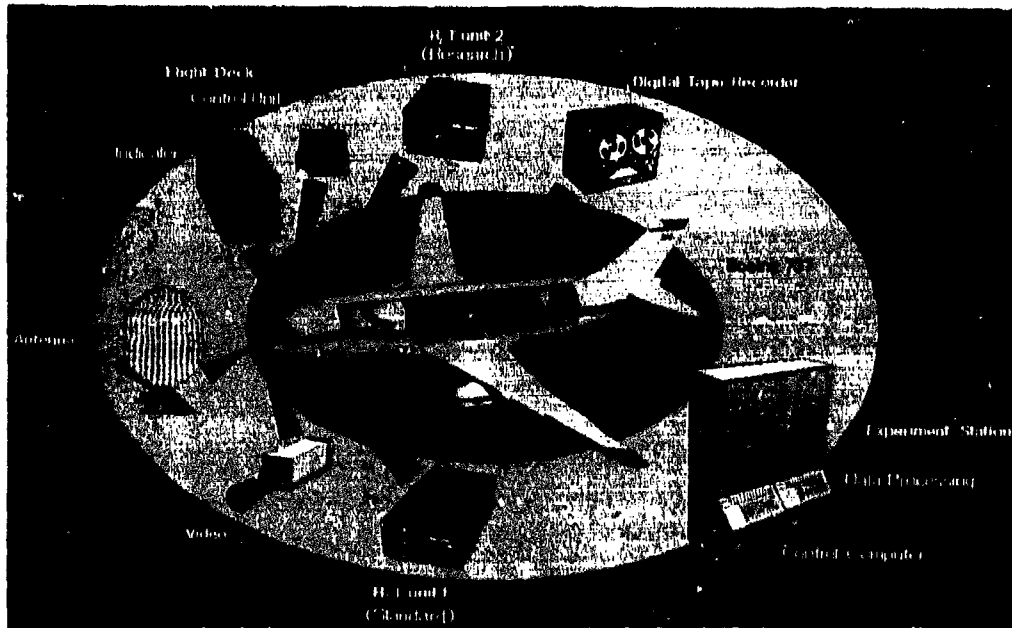
(UN) Figure 11.-Flow diagram of I and Q channels and detector log amplifier signal to storage and processing systems



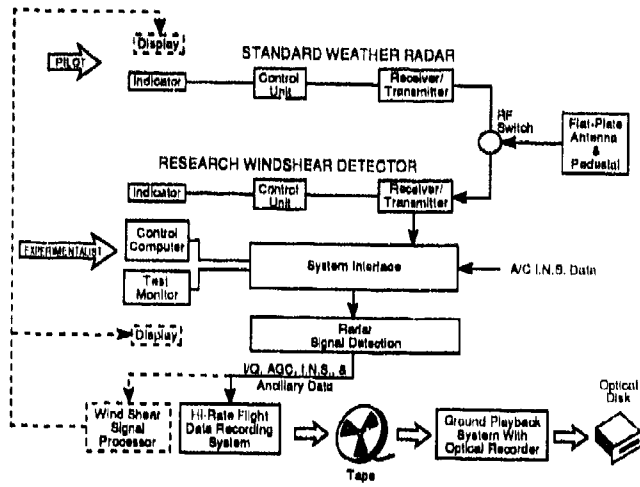
(UN) Figure 12.-Flight Sensor System



(UN) Figure 13.-Flight Data Recording System



(UN) Figure 14.-Location of experiment components in Boeing 737



(UN) Figure 15.-Flight experiment setup for the performance demonstration



## CONCEPT AND RESULTS OF THE DLR REALTIME SAR PROCESSOR

Alberto Morelra

German Aerospace Research Establishment (DLR)  
 Institute for Radio Frequency Technology  
 D-8031 Oberpfaffenhofen, Federal Republic of Germany

### ABSTRACT

A Realtime Azimuth Processor was developed for the airborne E-SAR system (Experimental Synthetic Aperture Radar) of DLR. The processor works with an unfocused compression method. This method greatly simplifies the data processing and is easily implemented by a moving average approach. A SAR image processed by a traditional unfocused processing method has a lower contrast, higher sidelobes and worse resolution than in the focused case. A new algorithm was developed, so that a triangular amplitude weighting could be implemented into the unfocused processing method without additional complications. Images processed in realtime are presented. They show good contrast and strong suppression of the sidelobes. The processor hardware can be implemented with reduced costs in small aircrafts and is suitable for several applications such as the detection of oil pollution over the sea.

### 1. INTRODUCTION

The use of synthetic aperture radar for remote sensing has increased largely in recent years due to the all-weather, wide swath and high resolution capabilities. Image formation from SAR data is well known and involves coherent processing between the received signal and the matched impulse response function, which is also called the reference function (Fitch, 1988; Beasley, 1982).

The E-SAR system of DLR (Horn, 1988) is operated experimentally in L-band without pulse compression (100 ns pulse duration) and in C-band with a FM pulse. In the latter case, range compression is performed by a SAW device. An azimuth processor was developed for the E-SAR system to produce real-time images. It offers some important advantages:

- the complete SAR sensor hardware can be tested in realtime,
- areas illuminated by the radar are monitored in realtime, facilitating for example the detection of oil spills at sea,
- the processed image contains only a reduced amount of data due to multilooks or to a smaller processed bandwidth. Hence the storage can be reduced in capacity and realised by a conventional video recorder,
- the realtime images can be used as a reference for the high resolution off line data processing.

### 2. CONCEPT OF THE REALTIME PROCESSOR

For small apertures ( $\varphi < 20^\circ$  in figure 1), the phase history of a point target is a quadratic function of the transmitted pulse number  $N$  and is given by (no squint angle is considered):

$$(2.1) \quad \psi(N) \approx \frac{2 \cdot \pi \cdot V^2 \cdot (PRI \cdot N)^2}{\lambda \cdot R_0}$$

where PRI is the pulse repetition interval and  $R_0$  is the minimum range between aircraft and point target. Differentiating the phase history yields, for a sufficiently small PRI, the doppler frequency as a function of pulse number, as follows:

$$(2.2) \quad f(N) \approx \frac{2 \cdot V^2 \cdot PRI \cdot N}{\lambda \cdot R_0} \approx \frac{2 \cdot V \cdot \varphi}{\lambda}$$

The assumed doppler bandwidth for processing can then be expressed as a function of the aperture  $\varphi$ :

AD-9005 853

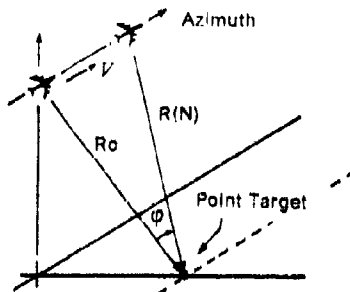


Figure 1. Considered imaging geometry.

where  $\phi \leq \frac{\alpha}{2}$ ,  $\alpha = \frac{\lambda}{D}$ ,  
 $2 \cdot \phi$  = processed aperture,  
 $\alpha$  = azimuth beamwidth of the antenna,  
 $D$  = azimuth length of the antenna,  
 $\lambda$  = wavelength and  $V$  = aircraft speed.

$$(2.3) \quad B \cong \frac{4 \cdot V \cdot |\varphi_{\max}|}{\lambda}, \quad |\varphi_{\max}| \leq \frac{\text{azimuth 3 dB beamwidth of the antenna}}{2}$$

The developed azimuth processor works with an unfocused processing method. In this case it processes only a small bandwidth of the backscattered azimuth signal. The azimuth signal is correlated with a simple rectangular function which does not correct its quadratic phase history. The correlation at doppler frequency zero is performed with an acceptable maximum phase error of  $90^\circ$ . This means a maximum two way range variation,  $2 \cdot [R(\pm N) - R_0]$ , of  $\lambda/4$ .

The unfocused processing method is based on the fact that the accepted phase error of  $90^\circ$  leads to sufficient image quality. For the determination of  $|\varphi_{\max}|$ , the one way range variation is limited by  $\lambda/8$ .

$$(2.4) \quad |\varphi_{\max}|_{\text{unfoc}} \cong \frac{1}{2} \cdot \sqrt{\frac{\lambda}{R_0}}$$

The azimuth spatial resolution,  $\rho$ , is indirectly proportional to the processed doppler bandwidth and is obtained by substituting (2.4) in (2.3).

$$(2.5) \quad \rho = \frac{\sqrt{\lambda \cdot R_0}}{2}$$

The azimuth resolution increases with the square root of range and is not constant as in the case of the focused processing method. Since the reference function is rectangular, the correlation process can be carried out very easily by the moving average approach. For a complex representation, the correlated response is given by:

$$(2.6) \quad g(N) = s(N) * [\text{rect}(\frac{N}{L}) + j \cdot \text{rect}(\frac{N}{L})]$$

where

$$\text{rect}(\frac{N}{L}) = 1 \quad \text{für} \quad \frac{L}{2} < N \leq \frac{L}{2} + 1, \\ = 0 \quad \text{elsewhere}$$

where  $*$  means the time domain convolution,  $L$  is the length of the rectangular reference function and  $s(N)$  is the received azimuth signal. The image detection is performed by calculating the absolute value of  $g(N)$ .

$$(2.7) \quad |g(N)| = \sqrt{2} \cdot \left[ \{s_r(N) * \text{rect}(\frac{N}{L})\}^2 + \{s_i(N) * \text{rect}(\frac{N}{L})\}^2 \right]^{1/2}$$

where  $s_r(N)$  and  $s_i(N)$  are the real and imaginary part of  $s(N)$ . The azimuth processing consists of averaging the real and imaginary components of the received signal. This can be easily performed by a moving average approach where the most recent value is added and the oldest value is subtracted for each correlated point. The computational requirements for this operation are greatly reduced and the processor realisation is very much simplified in comparison with the focused case.

## 2.1 THE POINT TARGET RESPONSE

Figure 2 left shows a simulated point target response (L-band,  $R_0 = 1500$  m) that was obtained with the unfocused correlation method. The response has high sidelobes with a peak sidelobe ratio (PSLR) of -9 dB and an integrated sidelobe ratio (ISLR) of -7 dB. An image processed with the unfocused method has low contrast and gives a blurred impression.

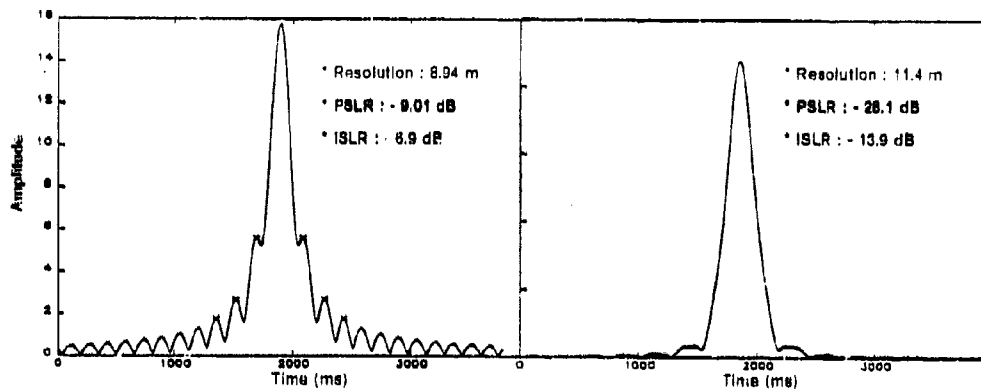


Figure 2. Simulated point target response with the unfocused method (left : without weighting ; right : with weighting).

A new algorithm was developed, so that a triangular amplitude weighting could be inserted in the unfocused processing method without additional complications. The algorithm consists basically of correlating the azimuth signal twice with a single moving average approach. This corresponds to a single correlation with a triangular function, which is the weighting function. Several simulations were done to optimize the processing parameters. The critical parameter to optimize is the duration of the reference function. A shorter reference function reduces the phase error of the processing, but the resolution becomes worse due to the lower time bandwidth product. An extremely long reference function cause a degradation of the image quality due to the greater phase error. The length of the reference function was chosen to achieve a good compromise between PSLR, ISLR, resolution and processing loss. Good results were obtained due to the fact that the triangular reference function gives little weight to the correlation with the largest phase errors. The optimized point target response is shown in figure 2 right. The processing loss due to weighting and phase errors totals about 2.5 dB. The weighted response has a PSLR of -26 dB and an ISLR of -13.9 dB and is superior to the non-weighted response.

The realtime azimuth processor is composed of units performing the following functions: corner turning (transposing of the received data), correlation with the reference function (moving average approach), resampling, weighting, image detection, output interface and test pattern generation. There is no pre-summing of the data before azimuth processing due to the fact that the moving average itself is a filter with a  $\sin(x)/x$  frequency response. The realtime azimuth processor was developed providing two modes of operation : 1. traditional unfocused processing and 2. unfocused processing with triangular weighting (Moreira, 1989). Comparisons can be made in realtime to show the improved image quality of the new approach. The power consumption totals only 18 W due to the use of modern CMOS circuits.

### 3. RESULTS

Some realtime images were selected for analysis and postprocessing. The following postprocessing techniques were used for image correction and enhancement :

- **Geometric Correction.** Linear interpolation of the image in range direction was performed in order to convert the pixel spacing from slant range to ground range. Linear interpolation was also used in azimuth direction to adapt the pixel spacing in azimuth to the pixel spacing in range.
- **Radiometric Correction.** This procedure corrects for the decrease of the backscattered signal power in range direction, which is basically dependent on target type and range, as well as on incidence angle and antenna pattern. The correction curve is generated by integrating the received radar signal over many seconds and then filtering spatially. The correction function is equal to the inverse filtered intensity curve. Within the corrected image the signal intensity is constant and range independent.
- **Spatial Filtering for Speckle Reduction.** Speckle appears in SAR images due to coherent processing of radar echoes of distributed target scatterers. It reduces the detectability of objects in the image (for example small ships on the sea) and also the capability to separate distributed targets (for example oil on sea surface). Speckle has the character of multiplicative noise, where the mean value is equal to the standard deviation in the intensity image. A simple mean filter reduces the speckle noise by one over the number of uncorrelated averaged pixels. The disadvantage of such a filter is that it tends to blur edges and decreases target intensities, when the size of the filter window becomes bigger than the

size of the target. The final image seems to be smeared and has lower contrast. The local statistic algorithm (Lee, 1988) was chosen for speckle reduction because it gives a good compromise between computational expense and effectiveness in speckle reduction without removing subtle details. It controls the local statistic averaging process according to the local mean and local variance values. The result is an image with sharp edges and conserved subtle details.

Figure 3 shows a 5 m<sup>3</sup> oil spill (dark region) that was detected during the Archimedes IIa campaign at the Dutch North Sea Coast (Moreira, Horn 1988). Radar is able to detect oil pollution on the sea surface by virtue of the attenuation of capillary waves by the oil spill. The ship, which discharged the oil intentionally for this experiment, can be seen at the top of this figure as a large bright spot due to its strong radar reflectivity. There is up to 9 dB dynamic range between sea and oil surface intensity in the final image. Although the transmitted peak power was only 50 W with 100 ns pulse width in L-Band it was possible to achieve a good image contrast. This contrast arises from the partially specular behaviour of the backscattered signal from the sea which becomes a gain in the correlation process. The signal to noise ratio is 0 dB in mid range for this image.

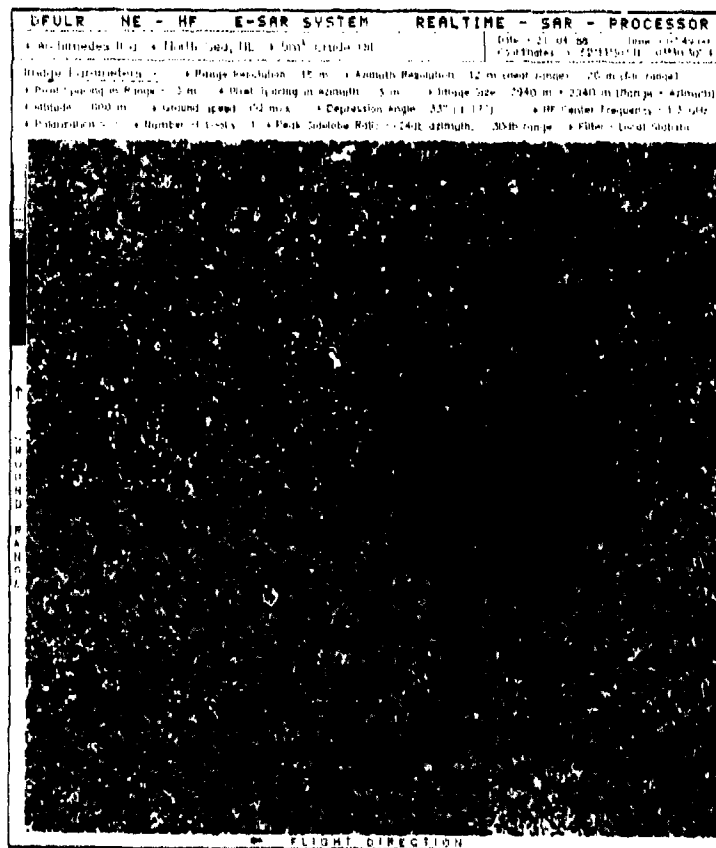


Figure 3. Image processed in realtime: oil pollution on the sea.

Figure 4 shows the airport at Oberpfaffenhofen near Munich (C-band). The original image of the realtime processor without filtering is shown in the lower half. The other part of this image was filtered with the local statistics algorithm. With this adaptive filtering, the speckle noise is greatly reduced (see area around the runway). The histogram of this area agrees well with the histogram of an image processed



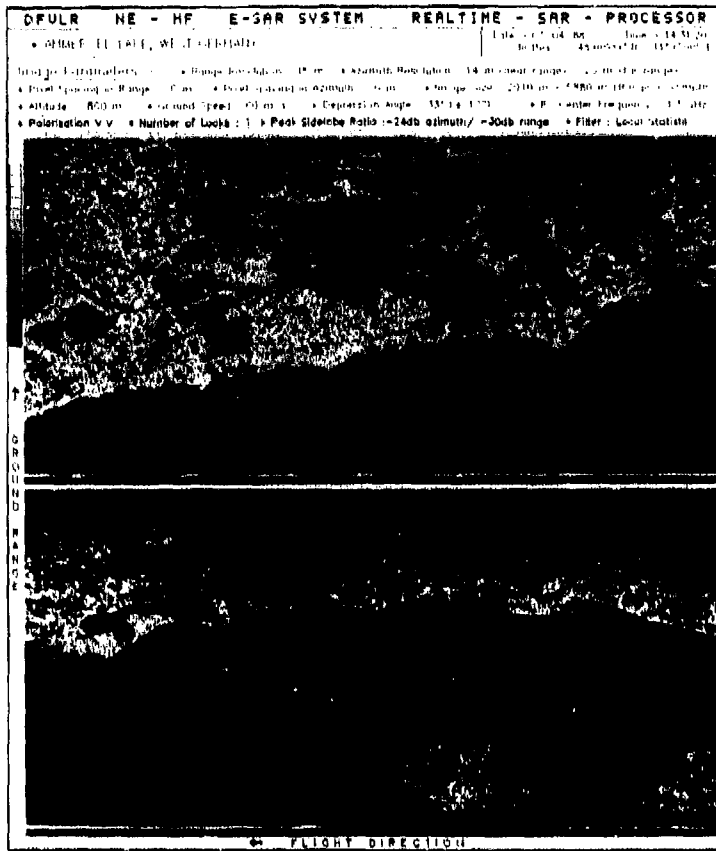


Figure 5. Image processed in realtime: Ammersee lake near Munich (released by "Regierung von Oberbayern" Nr. GS 300/272/88).

## 5. REFERENCES

- [1] Fitch, J.P.: Synthetic Aperture Radar. Springer, 1988.
- [2] Beasley, A.R.: Synthetic Aperture Radar Signal Processing for Airborne Applications, The Marconi Review, vol. XLV, N. 225, Apr. 1982.
- [3] Horn, R.: E-SAR - The Experimental Airborne L/C-Band SAR System of DFVLR. Proc. of IGARSS, Edinburgh, Sept. 1988.
- [4] Moreira, A.: Konzept und Ergebnisse des DLR Echtzeit-Azimuthprozessors fuer das E-SAR System. DLR Research Report, Apr. 1989.
- [5] Moreira, A.; Horn, R.: The Archimedes IIa Experiment on Oil Slick Detection over the North Sea - Measurement Results obtained by the E-SAR System of DLR. DLR Internal Report, Nov. 1988.
- [6] Lee, J.S.: Speckle Suppression and Analysis for Synthetic Aperture Radar Images. Optical Engineering, vol. 25, May 1986.



SIMULATION D'IMAGES DE CIBLES GEOMETRIQUES  
POUR RADAR A OUVERTURE SYNTHETIQUE

par  
J. M. NASR  
AEROSPATIALE D.S.S.S.  
Département Mesures (STS/M)  
Route de Verneuil  
78130 LES MUREAUX

FRANCE

RESUME

Une nouvelle technique de simulation d'images provenant d'un radar à ouverture synthétique est proposée. La méthode est axée sur l'incrustation d'une cible artificielle simulée dans une vraie image radar captée par une antenne opérationnelle portée par un satellite (SEASAT ou SIR-B). Nous avons travaillé dans les bandes L et C et les dimensions des cibles étudiées sont suffisamment grandes devant les longueurs d'ondes utilisées pour pouvoir se servir de techniques de calcul "hautes fréquences" de surfaces équivalentes radar. Le calcul de SER permet de remonter au signal brut reçu par l'antenne. On incruste ensuite l'image de la cible simulée sur le support extrait des bases de données de scènes existantes en tenant compte des restrictions exigées par ce procédé particulier. Bien que les possibilités de simulation soient réduites du fait de ces restrictions, les résultats sont suffisamment intéressants pour permettre d'étudier le comportement d'une cible particulière d'intérêt civil ou militaire en fonction des paramètres de l'onde radar (polarisation, fréquence ...).

1. INTRODUCTION

L'utilisation de l'imagerie radar comme outil de surveillance et de cartographie de la surface terrestre a pris un essor tout à fait remarquable quand on s'est aperçu que ces systèmes étaient bien différents de l'imagerie visible ou infrarouge. En effet, le radar imageur à synthèse d'ouverture a les avantages suivants :

- C'est un système tout-temps. Il est pratiquement indépendant de la couverture nuageuse du fait des longueurs d'ondes utilisées. Cet avantage n'est pas négligeable quand on sait combien les prises de vues optiques sont dégradées par la présence de l'atmosphère.
- Le deuxième avantage réside dans le fait que l'image radar donne une information très différente et surtout complémentaire de celle fournie par la source optique. En effet, si l'image optique est principalement représentative des propriétés chimiques du sol, l'image hyperfréquence est liée aux propriétés physiques et électromagnétiques.

Ces avantages ne vont pas sans certains inconvénients. En effet, l'obtention de données radar haute résolution passe par un traitement de signal très complexe qu'il est souvent difficile d'effectuer à bord du satellite porteur. Mais l'inconvénient majeur provient du fait que la connaissance que l'on possède sur ces systèmes est trop récente pour que toutes les applications militaires ou civiles des radars imageurs haute résolution soient connues. Or il est certain que la caractéristique "tout temps" de la télédétection hyperfréquence justifie à elle seule l'utilisation de radars comme moyen de surveillance par l'image.

Ainsi, comme dans de nombreux cas de physique expérimentale, il apparaît le besoin de faire des simulations de ce que l'on obtiendrait si un système SAR haute résolution était opérationnel. On pourra ainsi définir au mieux les caractéristiques de l'appareil et maîtriser les paramètres sensibles dans l'optique de l'amélioration de la détectabilité de cibles particulières dans une image radar.

L'article développé ici a pour objectif de présenter un nouveau type de simulateur d'image SAR. Celui-ci fonctionne de la manière suivante : On simule tout d'abord l'image radar d'une cible connue par ses dimensions et ses propriétés électriques. Cette simulation est effectuée en supposant que la cible est seule dans la fauchée du radar. L'image obtenue est ensuite incrustée sur un support provenant des images SEASAT ou SIR-B. L'algorithme est donc composé de deux étapes séquentielles qui feront l'objet des deux paragraphes suivants. Le troisième paragraphe présente les applications possibles de ce simulateur dans le domaine de la détectabilité et de l'identification de cibles dans des images radar.

## 2. SIMULATION DE L'IMAGE RADAR D'UNE CIBLE

Cette simulation est effectuée en quatre étapes. La cible à traiter est connue par ses dimensions, sa morphologie exacte et ses propriétés électriques (permittivité, perméabilité). On possède par ailleurs un modèle de Radar à Ouverture Synthétique compatible avec le système opérationnel ayant produit les supports d'incrustation. Ce modèle est caractérisé par :

Un porteur :	Vitesse	V	m/s
	Altitude	H	m
	Inclinaison orbite	$\alpha$	rd
Un radar à synthèse d'ouverture :	Longueur antenne	Dz	m
	PRF	PRF	Hz
	Fréquence	f <sub>0</sub>	GHz
	Longueur d'onde	$\lambda$	m
	Inclinaison faisceau	$\alpha$	rd
	Longueur impulsion	T	ms
Dande de modulation	$\Delta f$	Hz	
Longueur de fauchée	Lz	m	

Les quatre étapes sont les suivantes :

1. Décomposition de la cible en éléments géométriques simples (EGS ou Points brillants). En effet, quand la cible est grande devant la longueur d'onde, le signal rétrodiffusé est dû uniquement à un ensemble fini de réflecteurs.
2. Calcul des Surfaces Equivalentes Radar (SER) des EGS
3. Calcul de la SER générale de la cible
4. Calcul du signal brut reçu à l'antenne et de l'image brute de la cible.

## 2.1 Décomposition de la cible en EGS

Première étape du processus, elle correspond à la détermination des points brillants ou éléments géométriques simples sur la cible pour chaque position de celle-ci dans le lobe de l'antenne. En effet, si la cible est placée dans la fauchée du radar, elle occupera plusieurs positions discrètes dans le lobe de l'antenne du fait même de la nature impulsionnelle du système. Si ce nombre d'impulsions est N, on trouve (Equ 1) :

$$N = \frac{Lz}{y} = \frac{\lambda H PRF}{V Dz \cos(\alpha)} \quad (1)$$

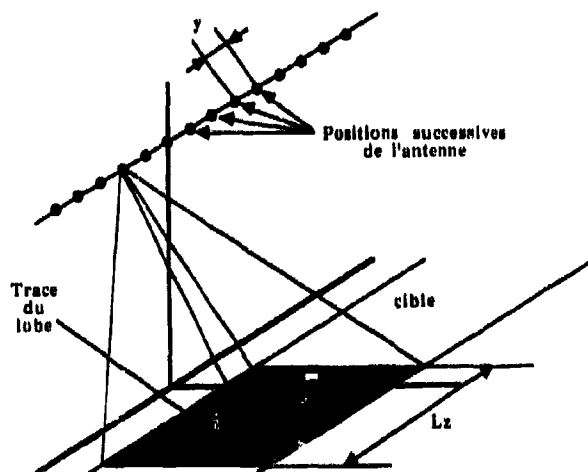


FIGURE 1 : Position: successives de l'antenne.

Les paramètres de cette équation sont représentés sur la figure 1.

Nous avons identifié trois types d'EGS suivant l'intensité de la rétrodiffusion produite. On trouvera dans le tableau ci-dessous ces trois classes :

**TYPE A :** Structures triédriques. Elles produisent une forte rétrodiffusion pour des incidences très variées. On trouvera les trièdres trirectangles mais aussi toutes les structures rétrodiffusant le rayon incident après trois réflexions internes.

**TYPE B :** Structures diédriques. On trouvera ici tous les EGS rétrodiffusant l'onde après deux réflexions internes. Le dièdre plan est la plus simple structure mais nous avons représenté en figure 2 quelques autres possibilités.

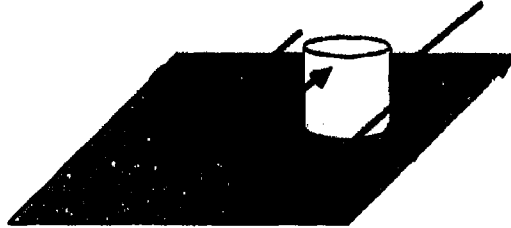


FIGURE 2: EGS de type B

**TYPE C :** Structures simples produisant une rétrodiffusion. Cela revient à trouver un plan tangent orthogonal au rayon incident. On citera le cylindre sous une incidence normale à l'axe, l'arête pour une incidence normale etc ...

## 2.2 Calcul des SER des EGS

Ceci est la deuxième étape de notre processus. Nous avons en entrée, pour chaque position de la cible dans le lobe, une collection d'EGS occupant une certaine position. Il s'agit maintenant d'évaluer la SER de ces EGS. Une fois de plus, ces SER devront être évaluées pour chaque position de la cible. Les cibles auxquelles nous nous intéressons sont de nature artificielle (fabriquées par l'homme) et ne sont pas rugueuses devant la longueur d'onde. C'est pourquoi, nous pouvons utiliser les techniques d'approximation haute fréquence suivantes (Développées en réf. 6) :

**A - Optique géométrique :** Théorie ancienne basée sur le principe de Fermat. On obtient un résultat très simple puisque la SER vaut  $\frac{r_1}{r_2}$  où  $r_1$  et  $r_2$  sont les rayons de courbure principaux de la cible au point d'interaction considéré.

**AVANTAGE :** Extrêmement simple à utiliser

**INCONVENIENT :** Tombe en défaut dès que  $r_1$  ou  $r_2$  tend vers 0 ou l'infini, ce qui est le cas pour toute surface contenant une droite ou une arête (cylindre, cône ou plan).

**B - Optique physique :** réf (7) Théorie basée sur la simplification de l'équation de Stratton-Chu permettant de calculer le champ électrique diffusé à partir du champ électrique reçu par la cible. L'intégrale résultat peut se simplifier si les trois conditions suivantes sont respectées :

- la cible est loin de la source (champ lointain)
- la cible est grande devant la longueur d'onde
- on peut assimiler, au niveau du point d'interaction, la cible à son plan tangent.

**AVANTAGE :** Assez simple d'utilisation. Prend en compte presque tous les EGS de type A et B.

**INCONVENIENTS :** Ne fonctionne plus dès qu'il n'y a plus de plan tangent, ce qui est le cas pour une arête ou toute autre structure diffractrice.

**C - Théorie Géométrique de la Diffraction (TGD) :** (réf. 2 et 3) Initialement développée par Keller, la TGD est une extension de l'optique géométrique qui prend en considération une nouvelle classe de rayons appelés rayons diffractés. On introduit alors un coefficient de diffraction  $D$  qui permet de calculer la SER dans les cas où l'optique physique tombe en défaut.

**INCONVENIENT :** Le Coefficient de diffraction tend vers l'infini dès que le rayon diffracté occupe deux positions particulières dépendantes de la géométrie de la cible et l'illumination.

**D - Théorie Uniforme de la Diffraction (TUD) :** réf (5) C'est une extension de la TGD qui prend en compte les positions du rayon diffracté pour lesquelles la théorie de Keller tombe en défaut. On recalcule le coefficient  $D$  à un ordre plus élevé.

**INCONVENIENT :** Théorie très lourde.

L'inconvénient global de ces théories est qu'elles ne donnent des résultats acceptables que sur des conducteurs parfaits ce qui n'est généralement pas le cas si l'on veut effectuer des simulations réalistes. Il importe donc de pouvoir se ramener à des diélectriques. On utilise la formule suivante, qui est valable en zone optique :

$$\sigma_{\text{diel}} = \sigma_{\text{cp}} |R_f|^2 \quad (2)$$

où  $\sigma_{\text{diel}}$  désigne la SER du diélectrique et  $\sigma_{\text{cp}}$  désigne la SER du corps parfaitement conducteur.  $R_f$  est le coefficient de réflexion de Fresnel calculé à l'interface entre deux milieux. Ce coefficient ne se calcule aisément que dans deux plans privilégiés qui sont le plan d'incidence (contenant la direction de propagation et la normale à l'objet au point d'interaction) et le plan orthogonal (contenant la direction de propagation et orthogonal au précédent). La figure 3 précise cette géométrie :

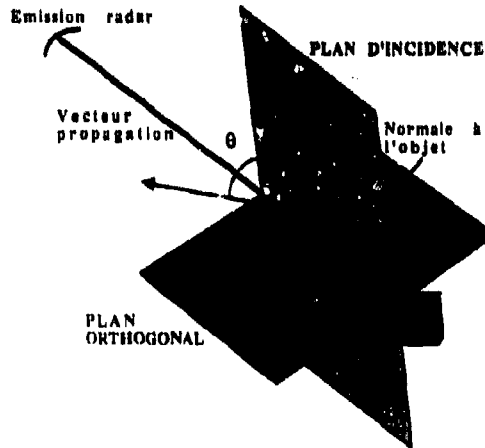


FIGURE 3: Plan d'incidence et plan orthogonal

La flèche représente le vecteur champ électrique qui fait un angle  $\theta$  avec le plan d'incidence. Cet angle est dit angle de polarisation. On définit ainsi au niveau de l'objet un repère orthonormé  $(//, \perp, w)$  où  $w$  est colinéaire au vecteur propagation,  $//$  est orthogonal à  $w$  dans le plan d'incidence et  $\perp$  est orthogonal à  $w$  dans le plan orthogonal. Le champ électrique incident peut se décomposer de manière unique sur  $//$  et  $\perp$  de la manière suivante :

$$E_i = \begin{pmatrix} E_{i//} \\ E_{i\perp} \end{pmatrix} \text{ où } E_{i//} = |E_i| \cos(\theta) \text{ et } E_{i\perp} = |E_i| \sin(\theta) \quad (3)$$

D'où le champ diffusé :

$$E_d = \begin{pmatrix} E_{d//} \\ E_{d\perp} \end{pmatrix} \quad (4)$$

La matrice de rétrodiffusion permet de calculer  $E_{d//}$  et  $E_{d\perp}$  en fonction de  $E_{i//}$  et  $E_{i\perp}$ . En effet, on obtient :

$$\begin{pmatrix} E_{d//} \\ E_{d\perp} \end{pmatrix} = \begin{pmatrix} a_{11} & a_{12} \\ a_{21} & a_{22} \end{pmatrix} \begin{pmatrix} E_{i//} \\ E_{i\perp} \end{pmatrix} \quad (5)$$

où

$$\begin{aligned} a_{11} &= \frac{\sqrt{\sigma_{//}} \omega \phi_{//}}{\sqrt{4\pi} r} & a_{12} &= \frac{\sqrt{\sigma_{//\perp}} \omega \phi_{//\perp}}{\sqrt{4\pi} r} \\ a_{21} &= \frac{\sqrt{\sigma_{\perp//}} \omega \phi_{\perp//}}{\sqrt{4\pi} r} & a_{22} &= \frac{\sqrt{\sigma_{\perp\perp}} \omega \phi_{\perp\perp}}{\sqrt{4\pi} r} \end{aligned} \quad (6)$$

Ici, les SER sont telles que

$$\sigma_{ij} = \sigma_{ij\text{cp}} |R_{fj}|^2 \quad \text{où } (i,j) \in \{//, \perp\}$$

où les  $\sigma_{ij}$  cp sont calculées à l'aide des formules d'approximation précédentes. Il s'agit maintenant de revenir au champ électrique reçu au niveau de l'antenne. En effet, supposons que l'on ait une émission parallèle au vecteur vitesse du satellite (ce qui est le cas pour SEASAT) et une réception directe. On nommera cette direction H par opposition à V qui sera orthogonale. La SER à calculer est :

$$\sigma_{HH} = \lim_{r \rightarrow \infty} 4\pi r^2 \frac{|E_{dh}|^2}{|E_i|^2} \quad (7)$$

où  $E_{dh}$  est le champ diffusé projeté sur la direction H. Pour passer du champ diffusé  $E_d$  de coordonnées  $E_{d//}$  et  $E_{d\perp}$  dans le repère d'incidence au champ  $E_{dh}$ , il suffit d'effectuer cette projection. Si les termes croisés de la matrice sont nuls, ce qui est le cas généralement en zone optique, on obtient :

$$E_{dh} = \frac{|E_i|}{\sqrt{4\pi r}} \left\{ |R_{//}| \sqrt{\sigma_{//}} e^{j(\varphi_{d//})} \cos^2(\theta) + |R_{\perp}| \sqrt{\sigma_{\perp}} e^{j(\varphi_{d\perp})} \sin^2(\theta) \right\} \quad (8)$$

Il suffit ensuite de repasser à la SER à l'aide de l'équation 7. On obtient :

$$\sigma_{HH} = \left| |R_{//}| \sqrt{\sigma_{//}} e^{j(\varphi_{d//})} \cos^2(\theta) + |R_{\perp}| \sqrt{\sigma_{\perp}} e^{j(\varphi_{d\perp})} \sin^2(\theta) \right|^2 \quad (9)$$

### 2.3 Calcul de la SER générale de la cible

Une fois que les SER sont calculées pour chaque EGS et pour chaque position de ceux-ci dans le lobe d'antenne, il faut calculer la SER générale de la cible par combinaison des SER élémentaires. Ce calcul est possible en utilisant l'équation suivante valide en zone optique : Supposons que la cible soit composée de m EGS : on obtient :

$$\sigma_t = \left| \sum_{i=1}^{i=m} \sqrt{\sigma_i} \exp(j \frac{4\pi d_i}{\lambda}) \right|^2 \quad (10)$$

où  $\sigma_t$  est la SER générale et  $\sigma_i$  ( $i \in \{1, \dots, m\}$ ) sont les SER élémentaires.  $d_i$  est la distance de l'EGS i à l'antenne et  $\lambda$  la longueur d'onde.

### 2.4 Calcul du signal brut et de l'image brute de la cible

Dernière étape de notre processus de simulation de cible, nous sommes maintenant en possession d'une collection de SER de la cible représentant son comportement vis-à-vis de l'onde hyperfréquence quand elle traverse le lobe de l'antenne. Il ne reste plus qu'à calculer le signal brut reçu par le radar en modulant la réponse impulsionnelle de celui-ci par cette SER. Pour cela, il faut choisir un modèle de SAR compatible avec le système ayant effectué les images support sur lesquelles l'incrutation doit prendre place.

Le modèle utilisé est le suivant :

Supposons qu'il y ait M réflecteurs dans le lobe de l'antenne,  
soit n l'impulsion courante,  
soit k la porte courante

soit  $\sigma(m)$  et  $e^{j\varphi_m}$  la SER complexe du réflecteur m,  
soient  $(X_m, Y_m, Z_m)$  les coordonnées du réflecteur m dans un repère lié à l'antenne,

soient  $(0, \frac{nV}{PRF}, H)$  les coordonnées de l'antenne relativement au même repère,

soit  $r_s$  la résolution en distance et  $F(x)$  la fonction de modulation en distance du radar.

On obtient le signal radar à l'impulsion n et à la porte k :

$$S(n,k) = \sum_{m=1}^{m=M} KP \sigma(m) e^{j\varphi_m} F(k \cdot X_m / r_s) AZ(m,n) \quad (11)$$

avec

$$AZ(m,n) = \exp \left( j \frac{4\pi}{\lambda} \sqrt{X_m^2 + \left( \frac{nV}{PRF} - Y_m \right)^2 + (H - Z_m)^2} \right) \quad (12)$$

Le signal brut est calculé ainsi, impulsion par impulsion et stocké sur un support. Il suffit de le corriger géométriquement et radiométriquement pour qu'il soit parfaitement compatible avec le support sur lequel il est destiné à être incrusté. On comprime alors ce signal brut en distance (compression d'impulsion) et en azimut (synthèse d'ouverture) et on obtient l'image complexe (module et phase) de la cible simulée prête à être incrustée.

### 3. INCRUSTATION

Nous sommes maintenant en possession de l'image brute de la cible simulée pour un certain type de SAR. L'incrustation peut alors être exécutée. Pour cela, certaines précautions devront être prises. Premièrement la zone sur laquelle l'incrustation devra prendre place devra répondre aux deux critères suivants :

- Elle devra être géométriquement plane. Cela signifie que la zone ne sera pas affectée de relief. En effet, si c'était le cas, il faudrait être capable de prévoir la forme que prendrait la réponse impulsionnelle du système SAR. Or, on ne connaîtra pas toujours un modèle numérique de terrain suffisamment précis pour pouvoir transformer cette réponse.
- Elle devra être radiométriquement plane. Cela signifie qu'il n'y aura pas de gros réflecteurs à proximité de la zone sur lesquels l'incrustation devra être réalisée. La présence d'une grande structure réflectrice pourrait engendrer des réflexions multiples qui seraient impossibles à maîtriser.

Nous avons choisi une zone centrée sur l'aéroport de Cherbourg Maupertus. En effet, le terrain d'aviation est plat et il n'y a pas de grandes structures réflectrices loin des installations aéroportuaires.

La deuxième précaution qu'il s'agit de prendre concerne le procédé d'incrustation lui-même qui est une addition complexe à complexe effectuée entre l'image brute du support et l'image brute simulée de la cible. Il est nécessaire en effet de mettre à 0 les pixels du support devant être remplacés physiquement par l'incrustation. De même, il faudra mettre à 0 les pixels concernés par l'ombre portée par la cible simulée sur le sol relativement à l'illumination radar. La position de ces pixels est représentée sur la figure 4.

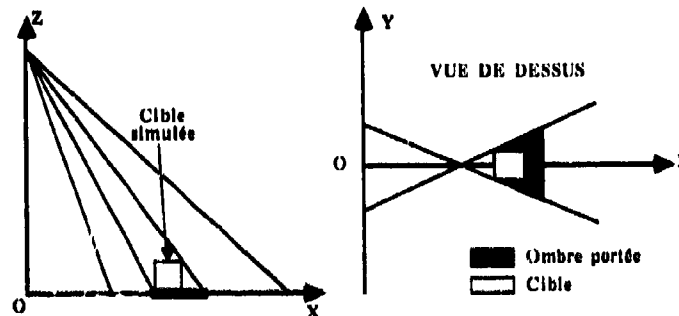


FIGURE 4: Pixels concernés par l'incrustation.

Une fois ces prétraitements sur le support effectués, il est possible de lancer l'incrustation pixel à pixel. On obtient l'image brute résultat sur laquelle on fait une détection quadratique pour obtenir les pixels en puissance.

### 4. RESULTATS DE SIMULATION ET CONCLUSION

Les résultats présentés au symposium concernent trois structures différentes qui nous ont permis d'identifier trois paramètres importants qui sont déterminants quand on parle de détectabilité d'une cible dans une image radar. Comme on pourra le remarquer, chacun d'entre eux peut faire en sorte que la détection de la cible soit impossible.

Première simulation : Il s'agit de cinq cylindres disposés à 200 m les uns des autres sur un axe faisant  $45^\circ$  avec le vecteur vitesse du satellite. Ces cylindres sont hauts de 25 m et de diamètre égal à 25 m. Ils ont été simulés pour SEABAT et incrustés sur la piste de l'aéroport de Cherbourg Maupertus (FRANCE). On reconnaît ces cylindres parce que, dans leur ensemble, ils forment une structure morphologiquement particulière. Il est sûr qu'un cylindre unique n'aurait pas pu être identifié. La morphologie de la cible est donc un paramètre déterminant.

Deuxième simulation : il s'agit d'une structure en U. Plusieurs simulations ont été effectuées pour plusieurs orientations de celle-ci relativement à l'illumination SEASAT. Elle n'est vraiment identifiable que si elle est placée perpendiculairement au faisceau radar. Ainsi, l'orientation de la cible est prépondérante.

Troisième simulation : il s'agit de deux arêtes disposées à  $90^\circ$  l'une de l'autre dans un plan perpendiculairement au faisceau. On remarque que si la polarisation linéaire du champ électrique est parallèle à une de ces arêtes, l'autre est invisible et réciproquement. Ainsi, la polarisation de l'onde émise et réfléchie peut faire en sorte qu'une cible donnée soit indétectable. Dans ce cas et dans celui-là seulement, certains traitements de polarimétrie peuvent être effectués si on dispose d'un SAR multipolarisation.

##### 5. REFERENCES

- (1) J.W. CRIPSIN et K.M. SIEGEL  
Methods of Radar Cross Section Analysis  
Academic Press - New York, Londres 1968
- (2) J.B. KELLER  
"A Geometrical Theory of Diffraction - Calculus of Variations and its Applications" Symposium of Applied Mathematics - Vol. 8  
Marc Graw Hill - New York pp. 27 - 52, 1957
- (3) E.F. KNOTT  
"A progression of High Frequency Prediction Techniques"  
Proc. IEEE - Vol. 73 n° 2 pp. 252 - 264, Février 1985
- (4) E.F. KNOTT ; J.F. SHAEFFER et M.T. TULEY  
Radar Cross Section  
Aitech House - New York - 1985
- (5) R.G. KOUJOUNJIAN - P.H. PATHAK  
"An uniform Theory of Diffraction for an edge"  
Proc. IEEE Vol. 62 n° 11 novembre 1974
- (6) J.M. NASR  
"Simulation d'images de cibles géométriques simples pour radar à ouverture synthétique embarqué sur satellite"  
Thèse de doctorat PARIS 7 - février 1989
- (7) G.T. RUCK ; D.E. BARRICK ; W.D. STUART et C.K. KRICHBAUM  
RADAR CROSS SECTION Handbook  
Plenum Press New York 1970
- (8) F.T. ULABY ; R.K. MOORE et A.K. FUNG  
Microwave Remote Sensing  
Addison Wesley Publishing Company Norwood 1982
- (9) J.J. VAN ZYL ; H.A. ZEBKER et C. ELACHI  
"Imaging Radar Polarization signatures"  
Radio Science Vol. 22 n° 4 pp. 529 - 543, Juillet/août 1987

## CODAGE D'IMAGES SAR

P. TOURTIER  
 THOMSON-CSF/LER  
 Avenue de Belle Fontaine  
 38510 CRESSON SEVIGNE  
 FRANCE

RESUME

L'imagerie SAR engendre des débits numériques très importants tant au niveau de la transmission qu'au niveau de l'enregistrement.

Les techniques de codage d'images ont pour but de réduire le débit tout en préservant la qualité originale, ce qui permet par exemple, d'alléger la capacité du canal de transmission et d'augmenter la durée d'enregistrement.

Cet article présente les différentes techniques de compression existant à l'heure actuelle. La technique la plus performante à base de transformée cosinus est décrite en détails.

Les résultats obtenus avec cette technique par THOMSON-CSF montrent qu'un taux de compression de l'ordre de 4 à 5 peut être atteint sans dégradation visible de l'image.

1 - INTRODUCTION

Une image contient une quantité d'informations importante, typiquement l'image noir et blanc est représentée après numérisation par une matrice de points pouvant avoir 256 niveaux de gris et elle nécessite donc pour être représentée sous forme originale un nombre de bits égal à 8 fois le nombre de points par le nombre de lignes.

Le but du codage d'images est de réduire cette quantité d'informations sans introduire de dégradations notables dans l'image reconstruite. Plus précisément, un algorithme de codage transforme l'image en une série de codes binaires qui permettent de reconstruire au décodeur une image dont le contenu est arbitrairement proche de celui de l'image originale. Si l'algorithme est efficace le nombre de bits de ces codes binaires est nettement inférieur au nombre de bits originaux.

Cette réduction dépend essentiellement de la corrélation intrinsèque existant entre les points de l'image et de la dégradation que l'on autorise à la reconstruction. La qualité de l'image reconstruite désirée dépend à son tour de l'utilisation ultérieure de l'image. L'efficacité d'un algorithme de codage est caractérisée par son taux de compression défini comme le rapport du nombre de bits à la sortie du codeur par le nombre de bits à l'entrée et la qualité de l'image reconstruite.

Cette qualité se mesure de 2 façons, objectivement par le rapport signal à bruit (RSB) défini comme suit :

$$RSB(\text{dB}) = 10 \log_{10} \frac{255^2}{\frac{1}{N^2} \sum_{i=1}^N \sum_{j=1}^N (\hat{x}_{ij} - x_{ij})^2}$$

où  $\hat{x}_{ij}$  est l'intensité du point de coordonnées (i,j) dans l'image reconstruite et  $x_{ij}$  celle de la valeur dans l'image originale,

et subjectivement selon des critères psychovisuels.

Les différentes méthodes de codage existantes à l'heure actuelle sont décrites au paragraphe 2.

La méthode basée sur la transformée cosinus qui conduit au meilleur taux de compression est décrite au paragraphe 3.

Des résultats obtenus sur des images SAR sont présentés au paragraphe 4.

## 2 - METHODES DE CODAGE

Toutes les méthodes de codage exploitent la redondance des informations présentes dans une image. Cette redondance est liée à la prédictibilité des données.

Certaines méthodes suppriment ainsi la redondance au niveau sur point courant de l'image en codant la différence entre sa valeur et la valeur prédite à partir des points voisins. Il s'agit de la modulation par impulsion codée différentielle (MICD) ou de la MICD adaptative (MICDA) selon que les poids servant au calcul de la valeur prédite soient fixes ou variables.

D'autres méthodes travaillent au niveau de blocs de points. Il s'agit dans ce cas de transformer cet ensemble de points en une combinaison linéaire de fonctions de base. Si l'ensemble de points est de taille adéquate c'est-à-dire approximativement égal au rayon de corrélation des données un nombre réduit de fonctions de base suffit à représenter le signal. De telles méthodes de codage s'appellent méthodes par transformées, parmi les plus connues on trouve la transformée de Karhunen Loe's (TKL), d'Hadamart, de Fourier et cosinus (TC).

Le meilleur compromis entre efficacité de compression et facilité d'implantation est obtenue avec la TC.

En effet, comme on le verra plus en détails par la suite, la plupart des méthodes de codage sont basées sur l'emploi de quantificateurs scalaires dont l'optimalité dépend de l'indépendance des coefficients transformés. Les théories de traitement du signal montrent que la TKL est optimale en ce sens, cependant ses fonctions de base sont liées au signal et donc inconnues au décodeur. C'est pour cette raison qu'on lui préfère la TC qui présente de très bonnes propriétés de décorrélation pour la plupart des images et dont les fonctions de base sont fixes.

Enfin, d'autres méthodes de codage tel que le codage sous bande [1] existent, elles correspondent à une combinaison des 2 autres types de méthode.

Dans la suite, nous nous intéressons à la méthode à base de TC car elle permet d'obtenir des taux de compression élevé et résiste bien aux erreurs de transmission comme le mentionne Jain [2].

## 3 - CODAGE PAR TC

### 3.1 - TAILLE DES BLOCS

Dans cette méthode, la TC est appliquée sur des blocs de l'image. Deux raisons principales permettent de justifier ce choix. D'une part, le regroupement de points de l'image ne présente d'intérêt que dans la mesure où la corrélation entre ces points est forte. Or les simulations effectuées sur des images ont montré qu'une telle corrélation est limitée à un voisinage de taille réduite, 4, 8 ou 16 points selon le type d'images.

D'autre part, la complexité de la TC croît rapidement avec la taille des blocs. Afin de faciliter l'implémentation de la transformée des algorithmes rapides ont été développés par CHEN [3], LEE [4] et HAQUE [5]. L'architecture de LEE à base de papillons a donné lieu à la réalisation d'un circuit VLSI [6] pour une taille de bloc égale à 16. En ce qui concerne l'implémentation logicielle, il existe des processeurs spécialisés.

### 3.2 - DEFINITION DE LA TC

Les définitions de la TC directe et inverse sont les suivantes :

directe :

$$F(u,v) = \frac{C(u) C(v)}{N^2} \sum_{j=0}^{N-1} \sum_{k=0}^{N-1} f(j,k) \cdot \cos\left(\frac{(2j+1)u\pi}{2N}\right) \cos\left(\frac{(2k+1)v\pi}{2N}\right)$$

$u, v = 0, 1, \dots, N-1$  où

$$C(w) = \begin{cases} \frac{1}{\sqrt{2}} & \text{pour } w = 0 \\ 1 & \text{pour } w = 1, 2, \dots, N-1 \end{cases}$$

inverse :

$$f(j,k) = \sum_{u=0}^{N-1} \sum_{v=0}^{N-1} C(u) C(v) F(u,v) \cdot \cos\left(\frac{(2j+1)u\pi}{2N}\right) \cos\left(\frac{(2k+1)v\pi}{2N}\right)$$

$j, k = 0, 1, \dots, N-1$

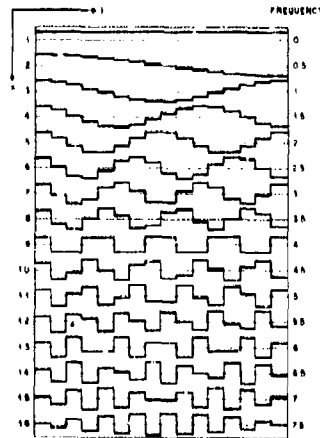
On peut montrer qu'il s'agit d'une transformée orthogonale. Cependant, contrairement à la transformée de Fourier, elle n'est pas symétrique et elle nécessite deux processeurs différents par la transformation aller et retour.

### 3.3 - PROPRIETES DE LA TC

La TC possède des propriétés qui expliquent les performances des algorithmes de compression qui en sont dérivés. Les plus importantes de ces propriétés sont données ci-après.

#### a) Notion de spectre

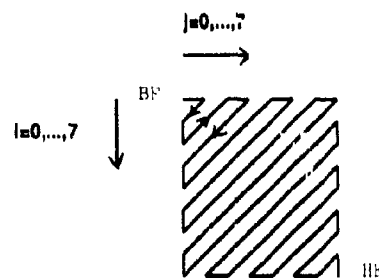
Il est possible d'associer à cette transformée la notion de spectre car chacune des fonctions de base correspond à un motif dont les variations sont de plus en plus rapides au fur et à mesure que l'on passe des premières fonctions à celles d'ordre plus élevé. Les fonctions sont représentées sur la figure 1.



Fonctions de base

Figure 1

L'ordre selon lequel sont traités les coefficients suit la répartition des fréquences croissantes. Il s'agit d'un balayage zig-zag représenté sur la figure 2.



Balayage du bloc et répartition des fréquences

Figure 2

#### b) Concentration de l'énergie

Les transformées orthogonales ont la propriété de modifier fortement la répartition de l'énergie tout en la conservant. L'aptitude de la transformée à concentrer l'énergie sur quelques fonctions de base permet de prédire les performances d'une méthode de codage. Des études ont montré que la TC était parmi les transformées indépendantes du signal la meilleure à cet égard [7].

#### c) Distribution

Afin de coder au mieux les coefficients, il est nécessaire de connaître leurs distributions. Des études approfondies ont montré que selon la nature des images, les distributions suivent une loi gaussienne, laplacienne ou de Cauchy.

De plus, les distributions sont centrées excepté pour le premier coefficient qui représente la valeur moyenne d'un bloc de l'image et qui est donc positif. Leur variance décroît du premier coefficient aux coefficients d'ordre supérieur. Autrement dit, les coefficients sont de moins en moins dispersés quand on passe des basses fréquences aux hautes fréquences.

#### d) Décorrélation

Comme cela a été mentionné précédemment, la TC décorrèle les informations présentes dans l'image et permet donc un traitement scalaire optimal.

#### e) Coefficients à valeurs réelles

La TC produit des coefficients à valeurs réelles, il faut donc les quantifier avant de pouvoir leur associer des codes binaires.

### 3.3 - PRINCIPE DU CODAGE PAR TC

La compression obtenue par les systèmes de codage à base de transformées provient de 2 opérations effectuées sur les coefficients :

#### a) Quantification

Il s'agit de l'opération irréversible qui vise à diminuer le nombre de niveaux servant à représenter un coefficient transformé. Cette opération introduit dans l'image une dégradation généralement assimilable à un bruit blanc [8].

Un soin particulier doit être apporté au dessin du quantificateur (seuil de quantification, niveaux de reconstruction) pour limiter les artéfacts.

Deux types de quantificateurs sont couramment utilisés :

- linéaire (QL) : les seuils sont équidistants.
- non linéaire (QNL) : les seuils sont choisis de façon à conserver une valeur constante au rapport de l'erreur de quantification sur la valeur réelle.

#### b) Codage à longueur variable (CLV)

Il s'agit de l'opération réversible qui associe des codes binaires aux niveaux du quantificateur. Afin de pouvoir décoder le train binaire reçu au décodeur, il est nécessaire d'imposer des contraintes sur le choix des codes.

Il existe 2 types de codes répondant à la contrainte de décodabilité.

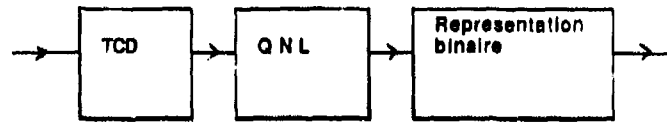
- codes à longueur fixe (CLF) : représentation binaire par exemple
- codes à longueur variable (CLV) : de type Huffman ou Huffman calculé.

Les CLV produisent par définition un nombre de bits variables. Cela pose un problème dans la plupart des applications où l'on désire obtenir un nombre de bits moyen constant. Dans le cas de séquences d'images, il faut prévoir une mémoire tampon et une contre réaction sur le pas moyen de quantification pour réguler le débit.

### 3.4 - SCHEMA DE CODAGE

Selon l'application choisie débit fixe ou variable, on utilise respectivement les schémas suivants :

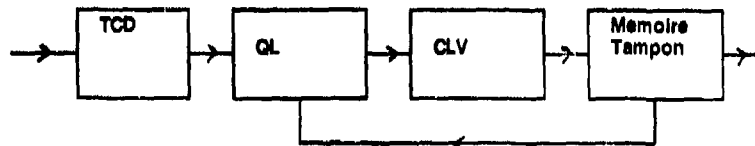
- a) QNL + CLF : voir figure 3



Schema a)

Figure 3

b) QL + CLV : voir figure 4.



Schema b)

Figure 4

La complexité matérielle des schémas est plus ou moins équivalente. La partie délicate du schéma a) réside dans le QNL qui nécessite une batterie de comparateurs tandis qu'en ce qui concerne le schéma b) la partie délicate est la réalisation du CLV et de la mémoire tampon où les codes sont concaténés au codeur et isolés au décodeur.

Les performances en terme de rapport signal à bruit sont comparables. Cependant, le schéma b) est beaucoup plus robuste car il code dans de bonnes conditions des images de nature différente de celles pour lequel il a été optimisé sans avoir à changer les codes. De même, il fonctionne bien sur une large plage de débit.

Bien que le RSB ne varie pas beaucoup, les performances du schéma a) diminuent considérablement dans ces conditions car il y a apparition d'artefacts dans l'image.

#### 4 - RESULTATS OBTENUS SUR DES IMAGES SAR

L'algorithme correspondant au schéma b) a été programmé sur un ordinateur VAX 8800. Les simulations permettent d'obtenir différents taux de compression en jouant sur la finesse du quantificateur.

Le tableau 1 donne les RSB obtenus sur plusieurs types d'images pour différents taux de compression.

Image 1

Taux de compression	Rapport signal à bruit (dB)
2	40.24
3	34.48
4	31.49
5	29.71
6	28.61
7	27.89

Image 2

Taux de compression	Rapport signal à bruit (dB)
2	40.07
3	34.44
4	31.44
5	29.66
6	28.55
7	27.83

Tableau 1

La qualité subjective des images obtenues est bonne, en particulier dans le cas de faibles taux de compression où aucune dégradation n'est visible.

De plus, des essais complémentaires effectués sur d'autres images SAR ont montré que l'algorithme est robuste.

#### 5 - CONCLUSION

Différentes techniques de compression d'images ont été brièvement présentées dans cet article. Celle basée sur la transformation cosinus a été décrite en détails. Elle fait partie des techniques les plus performantes à l'heure actuelle pour des applications où le taux de compression est élevé. Les résultats obtenus sur des images SAR sont tout à fait encourageants et l'on peut ainsi espérer améliorer les capacités de stockage des systèmes utilisés à l'heure actuelle.

#### REFERENCES

- [1] J.W. WOODS et al.,  
"Subband Coding of Images",  
IEEE-ASSP, vol. 34, n°5, octobre 1986, pp.1278-1288
- [2] A.K. JAIN  
"Image Data Compression : A review"  
Proceedings of IEEE, vol. 69, n°3, mars 1981, pp. 349-389
- [3] W.H. CHEN et al.;  
"A Fast Computational Algorithm for the DCT"  
IEEE Trans. on Com., vol. 25, n°9, septembre 1977.
- [4] B.G. LEE  
"A new Algorithm to Computer the DCT"  
IEEE - ASSP, vol. 32, n°6, décembre 1984, pp. 1243 - 1245
- [5] K.A. HAQUE,  
"A new Dimensional Fast Cosine Transform"  
IEEE - ASSP, vol. 33, n°6, décembre 1985, pp. 1532 - 1536
- [6]-N. DEMASGIEUX et al.  
"An optimized VLSI Architecture for a Multiformat DCT"  
ICASSP 1987
- [7] W.H. CHEN  
"Adaptive coding of monochrome and color images"  
IEEE Trans. on Com, vol. 25, n°11, novembre 1987, pp. 1285 - 1292
- [8] NB. JAYANT, P. NOLL  
"Digital coding of Waveforms"  
Prentice Hall 1984, pp. 158 - 161

REPORT DOCUMENTATION PAGE															
1. Recipient's Reference	2. Originator's Reference AGARD-CP-459	3. Further Reference	4. Security Classification of Document UNCLASSIFIED												
5. Originator	Advisory Group for Aerospace Research and Development North Atlantic Treaty Organization 7 rue Ancelle, 92200 Neuilly sur Seine, France														
6. Title	HIGH RESOLUTION AIR- AND SPACEBORNE RADAR														
7. Presented at	the Avionics Panel Symposium held in The Hague, Netherlands 8-12 May 1989.														
8. Author(s)/Editor(s) Various	9. Date October 1989														
10. Author's/Editor's Address Various	11. Pages 230														
12. Distribution Statement	This document is distributed in accordance with NATO Security Regulations and AGARD policies.														
13. Keywords/Descriptors	<table> <tbody> <tr> <td>High resolution radar</td> <td>Surveillance</td> </tr> <tr> <td>Synthetic aperture radar</td> <td>Target acquisition</td> </tr> <tr> <td>Inverse synthetic aperture radar</td> <td>Motion compensation</td> </tr> <tr> <td>SAR</td> <td>Signal processing</td> </tr> <tr> <td>ISAR</td> <td>Data processing</td> </tr> <tr> <td>Space based radar</td> <td>Avionics</td> </tr> </tbody> </table>			High resolution radar	Surveillance	Synthetic aperture radar	Target acquisition	Inverse synthetic aperture radar	Motion compensation	SAR	Signal processing	ISAR	Data processing	Space based radar	Avionics
High resolution radar	Surveillance														
Synthetic aperture radar	Target acquisition														
Inverse synthetic aperture radar	Motion compensation														
SAR	Signal processing														
ISAR	Data processing														
Space based radar	Avionics														
14. Abstract	<p>Imaging techniques are important sources of information in military operations. They may serve for purposes such as target detection and location, reconnaissance, classification and identification of fixed or moving objects as well as for orientation over unknown terrain. Despite considerable advances in electro-optical imaging systems the radar sensor has become an attractive alternative for several reasons: large range performance, penetration of weather, smoke, dust and foliage, day and night operation. On the other hand high resolution radar techniques such as synthetic aperture radar (SAR) and inverse synthetic aperture radar (ISAR) promise geometrical resolution of about 1m and less.</p>														

<p>AGARD Conference Proceedings No.459 Advisory Group for Aerospace Research and Development, NATO <b>HIGH RESOLUTION AIR- AND SPACEBORNE RADAR</b> Published October 1989 2,30 pages</p> <p>Imaging techniques are important sources of information in military operations. They may serve for purposes such as target detection and location, reconnaissance, classification and identification of fixed or moving objects as well as for orientation over unknown terrain. Despite considerable advances in electro-optical imaging systems the radar sensor has become an attractive alternative for several reasons: large range performance, penetration of</p> <p>P.T.O.</p>	<p>AGARD-CP-459</p> <p>High resolution radar Synthetic aperture radar Inverse synthetic aperture radar SAR ISAR Space based radar Surveillance Target acquisition Motion compensation Signal processing Data processing Avionics</p>	<p>AGARD Conference Proceedings No.459 Advisory Group for Aerospace Research and Development, NATO <b>HIGH RESOLUTION AIR- AND SPACEBORNE RADAR</b> Published October 1989 2,30 pages</p> <p>Imaging techniques are important sources of information in military operations. They may serve for purposes such as target detection and location, reconnaissance, classification and identification of fixed or moving objects as well as for orientation over unknown terrain. Despite considerable advances in electro-optical imaging systems the radar sensor has become an attractive alternative for several reasons: large range performance, penetration of</p> <p>P.T.O.</p>	<p>AGARD-CP-459</p> <p>High resolution radar Synthetic aperture radar Inverse synthetic aperture radar SAR ISAR Space based radar Surveillance Target acquisition Motion compensation Signal processing Data processing Avionics</p>
<p>AGARD Conference Proceedings No.459 Advisory Group for Aerospace Research and Development, NATO <b>HIGH RESOLUTION AIR- AND SPACEBORNE RADAR</b> Published October 1989 2,30 pages</p> <p>Imaging techniques are important sources of information in military operations. They may serve for purposes such as target detection and location, reconnaissance, classification and identification of fixed or moving objects as well as for orientation over unknown terrain. Despite considerable advances in electro-optical imaging systems the radar sensor has become an attractive alternative for several reasons: large range performance, penetration of</p> <p>P.T.O.</p>	<p>AGARD-CP-459</p> <p>High resolution radar Synthetic aperture radar Inverse synthetic aperture radar SAR ISAR Space based radar Surveillance Target acquisition Motion compensation Signal processing Data processing Avionics</p>	<p>AGARD Conference Proceedings No.459 Advisory Group for Aerospace Research and Development, NATO <b>HIGH RESOLUTION AIR- AND SPACEBORNE RADAR</b> Published October 1989 2,30 pages</p> <p>Imaging techniques are important sources of information in military operations. They may serve for purposes such as target detection and location, reconnaissance, classification and identification of fixed or moving objects as well as for orientation over unknown terrain. Despite considerable advances in electro-optical imaging systems the radar sensor has become an attractive alternative for several reasons: large range performance, penetration of</p> <p>P.T.O.</p>	<p>AGARD-CP-459</p> <p>High resolution radar Synthetic aperture radar Inverse synthetic aperture radar SAR ISAR Space based radar Surveillance Target acquisition Motion compensation Signal processing Data processing Avionics</p>

<p>weather, smoke, dust and foliage: day and night operation. On the other hand high resolution radar techniques such as synthetic aperture radar (SAR) and inverse synthetic aperture radar (ISAR) promise geometrical resolution of about 1m and less.</p> <p>Papers presented at the Avionics Panel Symposium held in The Hague, Netherlands 8-12 May 1989.</p>	<p>weather, smoke, dust and foliage: day and night operation. On the other hand high resolution radar techniques such as synthetic aperture radar (SAR) and inverse synthetic aperture radar (ISAR) promise geometrical resolution of about 1m and less.</p> <p>Papers presented at the Avionics Panel Symposium held in The Hague, Netherlands 8-12 May 1989.</p>
<p>weather, smoke, dust and foliage: day and night operation. On the other hand high resolution radar techniques such as synthetic aperture radar (SAR) and inverse synthetic aperture radar (ISAR) promise geometrical resolution of about 1m and less.</p> <p>Papers presented at the Avionics Panel Symposium held in The Hague, Netherlands 8-12 May 1989.</p>	<p>weather, smoke, dust and foliage: day and night operation. On the other hand high resolution radar techniques such as synthetic aperture radar (SAR) and inverse synthetic aperture radar (ISAR) promise geometrical resolution of about 1m and less.</p> <p>Papers presented at the Avionics Panel Symposium held in The Hague, Netherlands 8-12 May 1989.</p>